MIMO Antenna Systems for Next Generation Wireless Communications

Thesis by

Evangelos Michailidis

In Partial Fulfillment of the Requirements

for the Degree of

Doctor of Philosophy

Newcastle University

Newcastle upon Tyne, UK

2011

(Submitted)

To Eleftheria, Giorgos and Giannis

Acknowledgements

A journey of epic proportions is approaching its conclusion, intriguing and appealing as it was, gave birth to a deep realization that such journeys are viable only with the support of extraordinary people and institutions.

Foremost, I would like to thank, and express my sincere gratitude to my supervisor Dr. Charalampos Tsimenidis for his guidance, support and encouragement over the course of the PhD study. The motivation, intuition and insight offered to me, in diverse topics ranging from research technical issues to philosophical aspects of life, benefited and shaped an individual towards outstanding qualities, no mater the circumstances.

I will always be indebted to Newcastle University, for giving me the opportunity to study at an advance level in an excellent environment, and for the personal and professional training it provided. Special thanks must go to the Engineering and Physical Sciences Research Council (EPSRC) as it provided much needed funds that made it all possible. Wish also to thank Dr. Greame Chester for the brief yet fruitful discussions we had over the past years at Newcastle University.

My thanks also extend to the people that organise the European School of Antennas; they have created a beautiful theme. I was lucky enough to attend three schools and receive exceptional education in the field of antennas, meet with a truly international participant population and have plenty of fun.

Last yet certainly not least, I want to thank my parents and brother for their unconditional love and support, their patience and understanding during difficult times.

You all believed in me, I thank you for that.

Evangelos Michailidis

Newcastle upon Tyne, February 2010

Abstract

Multiple Input Multiple Output wireless communications systems require as the name implies multiple antennas at the transmit and receive side of a link, as all multiple elements operationally occupy the same spectrum, the capacity of carrying information is increased with no increase in the transmission bandwidth or power. Antennas destined for MIMO systems need to address the issue of adequate isolation between elements and the issue of the diversity performance of the array, these issues become challenging for mobile terminals. In this thesis dual band arrays for the mobile and the access point are proposed along with dual band mutual coupling reduction and radiation pattern improvement methods.

First a dual band two element printed inverted F stacked monopole array is proposed for the mobile terminal. The single elements in the array are easily tuneable and achieve impedance matching from an open stub. The configuration is compact, with radiators distanced at $0.13\lambda_0$. By use of a grid of parasitically coupled printed lines mutual coupling is reduced by 9dB, where at the lower band at 2.4GHz, $S_{12} = -18dB$.

Then a dual band two element printed dipole array is proposed for a pico–micro cell access point. The dipoles are fed by a printed balun which provides wide impedance bandwidth at two bands. To improve the radiation pattern at both frequencies the array is positioned above a dual band frequency selective surface, acting as an artificial magnetic conductor, thus allowing the screen to be placed $0.03\lambda_0$ from the array while maintaining good radiation efficiency.

Finally a brief discussion of dual band surface wave suppression for printed antennas is presented. Here it is suggested that the surface waves can be eliminated by a superstrate at one band and by an EBG lattice at the second band. Initial experiments with different size superstrates and three periods of mushroom type EBG, show that mutual coupling can be reduced and the radiation pattern can be modified.

Contents

List of Figures

List of Tables

Chapter 1

Introduction

"The mind is not a vessel to be filled but a fire to be kindled"

Plutarch

The proliferation of information, with the advance of communication theory and technology can bring new levels of global integration, steady economic development and prosperity, in addition to entertainment, security and biomedical breakthroughs. The demand for data and information has never been greater. New services and technologies are emerging every day with the potential user population increasing steadily. High quality of service, mobility, small size and cost and multi-functionality seem to be of paramount importance to the user, thus being also prerequisites for any service or product in order to be viable and successful.

Probably the first antenna ever used was a wire dipole and a rectangular loop in 1886, wire dipole elements exhibit narrow bandwidth and low gain in the order of 2.15 dB. Until the 20's most antennas were long wire antennas for long wave communications, to improve S/N and reduce interference experimentation drove the early pioneers to place long wire antennas in fresh water or even bury them underground, Taylor in 1917 found that in fresh water performance was 10 time better than underground. Many years later in 1928 Yagi and Uda in Japan discovered the end fire Yagi–Uda antenna which could offer gains in the region of 8–14 dB using parasitic directors but was still narrowband. By 1939 the resonant slot antenna was invented and open wave guide radiators reappeared since their discovery by Lodge and Bose (horn antenna) nearly thirty years ago. In the late 50's and during 60's bandwidth and gain increases were achieved by log periodic and spiral wire antennas (Spiral slot antenna by Turner 1955, equiangular and conical spiral antenna by Dyson 1955 and 1959 respectively, toothed vee log periodic antenna Duhamel and Isbell 1957). The

advancement of air-planes and missile technology required low profile antennas so in the mid 70's conformal (printed) antennas received much research attention, to this day due to mobile communications and the aforementioned, low profile conformal or printed antennas are very attractive and still under rigorous research [7], [8]. Marconi seems to be the first to use an antenna array for his transatlantic wireless telegraphy transmission in 1901. However the first published work of a successful phased array is by Artom, 1906 in Italy. A year later Bellini and Tosi demonstrated direction finding without need for antenna rotation [9], [7].

A brief historical review could not be complete if a time-line towards the discovery, formulation and experimental verification of electromagnetism is not presented. In 1820 H. C. Oersted demonstrated that an electric current produces a magnetic field, in 1831 M. Faraday demonstrated that a changing magnetic field near a conductor can induce an electric current. Maxwell in 1864 predicted radiation, united electricity and magnetism into a complete theory of electromagnetism by adding the displacement current term in Amperes law, he also postulated that light is an electromagnetic wave. Oliver Heavyside during 1885 -87 introduced vector notation and brought Maxwell's equations in the form we use today, these equations are the foundation of our modern society. Heinrich Hertz verified systematically the existence of radio waves in 1885 by demonstrating a dipole antenna attached to an induction coil as a transmitter and a rectangular one turn loop as receiver which he tuned by adding series inductance and shunt capacitance, detecting waves at a distance of 20 meters. Following Hertz, Tesla at Franklin institute, Popov in Russia, Bose in India and Marconi in Bologna demonstrated wireless telegraphy. During 1892 Tesla presented at IRE in London the transmission of intelligence without wires. In 1895 Tesla transmitted signals detected 80 km away, where at the same time in Calcutta India, Bose rang a bell using wireless signals and Popov presented his radio receiver in the Russian physical and chemical society[8]. During 1894–97 Oliver Lodge developed the coherer, a bi-conical dipole antenna, a tune-able LC circuit and a loading coil was also introduced. Marconi seems to be the man that made radio commercial, Marconi's patent on radio was preceded by one submitted by Tesla, a fact that much later was recognised by the US supreme court. Marconi in 1901 used 15 kW and a wavelength of 366 meters (820 kHz) for a transatlantic radio transmission of the letter *s* in Morse code. He appears to be the first person to measure and publish an

antenna polar diagram, in 1906 [10] [11] [7].

Modern wireless communication devices allow people and machines to communicate with each other freely in a totally mobile manner that is location independent. The most common and widely used wireless system to this day is the cellular GSM. But this is about to change with the development, evolution and arrival of wireless access technologies such as 4G (4th Generation) which will succeed 3G, this could be delivered by the continuous development of MIMO, OFDM and a combination of software defined and cognitive radio. IEEE 802.11n Wireless Local Area Network is an emerging protocol which will offer significant increases over past WLAN systems namely (802.11a,b,g), it can achieve rates of 600 Mbps at its initial deployment. IEEE 802.16 Worldwide interoperability for Microwave Access (WiMAX) which is marketed as a broadband wireless connectivity with data rates of up to 70 Mbps will cover urban, suburban, buildings, and rural areas mimicking the GSM–CDMA infrastructure. IEEE 802.15.4 and 802.15.1 Wireless Personal Area Networks describe the ZigBee and Bluetooth technologies which relate to short range communications and to wireless sensor networks, advances here might take the Ultra Wide Band approach, in [12] they propose data rates of 480 Mbps with average Tx power of -10.3 dBm, antennas of 0 dBi flat gain, operating in the frequency range of 3168–4752 MHz, employing multiband OFDM, also frequency hopping is mandatory where if a narrow band interferer is detected then sub band is switched off for coexistence and systems hops to alternative sub band.

Handheld mobile phones that can be found in the market today may be able to operate at up to four cellular GSM bands in addition to having GPS and Bluetooth functionality (some can even be Wi-Fi enabled). The ability to provide these functions in a board space so limited and cramped as the one found in mobile phones and PDAs clearly illustrates the advancement of antenna, RF front end and DSP technology.

In figure one a number of devices found in an average home is illustrated, there is a trend to move towards a wireless interconnectivity of all user hardware, for example one might want to stream satellite High Definition TV signals around different rooms in his property, or maybe send video or still images from a camera to a printer, a projector or a HD TV all wirelessly and virtually instantly need not forget the demand and requirements generated towards the operators and infrastructure,

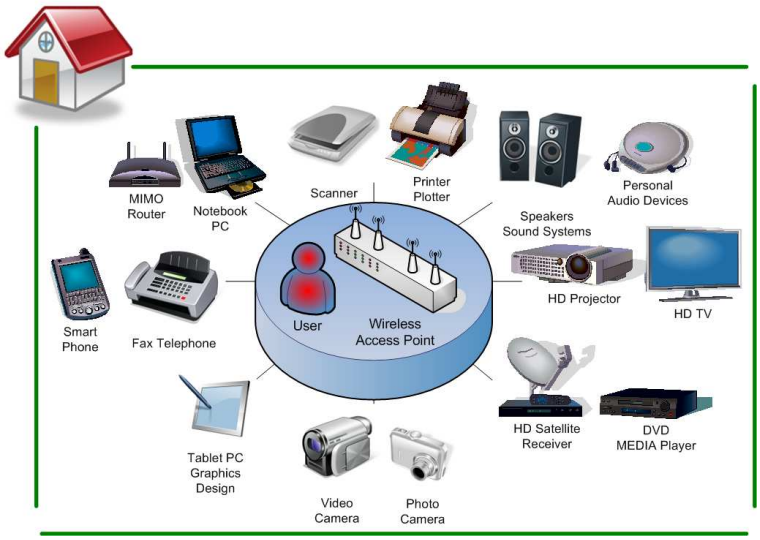

Figure 1.1: Personal, Home user applications

consider for example watching a live feed of your living room taken from your home video camera, on your smart phone while you are at another continent . There is one question that begs to be asked. Given the restrictions and the congestion of allocated spectrum, the small bandwidth assigned to different protocols, given the intense interference from other users and other appliances, given the restriction on power of mobile devices, and finally but most importantly the upper bound on a systems capacity imposed by Shannon law, is it possible to say goodbye to copper wires? Is it possible to make wireless the access technology in the majority if not all future platforms? Fortunately the answer seems to be a clear yes we can. So then a second question needs to be addressed, how?

The answer in this question, unfortunately is not as clear as before, nevertheless there exist a number of emerging technologies that can provide and accommodate the proliferation of information. One of the most promising is Multiple Input Multiple Output systems(MIMO), fairly one can claim MIMO as a Radio Renaissance, an improvement by orders of magnitude on existing systems.

MIMO systems were first proposed by Jack H Winters in 1987 [13], in this landmark paper, he investigated the data rates of multiple antenna systems. In the paper the authors study two communication cases. Case one considers communication between multiple mobile stations each with one antenna and a base station with multiple antennas. The base station has M antennas and the maximum data rate is observed as up to M mobile stations access the system. The second case

considers communication between two users each with multiple antennas, consisting of a receiver with up to M antennas and a transmitter with M antennas. The data rate for each of the channels between Tx and Rx is studied.

For the case of base station with M antennas and multiple M mobile stations attempting to access the system, under linear receiver processing at the base station the authors show that up to $M/2$ can access the system with an efficiency index that is approximate to the single channel efficiency index, while with M mobile stations the efficiency index is considerably lower than that of the equivalent single channel. When optimum non-linear processing is used at the base station then the efficiency index is approximately equal to the equivalent single channel as up to M mobile stations are accessing the system.

For the second case where two users are communicating, with M antennas at the transmit side and up to M antennas at the receive side once more the efficiency index is observed for two signal processing scenarios. The efficiency index per transmit antenna, ie per channel is similar to that per mobile station in case of multiple mobile stations under the same signal processing schemes.

Winters concluded that up to M independent channels can exist, each supporting the SISO data rate, thus producing a system of high spectral efficiency, achieving large capacities given a small and limited bandwidth. Eleven years latter Foschini and Gans published a paper [14] providing an analysis on the theoretical limit of MIMO systems, at the same period Telatar [15] wrote on the capacity of multi-antenna Gaussian channels. Foschini's team at Bell Labs proposed signal processing techniques that could achieve high rates [16] [17] [18]. The two signal processing approaches introduced at that time was V-BLAST and D-BLAST, standing for Vertical and Diagonal Bell Laboratories Layered Space Time respectively. A level of excitement also came when Alamouti [19] and Tarokh [20] published their work on space time trellis and block coding techniques in order to improve link level performance based on diversity. Alamouti investigated transmit diversity and concluded that a system with N transmit antennas and M receive antennas can achieve a diversity order of NM, with no increase in bandwidth and with system complexity comparable to Maximal Ratio Combining.

1.1 The Need for MIMO systems

There is a definitive need for MIMO systems in wireless communications, over the past decade every aspect of such systems is under intensive research by organizations and institutions across the globe, the research output is large and deployment is matter of short time. Nevertheless a short review of basic information theory developments will illustrate the necessity towards MIMO. In 1928 H. Nyquist investigated the maximum signaling rate without inter symbol interference over telegraph lines of given bandwidth using steady state characteristics. He formed the Nyquist sampling theorem which states that a function with highest frequency ω can be fully reconstructed by a series of samples spaced $\frac{1}{2}\omega$ seconds apart. The maximum pulse rate is 2ω. He also derived the optimum pulse shape [21] [22]

$$g(t) = \frac{\sin(2\pi\omega t)}{2\pi\omega t}. \tag{1.1}$$

Using this pulse shape, the function can be reconstructed by the samples, where α_n is the n^{th} sample

$$f(t) = \sum_{n=-\infty}^{+\infty} \alpha_n \frac{\sin(\pi(2\omega t - n))}{\pi(2\omega t - n)}. \tag{1.2}$$

At the same time in 1928 Hartley considered the amount of data that can be reliably transmitted over a band-limited channel using multiple amplitudes, thus introducing PCM. A system having M levels can store $\log_2 M$ information units (considering binary system). The channel can then possibly transmit $\log_2 M$ binary units on total time T. In other words M represents the number of different signal functions presented to the channel each of duration T. The rate or capacity is [23] [24]

$$C = \lim_{T\to\infty} \frac{\log_2 M}{T}. \tag{1.3}$$

C. Shannon in 1948 based on Nyquist and Hartley invented information theory, he developed a logarithmic measure of the information content of a source and defined channel capacity including the effects of transmit power, of bandwidth constrain and the additive white noise. Denoting P as the average transmit power, assuming white thermal noise of power N over band W, then by highly complex encoding,

transmission with low frequency of errors is possible at a rate [22]

$$C = W \log_2 \frac{P+N}{N}. \tag{1.4}$$

Today encoding techniques are very powerful, Turbo codes for instance invented by Berrou [25] in 1993 can achieve bit error rates of 10^{-5} at SNR within $1dB$ of the Shannon channel capacity [26]. Turbo codes are a combination of parallel concatenation of convolutional or recursive systematic block codes with non uniform interleaving and iterative decoding.

Shannon [22] clearly states that this rate can not be achieved by any finite encoding process, but can only be approximated closely. The equation clearly shows that the main effect of noise is not on the reliability of communication but on the speed of communication. Shannon also points out as we approximate more closely, then the transmitted signal approaches white noise in statistical properties, the frequency of errors approaches zero, also for noise levels higher than the designed value errors increase rapidly, and finally the required delays at TX and Rx increase indefinitely. Under these assumptions the channel capacity equation becomes

$$C = W \log_2 \Big(1 + \frac{P}{N}\Big). \tag{1.5}$$

Bandwidth efficiency is a measure of how efficiently a system uses its allocated bandwidth. It is defined as

$$\eta = \frac{TransmissionRate}{CannelBandwidth} \quad \text{bits/s/Hz}. \tag{1.6}$$

From the bandwidth efficiency definition the Shannon limit can be obtained and is as follows

$$\eta_{max} = \log_2(1+\varrho) \quad \text{bit/s/Hz}, \tag{1.7}$$

where ϱ stands for signal to noise ratio. Shannon law shows that there is a limit on the transmission rate dictated by the link SNR, it is clear however that for every extra bit/s/Hz we would need to roughly double the transmit power.

Let us now examine some ways to improve channel capacity and spectral efficiency. Considering single user communications, under the assumption of no other

technologies operating in the vicinity of the spectrum, signal to noise ratio can be increased by higher transmit power, however this is not a good idea for a myriad of reasons, as for example battery life of mobile terminals, amplifier linearity, heat dissipation and most importantly for health related issues to name a few. On the other hand multiple access systems allow many users to share the same spectrum resource, in addition to different technologies with multiple users sharing the same spectrum. In an environment of this kind SNR is dictated by thermal noise and by interference by other users and sources, so raising Tx power will increase interference problems.

Interestingly enough in 2006 a report [1] was compiled on behalf of Ofcom investigating the possibility and the effects of raising the power at the unlicensed band. The industry and regulators wanted to know if higher powers are viable and if there is a potential profit due to market expansion by better coverage servicing more users. Of course coexistence should always be in mind. Table 1.1 provides current power limits for the ISM bands.

Table 1.1: ISM Band Power Limits [1]

	Frequency GHz	**Use**	**Max EIRP**	**Typical Tx Power and Antenna Gain**
	2.4 - 2.483.5	indoor - outdoor	20 dBm	17 dBm Tx P, 3 dB AG
Band A	5150 - 5350	indoor only	23 dBm	15 dBm Tx P, 8 dB AG
Band B	5470 - 5725	outdoor nomadic (RLAN)	30 dBm	23 dBm Tx P, 7 dB AG
Band C	5725 - 5875	indoor - outdoor	33 dBm	23 dBm Tx P, 10 dB AG

The report [1] clearly identifies other systems that operate in these bands causing coexistence issues. At 2.4 GHz MoD seems to be a strong user having applications like fixed and mobile services and airborne telemetry. There are some active RFID devices operating in this band although the majorities work at 315 and 433 MHz. Also issues with AVI Automatic Vehicle Identification monitoring rail, Bluetooth and analogue video senders can be affected. In the same report they point out clearly coexistence issues for all three bands at 5 GHz. Band A shares spectrum with, fixed and mobile satellite services (ie. Globalstar offering satellite mobile telephony), with EESS (Earth Exploration Satellite Service) Europe operates Envisat here (affects Band B also), with MoDs radiolocation service having radars of fixed or hopping frequency (affects Band B and C). Band B shares spectrum with Maritime Radionavigation serving weapon radars and vessel trafficking, with Deep space

research stations, ESA operates a few. Finally Band C coexists with fixed satellite services in geostationary orbits and land mobile services of governmental use. So clearly the issue is complex and requires a more inventive approach than just raising the power.

An IEEE task group also addressed the issue of coexistence in a technical report [27] . They investigated geometric and temporal interfering. Symbiosis of 802.11n with IEEE 802.15.1 personal area network, IEEE 802.16 broadband wide area network and DECT telephony was examined. As opposed to [1], the authors here delve into the PHY layer and suggest issues and recommendations as some of the protocols were still on draft status

Evidently link performance can be enhanced not by increasing the Tx power but by diversity techniques and optimal combining methods. A multiple input single output system with an antenna array and channel information at the transmitter side can provide transmit diversity which will reduce the effects of multipath. A slow logarithmic grow of capacity relative to the number of antennas can be achieved.

$$\eta_{MISO} = \log_2 \left(1 + \frac{\varrho}{N} \sum_{i=1}^{N} |h|^2\right) \quad \text{bits/s/Hz} \ . \tag{1.8}$$

The received signal of a MISO system with two transmit antennas and one receive antenna is

$$y = \sqrt{P_t} h_1 \cdot w_1 x + \sqrt{P_t} h_2 w_2 x + n, \tag{1.9}$$

$$y = \sqrt{P_t} \begin{pmatrix} h_1 & h_2 \end{pmatrix} \begin{pmatrix} w_1 \\ w_2 \end{pmatrix} x + n, \tag{1.10}$$

where both antennas transmit the same set of data x, however the first antenna applies a weight w_1 to data and the second antenna applies weight w_2 to data, in essence creating Tx diversity by beamforming.

If we Consider a single input multiple output system, where one antenna exists at the Tx side and two antennas at the Rx, then the receiver can perform one of the diversity combining methods, the signal received by the antennas are

$$y_1 = \sqrt{P_t} \cdot h_1 \cdot x + n, \tag{1.11}$$

$$y_2 = \sqrt{P_t} \cdot h_2 \cdot x + n, \tag{1.12}$$

$$\begin{pmatrix} y_1 \\ y_2 \end{pmatrix} = \sqrt{P_t} \begin{pmatrix} h_1 \\ h_2 \end{pmatrix} x + \begin{pmatrix} n_1 \\ n_2 \end{pmatrix}. \tag{1.13}$$

The optimal diversity combining method is MRC (maximal ratio combining), assuming perfect CSI then the output of the MRC is

$$r = \sqrt{P_t}(|h_1|^2 + |h_2|^2)x + \begin{pmatrix} {h_1}^* & {h_2}^* \end{pmatrix} \begin{pmatrix} n_1 \\ n_2 \end{pmatrix}. \tag{1.14}$$

The capacity of a SIMO system is given by

$$\eta_{SIMO} = \log_2 \left(1 + \varrho \cdot \sum_{i=1}^{M} |h|^2\right) \quad \text{bits/s/Hz}. \tag{1.15}$$

A multiple input multiple output system in contrast with SISO, SIMO and MISO systems takes advantage of the multipath environment. Unique parallel spatial channels are enabled operating on identical frequencies and bandwidths. A linear growth of capacity in relation with number of antennas can be achieved. BLAST and all of its variants are spatial multiplexing techniques. Consider a 2×2 MIMO system. The input data x are split into two streams x_1 and x_2 which are respectively directed to the two transmit antennas. The transmitted vector is then given by

$$x = \sqrt{\frac{P_t}{2}} \begin{pmatrix} x_1 \\ x_2 \end{pmatrix}. \tag{1.16}$$

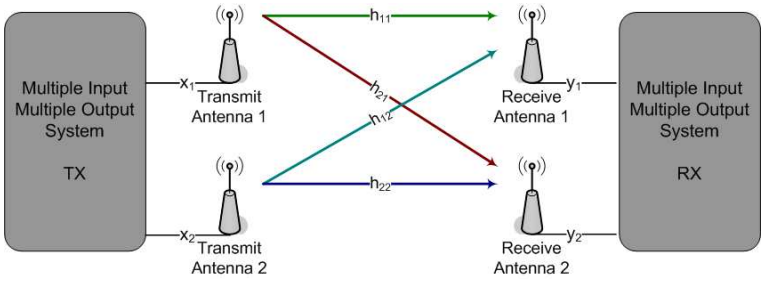

Figure 1.2: MIMO block diagram

The square root factor maintains the transmit power at PT. The noise vector has dimensions of 2x1 and is assumed to be white in both space and time with a

covariance matrix $\sigma^2 \cdot I$. The receive signals are

$$y_1 = \sqrt{\frac{P_t}{2}} h_{11} x_1 + \sqrt{\frac{P_t}{2}} h_{12} x_2 + n_1, \tag{1.17}$$

$$y_2 = \sqrt{\frac{P_t}{2}} h_{21} x_1 + \sqrt{\frac{P_t}{2}} h_{22} x_2 + n_2, \tag{1.18}$$

$$\begin{pmatrix} y_1 \\ y_2 \end{pmatrix} = \sqrt{\frac{P_t}{2}} \begin{pmatrix} h_{11} & h_{12} \\ h_{21} & h_{22} \end{pmatrix} \begin{pmatrix} x_1 \\ x_2 \end{pmatrix} + \begin{pmatrix} n_1 \\ n_2 \end{pmatrix}. \tag{1.19}$$

If we multiply the received vectors with the pseudo inverse of the channel matrix then the transmitted signals can be recovered. By doing so the effect of the channel on the transmit vector is removed [28]

$$\hat{X} = \frac{H^*}{\sqrt{\frac{P_t}{2}} H^* H} Y = X + \frac{H^*}{\sqrt{\frac{P_t}{2}} H^* H} N. \tag{1.20}$$

It is clear that the received noise vector is multiplied by H, this causes the noise to be amplified thus reducing the SNR and the probability of correct detection. The procedure described is called zero forcing equalisation and is not optimal [28]. Spatial multiplexing with M transmit and N receive antennas can transmit min(M,N) symbols per transmit vector, hence high spectral efficiency and bit rates are possible, however due to noise amplification it does not provide robust communication as the SNR varies considerably. The general equation providing the MIMO capacity is

$$\eta_{MIMO} = \log_2 \left[det(\mathbf{I_M} + \frac{\varrho}{M} \cdot \mathbf{H}\mathbf{H}^\dagger) \right] \quad \text{bit/s/Hz}. \tag{1.21}$$

In figure 1.3 on the left, a comparison of the spectral efficiency between a SISO (1×1), a MISO(1×4), a SIMO(4×1) and a MIMO(4×4) system are plotted against average SNR. The MIMO configuration seems to have nearly a five fold increase of spectral efficiency compared to the SISO case, however it must be stressed that this improvement is valid under certain conditions that are prerequisites for adequate excitation of all spatial data streams, a detailed discussion will follow later in the report. On the right the cumulative distribution function for all systems mentioned earlier is provided at a receive SNR of 10dB. The increase in capacity of MIMO

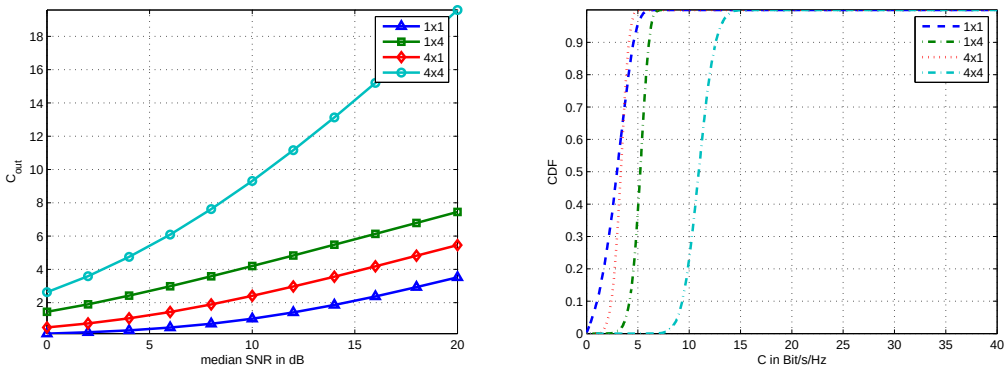

Figure 1.3: Capacity comparison

systems is amazing, this is also illustrated in table 1.2 where physical layer details of different 802.11 protocols are compared, the n standard with four antennas at each side of the link and with an increase on channel bandwidth from twenty to forty megahertz can achieve rates up to 600 Mbps.

Table 1.2: IEEE 802.11 PHY [2]

	802.11	**802.11b**	**802.11a**	**8802.11g**	**802.11n**
PHY	DSSS	DSSS/CCK	OFDM	OFDM DSSS/CCK	SDM/OFDM
Data Rate	1,2 Mbps	5.5,11 Mbps	6-54 Mbps	1-54 Mbps	6-600 Mbps
Frequency	2.4 GHz	2.4 GHz	5 GHz	2.4 GHz	2.4 and 5 GHz
Cnannel	25 MHz	25 MHz	20 MHz	25 MHz	20 and 40 MHz

1.1.1 The Physical Environment Factors

One very important factor to consider when a designer is to select a band is its propagation characteristics, path loss and attenuation due to scattering and absorption phenomena are important and should be taken in to account. At low frequencies radio waves propagate longer distances and penetrate materials easier, the drawback is that antennas need to be large. At high frequencies there is more bandwidth and small antennas can be fabricated, however path loss is high and antennas usually are of low gain due to their size. It seems there is a golden area in the spectrum which is desired by most radio operators, this is ideally in the range of 1 to 6 GHz due to the aforementioned.

The most important propagation phenomena that take place when radio waves interact with obstacles composed of any type material are illustrated in figure 1.4. Reflection at an interface between two media requires all or part of the waveform

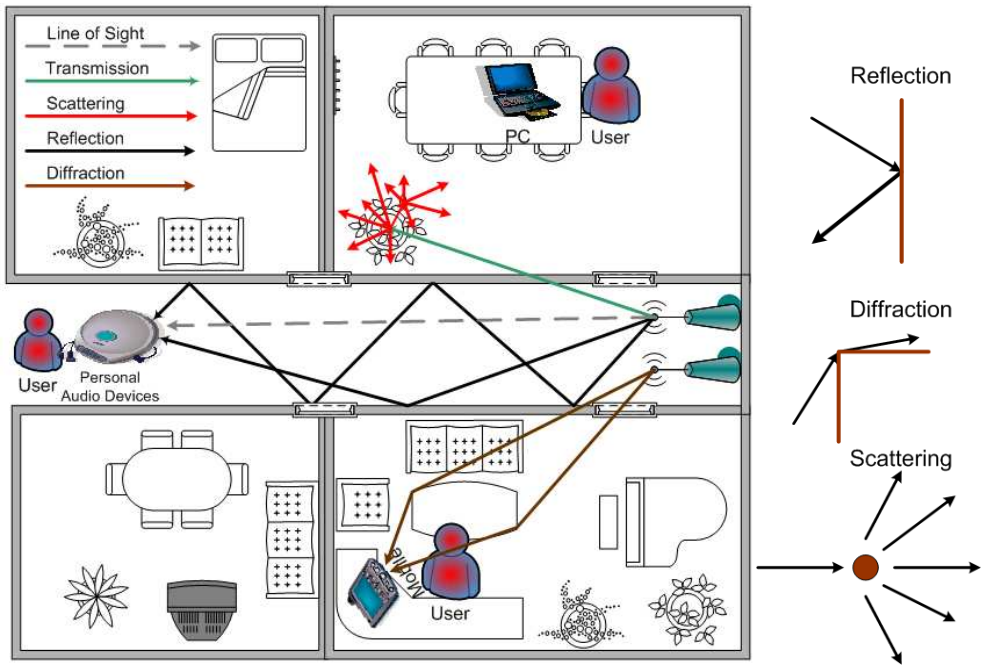

Figure 1.4: Simple indoor space

returning in the original media, in the picture is presented by the bouncing of rays on the walls. Scattering is the random dispersion of radiation over large spread due to electrically small non uniformities of the media, in the picture this is presented by the diffusion of rays that strike the plant. Refraction takes place when a wave changes its direction upon transmission into a different media due to the change of its speed. Diffraction is the bending of the radio rays usually due to sharp edges, an example is the deformation of light through an aperture, in the picture this is presented by the bending of rays at the edges of the table [29].

It worth pointing to an interesting report at this point. In [30] they examine the effects of using frequency selective surfaces as wall papers to buildings in order to control the propagation of radio waves in and out of buildings. This surfaces can act as band stop or band pass filters, thus enhancing coverage where needed (ie better TETRA coverage in black spots) or equivalently reducing it (ie for security, health issues, interference etc.)

1.1.2 Indoor Channel

A decent channel model must be able to accurately represent the angular power spectrum, the power delay profile the polarization and clustering of waves and the fact that the angle of arrival can depend on angle of departure. It is needless to

say that it should also be independent of the antennas so that can be applied to any system. Erceg [6] have proposed six channel models based on an extension of the Saleh–Valenzuela model. These models describe a range of different indoor propagation scenarios for example, they model propagation in environment like hot spots, large office space, small office and residential. The properties of channel B which is valid for residential use are given in table 1.3. Two main clusters are proposed in B, as a contrast to model F which represents a large space hot spot and consists of six clusters with much larger excess delay. The unit of excess delay at table 1.3 is nano seconds.

Table 1.3: Indoor channel model B [2]

		Cluster 1					**Cluster 2**				
Tap number	Excess delay [ns]	Power [dB]	AoA [deg]	AS Rx [deg]	AoD [deg]	AS Tx [deg]	Power [dB]	AoA [deg]	AS Rx [deg]	AoD [deg]	AS Tx [deg]
1	0	0	4.3	14.4	225.1	14.4					
2	10	-5.4	4.3	14.4	225.1	14.4					
3	20	-10.8	4.3	14.4	225.1	14.4	-3.2	118.4	25.2	106.5	25.4
4	30	-16.2	4.3	14.4	225.1	14.4	-6.3	118.4	25.2	106.5	25.4
5	40	-21.7	4.3	14.4	225.1	14.4	-9.4	118.4	25.2	106.5	25.4
6	50						-12.5	118.4	25.2	106.5	25.4
7	60						-15.6	118.4	25.2	106.5	25.4
8	70						-18.7	118.4	25.2	106.5	25.4
9	80						-21.8	118.4	25.2	106.5	25.4

For link budget and for range evaluation a path loss model in needed. Path loss leads to overall signal decrease. The shadowing effect modifies received power due to variation of particular obstructions between Tx and Rx. Fast fading results from multiple waves arriving at the receiver where they add constructively or destructively. The Friis transmission formula is [31]

$$\frac{P_r}{P_t} = G_a G_b \Big(\frac{\lambda}{4\pi r}\Big)^2. \tag{1.22}$$

Can be rearranged to express the free space path loss, note the square on r and λ

$$L_f = \frac{P_t G_a G_b}{P_r} = \Big(\frac{4\pi r}{\lambda}\Big)^2. \tag{1.23}$$

In decibels, with r in km and f in MHz

$$L_f(dB) = 32.4 + 20\log_{10} r_{km} + 20\log_{10} f_{MHz}. \tag{1.24}$$

Free space loss increases by 6 dB for each doubling of r or f. The indoor propagation

model proposed in [6] and used by the 802.11 task group consists of free space loss where slope of curve is 2 up to a breakpoint and after the breakpoint slope is 3.5. Breakpoint distance for channel model B is 5 meters while for E is 20. This path model [6] includes shadow fading due to particular obstructions [2], where in equation 1.26, L_f is the free space path loss, r is the distance between the Tx and Rx, and SF represents the shadow fading in decibels,

$$L_{dB} = L_f + SF \quad r < breakpoint, \tag{1.25}$$

$$L_{dB} = L_f + 35\log_{10}\frac{r}{r_{br}} + SF \quad r > breakpoint. \tag{1.26}$$

In these models line of sight conditions are assumed before the breakpoint and non line of sight after. If shadow fading is included in the path loss model then it can be considered as a random variable, as illustrated by equation 1.27, letting x denote the shadowing component, a zero mean Gaussian random variable with a standard deviation of σ_{SF} which is in decibels and depends on factors such as frequency and environment. At the breakpoint distance the shadow fading standard deviation can have a transition. The probability density function of shadow fading is usually modeled by a log normal function

$$\rho_{SF}(x) = \frac{1}{\sqrt{2\pi}\sigma_{SF}} e^{\left(\frac{-x^2}{2\sigma_{SF}^2}\right)}. \tag{1.27}$$

Simply stated this is due to the fact that on a radius of constant distance around a Tx the obstacles and obstructions will be significantly different, however the received signal power in decibels around this radius follows a log normal distribution.

1.2 Wave Equation

By inspection of Maxwell-Faraday equation (1.28) and Amperes law with Maxwell's correction (1.29) it is evident that a changing magnetic field creates a changing electric field, which automatically creates a changing magnetic field, which can also be created by electrical currents, thus supporting the propagation of energy. [3] Gauss law (1.30) describe the relation between electric field and electric charges which are physically realisable and do exist, while Gauss law for magnetism (1.31) states that

there are no magnetic charges and these do not exist in the real world. Nevertheless, although magnetic charge and thus magnetic current densities do not really exist, they are introduced to Maxwell's equations because they aid the formulation and solution of many complex problems. A fair and intuitive example of the use of fictitious impressed magnetic currents is contained in solutions that utilise the field equivalence principle. Following, Maxwell's equations are written in two columns, on the left the true real world equations are stated, while on the right hand side the same equations are reproduced with the addition of impressed magnetic current density and magnetic charge respectively.

$$\nabla \times \mathbf{E} = -\frac{\partial \mathbf{B}}{\partial \mathbf{t}}, \qquad \nabla \times \mathbf{E} = -\mathbf{M} - \frac{\partial \mathbf{B}}{\partial \mathbf{t}}, \tag{1.28}$$

$$\nabla \times \mathbf{H} = \mathbf{J} + \frac{\partial \mathbf{D}}{\partial \mathbf{t}}, \qquad \nabla \times \mathbf{H} = \mathbf{J} + \frac{\partial \mathbf{D}}{\partial \mathbf{t}}, \tag{1.29}$$

$$\nabla \cdot \mathbf{D} = \varrho_e, \qquad \nabla \cdot \mathbf{D} = \varrho_e, \tag{1.30}$$

$$\nabla \cdot \mathbf{B} = 0, \qquad \nabla \cdot \mathbf{B} = \varrho_m. \tag{1.31}$$

The integral form of Maxwell's equations can be obtained by the use of Stokes and divergence theorems.

The constitutive parameters are related to the molecular structure of materials and account for the alteration of electromagnetic waves due to the charged particles in the media. Materials in general can be classified as, linear when the constitutive parameters are not a function of the applied field or else non-linear, homogeneous when the parameters are not a function of position or else non-homogeneous, non-dispersive if the parameters are not a function of frequency or else dispersive, and as isotropic when the parameters are not a function of the direction of applied field or else anisotropic. [3] Consequently since they have such dependencies they are represented by a tensor of rank two (a dyad), where each entry can be complex. The electric flux density $\mathbf{D}$, the electric field intensity $\mathbf{E}$, and the permittivity tensor are related as follows,

$$\mathbf{D} = \varepsilon \cdot \mathbf{E} \Rightarrow \begin{bmatrix} D_x \\ D_y \\ D_z \end{bmatrix} = \begin{bmatrix} \varepsilon_{xx} & \varepsilon_{xy} & \varepsilon_{xz} \\ \varepsilon_{yx} & \varepsilon_{yy} & \varepsilon_{yz} \\ \varepsilon_{zx} & \varepsilon_{zy} & \varepsilon_{zz} \end{bmatrix} \begin{bmatrix} E_x \\ E_y \\ E_z \end{bmatrix}, \tag{1.32}$$

$$\mathbf{D} = \varepsilon \cdot \mathbf{E}, \tag{1.33}$$

$$\mathbf{B} = \mu \cdot \mathbf{H}, \tag{1.34}$$

$$\mathbf{J} = \sigma \cdot \mathbf{E}. \tag{1.35}$$

Equations 1.34 and 1.35 illustrate the relations of the permeability and conductivity tensors.

The partial differential equations 1.28 and 1.29 are coupled, to uncouple them their order must increase from first to second. After taking the curl of both sides and applying a vector identity the following two wave equations arise

$$\nabla^2\mathbf{E} = \nabla \times \mathbf{M} + \mu\frac{\partial \mathbf{J}}{\partial t} + \frac{1}{\varepsilon}\nabla\varrho_e + \mu\sigma\frac{\partial \mathbf{E}}{\partial t} + \mu\varepsilon\frac{\partial^2\mathbf{E}}{\partial t^2}, \tag{1.36}$$

$$\nabla^2\mathbf{H} = -\nabla \times \mathbf{J} + \sigma\mathbf{M} + \frac{1}{\mu}\nabla\varrho_m + \varepsilon\frac{\partial \mathbf{M}}{\partial t} + \mu\sigma\frac{\partial \mathbf{H}}{\partial t} + \mu\varepsilon\frac{\partial^2\mathbf{H}}{\partial t^2}. \tag{1.37}$$

These equations contain the fictitious magnetic charge and current and their physical electric counterparts, they represent regions where sources and losses are present. For source free but lossy regions just replace $J = \varrho_e = 0$ and $M = \varrho_m = 0$ thus

$$\nabla^2\mathbf{E} = \mu\sigma\frac{\partial \mathbf{E}}{\partial \mathbf{t}} + \mu\varepsilon\frac{\partial^2\mathbf{E}}{\partial \mathbf{t^2}}, \tag{1.38}$$

$$\nabla^2\mathbf{H} = \mu\sigma\frac{\partial \mathbf{H}}{\partial \mathbf{t}} + \mu\varepsilon\frac{\partial^2\mathbf{H}}{\partial \mathbf{t^2}}. \tag{1.39}$$

For time harmonic fields the partial derivatives can be replaced as follows $\partial/\partial t \Rightarrow j\omega$ and $\partial^2/\partial t^2 \Rightarrow -\omega^2$, hence the time harmonic, source free and lossy wave equations are

$$\nabla^2\mathbf{E} = j\omega\mu\sigma\mathbf{E} - \omega^2\mu\varepsilon\mathbf{E} = \gamma^2\mathbf{E}, \tag{1.40}$$

$$\nabla^2\mathbf{E} = j\omega\mu\sigma\mathbf{H} - \omega^2\mu\varepsilon\mathbf{H} = \gamma^2\mathbf{H}, \tag{1.41}$$

$$\gamma^2 = j\omega\mu\sigma - \omega^2\mu\varepsilon = j\omega\mu(\sigma + j\omega\varepsilon). \tag{1.42}$$

In rectangular coordinates the electric field can be represented as

$$E(x, y, z) = \hat{a}_x E(x, y, z) + \hat{a}_y E(x, y, z) + \hat{a}_z E(x, y, z), \tag{1.43}$$

for a source free but lossy region the following scalar equations can be obtained

$$\nabla^2 E_x(x,y,z) - \gamma^2 E_x(x,y,z) = 0, \tag{1.44}$$

$$\nabla^2 E_y(x,y,z) - \gamma^2 E_y(x,y,z) = 0, \tag{1.45}$$

$$\nabla^2 E_z(x,y,z) - \gamma^2 E_z(x,y,z) = 0. \tag{1.46}$$

If we now consider a uniform plane wave, existing in lossy media, having a y component and travelling along z then we have the following field expression

$$E(z) = \hat{a}E_y(z) = \hat{a}_y\Big({E_0}^+ e^{-\gamma z} + {E_0}^- e^{+\gamma z}\Big) = \hat{a}_y\Big({E_0}^+ e^{-\alpha z}e^{-j\beta z} + {E_0}^- e^{+\alpha z}e^{+j\beta z}\Big), \tag{1.47}$$

α and β are the real and imaginary parts of the propagation constant γ, which

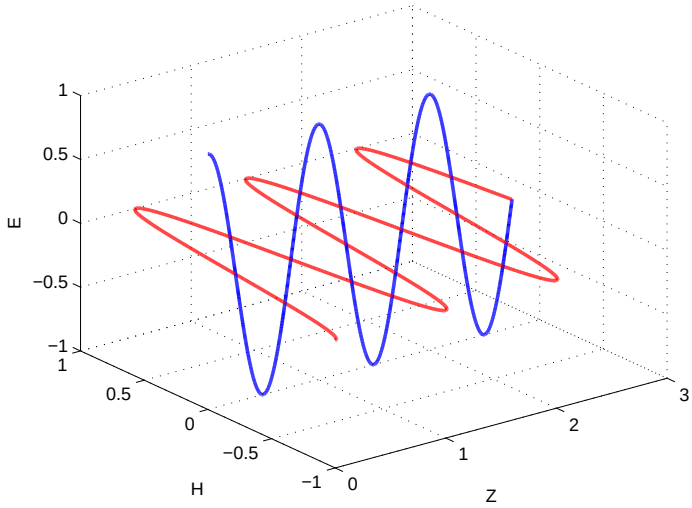

Figure 1.5: E and H fields

represent the attenuation and phase constant respectively, γ was introduced to the wave equation

$$\gamma = \alpha + j\beta = \sqrt{j\omega\mu(\sigma + j\omega\varepsilon)} = \sqrt{-\omega^2\mu\varepsilon + j\omega\mu\sigma}. \tag{1.48}$$

The values for α and β can be obtained from the following relations

$$\alpha = \omega\sqrt{\mu\varepsilon}\left\{\frac{1}{2}\left[\sqrt{1+\left(\frac{\sigma}{\omega\varepsilon}\right)^2}-1\right]\right\}^{\frac{1}{2}}, \tag{1.49}$$

$$\beta = \omega\sqrt{\mu\varepsilon}\left\{\frac{1}{2}\left[\sqrt{1+\left(\frac{\sigma}{\omega\varepsilon}\right)^2}+1\right]\right\}^{\frac{1}{2}}. \tag{1.50}$$

Thus, given the dielectric constant, the conductivity, the permittivity and the frequency of interest one can readily calculate the attenuation per unit distance and the phase (propagation) constant in the media under study. Lossy media are represented by non zero conductivity. Table 1.3 provides typical values for few common materials found in urban propagation.

Table 1.4: Conductivity and dielectric constant of materials [3]

Material	ε	σ	**tan** δ
Glass	4–7	10^{-12}	10^{-3}
Limestone	7.5	0.03	
Fresh water	81	0.01	
porcelain	6	10^{-14}	$14x10^{-3}$
dry soil	2.8	10^{-4}–10^{-3}	$7x10^{-4}$
plexiglass	3.45	$5.1x10^{-3}$	$4x10^{-2}$
paper	3		$8x10^{-3}$
rubber	2.5–3	10^{-15}	$2x10^{-3}$
dry wood	1.5–4		$1x10^{-2}$

The wave number vector (β or k) indicates spatial propagation properties of the field, it actually provides the number of waves per unit distance on any of the spatial directions

$$\beta^2 = \omega^2\varepsilon\mu = |k^2| = {k^2}_x + {k^2}_y + {k^2}_z. \tag{1.51}$$

1.2.1 Polarization

Polarisation of a wave describes the alignment and locus that the electric field vector projects over time relative to the propagation direction. All polarisation states can be represented by an electric field vector consisting of an x and y component. Depending on the magnitude of the two components and the phase difference between them, three polarisation states are defined, linear , circular and elliptic.[32]

$$E(z;t) = \hat{a}_x E_x(z;t) + \hat{a}_y E_y(z;t), \tag{1.52}$$

$$E(z;t) = E_x \cos(\omega t + kz + \phi_x) + E_y \cos(\omega t + kz + \phi_y). \tag{1.53}$$

Where, $E(z;t)$ is the instantaneous electric field, E_x and E_y are the x and y components of the field, ϕ is the phase angle, $\Delta\phi$ is the phase angle difference, z is the direction of propagation, ω is the angular frequency, t is the time, and k is the wave number, while CW and CCW represent clock wise and counter clockwise rotation of the electric filed vector.

- Linear

  The phase difference between the two field components must be as follows

$$\Delta\phi = \phi_y - \phi_x = n\pi \quad n = 1, 2, 3 \ldots \tag{1.54}$$

- Circular

  The two field components must be equal and the phase difference must be $90°/-90°$

$$|E_x| = |E_y|, \tag{1.55}$$

$$\Delta\phi = \phi_y - \phi_x = \begin{cases} +\left(\frac{1}{2} + 2n\right)\pi & n = 1, 2, 3, \ldots \quad CW \\ -\left(\frac{1}{2} + 2n\right)\pi & n = 1, 2, 3, \ldots \quad CCW. \end{cases} \tag{1.56}$$

- Elliptical The two field components are not equal and the phase difference is either a multiple of $\pm(\pi/2)$ or not

$$|E_x| \neq |E_y|, \tag{1.57}$$

$$\Delta\phi = \phi_y - \phi_x = \begin{cases} +\left(\frac{1}{2} + 2n\right)\pi & n = 1, 2, 3, \ldots \quad CW \\ -\left(\frac{1}{2} + 2n\right)\pi & n = 1, 2, 3, \ldots \quad CCW, \end{cases} \tag{1.58}$$

  or,

$$\Delta\phi = \phi_y - \phi_x \neq \pm\frac{n}{2}\pi \begin{cases} > 0 & n = 1, 2, 3, \ldots \quad CW \\ < 0 & n = 1, 2, 3, \ldots \quad CCW. \end{cases} \tag{1.59}$$

1.2.2 The propagation Environment

When a travelling radiowave comes into contact with a flat obstruction object having dimensions larger than the wavelength and with different material parameters than the propagation media, then part of the incident wave will be reflected and part

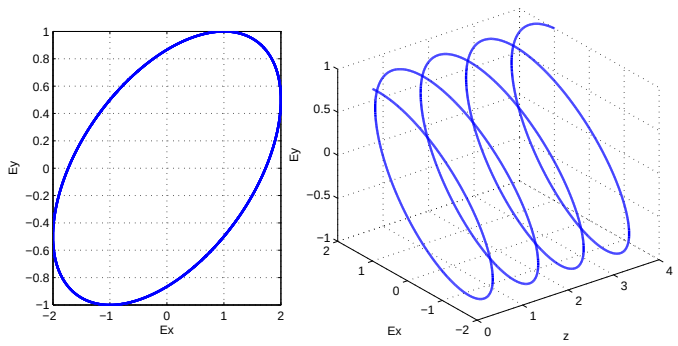

Figure 1.6: E Field Ellipticaly polarised

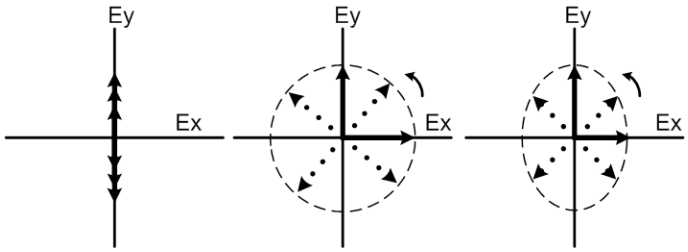

Figure 1.7: Polarisastion states

will be transmitted. For smooth and homogeneous objects Snells law applies, the angle of the transmitted wave is a function of the incident angle and the material properties and the angle of the reflected field is equal to the incident both referenced to the surface normal [4].

$$\frac{\sin(\theta_i)}{\sin(\theta_t)} = \sqrt{\frac{\varepsilon_2\mu_2}{\varepsilon_1\mu_1}} = \frac{n_2}{n_1}, \tag{1.60}$$

where n_1 and n_2 are the refraction indexes, defined as the ratio of the free space velocity to the velocity of the wave in the media

$$n = \frac{c}{v} = \sqrt{\frac{\varepsilon\mu}{\varepsilon_0\mu_0}}. \tag{1.61}$$

Considering figure 1.8, the incident, reflected and transmitted rays can be contained in one plane, each of these rays can have a perpendicular and parallel component with respect to the plane that contains them. For example in figure 1.8, the plane that contains the incident, reflected and transmitted waves which is called the reflection plane is the same as the plane of the page, therefore in this example they may have a component that is parallel to the plane of the page and one that may

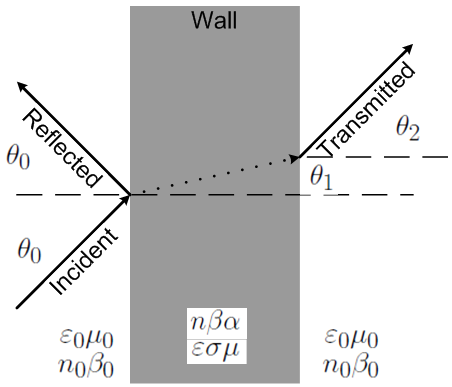

Figure 1.8: Incident, Reflected and Transmitted rays

be perpendicular. The wall shown in the figure is where the interaction occurs and is contained in a plane perpendicular to the page.

The Fresnel reflection coefficient valid for non perfect electric conductor surfaces are [4],

$$R_{\perp}(\theta) = \frac{\cos(\theta) - \sqrt{\epsilon' - \sin^2(\theta)}}{\cos(\theta) + \sqrt{\epsilon' - \sin^2(\theta)}}, \tag{1.62}$$

$$R_{\parallel}(\theta) = \frac{\epsilon' \cos(\theta) - \sqrt{\epsilon' - \sin^2(\theta)}}{\epsilon' \cos(\theta) + \sqrt{\epsilon' - \sin^2(\theta)}}. \tag{1.63}$$

The Fresnel transmission coefficients are

$$T_{\perp} = \frac{2\cos(\theta_i)}{\cos(\theta_i) + \sqrt{\epsilon' - \sin^2(\theta_i)}}, \tag{1.64}$$

$$T_{\parallel} = \frac{2\sqrt{\epsilon'}\cos(\theta_i)}{\epsilon' \cos(\theta_i) + \sqrt{\epsilon' - \sin^2(\theta_i)}}, \tag{1.65}$$

where lossy linear media are characterised by the complex valued

$$\epsilon' = \frac{\varepsilon}{\varepsilon_0} - \frac{j\sigma}{\omega\varepsilon_0} \quad with \quad \varepsilon = \varepsilon_r\varepsilon_0. \tag{1.66}$$

For a perfect electric conductor $R_{\perp} = +1$ and $R_{\parallel} = -1$, while $T_{\perp,\parallel} = 0$. Table 1.5 provides material properties of a few obstacles that can be found in buildings.

Figure 1.9 plots simulated values for the transmission and reflection coefficients of a wave with respect to the incidence angle to typical building wall. In the figure the coefficients for both parallel and perpendicular polarizations are shown. Considering the orientation of the reflection plane when the waves interact with a vertical wall

Table 1.5: Constitutive parameters of indoor obstacles [4]

Material	ε	σ	**Thickness**
External wall	6	0.34	25
Internal wall	2.9	0.15	10
Floor partitions	2.9	0.001	17
Doors	5.8	0.05	4

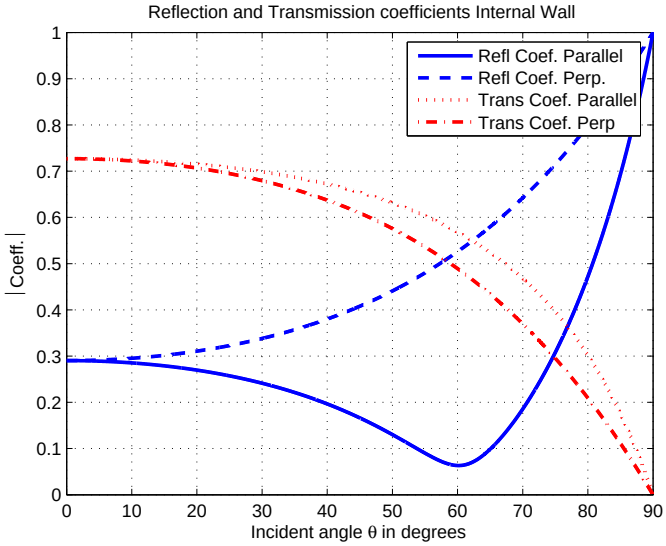

Figure 1.9: Reflection and transmission coefficients of an indoor wall

we can realise that the parallel component represents the vertical polarization, while the perpendicular component represents the horizontal.

We can also notice at figure 1.9 that at about 60 degrees incidence angle, the parallel reflected component is close to zero, while the perpendicular is reflected more efficiently, this approximates the Brewster angle or polarization angle.

1.3 Motivation

The purpose of this study is to produce novel antennas for Micro–Pico cell MIMO wireless communications. One of the most widely used such protocol will be the WLAN 802.11n. Interoperability and legacy issues require antennas to be dual band, power regulations put relaxed limits on the allowed gain, where if large gain is present a reduction in transmit power might be necessary. If the system is not ad hoc totally mobile then usually antennas at the base station or access point might have different attributes than the antennas at the mobile station. Antennas at the access point might be spaced further apart, have minimum and stable neighboring

scattering objects and require different angle of departure distribution. On the other hand elements on the mobile station often have low efficiency due to their size and do not usually have the luxury of space so there are strong interactions contributing to mutual coupling, modifying the radiation pattern and impedance. The random loading by nearby objects that come randomly can make these effects even more profound. Diversity at the access point is used for many years however in mobile systems is not so wide spread. In Japan the Personal Digital Communication (PDC) [33] network is already using diversity at the mobile. With the arrival of fourth generation systems diversity at the mobile might be a necessity. For the 802.11n protocol it is proposed that mandatory is the operation of two spatial streams with basic MIMO SDM and 20 MHz channel, optionally three to four spatial streams with transmit beamforming and space time block codes on a 40 MHz channel are suggested. For a successful MIMO system in general two main conditions must be met. First the received signals must be decorrelated hence the importance on diversity and secondly the received power levels on the elements must be similar. Different novel antennas are to be produced and a measurement campaign to be made so to evaluate their performance. An attempt to provide radiators that are relatively spaced closely, with low level of mutual coupling and pattern diversity so to enhance independence of signals and reduce direct radiation of an element to another at both operating bands is to be presented. Surface waves and currents in common ground planes are acknowledged and methods to reduce them are investigated. Balanced feeds and electromagnetic band gap structures are introduced for these reasons. Other periodic structures will be applied as superstrates to enhance radiation properties due to the reflection properties of the artificial magnetic conductors. Additionally parasitic loading will be investigated as a means to reduce mutual coupling of proximity radiators.

1.3.1 Problem Formulation

In the figure 1.10 below, a block diagram illustrates the main MIMO types, this can translate to antenna design requirements, as for example a beamforming system requires the use of smart antennas that allow radiation pattern to be steered freely and flexibly, on the other hand a system that uses spatial multiplexing with uniform

power allocated at all transmit antennas in its simplest form might be adequate with antennas of predefined pattern. In summary the following points highlighted in [34], are a good initial guide for MIMO antenna development across all of the platforms shown in figure.

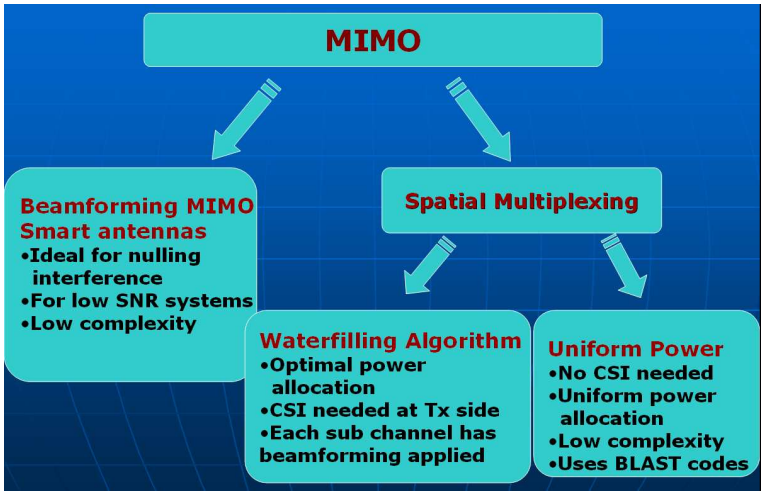

Figure 1.10: MIMO basic types

- The antennas must be terminated in matched loads, immune to loading from nearby objects.
- Mutual Coupling must be minimised, thus improving efficiency, reducing correlation, and achieving good SNR.
- The antennas could have cross polar discrimination, although in mobile environment this is relaxed.
- Radiation pattern of elements must have minimum overlapping regions.
- Some level of directivity must be present. There is no point sending energy to directions that will never reach the receiver.
- Antennas must be relatively electrically small, this will reduce the reactive near field region and the interactions between the elements, too small might affect the gain.
- Scattering of near objects can increase mutual coupling.
- Elements can radiate directly one to another. If possible locate them in each others nulls or low directivity regions

- Currents in the common ground plane can be a source of coupling. One possible solution is to use balanced structures that drive them selves and do not use structures that are directly driven from the ground plane.

- In planar antennas surface waves can be a source of coupling.
  Electromagnetic Band Gap (EBG) technique can minimise surface wave coupling. Another method that can minimise coupling through surface waves is the use of a balanced feed to the antenna.

1.4 Thesis Outline

The thesis is organised in six chapters
Chapter 2 covers the background theory and all the required concepts on MIMO systems and diversity. A brief literature review will be provided in each sub section. Antenna modeling for MIMO systems is to be is to be included.
Chapter 3 A parametric study on printed stcked inverted monopole antennas is outlined, with the data an array of two closely spaced PIFAs is formed and a novel way to to reduce coupling between them is presented. The diversity potential is assessed from theoretical measures.
Chapter 4 A dual band printed dipole array is proposed, wide band input impedance and low coupling are demonstrated, the array is fabricated and measured. Further simulations are then under taken to suggest improvements by use of high impedance surface.
Chapter 5 Two methods to reduce coupling by suppression of surface waves are presented. Dielectric covers and EBG structures are placed on a two element fundamental microstrip patch array.
Chapter 6 Conclusion and future work

1.5 Publications and Novel Work

Conference proceedings:

1. E. Michailidis, C. C. Tsimenidis and E. G. Chester, "Printed dipole array for MIMO wireless networks," *in Proc. Loughborough Antennas and Propagation*,

Loughborough, UK, April 2007.

2. E. Michailidis, C. C. Tsimenidis and E. G. Chester, "Mutual Coupling Reduction in a Linear Two Element Patch Array and its Effect on Theoretical MIMO Capacity," *in Proc. Loughborough Antennas and Propagation*, Loughborough, UK, March 2008.

3. E. Michailidis, C. C. Tsimenidis and E. G. Chester, "Parametric study of PIFA antenna," *Seminar on Wideband, multiband antennas for defence and civil applications*, the IET , March 2008

Chapter 2

On MIMO Systems

"I would rather understand one true cause
than be king of Persia"
Democritus.

Several topics that are fundamental and elementary in MIMO systems and channels are to be briefly presented. It is vital to review essential concepts of this modern wireless communication approach, as this will allow better understanding on the requirements demanded from the antennas and arrays that will serve such systems. This chapter will first introduce the basic MIMO systems model, and then move on to describe properties of the channel. Three of the most interesting and widely used channel models are outlined illustrating differences in the avenues taken to address the problem of capturing the physics of real environments with reasonable accuracy and reduced complexity and cost. Diversity measures and antenna network representation are also introduced. By no means the material contained is extensive, it merely provides the most cited and well established notions.

2.1 MIMO Systems

Consider a communication system with n_t transmit antennas and n_r receive antennas. Such a system block diagram is shown in figure 2.1 For a spatially multiplexing system, the data is split into n_t bit streams, modulated and transmitted simultaneously from the n_t antennas. The receiver recovers these individual bit streams and combines them in order to form the original bit stream. As MIMO takes advantage of random fading, delay and angle spread, a rich multipath scattering environment and diversity are required in order to ensure that signals arriving at the receiving

antenna elements are decorrelated. Capacity is strongly related to signal to noise ratio and to the correlation of the channel transfer function between different pairs of transmit and receive antennas. Figure 2.1 illustrates a 3×3 MIMO antenna system.

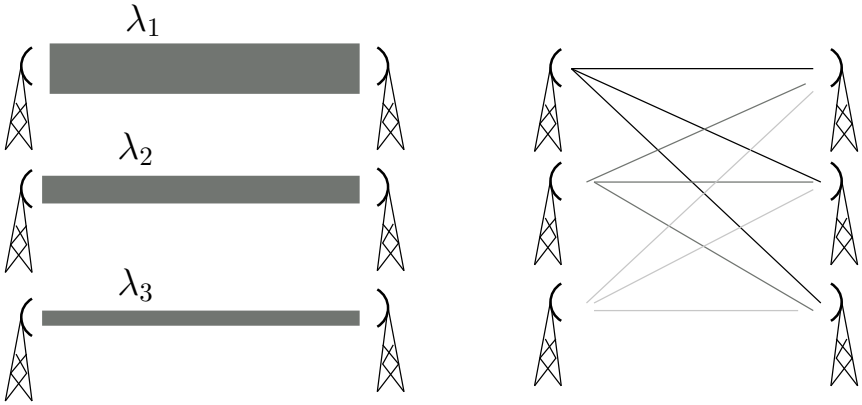

Figure 2.1: Equivalent parallel independent sub channels, quality is dictated by the eigen values

For the system shown nine ($n_r n_t = 9$) radio links between antennas exist. However assuming given favourable ideal conditions, three orthogonal independent sub channels are available. The magnitude of the eigen value represents the power gain for the respective sub channel. In its simplest form the input output relationship is given by the following expression

$$y = H \cdot S + n \tag{2.1}$$

$$\begin{pmatrix} y_1 \\ y_2 \\ \vdots \\ y_{Nr} \end{pmatrix} = \begin{pmatrix} h_{11} & h_{12} & \dots & h_{1M} \\ h_{21} & h_{22} & \dots & h_{2M} \\ \vdots & \vdots & \ddots & \vdots \\ h_{N1} & h_{N2} & \dots & h_{NM} \end{pmatrix} \cdot \begin{pmatrix} s_1 \\ s_2 \\ \vdots \\ s_M \end{pmatrix} + \begin{pmatrix} n_1 \\ n_2 \\ \vdots \\ n_N \end{pmatrix}, \tag{2.2}$$

The transmitted signals over one symbol duration form a vector with dimension of $n_t \times 1$, here denoted as S, where S_i is the i^{th} vector element representing the transmitted signal from antenna i. Assuming that the entries of S are complex Gaussian distributed random variables, then the transmit covariance is [35]

$$S(t) = [S_1(t), S_2(t), \dots, S_{n_t}(t)], \tag{2.3}$$

$$Q_{ss} = E\{(S-\mu)(S-\mu)^{\dagger}\}, \tag{2.4}$$

where, μ represents the first moment of a random variable and is the expected value or mean. For zero mean random variables μ equals zero, the first moment of a continuous random variable X is defined as,

$$\mu = E\{X\} = \int_{-\infty}^{\infty} x f_X(x) dx \tag{2.5}$$

$$Q_{ss} = E\{SS^{\dagger}\}, \tag{2.6}$$

where $E\{\}$ denotes expectation and $\{\}^{\dagger}$ is the complex conjugate transpose and Q_{ss} represents the transmit covariance. The diagonal elements of Q_{ss} represent the transmit power from each antenna. The off diagonal elements of Q_{ss} represent the correlation properties between the parallel transmit symbols. If the total transmit power is constrained to P, and the transmitter has no channel state information, the power is equally allocated to the n_t antennas, each having P/n_t, and if transmit signals are totally uncorrelated, then [36]

$$P = tr(Q_{ss}), \tag{2.7}$$

$$Q_{ss} = \frac{P}{n_t} I_{n_t}, \tag{2.8}$$

where tr is the trace of a matrix, being the sum of the diagonal elements, and I_{nt} is an identity matrix of dimensions $n_t \times n_t$. The additive noise introduced by the channel and the RF front end is denoted as n, and is a vector of dimensions $n_r \times 1$. if we assume that the elements of n are zero mean, complex independent Gaussian random variables, for uncorrelated entries of n with equal variance [35]

$$Q_{nn} = E\{nn^{\dagger}\}, \tag{2.9}$$

$$Q_{nn} = \sigma^2 I_{n_r}. \tag{2.10}$$

The channel matrix H is complex of dimensions $n_r \times n_t$. The element H_{ij} represents the transfer function between the j^{th} transmit antenna and the i^{th} receive antenna. Some factors which need not be neglected that influence the properties of the channel matrix and consequently the performance of the MIMO system are, antenna

impedance matching, mutual coupling, radiation pattern, element polarization, array topology and multipath propagation. The rank of the channel matrix, dictates the maximum number of independent spatial data streams that can be supported. In one of the most dominant and widely used channel models presented in [37][38] each tap of the channel impulse response can be represented by a line of sight component and a non LOS which is random Rayleigh distributed

$$h_{ij} = \sqrt{P}\left(\sqrt{\frac{K}{K+1}}e^{j\varphi_{ij}} + \sqrt{\frac{1}{K+1}}X_{ij}\right), \tag{2.11}$$

$$H = \sqrt{P}\left[\sqrt{\frac{K}{K+1}}\begin{pmatrix} e^{j\varphi_{ij}} & \dots \\ \vdots & \ddots \end{pmatrix} + \sqrt{\frac{1}{K+1}}\begin{pmatrix} X_{ij} & \dots \\ \vdots & \ddots \end{pmatrix}\right], \tag{2.12}$$

where X is a zero mean, Gaussian complex random variable, φ represents the angle of the LOS component, K is the Rice factor and P is the power of H element.
The received signal y is a vector $n_r \times 1$, each element of which represents each receive antenna signal. The average SNR at a receive antenna with power P_r is [39][36]

$$\rho = \frac{P_r}{\sigma^2}. \tag{2.13}$$

The covariance of the receive signal vector is

$$y(t) = [y_1(t), y_2(t), \dots, y_{n_r}(t)], \tag{2.14}$$

$$E = \{yy^{\dagger}\}, \tag{2.15}$$

$$Q_{yy} = HQ_{ss}H^{\dagger}. \tag{2.16}$$

By performing a singular value decomposition (SVD) of the channel matrix it is possible to represent the MIMO system as a set of equivalent parallel SISO channels. SVD states that a $n_r \times n_t$ matrix H can be written as the product of a $n_r \times n_r$ matrix U, which is unitary, the transpose of a unitary $n_t \times n_t$ matrix V^T, and diagonal matrix D $n_r \times n_t$ with positive or zero entries ordered indecreasing order, thus [2]

$$H_{nr\times nt} = U_{nr\times nr}D_{nr\times nt}V^T_{nt\times nt}. \tag{2.17}$$

Unitary matrices are defined as

$$UU^{\dagger} = I \quad VV^{\dagger} = I. \tag{2.18}$$

To determine the singular values the following equation must be solved

$$det(H^{\dagger}H - \lambda I) = 0, \tag{2.19}$$

$$(H^{\dagger}H - \lambda I)V = 0, \tag{2.20}$$

$$(HH^{\dagger} - \lambda I)U = 0. \tag{2.21}$$

Because U and V are invertible, it is possible to apply transformations and express the input output relationship of a MIMO system using the SVD theorem, as follows [35]

$$y = HS + n, \tag{2.22}$$

$$y = UDV^{\dagger}S + n, \tag{2.23}$$

$$u^{\dagger}y = U^{\dagger}UDV^{\dagger}S + U^{\dagger}n, \tag{2.24}$$

$$u^{\dagger}y = DV^{\dagger}S' + U^{\dagger}n. \tag{2.25}$$

But if we let $y' = U^{\dagger}y$ and $S' = VS$, where each of the columns of V is used as transmit weights and each row of $U^{\dagger}$ (column of U^{*}) is used as receive weights. This technique implies transmit beam forming by SVD, one must assume that full channel state information is known to both the transmitter and receiver. Then the system equation will become

$$y' = DS + U^{\dagger}n. \tag{2.26}$$

The diagonal matrix D has entries specified by $D = diag(\sqrt{\lambda_2}, \sqrt{\lambda_2}, \ldots)$, which are the singular values of H, that is the positive square roots of the eigenvalues of $HH^{\dagger}$. Thus it becomes apparent that the MIMO system is now represented as a set of equivalent parallel SISO eigen channels with signal powers given by the eigen values [35] [39] [36].Depending on the number of transmit and receive antennas, the

Wishart matrix Q can be formed as

$$Q = \begin{cases} HH^{\dagger} & for N_r < M_t \\ H^{\dagger}H & for N_r > M_t. \end{cases} \tag{2.27}$$

In general, to estimate the number of available independent sub channels for any size system, one of two simple mathematical approaches can be followed. As was shown earlier the singular value decomposition (SVD) of the channel matrix is one approach, the other being the eigen value decomposition (EVD) of the appropriate Wishart matrix (2.45)

$$\begin{array}{cc} \textit{Singular Value Decomposition} & \textit{Eignen Value Decomposition} \\ H = U\Sigma V^{\dagger} & R = V\Sigma^{\dagger}U^{\dagger}U\Sigma V^{\dagger} = V\Sigma^{\dagger}\Sigma V^{\dagger} \\ \Sigma = \begin{pmatrix} \sigma_1 & 0 & \dots & 0 \\ 0 & \sigma_2 & \dots & 0 \\ \vdots & \vdots & \ddots & \vdots \\ 0 & 0 & \dots & \sigma_k \end{pmatrix} & \Gamma = \Sigma^{\dagger}\Sigma = \begin{pmatrix} \lambda_1 & 0 & \dots & 0 \\ 0 & \lambda_2 & \dots & 0 \\ \vdots & \vdots & \ddots & \vdots \\ 0 & 0 & \dots & \lambda_k \end{pmatrix} \\ \sigma_1 \geq \sigma_2 \geq \ldots \geq \sigma_k \geq 0 & \lambda_1 \geq \lambda_2 \geq \ldots \geq \lambda_k \geq 0 \end{array} \tag{2.28}$$

$$\sigma_k^2 = \lambda_k \ ,$$

$$UU^{\dagger} = VV^{\dagger} = I \ .$$

If for any reason however beam forming is not an option and a simpler system is desired where the transmitter does not need to have full channel state information, which is normally estimated at the mobile station and then fed back, then the data can be applied directly at the transmit antennas, the receiver can produce an estimate of the transmitted signals by multiplying the received signals by the pseudo inverse of the channel matrix [35]

$$\hat{S} = H^{+}y, \tag{2.29}$$

The theoretical MIMO capacity can be obtained from the following expression

$$C = W \log_2 \det\left(I + \frac{P}{M_T \sigma^2} H H^\dagger\right) = W \sum_k \log_2\left(1 + \frac{\Gamma_k}{\sigma^2}\right), \tag{2.30}$$

where $HQ_{ss}H^\dagger = V\Gamma V^\dagger$, is an EVD operation on the received signal with no noise effects present. The above formula assumes equal power allocation to every transmit antenna, usually when the transmitter does not have CSI. However when channels information is available to transmitter it is possible to find the covariance Q_{ss} subject to the transmit power constraint $tr\{Q_{ss}\} < P_T$ that maximises the capacity. This implies adaptive transmit power allocation, based on the water filling algorithm. From the eigen values of the channel matrix, a decision is made to assign more power to sub channels with better state. The optimal Q_{ss} must be diagonal $diag(p_1, p_2, \ldots)$, assuming that the transmit streams are independent. The power constraint is [39]

$$\sum_{i=1}^{M_T} P_i = P. \tag{2.31}$$

With P_i equal to the power allocated to sub channel i , which is chosen as

$$P_i = \left(\mu - \frac{\sigma^2}{\lambda_i}\right)^+, \tag{2.32}$$

where μ is a constant that is determined from the power constraint. The capacity is

$$C = W \sum_{i=1}^{M_T} log_2\left(1 + \frac{1}{\sigma^2}(\lambda_i \mu - \sigma^2)\right). \tag{2.33}$$

In figure 2.2 the water filling algorithm is shown in graphics, considering a system which consists of eleven streams or sub channels, indicated by the bars lined along the horizontal axis. The blue bars indicate the magnitude of σ^2/λ_i. As mentioned earlier μ is a constant determined from the power constrain, its level is graphically shown on the side of the graph lined along the vertical axis. The yellow bars indicate the optimal power allocated to the sub channels that are being used, the decision is based on the positive values of $(\mu - \sigma^2/\lambda_i)$, sub channels that provide negative result are disregarded.

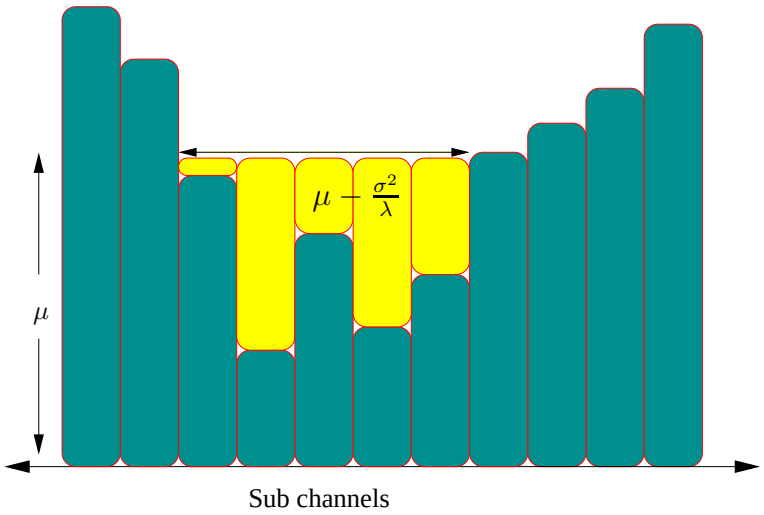

Figure 2.2: Waterfilling algorithm in graphics

2.2 A MIMO system example

Following the brief introduction of MIMO systems and channel it is essential to understand and illustrate how the environment and the wireless channel affect the capacity. As was mentioned earlier the properties of the channel matrix dictate the potential performance of candidate systems. A simple yet fictitious matrix with highly correlated entries as in (2.34) will result in an equivalent SISO communication as only one sub channel will be excited. This is manifested by the outcome of the SVD on the channel matrix.

$$H = \begin{pmatrix} 1+1j & 1+1j \\ 1+1j & 1+1j \end{pmatrix} \quad \Rightarrow SVD \Rightarrow \quad D = \begin{pmatrix} 2.8284 & 0 \\ 0 & 0 \end{pmatrix}. \tag{2.34}$$

On the other hand if the entries of H are rather random and de-correlated then the true benefits of MIMO can become viable. The computation of the SVD in (2.35) clearly allows two sub channels to be excited. It is from this operation that the requirement of rich multipath is necessary as it will ensure that the entries of H are independent.

$$H = \begin{pmatrix} 0.4456+0.276j & 0.7094+0.6551j \\ 0.6463+0.6797j & 0.7547+0.1626j \end{pmatrix} \quad \Rightarrow SVD \Rightarrow \quad D = \begin{pmatrix} 1.5797 & 0 \\ 0 & 0.433 \end{pmatrix}. \tag{2.35}$$

As an example, consider a system with $n_t = n_r = 2$ antennas at each side of the link. The antennas at the BS and at the MS side are separated by one wavelength.

The operating frequency of the system is 2.4GHz. The computational domain for this example consists only two dimensions (x,y), all the rays are launched in one plane and there is no height information. The base station, the mobile station, the rays and all the obstacles are at predetermined x and y coordinates and all lay in the $z = 0$ coordinate. The computational domain size is 80 meters along the y direction, starting at -20 and ending at 60, while the size of the x dimension is 90 meters, starting at -60 and finishing at 30 meters from origin. The full computational domain with the BS, MS and obstacles is shown in figure 2.4. The elements at the BS are aligned horizontally at (-50.0625,50) and (-49.9375,50) as the antennas are displaced along the x axis by an amount equal to one wavelength, while the ones at the MS are aligned vertically with initial coordinates (0,0.0625) and (0,-0.0625) as the antennas are displaced along the y axis by an amount equal to one wavelength. These coordinates are in the form (x,y) as this is a 2D problem, and the term horizontal and vertical refers to a two dimensional meaning of vertical and horizontal as with respect to the reader and the plane of the page. For the example the MS

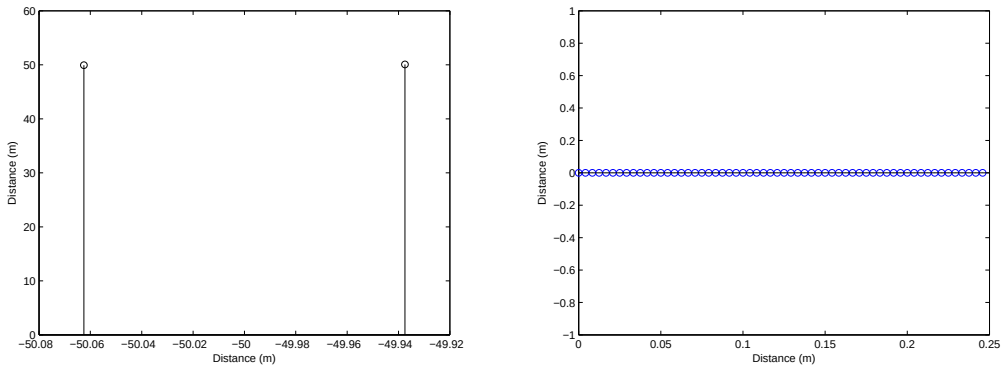

Figure 2.3: On the left figure the two BS antennas located at (-50.0625,50) and (-49.9375,50) are shown. The plot is a zoom of the computational space at the region of the base station antennas. On the left figure the plot shows the sampling points at the route of the mobile station as it travels from the origin to a distance of 0.25 meters. The plot is a zoom of the computational space in the region of the mobile station, consisting of sixty sampling points over a distance of 0.25 meters.

is set to travel approximately two wavelengths (0.25m), starting from the origin, and sample the fields along its path. A sampling rate of 30 samples per wavelength is applied. Two scenarios are to be examined. A relatively rich scattering against a low scattering. For both cases there is no line of sight component. For the rich environment forty random scatterers normally distributed with zero mean and

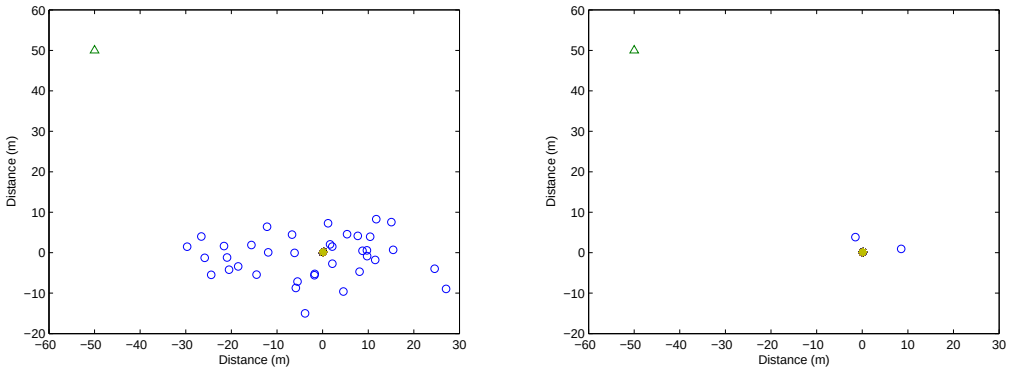

Figure 2.4: On the left figure the whole computational space is shown for the rich scattering scenario. The triangle represents the region of the two base station antennas. The asterisk at the origin represents the location of the mobile station before it starts moving along the positive x direction. The circles indicate the position of each of the 40 scattering objects. On the right figure the whole computational domain is shown for the case of a reduced, low scattering environment. The indicators in the figure have the same meaning as before, only now there are only two scattering obstacles in the space instead of 40 that were earlier.

standard deviation one are drawn and then their coordinates are expanded by a ratio of two to one along the x and y axis respectively. In detail the x randomly drawn coordinate is scaled by the equivalent of 15 meters while the y coordinate is scaled by 7 meters. For the second scenario the same holds for only two scatterers. From each BS antenna the distance vectors to each scatterer are computed from their coordinates. Then the distance vectors from each of the scatterers to each of the MS antennas is computed along the travelled route. The total path length is the sum of the two. The average power of the rays is set to $0dB$ by the Rayleigh parameter $2\sigma^2$. The amplitude contribution of every ray is constant with total number of rays being equal to the population of scatterers. Thus to control the average power of the resulting complex envelops the Rayleigh parameter is linked to the ray amplitude as follows [4]

$$\sum_{i=1}^{N} a_i^2 = 2\sigma^2. \tag{2.36}$$

Where in (2.36), N is the total number of rays, a_i is the amplitude of i^{th} ray and $2\sigma^2$ is the squared rms Rayleigh distribution value. The free space loss appropriate for the operating frequency and distance travelled by the wave is not taken in to account

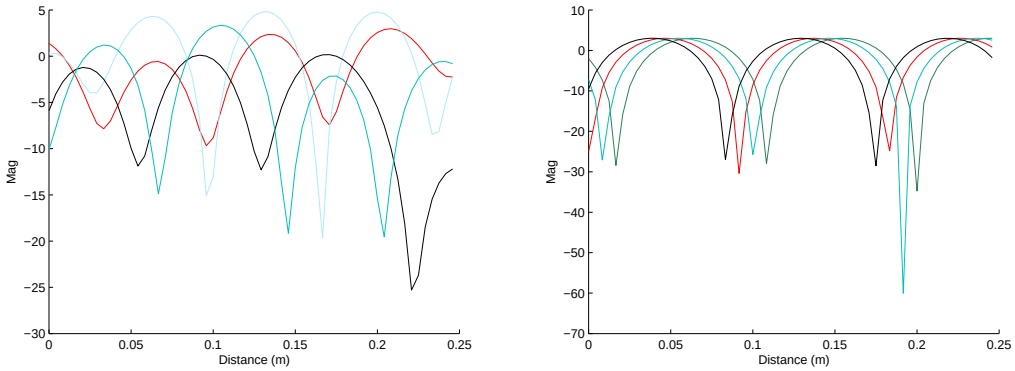

Figure 2.5: On the left figure received signals along the travelled route for the case of rich scattering environment. On the right figure received signals for the case of two scattering objects. No line of sight for either case. By first inspection of the series shown in the figures, one can expect significantly higher correlation between the received signals originating from the two scatterer simulation as opposed to the forty scatterer, resulting in a diagonal singular matrix with only one significant value other being negligible

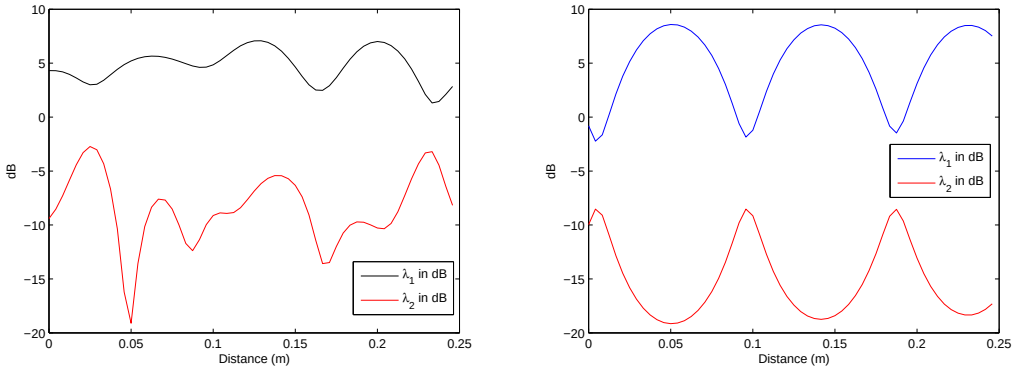

Figure 2.6: Performing a Singular Value Decomposition on the channel matrix, which is constructed from the complex envelop of all possible transmit receive signals between the multiple antennas, the eigen values are obtained by squaring the singular values and are plotted here in dB for both cases indicating the quality of the two independent modes. On the left figure the eigen values for the rich scattering are shown, while on the right figure the eigen values for the low scattering scenario are shown.

in this simulation. The scatterers do not have random phase terms associated with them, the signal variations are due to space sampling, however a pseudo random disrtibution of phase can be applied to each object if desired, in (2.37) the spaced

to the right phase term represents this option.[4]

$$r_{m,n} = \sum_{i=1}^{N} a_i e^{(-jkd_i^{mn}) \quad +j\phi_i^{mn}}, \tag{2.37}$$

where the subscripts m, n represent the transmit receive antenna pairs, while subscript i denotes the scatterer number. By the use of (2.36) the entries of H can be obtained. Having the channel matrix in hand, singular or eigen decomposition can be applied. Figure (2.7) compares the instantaneous capacity of a system with SNR of 20dB, under two very different channel environments. The radiation patterns

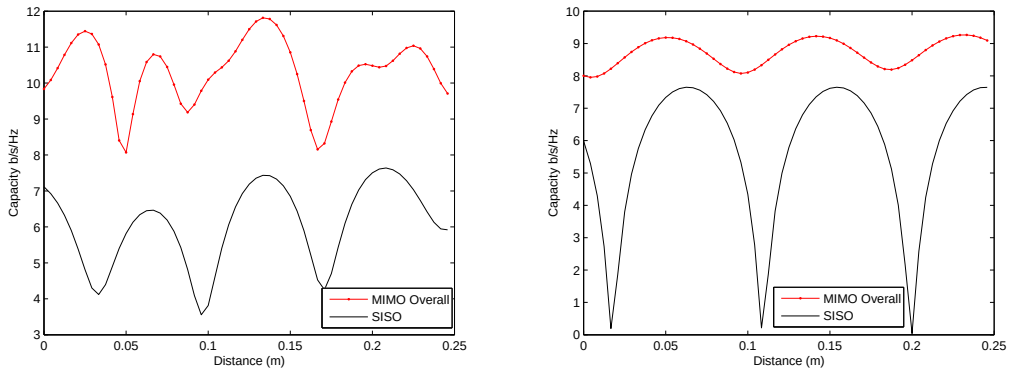

Figure 2.7: On the left figure, the instantaneous MIMO capacity in addition to the instantaneous SISO capacity for rich scattering scenario are provided, the SISO capacity is computed by the signal transfer function between transmit antenna one and receive antenna one. On the right figure the instantaneous MIMO capacity and the instantaneous SISO capacity are plotted for the low scattering environment.

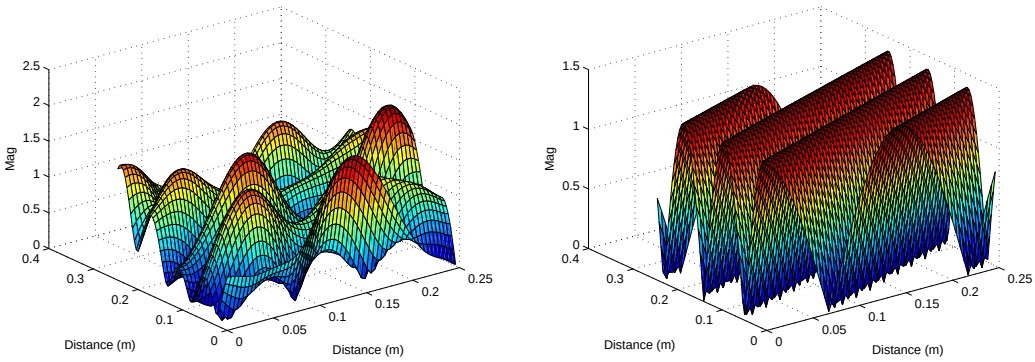

Figure 2.8: Sampled fields of a probe over a square area of approximately two wavelengths, here one Tx element illuminates the identical scatterer configuration as in the simulation of the MIMO system, a spatial standing wave pattern is observed for the field.

of the antennas in this two dimensional simulation are assumed to be isotropic and thus do not weigh incoming or departing signals depending on their angular identity, for more specific and accurate models actual radiation characteristics can be applied over two or three dimensional environments, additionally if antenna array data are available mutual coupling effects can be imposed on the channel computed. The MATLAB simulation plots are a result of a modified version of code found in [4]

2.3 The MIMO Channel

In contrast to single antenna systems(or equivalently MISO,SISO,SIMO) where the effect of channel is undesirable and often signal processing is applied to remove fading and temporal phenomena, MIMO communications draw their benefit from the structure of the channel matrix. Therefore accurate models are essential in estimating performance of space time systems, usually these need to capture the natural behaviour recorded in experimental measurement campaigns of various propagation environments. The directional spread of energy originating and impinging on system's arrays after interacting with the environment has a significant impact on the correlation of signals. Thus representation of angular distribution of energy at T_x and R_x seems a natural extension to fading and temporal modeling. Many channel models are available, offering different levels of accuracy, complexity and environment representation. In essence though the scope of all is to reproduce accurate statistical characteristics for the chosen environment and system setting based on the estimated entries of the channel matrix. Direct channel measurements are accurate for site specific scenarios but in general are prohibitive due to complexity and massive cost, as a result task groups as the European COST actions 259, 273 have as ultimate goal to construct and standardize propagation models that capture realistically the physics of the propagation environment.

- Deterministic – Ray tracing multipath estimation

  Can be applied to two or three dimensional environments. This approach of modeling is based on geometrical optics and diffraction theory(to account for shadowing). Advances have coupled full wave parabolic and integral equation methods in order to model features that are comparable to wavelength, due to the limitation of optics that ray wavelength should be small compared to size of

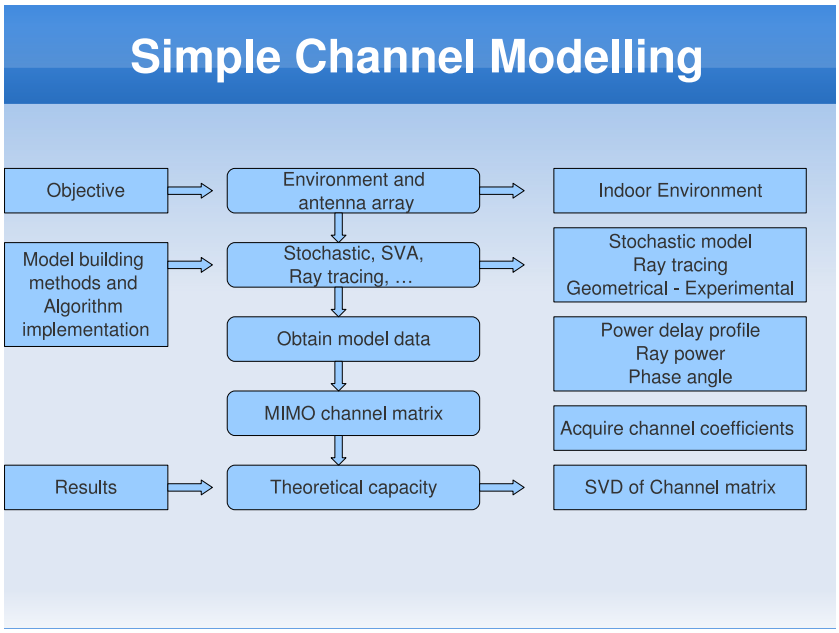

Figure 2.9: Simplified figure illustrating options and steps towards a MIMO channel model construction

targets. At the receiver information such as amplitude, phase and polarization can be determined. At most cases ray tracing models support line of sight, transmission trough materials, single and multiple reflections and diffracted components. Diffuse scattering is difficult to model and often neglected.

- Geometric discrete scattering

  Models of this category include the one ring[40], two ring [41], combined elliptical [42] and elliptical circular models. These models can predict the complex channel gains and phase shifts along with the AoD, AoA and ToA. The channel transfer matrix can then be determined from these data. The placement of scatterers can be random or engineered to represent specific cases as for example clustering. In ring or elliptical models the radii can control the ToA. Single or double bounce properties describe the number of scatterers that a wave can reflect upon. Accommodation of mobility is also possible in the simulated environment.

- Statistical random matrix models

  Represent the fastest and simplest method to simulate the MIMO channel. The matrix elements have amplitudes and phases that follow a Rayleigh and uniform distributions. Easily extended to Ricean.

- Statistical cluster models

  Turin [43] first observed and presented that the multipath components form clusters that decay exponentially. The Saleh Valenzuela model with Angle is derived from this work and addresses the modeling problem by assigning predetermined distributions on AoD, AoA, ToA and complex amplitude.

2.3.1 Channel Normalisation

In most studies the instantaneous or the ensemble average of a number of channel realisations is normalised. The logic and necessity behind the normalisation is to allow reasonable comparison of systems. The average power transfer, given by the channel coefficients, between a transmit and receive antenna pair is normally set to unity. Therefore SNR can then be varied quantitatively and effectively for meaningful comparison of performance, with no random yet consistent amplifications or attenuations imposed by a not normalised channel obtained across different systems or campaigns.

The Frobenius norm of a matrix $\mathbf{A}\epsilon\mathbf{C}^{m\times n}$, is defined as

$$\| A \|_F^2 = \sum_i \sum_j | a_{i,j} |^2 = tr(AA^\dagger), \tag{2.38}$$

where, $\| \star \|_F$ is the Frobenius matrix norm, a_{ij} represents the entry of the i^{th} row and j^{th} column of A, and $tr(\star)$ is the matrix trace defined as the sum of the elements on the main diagonal. The normalised channel H_{norm} can be computed by scaling the original sample matrix $\tilde{H}$ by a constant [44] [35]

$$H_{norm}^{(n)} = \tilde{H}^{(n)} \left[\frac{1}{NM_tN_r} \sum_{n=1}^{N} \| H^{(n)} \|_F^2 \right]^{-\frac{1}{2}}, \tag{2.39}$$

where in equation 2.39, M_t is the number of transmit antennas, N_r is the number of receive antennas, N is the number of channel snapshots, $H^{(n)}$ is the sampled channel matrix for a particular snapshot, and $H_{norm}^{(n)}$ is the normalised channel matrix. The index n, which takes the values $1 < n < N$ defines the number of snapshot. Having N equal to one, applies normalisation to each individual channel snapshot, otherwise the normalisation is over the ensemble average of the realisations.

2.3.2 Channel Correlation

Under certain conditions the MIMO capacity may appear larger than under some different conditions, an ideal uncorrelated channel matrix if used to estimate the performance may produce higher capacity estimates than a channel matrix that imposes a level of correlation on its elements due to occasionally possible effects such as a strong line of sight, strong mutual coupling, reduced scattering, among others. When the issue of evaluating correlation arises, there are several options based on the antenna pairs selected [45]

- $E\{H(n,m)H^{\dagger}(n,m)\}$ Correlation between same transmit–receive antenna pairs
- $E\{H(n,m)H^{\dagger}(q,m)\}$ Correlation between same transmit–different receive antenna pairs
- $E\{H(n,m)H^{\dagger}(n,p)\}$ Correlation between same receive–different transmit antenna pairs
- $E\{H(n,m)H^{\dagger}(q,p)\}$ Correlation between different transmit–different receive antenna pairs

The complex correlation coefficient $\rho_{c,ij}$ uses the magnitude and phase to evaluate correlation, considering the i^{th} and j^{th} antenna ports it is given by [46] [47] [48]

$$\rho_{c,ij} = \frac{E\{(V_i - \bar{V_i})(V_j - \bar{V_j})^*\}}{\left[E\{(V_i - \bar{V_i})^2\}E\{(V_j - \bar{V_j})^{2*}\}\right]^{\frac{1}{2}}}, \tag{2.40}$$

where, $E\{\}$ denotes the expectation, V_i and V_j are the open circuit voltage functions which have mean values $\bar{V_i}$ and $\bar{V_j}$ at the antenna ports i and j respectively, and $()^*$ is the conjugation.

The envelop correlation $\rho_{e,ij}$ does not take into account the phase, it can be calculated in the angular domain as follows,

$$\rho_{e,ij} = \frac{\left|\int_0^{2\pi}\int_0^{\pi} S(\theta,\phi)g_i^*(\theta,\phi)\cdot g_j(\theta,\phi)\sin\theta d\theta d\phi\right|^2}{\int_0^{2\pi}\int_0^{\pi} S(\theta,\phi)g_i^*(\theta,\phi)\cdot g_j(\theta,\phi)\sin\theta d\theta d\phi \int_0^{2\pi}\int_0^{\pi} S(\theta,\phi)g_i(\theta,\phi)\cdot g_j^*(\theta,\phi)\sin\theta d\theta d\phi}, \tag{2.41}$$

where $g(\theta,\phi)$ represents the electric field radiation pattern of one of the elements while the other is terminated with matched impedance, $S(\theta,\phi)$ is the angular power density, i.e. the *pdf* of the incident waves at the antenna locations, the term $sin\theta$

derives from the elemental solid angle, and $()^*$ denotes conjugation.
The envelop correlation coefficient ρ_e is approximately equal to the squared magnitude of the complex correlation coefficient ρ_c [49].

$$\rho_e \approx |\rho_c|^2. \tag{2.42}$$

2.3.3 Kronecker Model

The Kronecker channel structure offers easier analysis of systems performance and is selected by IEEE 802.11n as the model for simulations [6]. Most authors using the Kronecker model cite [40] [50] [51] as validations of its effectiveness. However other published work suggests that it can underestimate the MIMO capacity , and that it is effective only under strict restrictions. The most profound feature is that the receive correlation is bound to be the same regardless of the transmit antenna configuration and that transmit antenna correlation is also bound to be the same regardless of receive antenna configuration. This in effect means that the surroundings of the Tx and Rx antennas influence the correlation at each side with no coupling link between the correlation of the two sides. The Kronecker product of two matrices is

$$A \otimes B = \begin{pmatrix} A_{1,1}\mathbf{B} & \dots & A_{1,M}\mathbf{B} \\ \vdots & \ddots & \vdots \\ A_{N,1}\mathbf{B} & \dots & A_{N,M}\mathbf{B} \end{pmatrix}. \tag{2.43}$$

The channel matrix of a $n_R \times n_T$ MIMO system can be expressed as

$$H = [h_1, h_2, \dots, h_i, h_{n_R}]^T, \tag{2.44}$$

$$h_i = [h_{i,1}, h_{i,2}, \dots, h_{i,n_T}] \quad i = 1, 2, \dots, n_R, \tag{2.45}$$

A new vector can be created composed of vectors h_i, resulting in a vector of length $n_R n_T$

$$h = [h_1, h_2, \dots, h_i, h_{n_R}]. \tag{2.46}$$

The correlation of the channel matrix has dimensions $n_r n_t \times n_r n_T$, and is expressed as

$$R = E\{h^\dagger h\}, \tag{2.47}$$

$$R = E\{vec(H)vec(H^{\dagger})\}. \tag{2.48}$$

In the case where the elements of H are iid, the covariance is an identity matrix generating maximum capacity. The Kronecker model is based on two assumptions [52], separability between Tx and Rx and shift invariance. The shift invariance implies that antennas must be in far field scattering and that only displacement affects the covariance matrix. These assumptions allow correlation functions to be computed by single bounce discrete scattering models. In [40] they use the one ring model to estimate the spatial fading correlation of channel H. The operator $vec()$ stacks the columns of H. By interchanging the roles of BS and MS, the authors arrive at the following

$$R = cov\{vec(H)\} = R^R \otimes R^T. \tag{2.49}$$

If expression 2.48 holds, then the statistics of the channel matrix H are equal to $AH_wB^{\dagger}$, where $AA^{\dagger} = R^T$and $(BB)^{\dagger} = R^R$and H_w is a spatially white (Rayleigh i.i.d.) of dimensions $n_r \times n_t$[40]. In this case, as mentioned earlier using raytracing or geometrical model one can compute the channel covariance matrix $R = cov(vec(H))$. Then let $R = R^{1/2}(R^{1/2})^{\dagger}$, the correlated channel matrix is then

$$vec(H) = R^{\frac{1}{2}}vec(H_w). \tag{2.50}$$

Thus if correlation at Tx and Rx is modeled independently, then their covariance matrices can be defined as [50]

$$R^R = E\{(h_i^{\dagger}h_i)^T\} \quad i = 1, 2, \ldots, n_R, \tag{2.51}$$

$$R^R = R_r R_r^{\dagger}, \tag{2.52}$$

$$R^T = E\{(h_j h_j^{\dagger})\} \quad j = 1, 2, \ldots, n_T, \tag{2.53}$$

$$R^T = R_t R_t^{\dagger}. \tag{2.54}$$

R though is considered to be symmetrical, therefore it can be represented by two matrices one for receive and one for transmit correlation as follows

$$R = R^R \otimes R^T, \tag{2.55}$$

$$R^R = \begin{pmatrix} 1 & r \\ r^* & 1 \end{pmatrix}, \quad R^T = \begin{pmatrix} 1 & t \\ t^* & 1 \end{pmatrix}. \tag{2.56}$$

The transmit and receive correlation matrices have the form

$$R^T = \begin{pmatrix} 1 & \rho_{12} & \dots & \rho_{1M} \\ \rho_{21} & 1 & \dots & \rho_{2M} \\ \vdots & \vdots & \ddots & \vdots \\ \rho_{1M} & \rho_{2M} & \dots & 1_{MM} \end{pmatrix}, \quad R^T = \begin{pmatrix} 1 & \rho_{12} & \dots & \rho_{1N} \\ \rho_{21} & 1 & \dots & \rho_{2N} \\ \vdots & \vdots & \ddots & \vdots \\ \rho_{1N} & \rho_{2N} & \dots & 1_{NN} \end{pmatrix}. \tag{2.57}$$

Thus the correlated channel is now formed as

$$H_c = R_t H_w R_r. \tag{2.58}$$

In [53] Oestges examines the validity of the Kronecker model for correlated channels. In a section of the paper a summary of the mathematical and propagation validity conditions are stated. The mathematical conditions are, Tx and Rx correlation coefficients are independent in magnitude, the product of Rx and Tx correlation coefficients need to equate to the cross correlation coefficients. The author then links these mathematical conditions to propagation. The physical meaning of the first mathematical conditions that both Rx and Tx arrays need to have identical radiation patterns, be of same orientation and be spaced in proximity. The second mathematical condition is interpreted as that the AoD and AoA are statistically independent.

2.3.4 SVA Model

The original SV model was proposed in 1987 in [54]. The authors set a measurement campaign and developed a statistical model for indoor propagation. Those days MIMO systems where not around and the model was set to predict the power delay profile of the channel. The advent of MIMO systems required spatiotempo-

ral channel information for accurate simulations. In 2000 and 2001 the authors in [55] [56] proposed an extension to the SV model, allowing for angle of arrival and angle of departure estimation. In the original SV model, the authors based on the measurements they made observed that the received rays arrive in clusters. They proposed two parameters that describe the cluster arrival decay and the ray arrival decay over time. The distribution of the arrival time of the first ray of individual

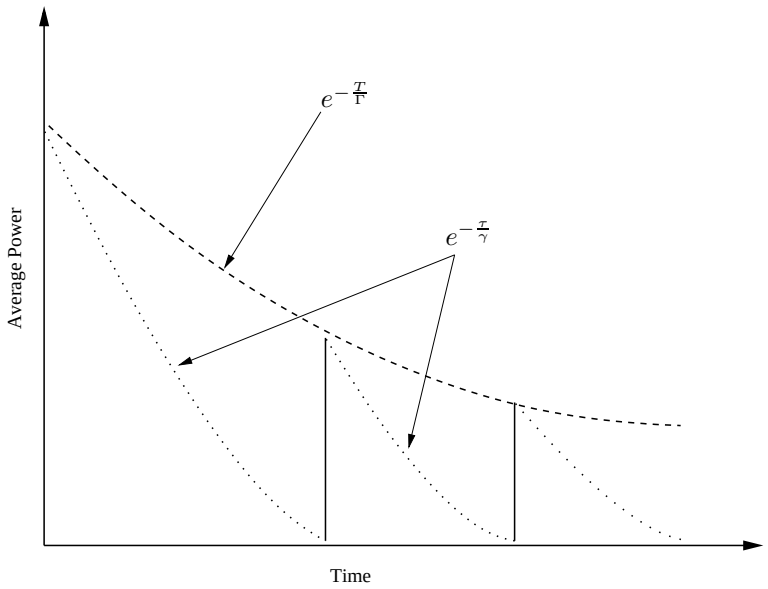

Figure 2.10: Exponential dacy rate

clusters is modelled as a Poisson process, an exponentially distributed random variable with a rate Λ dependable on the arrival time of the previous cluster. Each cluster is consisted by a number of rays, again the distribution of the rays within a cluster are a Poisson process with rate λ. These two Poisson distributions are assumed independent from each other

$$P(T_l|T_{l-1}) = \Lambda e^{(-\Lambda(T_l - T_{l-1})} \quad l > 0, \tag{2.59}$$

$$P(\tau_{kl}|\tau_{kl-1}) = \lambda e^{(-\lambda(\tau_{kl} - \tau_{kl-1})} \quad k > 0, \tag{2.60}$$

where T_l is the arrival time of cluster l, τ_{kl} is the arrival time of the k ray within cluster l. Noting that the arrival time of the first cluster is $T_0 = 0$ and that the arrival time of the first ray in an individual cluster is $\tau_{0l} = 0$. The impulse response

of the channel is

$$h(t) = \sum_{l=0}^{\infty} \sum_{k=0}^{\infty} \beta_{kl} e^{j\varphi_{kl}} \delta(t - T_l - \tau_{kl}), \tag{2.61}$$

where β_{kl} is the amplitude of the rays and is modelled as a Rayleigh distributed random variable. The mean square value of β_{kl} is dependent on T_l and τ_{kl}

$$\overline{\beta_{kl}^2} = \beta^2(T_l, \tau_{kl}) = \beta^2(0,0) e^{-T_l/\Gamma} e^{-\tau_{kl}/\gamma}, \tag{2.62}$$

where $\beta(0,0)$ denotes the average power of the first ray of the first cluster. The parameter φ_{kl} provides the phase of the arriving rays, it follows a uniform distribution of $[0, 2\pi]$ and is statistically independent. The extended model adds angle of arrival and angle of departure statistics on the original model. Jensen and Wallace [56] based on measured data, proposed that for indoor channel with identical set up of antennas at Rx and Tx, the AoD and AoA are assumed to follow the same distribution. They found and applied to their model the fact that AoD and AoD follow clustering phenomenon as well. The directional channel is [57]

$$h(\Theta^R, \Theta^T) = \frac{1}{LK} \sum_{l=0}^{L-1} \sum_{k=0}^{K-1} \beta_{kl} e^{j\varphi_{kl}} \delta(\Theta^T - \Theta_l^T - \omega_{kl}^T) \delta(\Theta^R - \Theta_l^R - \omega_{kl}^R), \tag{2.63}$$

where the receive and transmit angles are denoted as Θ^R and Θ^T, Θ_l^T and Θ_l^R are

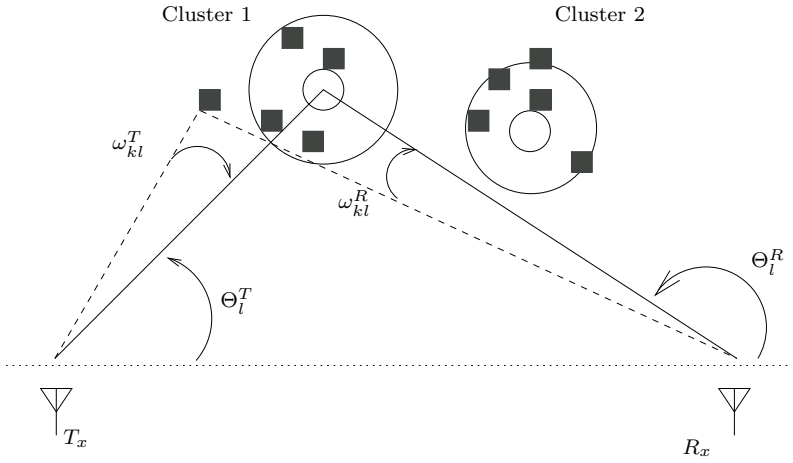

Figure 2.11: Extended SVA block model

the transmit and receive mean angles relative to the cluster l , and ω_{kl}^T ω_{kl}^R are the angles measured from the mean of the cluster l. figure 2.13 illustrates the concept. Using the complex antenna gain patterns the narrow band channel can be obtained

from the directional impulse response

$$h_{m,n} = \int_{2\pi}\int_{2\pi} W_m^R(\Theta^R)h(\Theta^R,\Theta^T)W_n^T(\Theta^T)d\Theta^T d\Theta^R, \tag{2.64}$$

where W_m^R and W_n^T represent the transmit and receive antenna patterns for elements n, m.

2.3.5 The Weichselberger Model

In the Kronecker model the transmit and receive correlation are assumed to be separable, meaning a complete independence of the Tx and Rx correlation properties. In contrast the Weichselberger model attempts to apply and allow an arbitrary coupling between the transmit and receive eigen base. Thus model the correlation at both ends jointly. The idea in this model is that the spatial eigen bases describe the radio propagation environment regardless of the transmit weights. Then the eigen values show how the radio propagation environment is illuminated, thus depend on the transmitter weight. The transmit and receive correlation matrices are eigen decomposed and only then applied to the channel model.
As was discussed earlier the Kronecker model generates a joint correlation matrix R, containing the correlation properties of both link ends, which is as follows,

$$R = E\{vec(H)vec(H^\dagger)\}, \tag{2.65}$$

where R is the joint correlation matrix, $E\{\}$ is the expectation, $()^\dagger$ is the matrix hermitian, $vec()$ stacks the columns of a matrix, and H is a channel matrix realization. The joint correlation matrix R can be approximated by the Kronecker product of the one sided correlation matrices $R_{Rx} = E\{HH^\dagger\}$ and $R_{Tx} = E\{H^T H^*\}$, representing the receive and transmit link ends respectively. Given a number of channel realizations the one sided correlation matrices can be estimated from,

$$\hat{R}_{Rx} = \frac{1}{T}\sum_{t=1}^{T} H(t)H^H(t), \tag{2.66}$$

$$\hat{R}_{Tx} = \frac{1}{T}\sum_{t=1}^{T} H^T(t)H^*(t), \tag{2.67}$$

where, $H(t)$ is one snapshot of a T number of channel realizations, and $\hat{()}$ denotes estimate. The eigen decomposition of the estimated $\hat{R}_{Rx}$ and $\hat{R}_{Tx}$ will provide the eigenbasis U_{Rx} and U_{Tx}, and the diagonal matrices Λ_{Rx} and Λ_{Tx} containing the eigenvalues of R_{Rx} and R_{Tx}. The eigen decomposition is as follows [45] [58]

$$R_{Rx} = U_{Rx}\Lambda_{Rx}U_{Rx}^{H}, \tag{2.68}$$

$$R_{Tx} = U_{Tx}\Lambda_{Tx}U_{Tx}^{H}. \tag{2.69}$$

The eigenbases represent the properties of the propagation environment, as for example, the position, number and strength of the scatters, while the eigenvalues give an insight on how the scatterer population is illuminated. With these statistics in hand a coupling matrix Ω is defined, the matrix describes the energy transfer between the corresponding receive and transmit eigenvectors, the coupling matrix can be estimated from the following relation,

$$\Omega = E\{(U_{Rx}^{\dagger}HU_{Tx}^{*}) \odot (U_{Rx}^{T}H^{*}U_{Tx})\} \tag{2.70}$$

where circle with dot is an element wise multiplication. Weichselberger proposed the following channel model

$$H = U_{Rx}(\tilde{\Omega} \odot G)U_{Tx}^{T}. \tag{2.71}$$

The U matrices are eigen modes at receiver and transmitter, G is an $i.i.d$ random matrix and $\tilde{\Omega}$ is the element wise square root of the coupling matrix Ω. In [59] they compare performance metrics of the Kronecker, the Weichselberger and Virtual Channel Representation.

2.4 Diversity

A fading signal can be though of consisting three components, path loss, large scale or shadow fading, and small scale multipath fading. Path loss originates from the expansion of waves as they propagate through space, and from interactions with matter, lossy materials, reflection, refraction, absorption, diffraction are among oth-

ers which contribute to this term. Shadow fading is due to large obstructions at distances of many wavelengths from receiver, and imposes amplitude and phase changes on the signal that can be considered as roughly constant for short periods of time because they are varying slowly with time. On the other hand small scale multipath fading creates random fast fluctuations of amplitude and phase on the received signal. The first two terms, path loss and shadowing usually are correlated and fairly similar among the elements of an antenna array, therefore the antennas in the array sample the same path loss and shadowing components, hence they have a limited use of providing a marginal benefit by increasing the SNR. Yet in small scale multipath fading the signal amplitude and phase varies rapidly over short periods of time, due to a dense scatterer population in the vicinity of the receiver where the field components can randomly add up destructively or constructively at each antenna, therefore elements in an array can readily sample independent signals, making the benefit substantial, as it becomes possible to recover from a deep signal fade. For these reasons diversity combining methods mainly address the small scale multipath fading.

Multipath propagation presents rapid random signal variations at the receiver, deep fades can degrade the SNR and link performance. Diversity techniques, which these days are plentiful, provide the receiver with numerous ideally independent versions of the transmitted signals, where if the probability of one of these signals be in deep fade is $P < 1$, then the joint probability of N diversity branches being in deep fade is $P^N << 1$.

The two main methods of maintaining channel capacity are signalling based diversity and antenna based diversity. In antenna diversity the independent fading signals are acquired by multiple antennas, which need to be designed and arranged in a manner as to maximise the de-correlation of received signals, which can then be combined if desired. The radiating elements themselves have three degrees of freedom, amplitude, phase and polarization. One must note however that major drawback of antenna diversity is the added complexity, cost, extra equipment(RF front end), real estate on mobile devices and possibly reduced battery life[46].

Modeling and optimizing diversity for truly mobile as opposed to fixed base stations has its differences. For example at the base station the angle of arrival of the incident field is usually narrow and this prohibits the effectiveness of space diversity

as very large spacings may be necessary to achieve low correlation, on the other hand at the mobile stations where angle of arrival of incident fields is often assumed uniform over the azimuth, small spacing of antennas can lead to small correlation. Also the polarization of scattered signals follows different behaviour around the BS and MS[60].

Nevertheless two golden rules exist for successful diversity scheme , low branch correlation and equal mean branch power, there is no sense in having a branch with high mean power and one with negligible mean power. In regard to MIMO systems diversity is one of the key parameters aiding and dictating potential performance. For example Space time codes take advantage of diversity across space and time. The main diversity schemes used in modern wireless communications are to be outlined [36]

- Array Gain

  Is a measure of the average increase in the signal to noise ratio at the receiver. Multiple antennas must be used at receiver or transmitter or both. Gain is due to coherent combining of received signals. Perfect channel state information must be available at the side/s of the link were the multiple antennas are located. Using CSI transmit and/or receive arrays are multiplied by weights.

- Diversity Gain

  - Temporal Diversity

    Battles multipath fading by providing replicas of the transmitted signals across time. This can be achieved with the use of channel coding and time interleaving techniques. The channel must vary in time so to provide a new replica (channel coherence time less that interleaved symbol duration).

  - Frequency Diversity

    This method produces replicas of the transmitted signal in the frequency domain. Different band of the spectrum undergo different fading. The coherence bandwidth of the channel must be smaller the bandwidth of the signal.

  - Spatial Diversity

Spatial diversity relies upon the physical separation of the antennas at the respective side of a communication link. Under certain conditions which are to be discussed in section 2.4.2.4 the elements can receive independent uncorrelated signals therefore reducing the probability of a deep signal fade.

- Polarization Diversity

  The propagation medium can depolarize the transmitted signal. Polarization diversity is based on physically separated or even co- located antennas that sample different field polarizations. The antennas are designed as to have a level of polarization discrimination, receiving one of the polarizations more efficiently than the other. Polarization diversity is discussed in section 2.4.2.2

- Pattern(Angle) Diversity

  Antennas have three dimensional radiation properties that are functions of space coordinates, effectively providing more significant gain in different directions, this fact coupled with the three dimensional power angular spectrum distribution of the incident fields can create the possibility on increased signal decorrelation at the antenna terminals. Angular diversity is discussed in section 2.4.2.1

2.4.1 Combining Methods

Having multiple antennas at either or both sides of a wireless link is the first step towards a more robust system, the next step is to decide how to utilize the this new degree of freedom. There are four main categories of diversity combining methods which will be briefly presented. Selection diversity allows for logarithmic growth of SNR (lnN) as the number of receive paths in increased. EGC and MRC provide average receive SNR that increases linearly with the number of available branches[60].

2.4.1.1 Switched combining

Switched combining has the benefit of needing only one RF front end for N antennas, this is graphically shown on the left of figure 2.12. A branch is used until its SNR has fallen bellow a predetermined threshold. Then the next branch with SNR above

the threshold is selected, performance is worse than selection combining as there may be signals with high SNR that have not been selected for use.

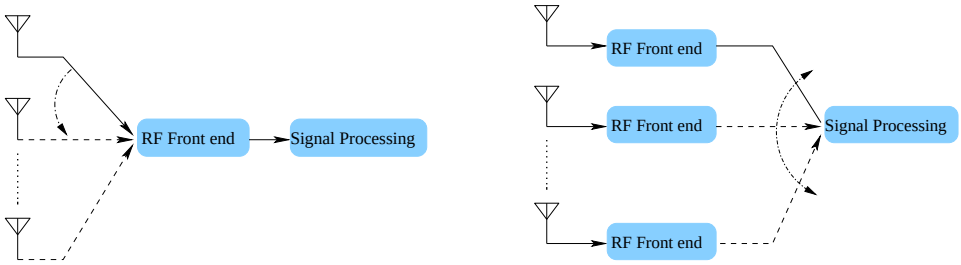

Figure 2.12: On left block diagram, switched combining. On right, selective combining

2.4.1.2 Selective combining

A selection combining diversity system with N branches monitors the SNR of all received signals and selects the highest one. As is shown on the right of figure 2.12, this scheme requires N, RF front ends and only needs to measure signal power, no variable gain or phase shifting is applied. It requires a floating threshold which is difficult to realise. Figure 2.13 coarsely demonstrates the operation of such a system. A four branch diversity is assumed, thus four fading time series are plotted in the figure which correspond to the received signals of each of the four diversity antennas, the selective combining receiver monitors all received signals and continuously selects the highest one amongst them, where in figure this is illustrated by the bold black dashed line.

The outage probability is expressed as [31]

$$P(\gamma < \gamma_s/\Gamma) = \left[1 - e^{-\frac{\gamma_s}{\Gamma}}\right]^N. \tag{2.72}$$

The CDF is valid for a Rayleigh channel and manifests an outage probability that decreases exponentially with N, the number of branches. Γ is the mean SNR assumed equal among all branches, γ is the instantaneous SNR and γ_s denotes an SNR threshold value. $P(\gamma < \gamma_s/\Gamma)$ is the probability that the SNR will fall bellow the threshold value of γ_s/Γ.

Figure 2.14 illustrates the performance of a selection combining system. The x

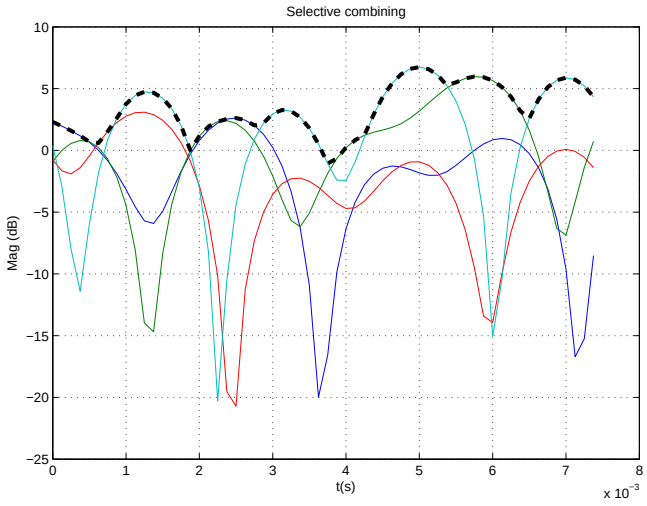

Figure 2.13: Figure illustrates four fading time series generated with a geometric discrete channel model, a selection combiner monitors all individual signal to noise ratios simultaneously and selects the best among them.

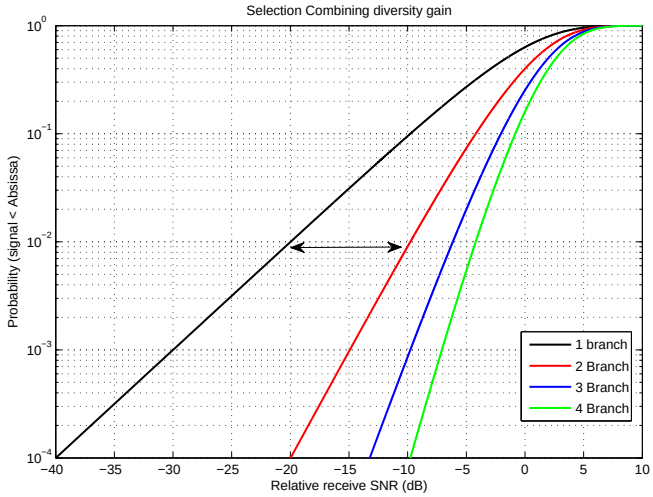

Figure 2.14: CDF of Rayleigh fading diversity gain, one to four branches using selective combining.The double arrow in figure point to the diversity gain at $P(\gamma < \gamma_s/\Gamma) = 1\%$, reliability of 99%, mean SNR is set to 10dB

axis of the figure represents the ratio of the threshold value γ_s to the mean SNR across all branches Γ, the ratio γ_s/Γ in the figure is defined in decibels. The y axis represents the probability of a respective threshold value being met, meaning that the instantaneous signal to noise ratio will fall bellow the given threshold γ_s/Γ. For example as shown in figure 2.14, for an outage probability of 1%, for one branch system, the relative receive SNR (γ_s/Γ), will be below $-20dB$, while for a two

branch system at the same probability the ratio of the threshold value γ_s to the mean receive SNR Γ is $-10dB$, a diversity gain of $10dB$ is possible.

2.4.1.3 Equal Gain Combining

It is by far more efficient to combine the branch signals than to just monitor and-or select only one of them, as the energy in the $(N-1)$ redundant branches is to go to waste. Equal gain combiners apply a unit gain and add coherently by phase locking the complex signals present at the receive branches, in this process noise is summed incoherently. Each branch signal is multiplied by a complex phasor θ_i relating to the phase of channel i. Figure 2.15 illustrates a block diagram of an equal gain combiner where an N number of branches are phase corrected to add up coherently with unity gain applied to them.

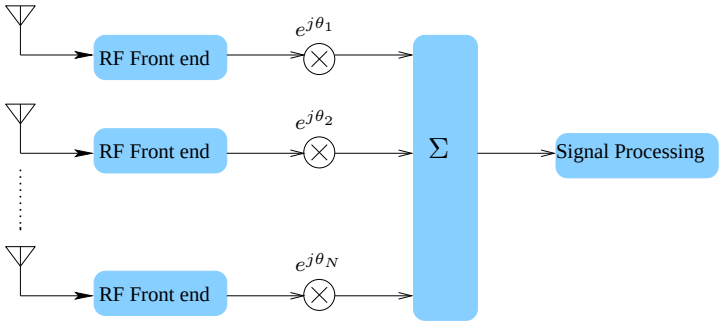

Figure 2.15: Block diagram of Equal Gain Combiner

2.4.1.4 Maximal Ratio Combining

Maximal ratio combining is optimal in terms of final output receive SNR. Figure 2.16 shows a block diagram of a MRC diversity system, where phase and gain correction terms are applied to the received signals. The output SNR is the weighted sum of each branch, the weights are chosen as the complex conjugate channel gains, similar to a matched filter for the fading signal. The algorithm used for estimating and implementing the appropriate gain weights and phase delays is fairly similar to RAKE receivers and equalisers. Both MRC and EGC require phase information to be estimated, however MRC also needs estimates on gains this can add to complexity as dynamic range of fading signals can be large. MRC performs marginally superior to EGC. Expression 2.73, shows the linear growth of SNR with the number of

branches, in effect is the coherent addition of the mean SNR of each branch[61].

$$\bar{\gamma} = \sum_{i}^{N} \bar{\gamma}_i = \sum_{i}^{N} \Gamma = N\Gamma. \tag{2.73}$$

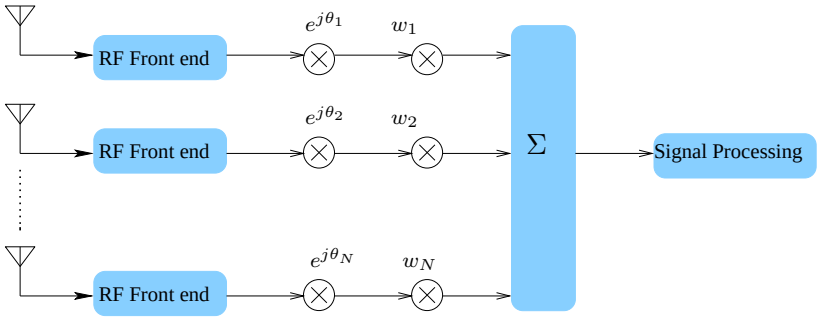

Figure 2.16: Block diagram of Maximal Ratio Combiner

2.4.2 Types of antenna Diversity

We already mentioned that for MIMO system to be efficient the received signals must be decorrelated (unique). Proper antenna design through diversity techniques can ensure minimum correlation between the received signals, that is if the propagation environment is rich enough to allow this. The choice of antenna element, the array configuration and the performance parameters of both can greatly affect the properties of the channel matrix and the SNR. Thus, affecting the capacity of the system. Consider a uniform linear array of two arbitrary radiating elements as shown in figure 2.17. In the Cartesian space shown in figure 2.17 they are placed at $d_0 = -(d/2) \cdot \hat{x}$ and $d_1 = (d/2) \cdot \hat{x}$ The radiation pattern of the elements is

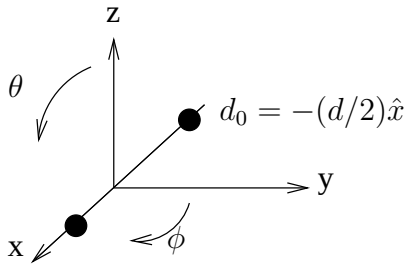

Figure 2.17: Uniform linear array topology, symetrical element separation

$\mathbf{e_1}(\theta, \phi)$ and $\mathbf{e_2}(\theta, \phi)$. The incident field distribution on the array depends on the

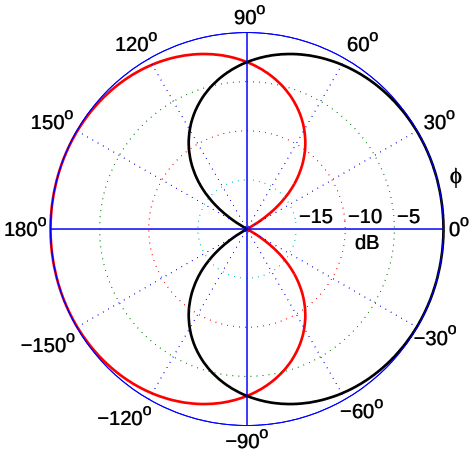

Figure 2.18: Example of possible pattern diversity, the red gain pattern could belong to one of the antennas in the uniform linear array and the black gain pattern to the other. Thus weighting incoming multipath in a near orthogonal way.

propagation environment and in expressions 2.74 and 2.75 is represented by L plane waves each having complex strength A_l and angle of arrival (θ_l, ϕ_l). The polarization of the random impinging multipath is denoted as $\mathbf{p_l}$. Both planes are taken into account with θ being the elevation or polar plane angle measurement and ϕ being the azimuthal plane angle. The received signals will be [62]

$$r_1 = \sum_{l=1}^{L} A_l\big(\mathbf{e_1}(\theta_l, \phi_l) \cdot \mathbf{p_l}\big) e^{-jk\frac{d}{2}\sin(\theta_l)\cos(\phi_l)}, \tag{2.74}$$

$$r_2 = \sum_{l=1}^{L} A_l\big(\mathbf{e_2}(\theta_l, \phi_l) \cdot \mathbf{p_l}\big) e^{jk\frac{d}{2}\sin(\theta_l)\cos(\phi_l)}, \tag{2.75}$$

where $k = \frac{2\pi}{\lambda}$. Examination of equations for the received signals in the uniform linear array, intuitively exhibit all the possible forms of antenna diversity. The distance(location) term will provide for the spatial diversity. The individual radiation patterns will allow for angle diversity, an example of possible angle diversity is shown in figure 2.18, where the two elements have near orthogonal patterns, effectively sampling efficiently with higher gain signals arriving from different directions. And the dot product of the radiation pattern with the polarization state of the incoming wave will give polarization diversity. A brief review of these antenna diversity techniques is to follow.

2.4.2.1 Pattern Diversity

The radio propagation environment has been investigated to an extent, it is well known that the distribution of polarization states and the distribution of fields over azimuth and elevation can vary depending on operational habitat, being rural, urban, indoor, satellite and so forth. Upon gaining the knowledge of the physical statistics of the environment a fundamental challenge arises, how to capture fields and illuminate space in the most efficient manner. In regard to multi–antenna signalling diversity is the key, thus the complexity of the challenge is one order higher as now propagation statistics and antenna diversity must be combined to yield an integrated solution.

The radiation pattern $\mathbf{e_p}$ is being composed of the θ and ϕ polarization gain patterns, with $\hat{\theta}, \hat{\phi}$ being the unit vectors in zenith and azimuth respectively considering a spherical coordinate system,

$$\mathbf{e_p}(\theta,\phi) = \mathbf{e_{p\theta}}(\theta,\phi)\hat{\theta} + \mathbf{e_{p\phi}}(\theta,\phi)\hat{\phi} = \begin{pmatrix} \mathbf{e_{p\theta}}(\theta,\phi) \\ \mathbf{e_{p\phi}}(\theta,\phi) \end{pmatrix}. \tag{2.76}$$

An instructive example will be considered, the analysis is found in [63], the author presents the power gain pattern of a wire half wave dipole. Assuming sinusoidal current distribution along the length of the dipole,

$$I = I_0 \cos\frac{2\pi}{\lambda} l, \qquad -\frac{\lambda}{4} < l < \frac{\lambda}{4}. \tag{2.77}$$

The dipole antenna gain pattern broken into the θ and ϕ components is

$$e_\theta = 1.641\{\cos(\theta)\cos(\phi)\sin(\alpha) - \sin(\theta)\cos(\alpha)\}^2 \cdot \frac{\cos^2(\pi\xi/2}{(1-\xi^2)^2}, \tag{2.78}$$

$$e_\phi = 1.641\sin^2(\phi)\sin^2(\alpha) \cdot \frac{\cos^2(\pi\xi)/2}{(1-\xi^2)^2}, \tag{2.79}$$

$$\xi = \sin(\theta)\cos(\phi)\sin(\alpha) + \cos(\theta)\cos(\alpha). \tag{2.80}$$

Considering figure 2.19, we can observe a Cartesian space (x, y, z), the dipole of the example is located at the origin and has it's main axis aligned vertically along the z axis. The term α in equations 2.78 - 2.80 represents the inclination angle in the

zy plane with respect to the z axis. The dipole's main axis is rotated from vertical to horizontal in the vertical zy plane.

For illustration purposes the equations were simulated parametrically and three dimensional patterns were produced for dipole inclination angles of $\alpha = 0°$, $\alpha = 45°$ and $\alpha = 90°$. Figures 2.19 and 2.20 show the results of the parametric simulation, where the the θ and ϕ gain pattern are plotted for three different inclination angles α. The author in [63] points an interesting fact, as the dipole is linearly polarised, when aligned vertically there is no e_ϕ pattern component, however when the dipole is aligned horizontally $\alpha = 90°$ there exists a horizontal and vertical gain pattern components.

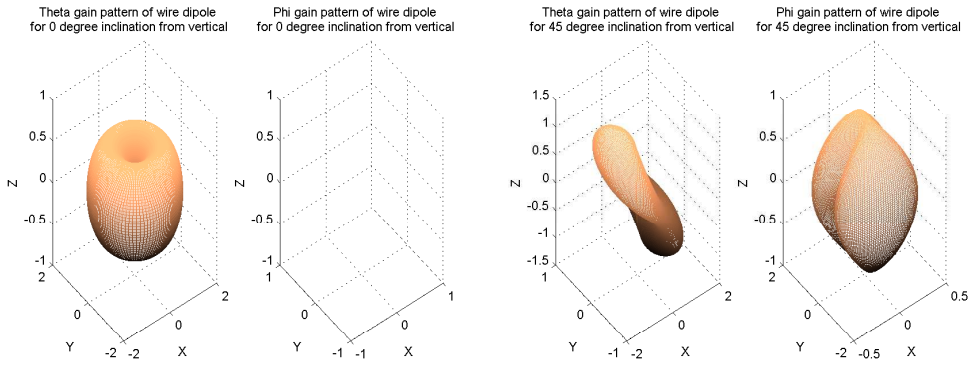

Figure 2.19: Wire dipole gain pattern components evaluated relative to inclination from vertical

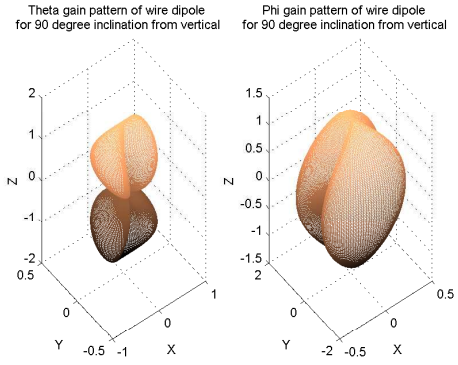

Figure 2.20: Wire dipole gain pattern components evaluated relative to inclination from vertical

The incident waves can be stochastically represented and referenced to the diversity antenna coordinates, the actual physical source electric field can be defined in

volt/meter/steradian

$$P_{inc}(\theta,\phi) = P_{inc,\theta}(\theta,\phi)\hat{\theta} + P_{inc,\phi}(\theta,\phi)\hat{\phi} = \begin{pmatrix} P_{inc,\theta}(\theta,\phi) \\ P_{inc,\phi}(\theta,\phi) \end{pmatrix}. \tag{2.81}$$

Usually the orthogonal polarization components of the incident field are assumed uncorrelated, each satisfying the angular correlation function

$$E\{P_{inc}(\theta_1,\phi_1)P_{inc}^{\dagger}(\theta_2,\phi_2)\} = S(\theta,\phi)\delta(\theta_1-\theta_2)\delta(\phi_1-\phi_2), \tag{2.82}$$

$$S(\theta,\phi) = E\{P_{inc}(\theta,\phi)P_{inc}^{\dagger}(\theta,\phi)\}, \tag{2.83}$$

where $S(\theta,\phi)$ is the probability density function of the power density time averaged per steradic square of the incident field. A polarization matrix for the incident fields can be defined, where the diagonal elements represent the average power in each polarization and and the off–diagonal elements the coupling from one polarization to the other, the dyadic power angular spectrum matrix is

$$S(\theta_1,\phi_1;\theta_2,\phi_2) = \begin{bmatrix} S_{\theta\theta} & S_{\theta\phi} \\ S_{\phi\theta} & S_{\phi\phi} \end{bmatrix}, \tag{2.84}$$

the elements of the matrix are populated from the following operation

$$S_{\phi,\theta}(\theta_1,\phi_1;\theta_2,\phi_2) = E\{P_{inc,\phi}(\theta_1,\phi_1)P_{inc,\theta}^{\dagger}(\theta_2,\phi_2)\}, \tag{2.85}$$

the open circuit voltage of a diversity antenna n can be computed from the incident field vector and the antenna open circuit radiation pattern vector

$$v_n = \int_{\Omega} \mathbf{e_n} \cdot \mathbf{P_{inc}} d\Omega. \tag{2.86}$$

Considering the n and m elements in an array the covariance matrix of the antenna terminal voltages can be obtained from

$$\rho_{n,m} = E\{v_n v_m^{\dagger}\}, \tag{2.87}$$

$$\rho_{n,m} = E\left\{ \int_{\Omega} \mathbf{e_n} \cdot \mathbf{P_{inc}} d\Omega \int_{\Omega} \mathbf{e_m^{\dagger}} \cdot \mathbf{P_{inc}^{\dagger}} d\Omega \right\}. \tag{2.88}$$

The diagonal elements of the terminal voltage covariance matrix ($n = m$) describe the received power and thus the signal to noise ratio for each diversity antenna, the off–diagonal elements provide the level of orthogonality between the antenna patterns and the relative power angular spectrum. Based on work done by Vaughan initially [46] and latter [64][49], most modern publications addressing angle diversity state that the following function should be minimized [65]

$$\rho_{n,m} = |\phi|^2 \int_{\Omega} \mathbf{S}(\Omega) \mathbf{e_n}(\Omega) \mathbf{e_m^{\dagger}}(\Omega) d\Omega. \tag{2.89}$$

In the expression $\rho_{n,m}$ is the open circuit signal correlation between antenna terminals n, m, $\mathbf{e}(\Omega)$ represents the radiation pattern of the antennas and $\mathbf{S}$ is the power angular spectrum, thus tensor that contains the field probability density functions over a solid angle for all polarization states. Britton and Jensen [65] perhaps in one of the most interesting treatments go a step further and compute the optimum current distributions for the multi–antenna terminal. The radiation pattern can be expressed in terms of the radiating current and the appropriate green function

$$\mathbf{e_n}(\Omega) = \int_{V} \bar{\bar{\mathbf{G}}}(\Omega, \bar{\mathbf{r}}) \cdot \mathbf{j_m}(\bar{\mathbf{r}}) d\bar{\mathbf{r}}, \tag{2.90}$$

$$\mathbf{j_m}(\bar{\mathbf{r}}) = \sum_{n} B_{nm} \bar{\mathbf{f}}_{\mathbf{n}}(\bar{\mathbf{r}}). \tag{2.91}$$

The integration is over a volume containing the currents. They then conclude by solving for the optimum currents, thus providing an antenna synthesis procedure. In follow up work [66] and [67] [68] extended this approach of modeling the spatial transmit and receive currents.

In [69] Forenza and Heath perform a comprehensive analysis and comparison of a circular patch array over a uniform linear array of dipoles, both consist of two elements. Basing analysis on the benefit of pattern diversity, they through simulations show that the CPA with the angle diversity qualities, in most scenarios outperforms the dipole ULA. The authors in [70] present a more minimal and intuitive simulation of the effect of directivity on MIMO capacity. In a section, a ULA of four ideal fictitious elements is considered and for simulation purposes two cases are assumed,

omnidirectional and beam–width of $\frac{\pi}{2}$ each, capturing individual quadrants over 2D azimuth plane. The directive array appears to outperform the omnidirectional ULA in a correlated scenario. Dong et al [71] using ray–tracing simulations and collocated antennas examine and compare pattern and polarization diversity. Perini and Holloway [72] compare angle and space diversity based on a measurement campaign through a rural and urban cellular radio scenario.

On a different note, from an antenna designers point of view there are numerous ways to achieve pattern diversity, for example in [73] they present a spiral and sinuous antenna, these can be efficiently excited into different radiation modes, having each distinguishable patterns in gain and in polarization between the modes. In [74] they explore pattern diversity by using switched parasitic elements, providing a basic adaptive system.

Nevertheless the possible true answer regarding pattern diversity lies with $\bar{\bar{\mathbf{S}}}(\Omega)$, following a decision on the dominant operational environment, appropriate probability density functions can be acquired thus allowing the optimization of the antenna gain patterns.

2.4.2.2 Polarization Diversity

Polarization diversity theoretically can provide two uncorrelated diversity branches at the base and mobile station, by the use of two orthogonal polarized antennas with no spatial separation restrictions, ie co–located or not. In the early days polarization diversity was investigated due to the fact that antennas at base stations needed extremely large spatial separations to obtain de–correlated signals, this is so because of the narrow spread of angle of arrival typically found at base stations. Lee and Yeh [75] in a classic paper demonstrated the benefit of polarization diversity. They point out that spatial diversity would require antennas at base stations to be spaced at 30λ for broadside incidence and more for in–line. On the mobile space diversity is efficient due to the large angle spread, thus even 0.5λ can be bring sufficient de–correlation of branches. Kozono [76] investigated base station antennas polarized at ± 45, which were receiving signals of a vertically or horizontally polarized mobile. Once more achieving large diversity gains compared to traditional systems. Vaughan [77] in an article on polarization diversity for mobile communications complemented the theory developed by others and at the introduction points the effectiveness of

the scheme and yet the so very few publications on the subject. Eggers and Oprea [78] present results on integration of polarization with space diversity at base stations in urban small and micro cells. The authors in all studies mentioned verified the findings through measurement campaigns. In a MIMO context Svanteson [79] examines the potential of implementing all six, electric and magnetic polarization states. Pulraz [37] investigates the performance of MIMO systems that use spatial multiplexing and Alamouti schemes under dual polarized antennas. The following articles also address polarization diversity and MIMO systems [80] [81]. However it appears that there is not a significant volume of work on polarization diversity at the mobile, backed by measurement campaigns.

Following the theory and suggestions found in the cited documents a brief introduc-

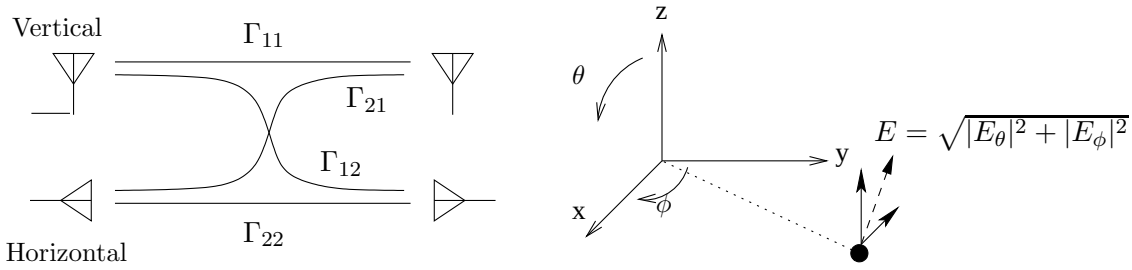

Figure 2.21: Polarization cross coupling on the left figure, and field components on the right figure

tion of the concept will be provided. Figure 2.21 shows a base station transmitting in vertical and horizontal polarizations, the mobile receives in respect these. Γ_{11} is a complex Gaussian random variable representing the voltage transfer between vertical co polarized antennas at the sides of the link, Γ_{22} is similar for the horizontal field, the terms Γ_{12} Γ_{21} provide the leakage or cross coupling of one polarization into the other due to depolarization of fields from the propagation medium, this takes place from wave and media interaction. In early measurement set ups a wire dipole and a wire loop antenna were used in orthogonal placement to receive the two components with reasonable accuracy, loading artefacts and surrounding objects like finite ground planes in proximity to the base of mobile antennas could affect the distinguishing purity. The voltages received by the two orthogonal receive antennas can be expressed as [75]

$$V_V = \Gamma_{11} + \Gamma_{21}, \tag{2.92}$$

$$V_H = \Gamma_{22} + \Gamma_{12}. \tag{2.93}$$

By first inspection of the system shown in figure 2.21, a major disadvantage is the splitting of power in two, thus a $3dB$ reduction. The Γ terms can be described by short and long term statistics. The short term statistics show random Rayleigh fading, thus uncorrelated, providing two possible diversity branches with no dependence on space separation. The long term statistics, show that local means exhibit similar shadowing, however means are not equal, variance of the means of the two channels is correlated and comparable with small ratio, within $\pm 3dB$ for about 90% of the time [75].

In a spherical coordinate system the vertically polarized component can be projected on to θ and the horizontal on to ϕ coordinate components

$$\mathbf{S}(\theta,\phi) = \mathbf{S}_\theta(\theta,\phi)\hat{\theta} + \mathbf{S}_\phi(\theta,\phi)\hat{\phi} = \begin{pmatrix} \mathbf{S}_\theta(\theta,\phi) \\ \mathbf{S}_\phi(\theta,\phi) \end{pmatrix}. \tag{2.94}$$

If P_V is the average power that could be received by a θ polarized isotropic antenna and P_H is the average power received by a ϕ polarized isotropic antenna, the ratio P_V/P_H represents the average power of the cross polarization components in the propagation environment. The cross polarization power ratio (XPR) is derived from measurements as $20log(E_V/E_H)$ [82]

$$XPR = \frac{P_V}{P_H} = 20\log_{10}\frac{E_V}{E_H}. \tag{2.95}$$

Considering a transmitting antenna, the radiated power, depending on the antenna power gain pattern (equation 2.70) will be distributed into the two polarization components accordingly. At the receive antenna, the incoming wave power of the cross polarized fields is related to the power supplied from the transmit antenna into each component plus the depolarizing effects of the propagation medium, allowing power to leak from one polarization to the other [81].

$$S_\theta^R = S_\theta^T\frac{XPR}{1+XPR} + S_\phi^T\frac{XPR}{1+XPR}, \tag{2.96}$$

$$S_\phi^R = S_\theta^T\frac{1}{1+XPR} + S_\phi^T\frac{1}{1+XPR}. \tag{2.97}$$

$S_\theta(\theta,\phi)$, $S_\phi(\theta,\phi)$ are the probability density functions of the power angular spectrum of incoming waves in elevation and azimuth respectively. These functions are usually normalized as to allow meaningful comparison between different distributions. Normalisation must satisfy the following condition

$$\int_0^{2\pi}\int_0^{\pi} S_\theta(\theta,\phi)\sin\theta d\theta d\phi = 1, \tag{2.98}$$

$$\int_0^{2\pi}\int_0^{\pi} S_\phi(\theta,\phi)\sin\theta d\theta d\phi = 1. \tag{2.99}$$

Recalling that the antenna power gain pattern $g(\theta,\phi)$ is consisted of the θ and ϕ components, $g_\theta(\theta,\phi)$ and $g_\phi(\theta,\phi)$, it can too be normalised for meaningful comparison of various experimental system configurations, the following condition is to be satisfied

$$\int_0^{2\pi}\int_0^{\pi} \{g_\theta(\theta,\phi)+g_\phi(\theta,\phi)\}\sin\theta d\theta d\phi = 4\pi. \tag{2.100}$$

In any given scenario the total average incident power is equal to the sum of the power in the two polarizations $P_V + P_H$. The actual received power of an antenna under test is P_{rec}, that is the mean power at the antenna terminals obtained from a random route in the environment. The mean received power of an antenna can be expressed as

$$P_{rec} = \int_0^{2\pi}\int_0^{\pi} \{P_V g_\theta(\theta,\phi)S_\theta(\theta,\phi) + P_H g_\phi(\theta,\phi)S_\phi(\theta,\phi)\}\sin\theta d\theta d\phi. \tag{2.101}$$

2.4.2.3 Mean Effective Gain

At this point a valuable performance metric on antennas in mobile communication environments can be defined. The Mean Effective Gain is the ratio of the mean received power of the antenna under test over the mean incident power, both obtained and averaged across a random measurement. This metric is especially important in multi–antenna systems, as it will provide a fair comparison of the operational efficiency of the antennas in the environment under consideration, as MEG is dictated by the mutual interaction of the antennas radiation pattern and the propagation statistics of the environment. It can be expressed as

$$MEG = \frac{P_{rec}}{P_V + P_H}, \tag{2.102}$$

$$MEG = \int_0^{2\pi} \int_0^{\pi} \left\{ \frac{XPR}{XPR+1} g_\theta(\theta,\phi) S_\theta(\theta,\phi) + \frac{1}{1+XPR} g_\phi(\theta,\phi) S_\phi(\theta,\phi) \right\} \sin\theta d\theta d\phi. \tag{2.103}$$

Evidently, polarization diversity and angle or pattern diversity are tightly coupled and linked.

2.4.2.4 Spatial Diversity

Space diversity is a common and simple method of diversity that is mainly used in base stations, however recently and in the future space diversity will be used increasingly at the mobile side due to high operating frequencies and devices such as laptops and PDA allowing just enough space to accommodate additional antennas. Having antennas separated by a distance in space can provide a decreased correlation of the received signals due to the superposition of multiple rays at each antenna each with different phase delays proportional to the path length from the scatterers to the respective antenna. When considering space diversity the environment at the base station and the one at the mobile are considerably different and thus are modelled appropriately, as at an elevated base station signals arrive from a small angular region while the mobile is surrounded with scatterers providing arriving signals of large angular spread.

To asses spatial correlation the orientation of the array has an effect. The angle γ

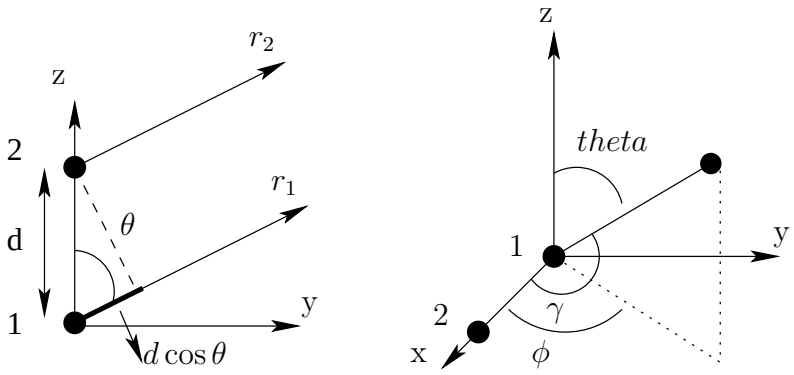

Figure 2.22: A uniform linear array of two isotropic radiators aligned along the z axis on the left figure and along the x axis on the right figure, considering two and three dimensional variation respectively

can be obtained from the dot product of the unit vector along the axis hosting the array and the unit vector in the direction of the incoming wave. Figure 2.22 provides an example of a uniform linear array placed along two principal axis. The unit vector

can be decomposed to respective components. Depending on the orientations of the array $\cos\gamma$ can be evaluated from [32]
for z, x or y aligned array respectively

$$\cos\gamma = \hat{a}_z \cdot \hat{a}_r = \hat{a}_z \cdot (\hat{a}_x \cos\phi \sin\theta + \hat{a}_y \sin\theta \sin\phi + \hat{a}_z \cos\theta) = \cos\theta, \quad (2.104)$$

$$\cos\gamma = \hat{a}_x \cdot \hat{a}_r = \hat{a}_x \cdot (\hat{a}_x \cos\phi \sin\theta + \hat{a}_y \sin\theta \sin\phi + \hat{a}_z \cos\theta) = \cos\phi \sin\theta, \quad (2.105)$$

$$\cos\gamma = \hat{a}_y \cdot \hat{a}_r = \hat{a}_y \cdot (\hat{a}_x \cos\phi \sin\theta + \hat{a}_y \sin\theta \sin\phi + \hat{a}_z \cos\theta) = \sin\theta \sin\phi. \quad (2.106)$$

The steering vector for an array aligned with the x axis is $[1 \quad e^{jkd\cos\phi\sin\theta}]$.

Figure 2.23 shows a uniform linear array on the receive side of a MIMO system with

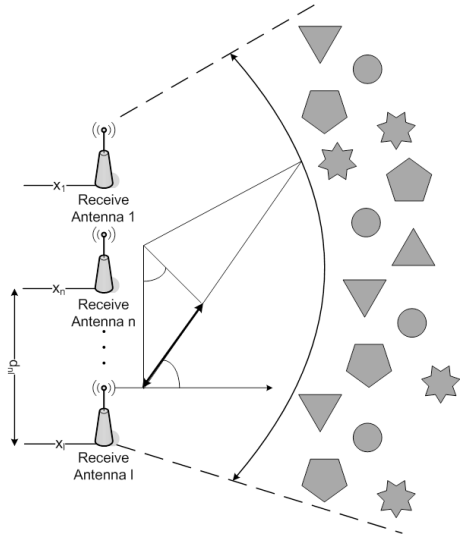

Figure 2.23: Scattering environment for ULA, element distance and angle spread affect correlation of received signals

n_R antennas illuminated by a scatterer population some distance from the receive array. Antenna effects such as pattern and coupling are neglected . The distribution and properties of scatterers around the receive antennas will create an effective angular spread S. Within this angular spread a probability distribution can be defined that describes the direction of arrival, usually for the mobile side of the link, the probability distribution is uniform between $-\pi$ and π. Assuming uncorrelated incoming wave magnitudes and using the steering vector of an x aligned array the correlation between received signals is [60]

$$E\{x_1 x_2^\dagger\} = \int_0^\pi \int_0^{2\pi} e^{-jkd\cos\phi\sin\theta} p_{\theta,\phi}(\theta,\phi) d\phi d\theta, \tag{2.107}$$

where $p_{\theta,\phi}$ is the *pdf* of the power angular spectrum, for convenience the *pdf* can be represented by the product of $p_{\theta,\phi}(\theta,\phi) = p_\theta(\theta)p_\phi(\phi)$. At the mobile a simple assumption is that the power angular spectrum in the azimuthal plane follows a uniform *pdf* [60]

$$p_\phi(\phi) = \frac{1}{2\pi} \quad 0 < \phi < 2\pi, \tag{2.108}$$

leading to a correlation function

$$\rho = \frac{1}{2\pi} \int_0^\pi \int_0^{2\pi} e^{-jkd\cos\phi\sin\theta} p_\theta(\theta) d\phi d\theta, \tag{2.109}$$

$$\rho = \int_0^\pi J_0(kd\sin\theta) p_\theta(\theta) d\theta, \tag{2.110}$$

the Bessel function of zero order and first kind is

$$J_0(x) = \frac{1}{2\pi} \int_0^{2\pi} \cos(x\cos\phi) d\phi. \tag{2.111}$$

If one lets $p_\theta(\theta) = \delta(\theta - \theta_0)$ then the correlation becomes $\rho = J_0(kd\sin\theta_0)$, this will allow the evaluation of the function with elevation fixed, for example setting $\theta_0 = \pi/2$ is equivalent to fixing the elevation angle to the azimuth plane. This however might not be adequate and not follow realistic conditions, then different *pdf* for $p_\theta(\theta)$ can be imposed that suit the environment, for example $p_\theta(\theta) = ae^{-b\cos\theta}$ which assumes that most power arrives from elevation angle of $\pi/2$ and falls off exponentially, the constants can be determined from measurements or channel models. The same is true for $p_\phi(\phi)$, in general the correlation integrals are difficult to solve analytically and numerical evaluation is needed [60].

In figure 2.24 the spatial correlation against the antenna spacing in wavelengths is plotted for three different angle spreads. The arrival angles at the receiver can be of a limited range. For the angle spreads shown in figure all arrival angles within the range are equally likely. It is apparent that as the angle spread decreases the correlation for a given antenna spacing increases. The curves in figure attempt to approximate the correlation of the fields based on the antenna spacing, however the correlation at the antenna terminals may be different due to effects such as mutual

coupling which is not taken into account in this evaluation of correlation.

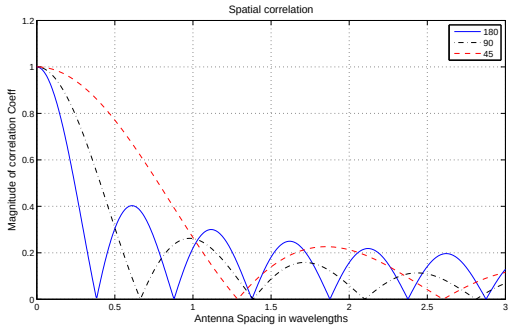

Figure 2.24: Spatial correlation for ULA, uniform distribution is assumed and three different angle spreads are plotted

The base station in a macro cell is usually located considerably higher above ground level compared to the mobile, as a result signals arrive from a narrow elevation angle. In azimuth due to the scatterers surrounding the mobile the angle spread is larger. A simple model is shown in figure 2.25 .The distributions can be chosen arbitrarily depending on environment under investigation. Seminal work on effects on correlation between base station antennas is presented in [83], a laplacian distribution and an analytical solution is presented in [84] and a Gaussian function is discussed in [85]. For fixed elevation angle $p_\theta(\theta) = \delta(\theta - \theta_0)$, then the correlation function becomes [60]

$$\rho = \int_{-\beta_{max}}^{\beta_{max}} e^{-jkd\cos(\phi+\beta)\sin\theta_0} p_\beta(\beta) d\beta. \tag{2.112}$$

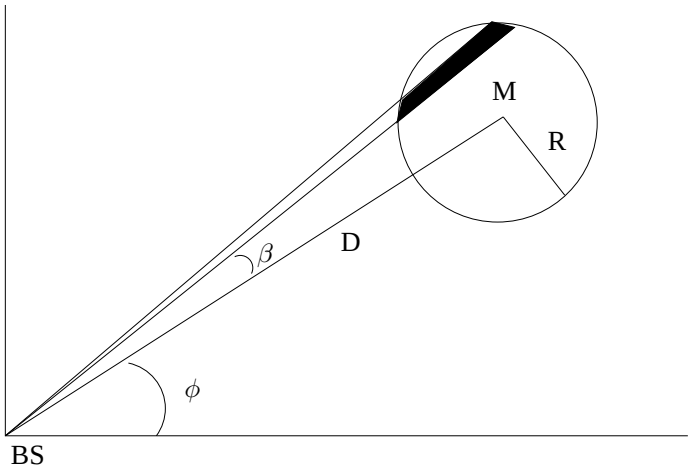

Figure 2.25: Scattering model relating mobile station to base station, view from top at the azimuth plane

2.4.2.5 Angle Distribution

The angular distribution of incident energy is of great interest and importance to mobile communication systems. It is always possible to statistically represent the spectrum of the vertical and horizontal components of the electric field in relation to their angle of arrival in elevation and azimuth. The vertical polarized component following propagation through the medium will have dependence on the spherical coordinates (θ, ϕ) and the same is true for the horizontal component. Hence each will have distribution in elevation and azimuth. Correlation coefficient is mainly dictated by distance between the elements and by the cooperative combination of the antenna radiation pattern with the Power Angular Spectrum. Often the highest intensity is concentrated in directions toward the transmitter.

To fit measurements of angular power density, mainly three statistical distributions have been proposed, uniform, Gaussian and Laplacian. Choosing the right distribution appears to be a challenge as published work depending on measurement set up and location does not share a common framework. In [86] they perform measurements in Helsinki for macro, micro and pico cells. In azimuth they find that some directions are more probable than others however due to the random route and orientation of mobile, uniform distribution can be assumed, in elevation they propose a Gaussian and Laplacian distributions that are closely linked to base station antenna height, base to mobile distance and environment supporting LOS or not. In a more recent study [87] they investigate LOS microcells with low base station antennas, they propose that distribution of incoming waves is Gaussian in both elevation and azimuth. Considering outdoor urban and rural areas the authors in [84] find that the azimuth power spectrum follows a Laplacian function, they state that the spread increases as the base station height decreases. In [88] the authors evaluate theoretical diversity performance and MIMO capacity through Monte Carlo simulation which includes and imposes the effects of angular power spectrum and polarization.

$$P_\theta(\theta, \phi) = P_\theta(\theta) P_\theta(\phi), \tag{2.113}$$

$$P_\phi(\theta, \phi) = P_\phi(\theta) P_\phi(\phi), \tag{2.114}$$

- Uniform distribution

$$P_{\phi}(\phi) = \frac{1}{2\pi - 0} \quad 0 \leq \phi \leq 2\pi, \tag{2.115}$$

- Gaussian distribution

$$P_{\theta}(\theta) = A_{\theta} exp\left[- \frac{\left\{\theta - \left[\frac{\pi}{2} - m_v\right]\right\}^2}{2\sigma_v^2}\right] \quad 0 \leq \theta \leq \pi, \tag{2.116}$$

$$P_{\phi}(\theta) = A_{\theta} exp\left[- \frac{\left\{\theta - \left[\frac{\pi}{2} - m_v\right]\right\}^2}{2\sigma_v^2}\right] \quad 0 \leq \theta \leq \pi, \tag{2.117}$$

- Laplacian Distribution

$$P_{\theta}(\theta) = A_{\theta} exp\left[- \frac{\sqrt{2}\left|\theta - \left[\frac{\pi}{2} - m_v\right]\right|}{\sigma_v}\right] \quad 0 \leq \theta \leq \pi, \tag{2.118}$$

$$P_{\phi}(\theta) = A_{\phi} exp\left[- \frac{\sqrt{2}\left|\theta - \left[\frac{\pi}{2} - m_h\right]\right|}{\sigma_h}\right] \quad 0 \leq \theta \leq \pi, \tag{2.119}$$

Gaussian distribution

$$P_{\theta}(\theta, \phi) = A_{\theta} exp\left[- \frac{\left\{\theta - \left[\frac{\pi}{2} - m_v\right]\right\}^2}{2\sigma_v^2}\right] exp\left[- \frac{(\phi - u_v)^2}{2\sigma_v^2}\right] \quad 0 \leq \theta \leq \pi, 0 \leq \phi \leq 2\pi, \tag{2.120}$$

$$P_{\phi}(\theta, \phi) = A_{\phi} exp\left[- \frac{\left\{\theta - \left[\frac{\pi}{2} - m_h\right]\right\}^2}{2\sigma_h^2}\right] exp\left[- \frac{(\phi - u_h)^2}{2\sigma_h^2}\right] \quad 0 \leq \theta \leq \pi, 0 \leq \phi \leq 2\pi. \tag{2.121}$$

As stated earlier measurement campaigns for angle and polarization distributions usually do not share a common framework, hence in published literature there is a small deviation in the values of the parameters for the appropriate distribution functions under an assumed environment. Tables with values for mean elevation angle (m_v, m_h), mean azimuth angle (u_v, u_h) and standard deviations (σ) obtained through measurements can be found in [63] [87] [86]. The table 2.1 provides parameter values from a COST 273 work group [5]

Table 2.1: Angular power distribution for indoor and outdoor scenarios [5]

	Laplacian/Uniform	**Gaussian/Uniform**
Distribution	$P_\theta(\theta) = Laplacian$	$P_\theta(\theta) = Gaussian$
	$P_\phi(\theta) = Laplacian$	$P_\phi(\theta) = Gaussian$
	$P_\theta(\phi) = 1$	$P_\theta(\phi) = 1$
	$P_\phi(\phi) = 1$	$P_\phi(\phi) = 1$
Indoor	$m_v = 20°$	$m_v = 20°$
	$m_h = 20°$	$m_h = 20°$
	$\sigma_v = 30°$	$\sigma_v = 30°$
	$\sigma_h = 30°$	$\sigma_h = 30°$
	$XPR = 1dB$	$XPR = 1dB$
Outdoor	$m_v = 10°$	$m_v = 10°$
	$m_h = 10°$	$m_h = 10°$
	$\sigma_v = 15°$	$\sigma_v = 15°$
	$\sigma_h = 15°$	$\sigma_h = 15°$
	$XPR = 5dB$	$XPR = 5dB$

In [63] the authors perform a measurement campaign in an urban environment in Japan. They attempt to measure and statistically represent the angular density functions of the vertically and horizontally polarized components of the incident field. They argue that with a valid statistical model of urban angular density function the Mean Effective Gain of antennas can be estimated with no need for a measurement campaign. It is reported in the paper that five or six principal incident waves arrive at an antenna standing still at an urban environment. They then propose that each of the incident vertical and horizontal polarized waves has an angular density function that is Gaussian in elevation and uniform in azimuth. From their measurements taken in a pseudo random urban route, they found that both polarization components of the five to six principal incident waves with respect to azimuth , were equally likely to occur from any direction thus they argue the validity of the uniform distribution in azimuth. Furthermore by averaging the receive power patterns from all route sample points with respect to elevation angle they find that measured values fit a Gaussian distribution. Having measured the horizontal and vertical components of the incident waves they provide values for XPR.

The statistical parameters of table 2.1 provide information about each of the vertical and horizontal components of the incident waves, their distribution in azimuth and elevation as well as the XPR, for indoor and out door scenarios based on recommendations from the COST 273 work group.

The authors in [89] [2] [6] argue that when evaluating correlation coefficient as a

function of distance the most significant factors are the power azimuth spectrum (not power angular spectrum which may contain elevation information) and the antenna radiation patterns. The complex correlation coefficient is [83] [84]

$$\rho = R_{XX} + jR_{XY}, \tag{2.122}$$

where R_{XX} represents the cross correlation between the real parts of the correlation function (equal to the cross correlation of the imaginary parts) and R_{XY} represents the cross correlation between the real and imaginary parts. Considering a power distribution in azimuth and $D = 2\pi d/\lambda$, they are expressed as [6] [2]

$$R_{XX}(D) = \int_{-\pi}^{\pi} \cos(D\sin\phi) PAS(\phi) d\phi, \tag{2.123}$$

$$R_{XY}(D) = \int_{-\pi}^{\pi} \sin(D\sin\phi) PAS(\phi) d\phi. \tag{2.124}$$

The truncated laplacian distribution used in the model can be computed from

$$PAS(\phi) = \frac{1}{A} \sum_{n=1}^{N} \frac{p_n}{\sigma_n} e^{\frac{-2\sqrt{2}|\phi-\psi_n|}{\sigma_n}}, \tag{2.125}$$

where N is the number of clusters, p_n is the power of the cluster, σ_n is the tap angle spread and ψ_n is the tap angle of incidence. A is used to normalise the *pdf* and is computed as [2]

$$\int_{-\pi}^{\pi} = PAS(\phi) d\phi = 1, \tag{2.126}$$

$$A = \int_{-\pi}^{\pi} \sum_{n=1}^{N} \frac{p_n}{\sigma_n} e^{\frac{-2\sqrt{2}|\phi-\psi_n|}{\sigma_n}}. \tag{2.127}$$

Figure 2.26 shows a truncated Laplacian distribution of the power azimuth spectrum with data from table 2.2, which describe the indoor channel model F used by the 802.11n task group. The plot shows the three cluster in model F for the receive side of the link and for channel tap 9.

Table 2.2: Indoor channel model F channel tap 9 [2][6]

		Cluster 1			**Cluster 2**			**Cluster 3**		
Tap number	Excess dealy[nS]	Power dB	AoA deg	AS Rx deg	Power dB	AoA deg	AS Rx deg	Power dB	AoA deg	AS Rx deg
9	180	-8.2	315.1	48	-5.3	180.4	55	-5.7	74.7	42

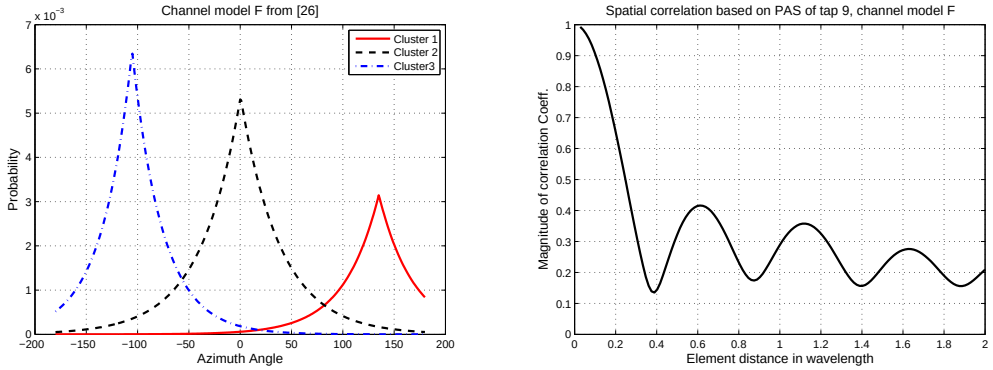

Figure 2.26: Laplacian distribution, data from 802.11n model F, ninth channel tap

Using the data for the 9^{th} tap from channel model F for the receive side and with antenna separation of half a wavelength the correlation matrix for the receive antenna can be computed from the equations given above

$$R_{rx} = \begin{bmatrix} 1 & -0.3214 - j0.0188 \\ -0.3214 + j0.0188 & 1 \end{bmatrix}. \tag{2.128}$$

A similar matrix can be formed for the transmit side and used to impose correlation effects on a simulated channel model.

2.5 N–Port network representation of antenna array

When modeling and analysing antennas either in isolation or in array configuration or ones with near objects that can act as parasitic elements it is essential, intuitive and constructive to represent the radiators by their physical electric equivalent circuits. N-Port network model and the appropriate impedance and scattering parameters are frequently used to asses important characteristics of the designed elements. In a multiple antenna system diversity performance is affected by mutual coupling, matching of network components to respective impedances and by near object parasitic absorption and scattering.

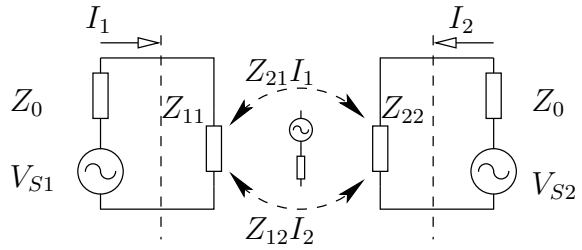

Figure 2.27: Two antennas in transmit mode, equivalent circuit

2.5.1 Antenna modeling

Figure 2.27 shows two antennas in transmit mode. Each of the two antennas has a self impedance Z_{11}, a source impedance Z_0 and a mutual impedance Z_{12}. The voltage transfer due to coupling is a function of the mutual impedance and the respective currents. In a tutorial paper the authors in [90] explain how often the equivalent circuits are used incorrectly. Receive antennas can be wrongly assumed minimum scattering implying that equal power is absorbed and delivered to a matched load as the power scattered, however the authors point out that the scattered power can be smaller, equal or greater than the absorbed power due to the possibility of additional sources in proximity of the receiver, as for example a parasitic element.
Based on N-port network representation the antenna system of figure 2.27, which contains two elements can be represented as a two port network having current and voltage relations of the form,

$$\mathbf{V_S} = (\mathbf{Z_A} + \mathbf{Z_S})\mathbf{I}, \tag{2.129}$$

where $\mathbf{V_S}$ is a vector containing the source voltages, $\mathbf{Z_A}$ is the antenna impedance matrix and $\mathbf{I}$ is a vector containing the respective currents. Following the circuit diagram of figure 2.27, matrices representing antenna and source impedances can be formed, a similar formulation can be applied to the receive side where the source impedance matrix is replaced by the load impedance matrix.

$$\mathbf{Z_A} = \begin{pmatrix} Z_{11} + Z_{12} & Z_{12} \\ Z_{21} & Z_{22} + Z_{21} \end{pmatrix} = \begin{pmatrix} z_{11} & z_{12} \\ z_{21} & z_{21} \end{pmatrix}, \tag{2.130}$$

$$\mathbf{Z_S} = \begin{pmatrix} Z_0 & 0 \\ 0 & Z_0 \end{pmatrix}, \tag{2.131}$$

where the elements of the antenna impedance matrix $\mathbf{Z_A}$ are defined as, Z_{11} and Z_{22} are the isolated self impedances when the antennas are radiating in absence of any other element or obstacle in an unbounded medium, Z_{21} is the mutual impedance at port one when port two is exited and port one open circuited, it represents the coupling characteristic from the exited terminal to the open circuited terminal, quantifying the voltage gained at the open circuit terminal due to the current flowing at the excited terminal . A similar definition holds for Z_{12} with the respective port numbers reversed. An expansion of this topic is included in section 2.5.2

Modern high frequency multi-port measurement equipment can provide simultaneous and/or switched port measurements, knowledge of the scattering and impedance parameters of a multi-element antenna is highly beneficial to signal processing and antenna design, in [91] they evaluate the diversity performance of mobile indoor antennas by first obtaining the impedance parameters by switched port measuring over a number of locations to average and factor the statistical nature of the z parameters in mobile communications. The relations between the parameters are [11]

$$S_{11} = \frac{(Z_{11}-Z_0)(Z_{22}+Z_0)-Z_{12}Z_{21}}{(Z_{11}+Z_0)(Z_{22}+Z_0)-Z_{12}Z_{21}}, \qquad z_{11} = Z_0\frac{(1+S_{11})(1-S_{22})+S_{12}S_{21}}{(1-S_{11})(1-S_{22})-S_{12}S_{21}}, \tag{2.132}$$

$$S_{22} = \frac{(Z_{11}+Z_0)(Z_{22}-Z_0)-Z_{12}Z_{21}}{(Z_{11}+Z_0)(Z_{22}+Z_0)-Z_{12}Z_{21}}, \qquad z_{22} = Z_0\frac{(1-S_{11})(1+S_{22})+S_{12}S_{21}}{(1-S_{11})(1-S_{22})-S_{12}S_{21}}, \tag{2.133}$$

$$S_{12} = \frac{2Z_{12}Z_0}{(Z_{11}+Z_0)(Z_{22}+Z_0)-Z_{12}Z_{21}}, \qquad Z_{12} = Z_0\frac{2S_{12}}{(1-S_{11})(1-S_{22})-S_{12}S_{21}}, \tag{2.134}$$

$$S_{21} = \frac{2Z_{21}Z_0}{(Z_{11}+Z_0)(Z_{22}+Z_0)-Z_{12}Z_{21}}, \qquad z_{21} = Z_0\frac{2S_{21}}{(1-S_{11})(1-S_{22})-S_{12}S_{21}}. \tag{2.135}$$

2.5.2 Mutual coupling

When antennas are in close proximity will interact. This interaction could alter the current distribution, the fields radiated or received and the input impedance of each element. The amount of interaction depends primarily on the radiation characteristics, relative orientation and relative separation of each element. Figure 2.28 shows three mechanisms that contribute to mutual coupling.

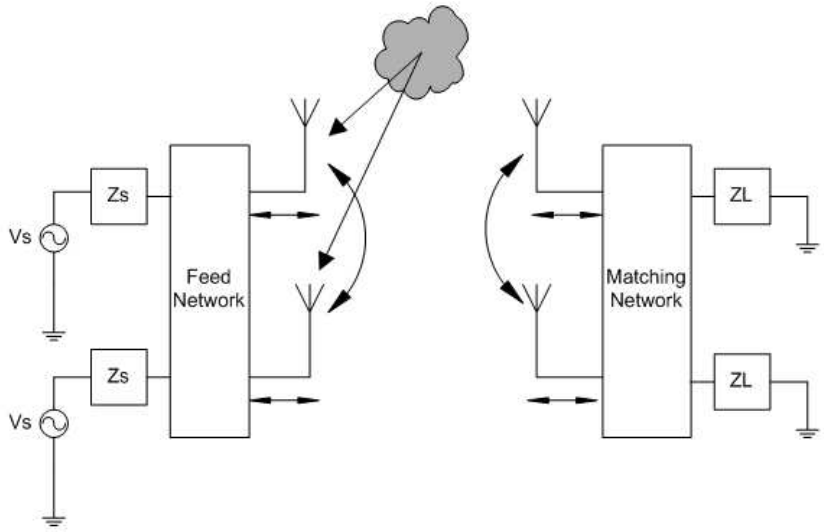

Figure 2.28: Mutual coupling diagram, showing common coupling mechanisms

The first mechanism is direct transfer of energy from one element to the other, second is indirect transfer of energy due to scattering of near by objects and third is the feed network. However there are other factors that cause interchange of energy, for example in planar antennas build on substrates, surface waves can contribute to coupling.

When an excited antenna is placed near another element, radiation from the driven antenna will induce currents on the second element which will then radiate and influence the currents on the first antenna. The second element can be excited or not (parasitic). In receiving mode an incident wave will strike antenna one and generate a current. Some of the energy induced in antenna one due to the incident wave will be absorbed and some radiated. At antenna two the incident wave will add vectorially with the wave radiated from antenna one. Hence to reduce coupling, elements must be matched to the termination impedance, as this can control to a level how much energy is absorbed and how much is radiated [32]

An antenna array with N elements can be represented as an N port network. For simplicity we will consider a two port network, using circuit theory the voltage current relations are [32]

$$V_1 = Z_{11}I_1 + Z_{12}I_2, \tag{2.136}$$

$$V_2 = Z_{21}I_1 + Z_{22}I_2, \tag{2.137}$$

$$Z_{11} = \frac{V_1}{I_1}\Big|_{I_2=0} \quad , Z_{12} = \frac{V_1}{I_2}\Big|_{I_1=0} \quad , Z_{21} = \frac{V_2}{I_1}\Big|_{I_2=0} \quad , Z_{22} = \frac{V_2}{I_2}\Big|_{I_1=0}. \tag{2.138}$$

Z_{11} is the single isolated element impedance. Z_{21} is the mutual impedance between terminal one and two and is defined as the open circuit voltage at terminal two divided by the current supplied to the first. By reciprocity $Z_{12} = Z_{21}$ and if the antennas are identical $Z_{11} = Z_{22}$. However the input impedance of an antenna in presence of mutual coupling is called driving point impedance and depends on the self and mutual impedances as well as to the ratio of excitation currents. The driving point impedance for the two port network is written as [32]

$$Z_{1d} = \frac{V_1}{I_1} = Z_{11} + Z_{12}\Big(\frac{I_2}{I_1}\Big), \tag{2.139}$$

$$Z_{2d} = \frac{V_2}{I_2} = Z_{22} + Z_{21}\Big(\frac{I_1}{I_2}\Big). \tag{2.140}$$

If we consider the case where the second antenna is connected to a load impedance Z_{L2} . Then the induced voltage at antenna two can be expressed as $V_2 = -Z_{L2}I_2$. We can then write [92]

$$-Z_{L2}I_2 = Z_{12}I_1 + Z_{22}I_2. \tag{2.141}$$

Solving for I_2

$$I_2 = \frac{-Z_{21}I_2}{Z_{22} + Z_{L2}} = \frac{-Z_{12}I_1}{Z_{22} + Z_{L2}}. \tag{2.142}$$

Substituting into equation 2.141 and dividing by I_1 will give [92]

$$\frac{V_1}{I_1} = Z_{1d} = Z_{11} - \frac{(Z_{12})^2}{Z_{22} + Z_{L2}}. \tag{2.143}$$

Equation 2.143 allows to define the input impedance of antenna one in terms of the two self impedances, the mutual impedance Z_{12} and the load impedance connected the terminals of the unexcited antenna two.

The presence of two antennas in proximity and the coupling effect will influence the radiation pattern of the elements. Impedance changes and phase shifts due to induced currents can be factored in the resulting radiation pattern.

Considering an array of two radiating elements, $E_n(\theta, \phi)$ represents the radiation pattern of the array when the n^{th} element is excited by a unit voltage with a generator impedance of Z_n while the other element is terminated with its generator impedance of Z_m. The array elements are assumed to be identical and $E_0(\theta, \phi)$ is defined as the isolated radiation pattern in absence of the other element or any obstacle. In such a case the element radiation pattern $E_n(\theta, \phi)$ valid when in the presence of the other terminated element can be obtained from the product of the isolated radiation pattern with the sum over the two array elements with currents as coefficients.

The current $I_{(m)}^{(n)}$ is evaluated on element m which is terminated by the generator impedance Z_m while antenna n is excited by unit voltage with a generator impedance Z_n. Therefore $I_{(m)}^{(n)}$ originate from mutual coupling. Equally $I_{(n)}^{(n)}$ represent the feeding current evaluated on antenna n excited by a unit voltage and having a generator impedance Z_n while all other elements are terminated by their associated impedances.

The patterns $E_1(\theta, \phi)$ and $E_2(\theta, \phi)$ can be expressed in the coordinate system of antenna 1 and 2 respectively, in such case they may need to be translated at the origin of the array coordinate system, this depends on the problem. Here we assume the origin of the array coordinate system to coincide with the centre of antenna one, therefore the phase adjusted unit excitation radiation patterns of each element can be computed from the following expressions [45] [93],

$$E_1(\theta, \phi) = E_0(\theta, \phi)\big[I_{(1)}^{(1)} + I_{(2)}^{(1)} e^{j\mathbf{k}\cdot\mathbf{d}}\big], \tag{2.144}$$

$$E_2(\theta, \phi) = E_0(\theta, \phi)\big[I_{(1)}^{(2)} + I_{(2)}^{(2)} e^{j\mathbf{k}\cdot\mathbf{d}}\big], \tag{2.145}$$

where, $\mathbf{d}$ is a vector from array origin to the centre of the i^{th} element, and $\mathbf{k}$ is the free space wave vector. We can substitute for the currents and obtain,

$$E_1(\theta, \phi) = E_0(\theta, \phi) I_{(1)}^{(1)} \left(1 - \frac{Z_{21}}{Z_{22} + Z_{L2}} e^{j\mathbf{k}d}\right), \tag{2.146}$$

$$E_2(\theta,\phi) = E_0(\theta,\phi) I_{(2)}^{(2)} \left(e^{j\mathbf{k}d} - \frac{Z_{12}}{Z_{11}+Z_{L1}} \right). \tag{2.147}$$

When estimating the correlation between a set of radiators the coupling effects should be included as the voltage vector at the output terminals of the coupled antennas depends on the impedance and phase shifts introduced by induced currents. Figure 2.29 illustrates a network equivalent of a two element antenna system at the

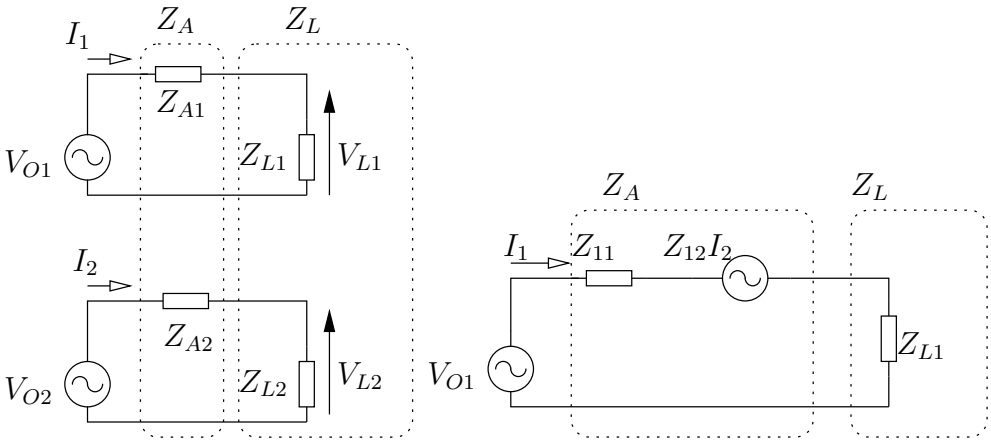

Figure 2.29: The left side of figure shows an equivalent circuit for a terminated two element receiving array, while on the right side the equivalent circuit for a single element is shown.

receive side of the link. If the system operates in the context of diversity a statistical nature of mutual impedances is implied due to the random nature of the currents [46]. It is possible using fundamental circuit and matrix theory to relate the open circuit voltages, impedances and terminal currents as follows

$$V_O = [V_{O1}, V_{O2}, \ldots], \quad V_L = [V_{L1}, V_{L2}, \ldots], \quad I = [I_1, I_2, \ldots], \tag{2.148}$$

where V_O is the open circuit voltage vector, V_L is the load voltage vector and I is the vector with the respective currents. Leading to

$$V_O = (Z_L + Z_A)I, \quad I = V_O(Z_A + Z_L)^{-1}, \quad V_L = Z_L(Z_A + Z_L)^{-1}V_O, \quad V_L = Z_L I. \tag{2.149}$$

Using impedance parameters obtained from measurement or from numerical techniques the effects of mutual coupling and impedance mismatch can be included in models, thus allowing for correlation of the load voltages to be estimated with actual or simulated coupling and matching effects of of the respective antenna array. Equa-

tion 2.150 represents a transfer function from the open circuit voltages of a receive array to the voltages delivered to the loads, a similar approach can be applied to find the open circuit voltages.

$$Z_L(Z_A+Z_L)^{-1}=\begin{pmatrix} \frac{(z_{22}+Z_L)Z_L}{(z_{11}+Z_L)(z_{22}+Z_L)-z_{12}z_{21}} & \frac{-z_{12}Z_L}{(z_{11}+Z_L)(z_{22}+Z_L)-z_{12}z_{21}} \\ \frac{-z_{21}Z_L}{(z_{11}+Z_L)(z_{22}+Z_L)-z_{12}z_{21}} & \frac{(z_{11}+Z_L)Z_L}{(z_{11}+Z_L)(z_{22}+Z_L)-z_{12}z_{21}} \end{pmatrix}=\begin{pmatrix} a & b \\ c & d \end{pmatrix}, \tag{2.150}$$

$$\begin{pmatrix} V_{L1} \\ V_{L2} \end{pmatrix}=\begin{pmatrix} a & b \\ c & d \end{pmatrix}\begin{pmatrix} V_{O1} \\ V_{O2} \end{pmatrix}. \tag{2.151}$$

2.5.3 S–Parameter representation and matching networks

Mismatching and mutual coupling between ports of a network influences SNR and the properties of the channel matrix H. At the base station antennas where space may be available coupling may be small and negligible, however a matching network can still allow optimum power transfer, on the other hand at mobile terminals where antennas are compact and close to each other coupling can be significant and affect the efficiency and power gain of the antennas in the array. By introducing appropriate matching circuits between the antennas and loads or sources connected to them mutual coupling and power transfer can be optimised. In [94] based on the work of [95] they present a simple and interesting approach for evaluating matching networks. The model is based on impedance matrices and S parameters. They assume a $2x2$ MIMO system with identical radiating elements. In this case $Z_{11}=Z_{22}, Z_{12}=Z_{21}$ and the transmit receive impedance matrices are denoted as Z_{TT} and Z_{RR} respectively.Thus

$$Z_{TT}=\begin{pmatrix} Z_{T11} & Z_{T12} \\ Z_{T21} & Z_{T22} \end{pmatrix}, \quad Z_{RR}=\begin{pmatrix} Z_{R11} & Z_{R12} \\ Z_{R21} & Z_{R22} \end{pmatrix}. \tag{2.152}$$

The impedance matrices can be related to S parameters matrices by the following relation [11]

$$\mathbf{S}=(\mathbf{Z}+Z_0\mathbf{I})^{-1}(\mathbf{Z}-Z_0\mathbf{I}). \tag{2.153}$$

It is possible now to construct an S parameter matrix that can include the channel transfer function. Where, S_{TT} and S_{RR} represent Z_{TT} and Z_{RR} respectively in S parameters. S_{TR} represents transmission coefficients from receiver to transmitter and

it is assumed to be zero. S_{RT} represent transmission coefficients from transmitter to receiver

$$S_H = \begin{pmatrix} S_{TT} & S_{RT} \\ S_{TR} & S_{RR} \end{pmatrix}. \tag{2.154}$$

In the same articles [94][95] the authors suggest that S_{RT} can be estimated using the following expressions

$$\Big(Z_{RT}\Big)_{ij} = \sum_{n=1}^{N} E_i^R\Big(\theta_n^{AoA}\Big)\beta_n e_j^T\Big(\theta_n^{AoD}\Big), \tag{2.155}$$

$$S_{RT} = \left(I + \frac{Z_{RR}}{Z_0}\right)^{-1}\frac{Z_{RT}}{Z_0}(I - S_{TT}). \tag{2.156}$$

Where E_i^R is the reception pattern of antenna i, e_j^T is the radiated field per unit excitation current of antenna j, β_n is the complex gain of the n^{th} path and θ^{AoA}, θ^{AoD} represent angle of arrival and angle of departure respectively. The procedure described is based on the assumption that the fields radiated from antenna j ($e_j^T(\theta)$), can be derived from the field of a single element when others are open circuited and Z_{TT}. The same assumption is made for the receiver side. Z_{RT} relates transmit antenna currents to receive antenna voltages. However this is a two dimensional path based model with single polarization [95], the authors of [96] propose a more advance three dimensional polarimetric model that estimates the S parameter transfer matrix for each path. A polarization transfer matrix with gain and phase values for each path can be defined as

$$\Gamma_p = \begin{pmatrix} \Gamma_{\theta\theta,p} & \Gamma_{\theta\phi,p} \\ \Gamma_{\phi\theta,p} & \Gamma_{\phi\phi,p} \end{pmatrix}. \tag{2.157}$$

Considering the transmit antenna m and the receive antenna n, the transfer matrix can be populated from the following expression [96]

$$S_{RT,nm} = \sqrt{\frac{Z_{0,m}}{Z_{0,n}}}\sqrt{\frac{\Re\{Z_{A,n}\}}{\Re\{Z_{A,m}\}}}\sqrt{\left(\frac{\lambda_0}{4\pi}\right)^2 G_n G_m}\cdot\sum_{p=1}^{P}\begin{pmatrix} C_{\theta,n}(\theta_p^n,\phi_p^n) \\ C_{\phi,n}(\theta_p^n,\phi_p^n) \end{pmatrix}^T \Gamma_p \begin{pmatrix} C_{\theta,m}(\theta_p^m,\phi_p^m) \\ C_{\phi,m}(\theta_p^m,\phi_p^m) \end{pmatrix}. \tag{2.158}$$

Where $\Re\{Z_A\}$ is the real part of the antenna self impedance, G denotes the active gain, C_θ, C_ϕ is the angular pattern of the antennas in θ and ϕ polarization and P is the number of paths simulated in the model. The authors of the articles [94] [95] present three impedance matching networks. The S parameter matrix of the

matching network is defined as

$$S_M = \begin{pmatrix} S_{11} & S_{12} \\ S_{21} & S_{22} \end{pmatrix}. \tag{2.159}$$

The first matching case considered is the characteristic impedance match. Here

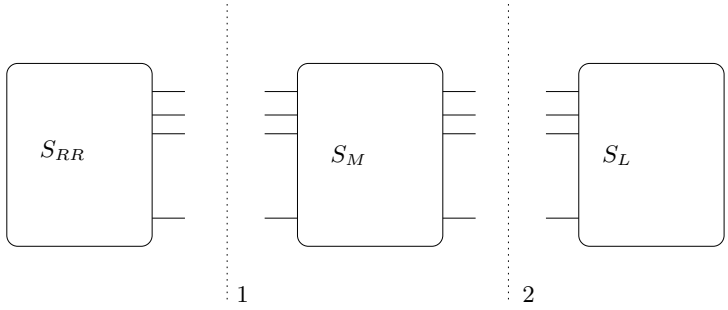

Figure 2.30: S Parameter network model for the receive side of the link, were S_{RR} are the S parameters of the antenna array, S_M are the S parameters of the matching network and S_L are the S parameters of the load connected to them

there is no matching network and each antenna is terminated in the characteristic impedance of the system (Z_0). Referring to the matching network S_M matrix, $S_{11} = 0$ and $S_{22} = 0$. The second case is the self impedance match where $S_{11} = diag\{S^*_{RR}\}$. Here the antennas are terminated in a load impedance that is the complex conjugate of the antenna self impedance ($Z_L = Z^*_{11}$) The third case is multi–port conjugate match. In this configuration the matching network provides a conjugate match on the antennas side as well as providing a conjugate match at the load side. This requires, $S_{11} = S^\dagger_{RR}$ and $S_{22} = S^\dagger_L$, proof and rigorous treatment of the three matching cases can be found in [97]. From the conservation of energy theorem the transmission coefficients of the matching network can be evaluated from [94] [11]

$$S^\dagger_{11}S_{11} + S^\dagger_{21}S_{21} = I, \tag{2.160}$$

$$S^\dagger_{12}S_{12} + S^\dagger_{22}S_{22} = I. \tag{2.161}$$

If we assume that the antennas are lossless (neglecting dielectric, scattered and conductor losses) then we can easily calculate the matching efficiency due to impedance mismatch. Based on this assumption the efficiency in transmitting mode is defined

as the ratio of the radiated power to the power delivered at the input

$$\eta = 1 - |\Gamma|^2, \tag{2.162}$$

where Γ, is the reflection coefficient. The reflection coefficient matrix with a matching network in place at the transmitter side looking into the matching network from the source is given in [23][26] and is

$$\Gamma = S_{22} + S_{21}(I + S_{TT}S_{11})^{-1}S_{TT}S_{12} = \begin{pmatrix} r_{11} & r_{12} \\ r_{21} & r_{22} \end{pmatrix}. \tag{2.163}$$

Matching efficiency is defined in [23][26] and in given as

$$\eta = 1 - |r_{11}|^2 - |r_{12}|^2. \tag{2.164}$$

Chapter 3

Printed Inverted F Monopole Antenna

"Nothing is more active than thought, for it travels over the universe, and nothing is stronger than necessity for all must submit to it"

Thales

3.1 Introduction

Earlier chapters addressed fundamental propagation and multi–element antenna concepts, characteristics and performance metrics. Many different antenna types are being considered and further developed for MIMO applications for both the base and mobile terminal, in summary the essential requirements are that the antennas exhibit high isolation and high diversity gain, in addition to the traditional requirements of adequate efficiency and good impedance matching. Radiators destined for mobile terminals often operate on ground planes of finite size (comparable to the wavelength) which influences the impedance bandwidth, the radiation pattern and the matching to the RF front end [98] [99]. Coupling to the battery casing also can introduce undesired effects [98], as does the immediate surrounding environment (ie user hand and head). The electrical size of an antenna compared to its operating wavelength is directly linked with its performance, Chu's seminal work [100], and work done later by others [101] [102] provides a lower bound on the achievable performance metrics of a theoretical antenna occupying a predetermined defined volume.

Modern mobile communication devices evolve continuously with a fast and constant rate, for instance a fairly average device today will possibly be equipped with GSM,

GPS, Wi-Fi and Bluetooth. Considering the space constraint of mobile devices one can deduct that antenna evolvement and improvement is taking place at an equally fast pace. Where soon with the advent of MIMO enabled mobile systems, space and diversity performance will be the key issues to be addressed.

In literature PIFA seems to relate to two intrinsically different antenna topologies. The first is essentially a quarter wave patch antenna with a shorting wall or pin to the ground and is fed usually with a probe. In many cases to achieve adequate bandwidth a thick air substrate is present over a ground plane that is larger than the patch radiating element. In order to achieve wide and multi band operation a variety of slots, slits, notches or even stacking of patches can be applied [103] [104] [105] [106]. The second topology [107] [108] [109] [110] usually consists of one or two coupled monopoles having different electrical lengths fed through a microstrip line. A vertical side line helps reduce the required length of the monopoles and achieve good impedance matching at two frequencies. In most cases the vertical side line ends to a via that shorts it to the ground. This arrangement is sometimes also called stacked inverted F monopole antenna [111].

In this chapter the second topology mentioned, the stacked inverted F monopole antenna is initially under parametric study investigation. The aim is to improve and evaluate the behaviour of a relatively compact antenna and examine multi band and wide band operation scenarios for potentially latter use in a MIMO system antenna array. One realisation that was fabricated and measured meets the required spectral mask for the IEEE 802.11 standard at both operating bands (2.4–2.485 GHz and 5.2–5.9 GHz)making it suitable for compact mobile terminals with Wi–Fi capability. One other measured realisation of the element exhibits wide bandwidth in the order of 1.8 GHz and a second resonance of 350 MHz bandwidth. For indoor IEEE 802.11a/b/g applications the antennas should have radiation patterns as omni directional as possible which dictates radiation patterns of low peak gain that is larger than 0 dBi.

The real challenge however arises when an array is to be designed in the confined available space of mobile terminals. Recalling that small antennas inherently suffer from inferior performance due to their electrical size placing them in close proximity the strong coupling between them can significantly further reduce their efficiency in terms of radiation and diversity. In [112] the authors propose a dual band an-

tenna for WLAN, the elements are spaced 0.5λ at the lowest operating frequency. At $2.5GHz$,$S_{12} = -10dB$ and at $5.4GHz$, $S_{12} = -25dB$. In [113] the authors present a tri–band antenna array with elements spaced 0.25λ at $2.45GHz$, the off diagonal scattering parameters are in the order of $-14dB$ for all operating frequencies. The authors of [114] examine possible decoupling of PIFA antennas on a common ground plane, spaced half a wavelength apart at $1.8GHz$, initially they find $S_{12} = -9dB$ even though antennas are spaced by $\lambda/2$, by introducing resonant slits on the ground plane S_{12} drops to below $-23dB$ for the whole bandwidth of interest. Clearly strong coupling of radiators in mobile terminals is imminent thus decoupling efforts are highly desirable and possibly necessary if board real estate is inadequate to accommodate multiple elements.

Here, a novel 2×2 dual band printed stacked inverted F monopole antenna array is proposed and studied. The antennas are placed extremely close together with a separation of 0.13λ at $2.4GHz$. Coupling is suppressed by a grid of parasitically coupled microstrip lines.

3.2 Single Inverted F stacked monopole antenna

First, the design and performance characteristics of the single element will be presented. CST Microwave Studio was employed to simulate and optimize the antenna, the transient solver of the software uses the Finite Integral Technique to obtain solutions for EM problems over the computational domain.

3.2.1 Antenna layout and design considerations

The antenna is printed on a high frequency laminate, thus maintaining low profile, ease of fabrication and good fabrication tolerances. The substrate chosen is Rogers RO 3003 with dielectric constant of 3.04 and thickness of 1.52mm. The overall dimensions of the board shown in figure 3.1 are $40 \times 45 \times 1.52$ mm. In[111] the length of the monopoles is suggested to be close to quarter wavelength, that is the length of the arm added to the length of the vertical side line ($\frac{\lambda}{4} = l + h$), however due to coupling of the elements and in this case the absence of the via that shorts to ground the vertical impedance matching line, the length for both monopoles is

closer to half a wavelength (0.4λ) at 2.62 GHz and (0.39λ)5.49 GHz for upper and lower arm respectively . If the overlapping region of the side line with the ground plane is neglected then the total length becomes (0.365λ) at 2.62GHz and (0.32λ) at 5.49GHz. Nevertheless at 5.49 GHz the small lower arm behaves as a quarter wave resonator if we neglect the length of the side line due to the fact that virtually little current is concentrated at that region at this frequency.

If a via was present means to match the two resonances is by changing the distance of the vertical line and via from the feed microstrip line, however here matching is achieved by changing the length of the vertical line having fixed the distance from the microstrip line, this can be beneficial as if other dimensions would be fixed, then matching can be done without increasing the horizontal dimension of the element. One more thing to consider is that the width of the vertical line is narrower than the width of the arms. An optimum miter bend can be introduced at the right angle bend of the horizontal and vertical part of the antenna tracks to allow for optimum current flow, thus reduce the abrupt microstrip discontinuity created by the sudden ninety degree change. The distance of the top arm from the ground plane is 14 per

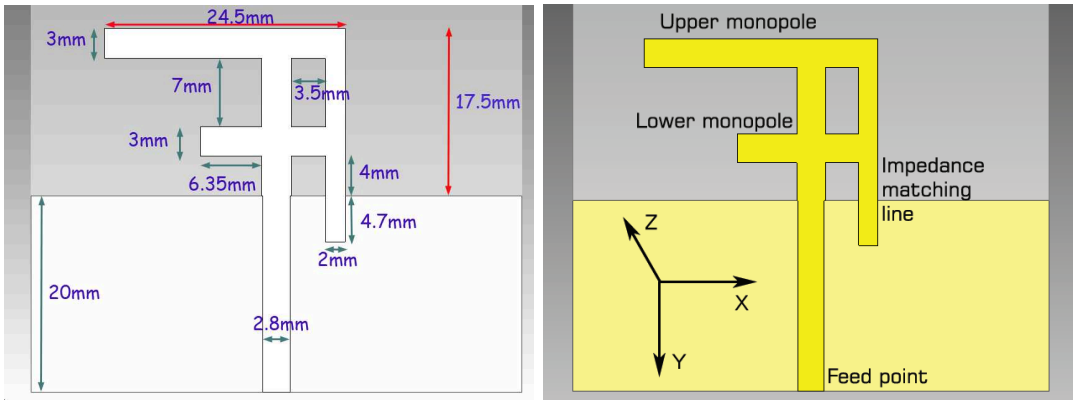

Figure 3.1: Inverted F stacked monopole antenna topology and dimensions. The coordinate system has the Z axis perpendicular to the substrate surface.

cent of the wavelength at 2.4 GHz while the distance for the lower arm is 7 per cent of the wavelength at 5.2 GHz. The dimensions shown in figure two are for the dual band case. The wide band element has the following differences, the length that is over the ground plane of the vertical impedance matching line is 0.5 mm, the length of the short arm is 14.4 mm and the length of the upper longer arm is 19 mm, all other parameters are the same.

3.2.2 Parametric study

A parametric study on the physical attributes of a planar inverted F antenna is to be presented. The PIFA under investigation does not have a shorting via to the ground in contrast to most other designs. The folding of the copper track that extends beyond the ground plane is done to reduce its profile while sustaining the resonant length, however the parallel section of the monopole with the ground plane introduces capacitance to the input impedance of the antenna, usually an inductive short circuit via is added to the end of the vertical side line to counter the capacitance, here matching is achieved by varying the length of an open circuited narrower line.

There are many degrees of freedom to vary however we will concentrate on four straight forward parameters, namely ground plane size, upper and lower monopole length and length of the vertical side line.

As the vertical side line has a profound effect on input impedance match it was the first parameter to study, Figure 3.2 shows return loss curves for ten different lengths of line each being incremented by 1.1 mm from the previous value. The resonance centred at 5.5 GHz is stable and does not shift, small improvement or deterioration of return loss magnitude can arise at this band. At the lower resonant band the variation in length has a massive effect, shifting of the operating band and broadband matching is possible. Reasons for this behaviour will become clearer by inspection of the surface currents at figure 3.6. For clarity and because the variation of this parameter affects mainly the lower band the input impedance is plotted for the frequency band between 2GHz–3GHz on the smith chart on the right of figure 3.2, three different length of line are simulated and it is clear that as the length of the stub reduces the input impedance increases and becomes more capacitive.

The length of the upper monopole was incremented by 1.2 mm and the simulation results are presented in figure 3.3. A small shift in frequency and some control over matching conditions around 2.5 GHz region is possible. It is worth noting that while the upper resonance is controlled mainly by the short monopole, careful selection of the physical parameters of the vertical side line and the upper monopole can produce a variety of return loss responses.

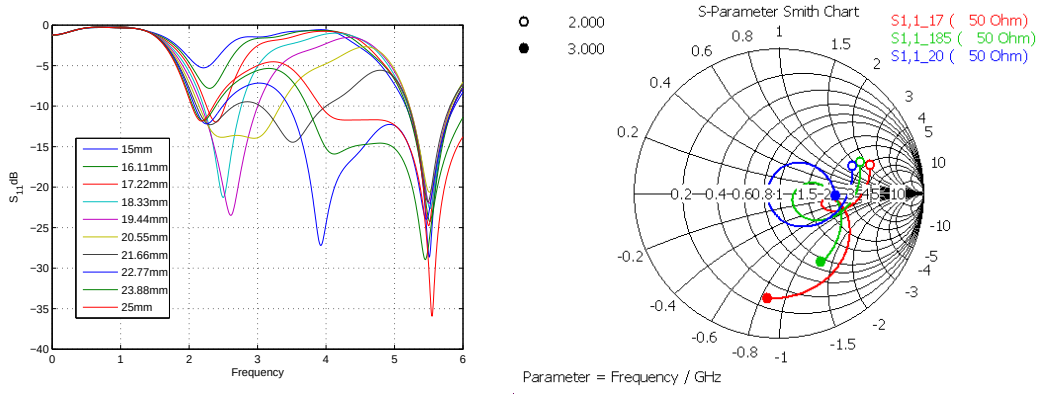

Figure 3.2: Simulated effect of varying the length of the vertical side impedance matching line on return loss(left), input impedance of antenna as a function of the length of the vertical line(right)

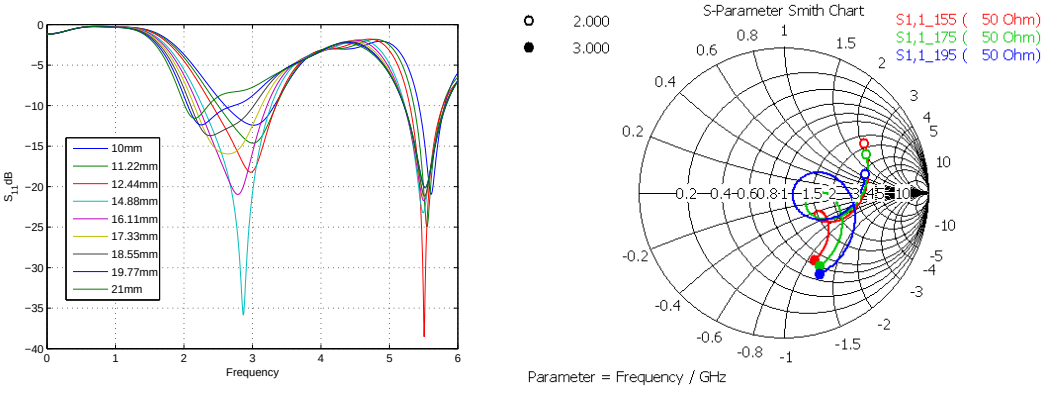

Figure 3.3: Simulated effect of varying the length of the long upper monopole on return loss(left), input impedance of antenna as a function of the length of the top long arm(right)

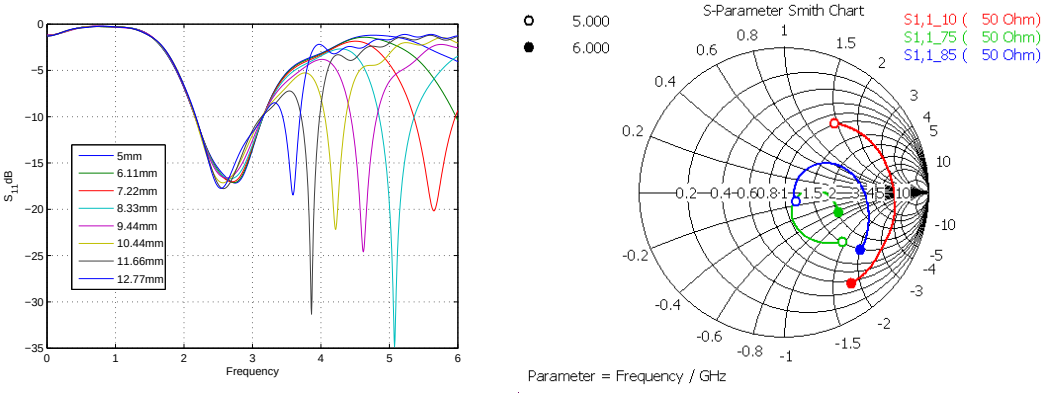

Figure 3.4: Simulated effect of varying the length of the short lower monopole on return loss(left), input impedance of antenna as a function of the length of the lower short arm(right)

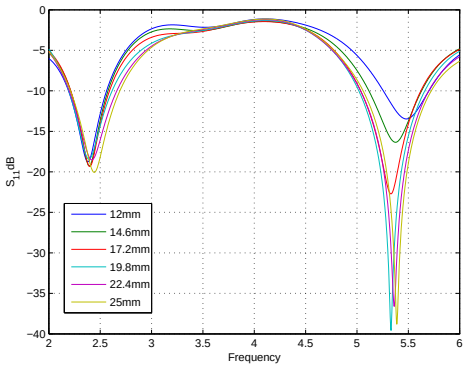

Figure 3.5: Simulated effect of varying the length of the ground plane on return loss

Input impedance of the antenna for the frequency band of 2GHz–3GHz is provided on the right of figure 3.3 on the smith chart. It is evident that as the length of the upper monopole is reduced input impedance increases and becomes more capacitive.

The length of the short lower monopole can shift the upper resonant band from about 3.6 GHz to over 6 GHz while the lower operating frequency band remains stable relative to frequency and impedance matching. In figure 3.4 the length of the monopole is incremented by 1.1 mm in every step. Varying the length of the longer upper monopole does not produce such a clear result as in figure 3.4 due to the fact that the resonance at 2.5 GHz originates from close coupling of the physical parameters of the top monopole with the physical parameters of the vertical side line, as we saw earlier in figure 3.2, once more the smith chart provides the input impedance of the antenna, however this time the frequency band plotted is between 5GHz–6GHz. The locus of the impedance curve clearly suggests that as the length of the lower monopole is reduced then the input impedance tends to reduce and become more capacitive.

The ground plane is important, induced currents contribute to the total radiation characteristics of the antenna. In [108] they explain that on a finite ground plane the structure behaves as an asymmetric dipole, where the difference in the current distributions on the actual monopole arm and the image on the ground plane create distortions in the radiation pattern, the best place for the PIFA is close to the edge of the ground, a good size for the ground is to be close to $\lambda/4$, for different sizes multilobed pattern and tuning difficulties may appear, they also point that there is potential for resonances to develop in the ground and filter through in the pass–band

of the antenna thus modifying and distorting impedance matching conditions.
The ground plane size might be modified in order to alter the radiation characteristics; a ground plane of 20 × 20 mm instead of 20 × 45 mm shown in figure 3.1 will produce a pattern of faintly greater omni directionality, however this is specific to the simulated dimensions. Five ground plane sizes were simulated, size was incremented by 2 mm and the effect on the impedance match at the two resonances is shown in figure 3.5.
The lower operating band remains virtually unaffected while at the upper band light shifting and considerable improvement in matching can be achieved. In [115] they show that for a quarter wave patch PIFA a ground plane size of 0.6λ produces a relative bandwidth of about 5 per cent and a ground plane size of 0.95λ produces a relative bandwidth of 10 per cent verifying the sensitivity and necessity of large ground plane for this type of radiators.

3.2.3 Surface current distribution

Surface current distribution was simulated and plotted for the PIFA with dimensions as shown in figure 3.1, which represent the dual band realisation. Figure 3.7 provides measured vs simulated return loss for the element shown in figure 3.1. Therefore by observing the graph, surface current distribution was simulated for both operating frequencies at the point of maximum resonance.
Figure 3.6 illustrates the current concentration at 2.5 GHz. It is clear that current flows in the same direction and is concentrated at the top long monopole and at the vertical side line with very little current being on the short lower monopole. At 5.5 GHz current density is high at the region of the short lower monopole while low densities are observed at the vertical side line and low to medium on the upper longer monopole. The current distributions shown in figure 3.6 support the findings of the parametric study presented in the previous section.

3.2.4 Single element measured and simulated results

Simulations are validated by experimental measurement of two fabricated elements, the design goal was to produce a dual band element that covers the IEEE 802.11 spectral mask requirements and another that is wide band within the two 802.11

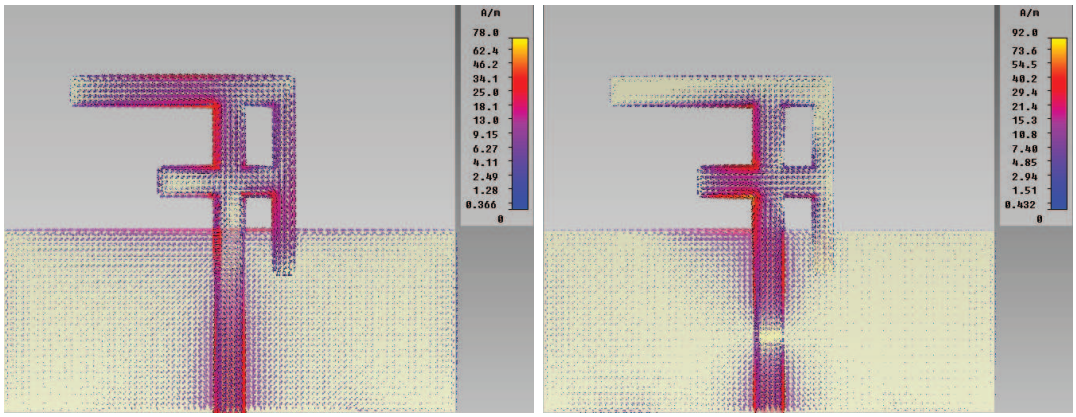

Figure 3.6: Current density for dual band element at 2.45 GHz(left) and at 5.5GHz (right).

bands. One exhibits dual band operation with measured impedance bandwidth of 250 MHz centred at 2.6 GHz and a bandwidth of 750 MHz centred at 5.49 GHz, while the other fabricated element has an impedance bandwidth of 1.8 GHz centred at 5 GHz and a second lower resonance centred at 2.95 GHz of 350 MHz bandwidth. Figure 3.7 compares simulated and actual measured S_{11} for both prototypes. The measurements were performed with an Agilent four port network analyser, the effects of the cables were removed by calibration.

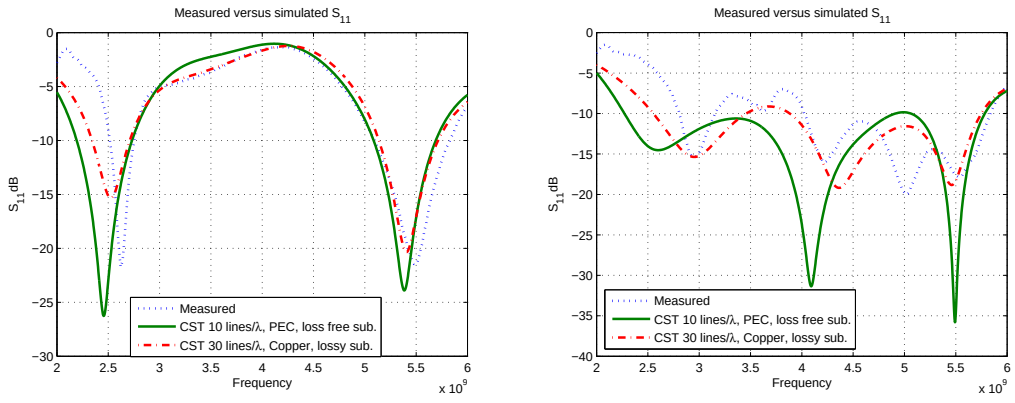

Figure 3.7: Left figure shows the measured versus the simulated S_{11} of the dual band element. Right figure shows measured versus simulated S_{11} of the wide band element. In both figures the lines/λ (wavelength), indicate a change in the simulation computational domain mesh, more lines per wavelength will provide a finer mesh

Figure 3.7 provides a comparison of simulation and measurement results. Two curves exist for simulation, one was obtained by a simple model consisting 10 lines per wavelength, a perfect electric conductor for the metallic parts and a loss free substrate, the other was obtained by a more realistic model assigning 30 lines per

wavelength and copper for the metallic parts in addition to a lossy substrate model. The number of lines per wavelength is linked to the wavelength of the highest frequency set for simulation. This classifies the spatial sampling rate of the fields inside the computational domain, therefore defines the minimum number of mesh lines for each coordinate direction that the solver uses for a distance equal to the wavelength of the highest frequency. The definition of lines per wavelength has an important effect on the accuracy of results and on the simulation time. A higher number will increase accuracy and computation time. Setting the value of lines per wavelength to 10, means that a plane wave propagating along one of the coordinate directions in the computational space will be sampled at least ten times relative to the wavelength of the highest frequency [116]. The lines per wavelength affect the meshing and the size of the spatial discretisation of the simulated structure. This was initially done to calibrate and verify the solution accuracy obtained by the models simulated in CST. Of course other parameters influence the accuracy such as the size and choice of ports and the frequency span set for the computation, as the solutions are obtained from a time domain solver, the shape and duration of the excitation pulse and the number of maximum pulses allowed will affect simulation time and the propagating energy content in the computational domain.

Table 3.1: Measured resonant frequencies and bandwidth(defined at S_{11} -10dB)

Element	f_{lower}	f_{upper}	$BW_{measured}$
Dual band (band 1)	$2.5GHz$	$2.75GHz$	$250MHz$
Dual band (band 2)	$5.1GHz$	$5.85GHz$	$750MHz$
Wide band (band 1)	$2.775GHz$	$3.125GHz$	$350MHz$
Wide band (band 2)	$4.1GHz$	$5.9GHz$	$1.8GHz$

Table 3.1 summarizes the measured impedance characteristics of the two prototypes that where fabricated, obtained from a network analyser, the bandwidth is defined at the points where S_{11} crosses the -10dB values. Reasonable bandwidth can be easily achieved with this kind of strucure, with very low cost, good repeatability and fabrication toloerances.

Before we move on to present the radiation characteristics of the PIFA elements a brief definition of antenna directivity and antenna gain will be provided in order to enhance and make the meaning of data presented clearer.

The directional properties of the radiation pattern of an antenna are described by

its directivity D, which is defined as the ratio of the radiation intensity in a given direction over that of an isotropic source.

An isotropic source has a radiation intensity equal in all directions, thus its directivity being equal to the total radiated power divided by 4π, the total solid angle of a sphere. The radiation intensity of an isotropic source U_0 is given by,

$$U_0 = \frac{P_{rad}}{4\pi}, \tag{3.1}$$

therefore the directivity of the antenna under test is defined as,

$$D = \frac{U}{U_0} = \frac{4\pi U}{P_{rad}}, \tag{3.2}$$

where, D is the directivity of the antenna, U is the radiation intensity of the antenna in a given direction, U_0 is the directivity of an isotropic source and P_{rad} is the total radiated power.

The gain of an antenna is essentially equivalent to the directivity with the antenna efficiency being taken into account, where now instead of the total radiated power, the input power at the antenna terminals is used in the definition, the gain is given as

$$G = \frac{4\pi U}{P_{in}}, \tag{3.3}$$

$$P_{rad} = eP_{in}, \tag{3.4}$$

$$G = eD, \tag{3.5}$$

where, G is the gain of the antenna in a given direction, U is the directivity of the antenna in a given direction, P_{in} is the input power at the antenna terminals, and e is the antenna efficiency accounting for losses due to reflections, conduction, and dielectrics.

Following the brief definition of antenna directivity and gain, it is appropriate to define a relative coordinate axis that the directive properties of the antenna can relate to. Figure 3.1 shows the topology of the PIFA with a three dimensional axis included. In the axis system shown in figure, Z is normal to surface of the substrate. The three principal axis cuts, ZX, ZY, and XY, if it were to be translated to a

spherical system they would be defined as,

$$XY \rightarrow \quad \text{vary}, \phi \quad \theta = 0$$

$$ZX \rightarrow \quad \text{vary}, \theta \quad \phi = 0$$

$$ZY \rightarrow \quad \text{vary}, \theta \quad \phi = 90$$

where $\theta = 0$ would start from the positive Z axis in the ZX and ZY planes and $\phi = 0$ would start from the positive X axis in the XY plane.

The two dimensional radiation plots provide an intuitive illustration on how the elements radiate or sample the fields relative to angle over the entire space. Maximum simulated directivity is 2.35dBi at 2.47GHz and 4.54dBi at 5.39GHz for the dual band element.

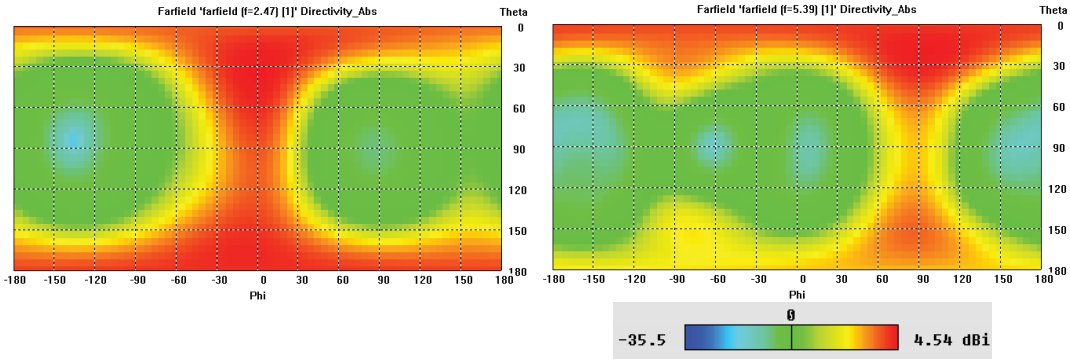

Figure 3.8: Simulated radiation pattern for dual band element in 2–dimensional plot, on left pattern at 2.47GHz and right at 5.39GHz

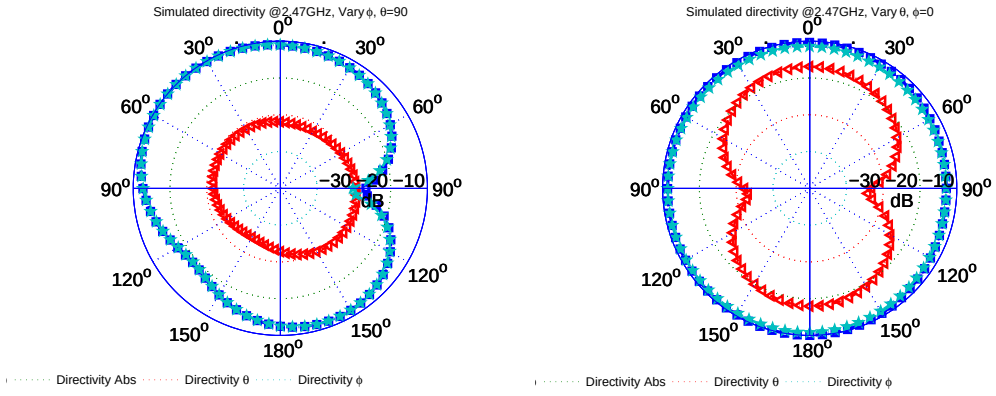

Figure 3.9: Simulated polar plot of dual band element, pattern is ploted at 2.47GHz. The absolute value directivity, the directivity in θ and ϕ components is shown in traces. In reference with figure 3.1, the principal axis cuts plotted are, the XY plane (left figure) and the ZX plane (right figure).

The polar plots in figures 3.9 –3.12 give a representation of the contribution of each field component with respect to angle for each simulated resonant frequency and at three principal axis cuts. At 2.47GHz it appears that the element is mainly sensitive to ϕ polarized field except the ZY plane shown in figure 3.10 where for an angle spread of 120 the ϕ component is stronger or equal to the θ , for the ZX plane the θ component power is for most angles 20dB below the ϕ which in this plane makes virtually all the contribution to the total directivity, at XY plane the ϕ component is still the dominant while the θ is ranging from 10 to 20dB below the ϕ.

At 5.39GHz for the ZX plane the ϕ component is once more the main contributor to the received power, however for the XY plane both components θ and ϕ play a significant part on the magnitude of the received power, for the ZY plane the ϕ component is higher yet for wide range of angle the θ is only few decibels down from the ϕ.

The reception of both polarisations can be highly beneficial to antennas destined for mobile handsets due to random stochastic nature of the received signal polarisation and the random orientation of the device.

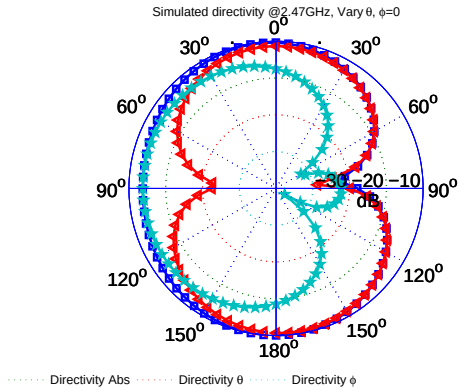

Figure 3.10: Simulated polar plot of dual band element, pattern is ploted at 2.47GHz. The absolute value directivity, the directivity in θ and ϕ components is shown in traces. In reference with figure 3.1, the principal axis cuts plotted is the the ZY plane.

Radiation patterns were recorded in an anechoic chamber, with a horn antenna providing the transmit field. High profile thick RF cables were present near the test and source antenna as was other small reflective surfaces from the support of the test antenna. These may introduce deviations and potential nulls at polar angles. The patterns were measured in ten degree steps at two frequency bands for each prototype.

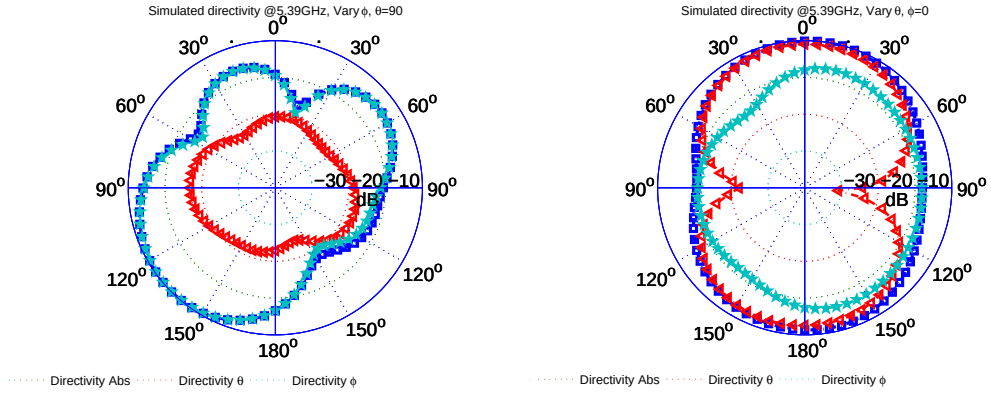

Figure 3.11: Simulated polar plot of dual band element, pattern is ploted at 5.39GHz. The absolute value directivity, the directivity in θ and ϕ components is shown in traces. In reference with figure 3.1, the principal axis cuts plotted are, the XY plane (left figure) and the ZX plane (right figure).

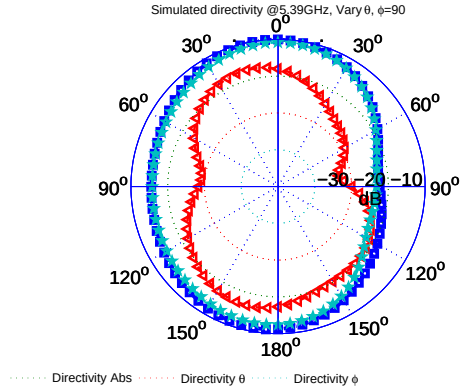

Figure 3.12: Simulated polar plot of dual band element, pattern is ploted at 5.39GHz. The absolute value directivity, the directivity in θ and ϕ components is shown in traces. In reference with figure 3.1, the principal axis cuts plotted is the the ZY plane.

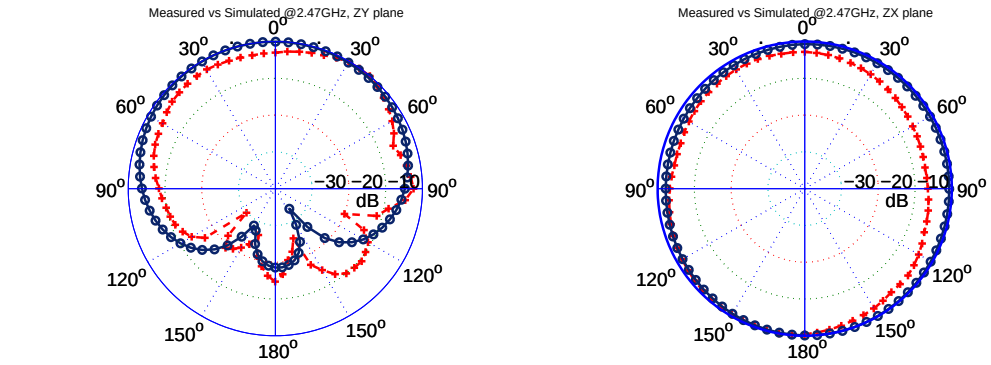

Figure 3.13: Measured(red) versus simulated directivity(black) at 2.74GHz for the dual band element. Polar plot on left is valid for the ZY plane, while the polar plot on right of figure is taken in the ZX plane. Both compare the ϕ component.

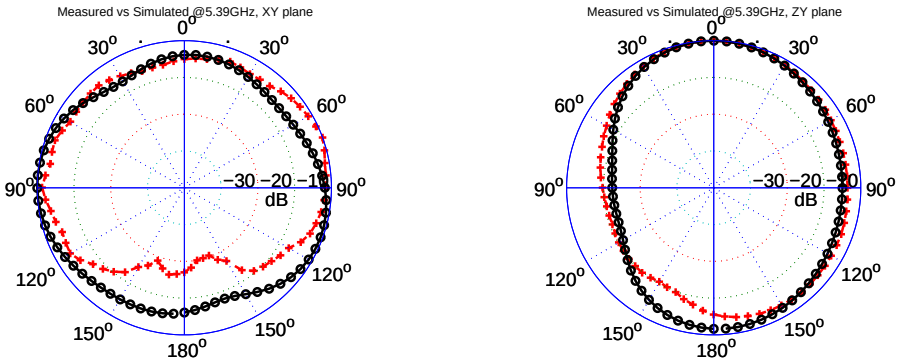

Figure 3.14: Measured(red) versus simulated(black) directivity at 5.39GHz. Polar plot on left is valid for the XY plane, while the polar plot on right of figure is taken in the ZY plane.

Measured radiation patterns shown in figures 3.13 3.14, are nearly omni-directional in one plane and have large half power beam widths in the other plane. There is a fair agreement of simulated and measured radiation patterns. The simulated data especially, compares favourably with cited literature, and most notably with [117]. The simulated directivity traces for the θ and ϕ components shown in figures 3.9–3.12 and consequently on all further similar plots are normalised with respect to the absolute directivity, this allows to observe the contribution of each component to the total directivity. For example considering figure 3.9 and the XY plane by normalising the traces in this fashion it is clear the directivity of the θ component is 20dB below the ϕ and in effect to the total directivity. If the traces were normalised with respect to their own maximum values then this insight on the contribution of each polarization would have not been possible. In contrast to this procedure, measured directivity data are normalised with respect to each polarization maximum and compared with equivalently normalised component directivities obtained from the simulations.

Figures 3.15 to 3.21 provide simulated and measured radiation characteristics of the wide band realisation. For the wide band element the maximum simulated directivity was 2.81dBi at 2.95GHz, while at 5GHz the simulated directivity was 3.97dBi. This was an exercise to get a brief view of how the radiation pattern might vary for other resonant frequencies obtained through various monopole lengths with coupled resonances. As is evident from the polar diagrams the angular behaviour towards the electric field components is of similar nature to the dual band realisation

discussed earlier.

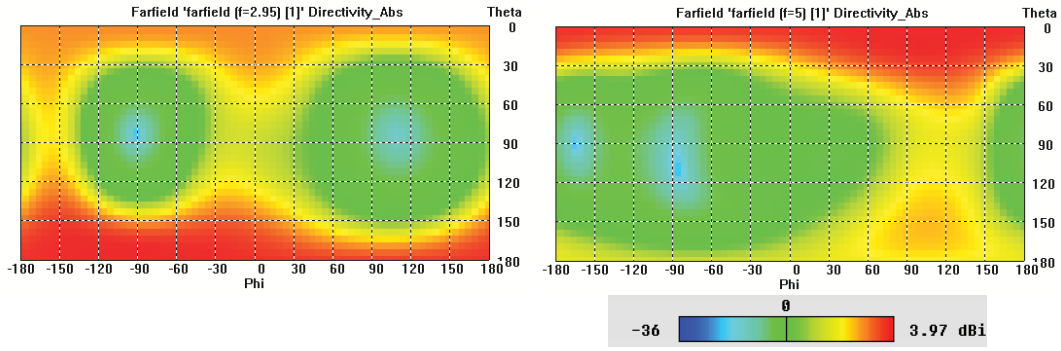

Figure 3.15: Simulated radiation pattern for wide band element in 2–dimensional plot, on left pattern at 2.95GHz and right at 5GHz

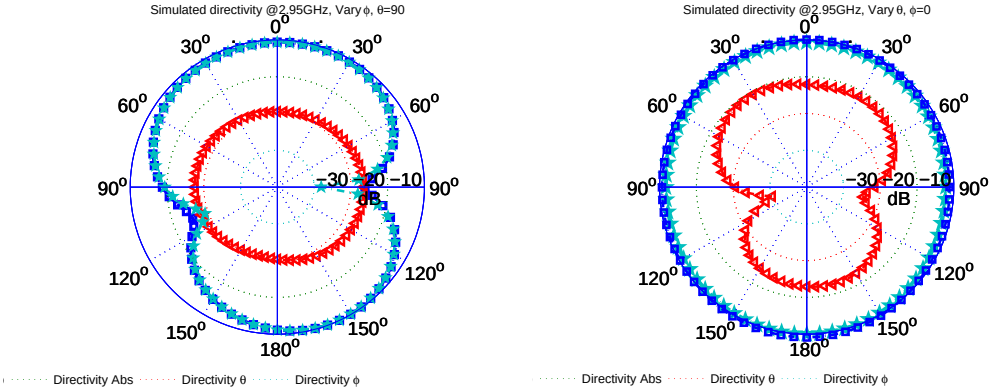

Figure 3.16: Simulated polar plot of wide band element, pattern is ploted at 2.96GHz. The absolute value directivity, the directivity in θ and ϕ components is shown in traces. In reference with figure 3.1, the principal axis cuts plotted are the XY plane (left figure) and the ZX plane (right figure).

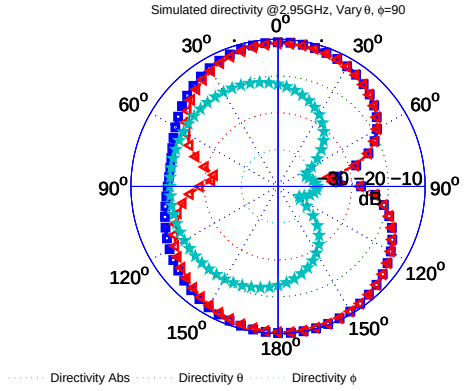

Figure 3.17: Simulated polar plot of wide band element, pattern is ploted at 2.96GHz. The absolute value directivity, the directivity in θ and ϕ components is shown in traces. In reference with figure 3.1, the principal axis cuts plotted is the ZY plane.

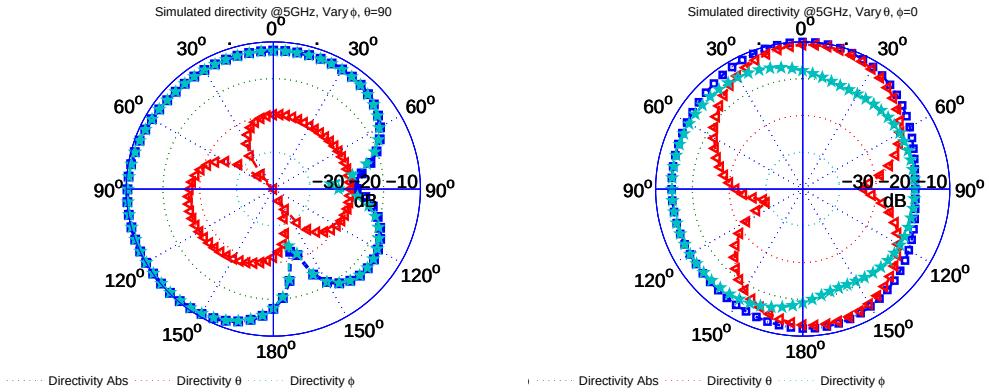

Figure 3.18: Simulated polar plot of wide band element, pattern is ploted at 5GHz. The absolute value directivity, the directivity in θ and ϕ components is shown in traces. In reference with figure 3.1, the principal axis cuts plotted are the XY plane (left figure) and the ZX plane (right figure).

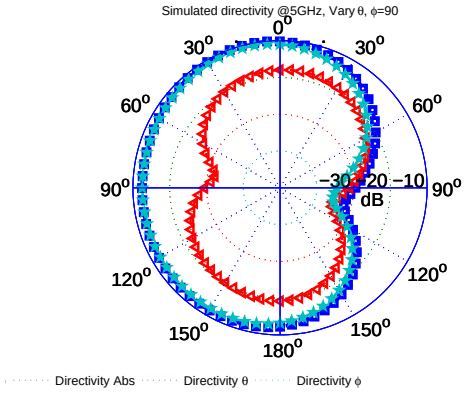

Figure 3.19: Simulated polar plot of wide band element, pattern is ploted at 5GHz. The absolute value directivity, the directivity in θ and ϕ components is shown in traces. In reference with figure 3.1, the principal axis cuts plotted is the ZY plane.

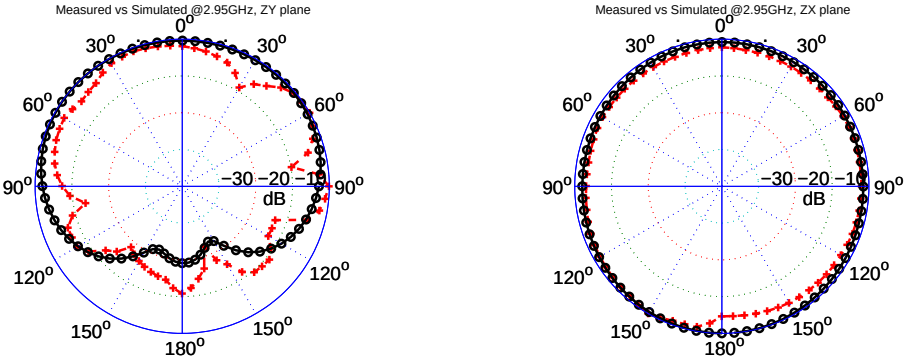

Figure 3.20: Measured(red) versus simulated(black) directivity at 2.95GHz for the wide band element. Polar plot on left is valid for the ZY plane, while the polar plot on right of figure is taken in the ZX plane. Both compare the ϕ component.

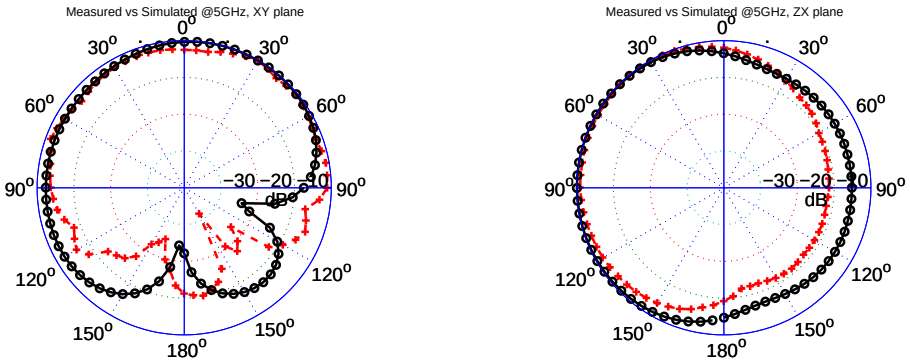

Figure 3.21: Measured(red) versus simulated(black) directivity at 5GHz for the wide band element. Polar plot on left is valid for the XY plane, while the polar plot on right of figure is taken in the ZX plane. Both compare the ϕ component.

3.3 Two element inverted F stacked monopole array

The following sections will be dedicated to the design and performance characteristics of a two element inverted F stacked monopole array, having a spacing of $0.13\lambda_0$. The goal here is to reduce the mutual coupling between the antennas and obtain reasonable radiation patterns over space. First mutual coupling will be observed for a structure built on a common shared ground plane. Next the same structure is simulated with separated ground planes each now supporting the individual elements, the coupling level is once more examined. Finally parasitically coupled printed lines are introduced in proximity of the antennas and the mutual coupling and radiation characteristics will be examined and illustrated.

3.3.1 Layout and design considerations

The dual band PIFA element described in the earlier sections is used as the antenna element to form the array. Due to the effects of the second antenna and the modified ground, small tuning of the monopoles and the side line was necessary, the dimensions are as specified in figure 3.1, in reference to them, the length of the upper monopole is 2.25mm shorter, the length of the lower monopole is 0.75mm shorter and the length of the side line is 1.77mm longer.

The substrate chosen is Taconic RF-30 and has similar performance to the one used for the single elements. The thickness of the substrate is 1.52mm, the dielectric

constant is $\epsilon_r = 3$ and the loss factor is 0.0014. For all subsequent models and simulations the spacing of the radiators is fixed at 16mm ($0.13\lambda_0$ at 2.45GHz).
Thirty lines per wavelength is set for global meshing over the computational domain, components of the structure were assigned local mesh edge refinement factor of seven, which increases the refinement around the edges of the object by the specified factor, in addition to assigning a local mesh volume refinement factor, which increases the mesh refinement within the boundary of the object. All metallic parts were modelled as copper and substrates were assigned as lossy, the data used are from the built in CST material library.

3.3.2 Array with mutual ground

To begin with and for having a frame of reference for the possible improvement, the PIFA elements were placed on a common ground of 80×20mm printed on a substrate of $80 \times 50 \times 1.52$mm. The simulated S–parameters indicate that there is shifting of the resonances towards the higher end of the spectrum by a small amount, input impedance of the antennas is also modified and tuning is necessary to improve and shift the resonances at a desired location.
The elements still appear to be well matched at two operating bands, for the lower band at the point of minimum S_{11} which is at 2.66GHz the coupling level is $S_{12} = -7dB$. This is not at all surprising given the close spacing and the common ground.

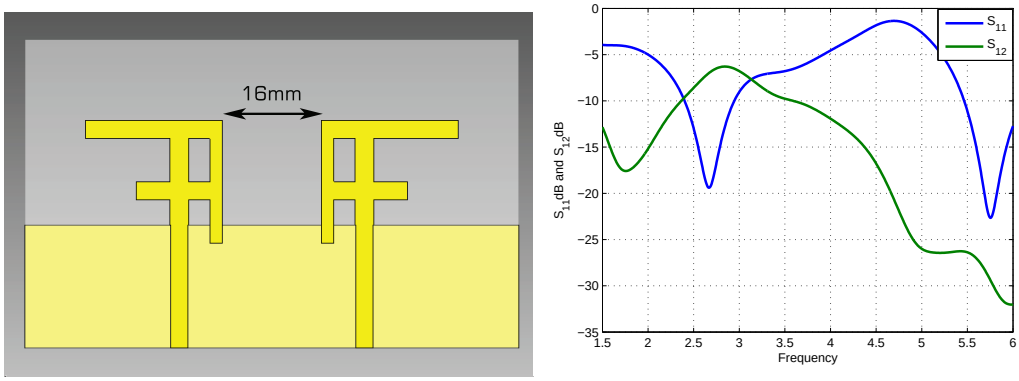

Figure 3.22: On the left of figure the topology of the array is shown, both elements share the shame ground plane and are separated by 16mm. On the right figure the simulated scattering parameters are provided.

3.3.3 Array with separate ground

It has been already shown [114] [117] that by introducing quarter wave resonant slits on the common ground a considerable reduction in coupling due to suppression of currents on the common ground can be achieved with no expense to the profile and dimension of the array. Instead of trying this approach, the common ground was separated by a gap of 4mm, thus making each ground plane equal to 38×20mm on a substrate of dimensions equal to $80 \times 50 \times 1.52$mm. This simple simulation was once more performed to get a frame of reference of the coupling between the antennas and thus allow for comparison latter.

Separating the ground had little effect on the matching of the two operating bands of the antennas, the level of S_{11} appears to be almost unaffected in terms of level and in terms of position in frequency. The level of coupling which can be estimated from S_{12}, in this case is reduced by $2dB$ from $-7dB$ that is was before to $-9dB$.

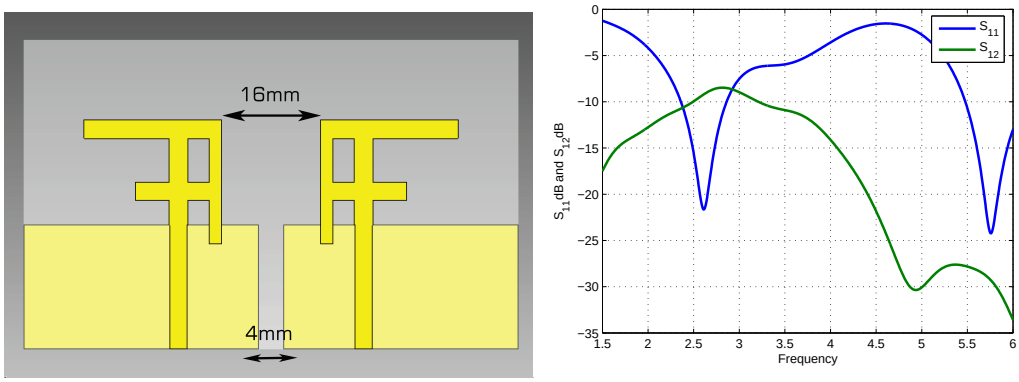

Figure 3.23: On the left of figure the topology of the array is shown, the ground plane is split and separated by 4mm gap, distance between the antennas is 16mm. On the right figure the simulated scattering parameters are provided.

3.3.4 Array with separate ground and coupling compensation

Having briefly examined the performance of the compact array in terms of simulated S–parameters, it is apparent that two well matched resonant bands can be defined of adequate bandwidth, however at best the transmission coefficient between the antennas at the lower band was $S_{12} = -9dB$, as was illustrated in the previous section.

To suppress the mutual coupling between the antennas a grid of printed parasitic lines was introduced. The parasitic elements were placed on a substrate block of equal size to the one hosting the PIFAs, all copper was removed from the new substrate block, leaving only the printed lines.

Figure 3.24 shows the topology of the array. Two substrate blocks of size $80 \times 50 \times 1.52$mm are aligned and joined, thus making the height profile 3.04mm, an increase by 1.52mm, compared to the previous cases, this was necessary to accommodate for the lines. At the top surface of substrate block one are the printed PIFA, at the back surface of substrate block one are the ground planes of each element. At the top surface of substrate block two all copper is removed and the parasitic lines are placed at the bottom surface.

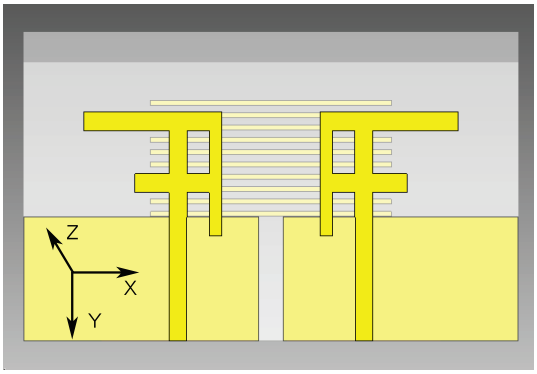

Figure 3.24: Layout and topology of the PIFA array with separated ground and a grid of parasitic lines, the lines are printed and placed at a new substrate block with the rest of the copper cladding totally removed, thus increasing the profile of the structure by 1.6mm

Figure 3.25 shows a photo of the fabricated array. The dimensions of the parasitic lines are as follows, length is 39mm, width is 0.8mm, and the spacing between them is 1.2mm from edge to edge. The number of lines used in the simulations and found on the fabricated element is nine in total.

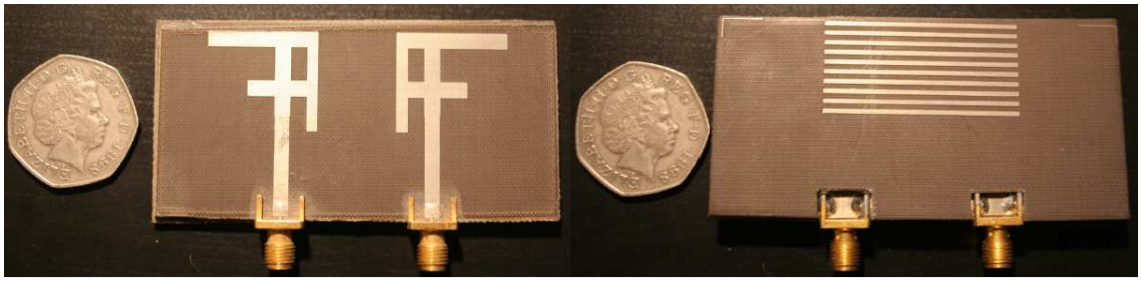

Figure 3.25: Photograph of the fabricated array, front and back view.

3.3.4.1 Parametric study

Considering the proposed topology of figure 3.24, there is a plethora of parameters that can be optimized and varied. There are many degrees of freedom to explore, however in this section only the effect of the length and width of the parasitic lines will be briefly covered, as this will mainly influence the resonant behaviour of the grid of lines and in a manner the level of coupling between the structures.

The length of the lines was incremented by steps of 1mm. The length shown at the legends of figure 3.26 and 3.27 is half of the actual physical length and this is true for the width values shown in the legend of figure 3.28. At the lower band multiple resonances appear, these are manifested as loops near the centre of the smith chart, changing the line length affects each of the resonances within the band width of the lower band individually and thus makes difficult to interpret the direct effect on the input impedance of the antenna at this band. At 5.5GHz, by increasing the length, at the point of resonance the real part of the input impedance reduces.

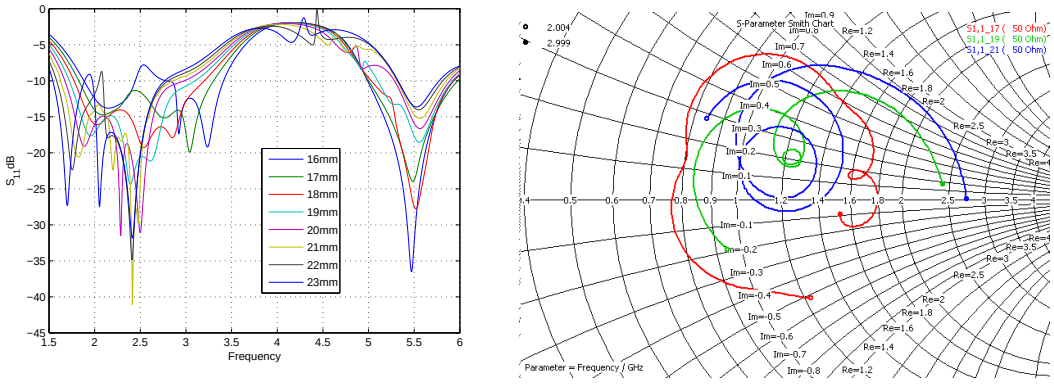

Figure 3.26: Effect of varying the length of the grid lines on S_{11}, on the right the locus of input impedance is shown between the frequency range 2–3GHz.

Inspecting the simulated parametric results for S_{12} provides useful information however it is not enlightening. It is clear that the stop band around 2.4GHz and 5GHz can be shifted and its bandwidth modified. For example considering the blue curve representing a length of 34mm, it produces a sharp deep fade in the transmission coefficient at 2.5GHz intuitively this is expected as all of the resonators have the same lengths, however when inspecting the red curve which stands for a line of 42mm the band width of the stop band has increased considerably and there appears to be coupling of two individual resonances, it is not clear how some of the resonances come to exist. Also it is worth noting that the fabricated array had a length of lines

equal to 39mm, from figure 3.27 we can see that a length of 42 potentially provide wider bandwidth, nevertheless the chosen length appealed due to the clear sharp and deep fade at transmission.

The width of the lines was stepped from 0.4mm to 1.4mm in four equal steps, this implies that the distance from edge to edge of the lines was stepped from 1.6mm to 0.6mm as the absolute position of the centres was kept fixed. The curves for S_{11} and S_{12} suggest that the simulated widths with the respective distances from edge to edge, do not affect either of the scattering parameters.

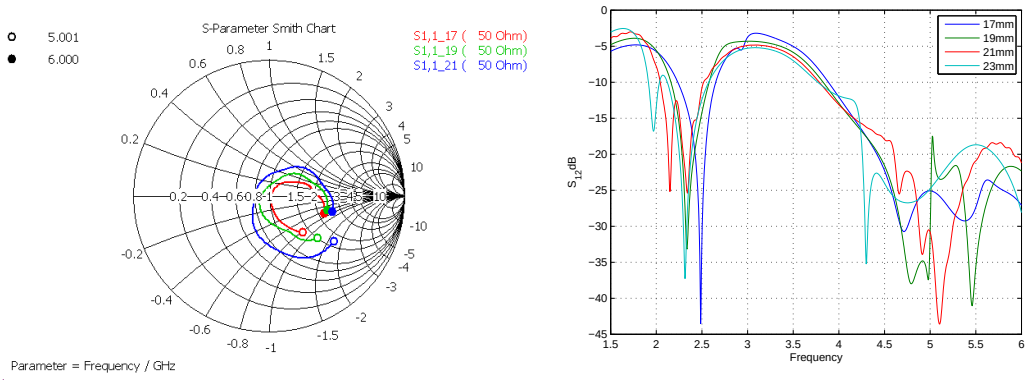

Figure 3.27: Left figure illustrates the input impedance of the first element of the array for the frequency range 5–6GHz. On the right effect of varying the length of the grid lines on S_{12}, four line lengths are shown

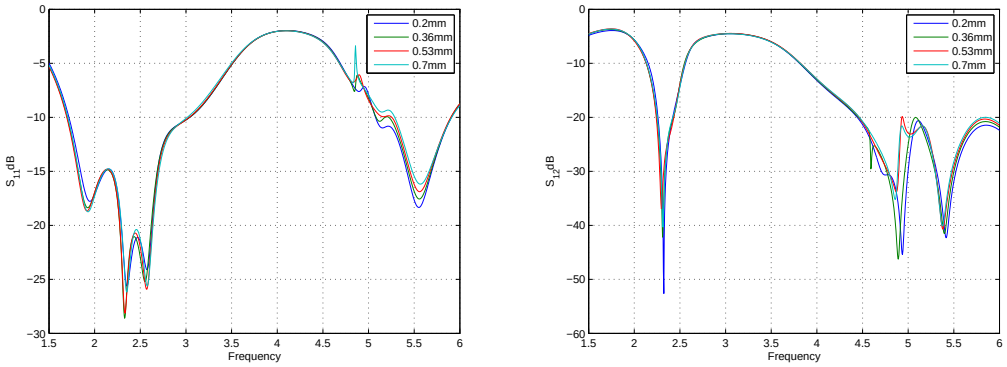

Figure 3.28: Effect of varying the width of the grid lines on S_{11} (left) and S_{12} (right)

3.3.5 Surface currents and E–field distributions

To acquire a fair understanding one must investigate the surface distribution of the RF currents, the resulting E–field distributions and the magnetic fields. Most modern software packages provide adequate and sometimes powerful visualizing aids,

which always reveal much more than typical S–parameter plots.

A grid of metal strip lines like the ones defined at the back side of the array can naturally resonate in two ways, depending on the polarization of the excitation field, which can be perpendicular or parallel to the strips, of course other incident angles are possible, however the two orthogonal states provide a simple insight. When the electric field is perpendicular the strips behave as the charged alternating plates of a capacitor, the little distance that is available for the electrons in the metal to oscillate require a small wavelength (i.e. high frequency) otherwise they stay inactive, not absorbing energy, until the incident field changes direction. When the electric field is parallel to the strip lines then the electrons in the metal have the possibility to move along the length for larger periods thus absorbing more efficiently longer wavelengths. It is worth pointing that an oscillating electron will radiate as an electric dipole, with the radiation being directed over the plane that is orthogonal to the oscillation axis. To overcome the polarization sensitivity if one desires can use meshing of strips. A comprehensive treatment on the transmission, reflection and impedance of a grid of wires can be found in [118]

By first inspection of the surface currents at 2.27GHz when one element is excited and the other terminated, it is clear that there is a strong current on the parasitic lines that actually flow in opposing directions. It is worth noting that as the authors of [119] point, when the current vectors in close coupled parallel lines are in–phase and flow opposing to each other, they tend to cancel, they also continue and explain that this may reduce the self inductance, thus the effective length too.

Due to the geometry the current on the two grounds flows in opposing directions and so do the currents on the parasitically coupled terminated antenna compared to the excited one, also due to the flow of currents the coupling of the side impedance line with the ground is cancelled. For the same case of excitation at 5.42GHz the currents on the lines seem to be distributed as in a open resonating line of length λ forming a standing wave on the lines.

Recalling that the length of the lines is 39mm, that in terms of guided wavelength is $0.51\lambda_g$ at 2.27GHz and $1.22\lambda_g$ at 5.42Ghz, interestingly enough, considering the upper frequencies, simulations show two stop bands, one centered at 5.42GHz and one centered at 4.85GHz, in the next section were measurement results are provided it becomes clear that the stop band at 5.42GHz corresponding to $1.22\lambda_g$ is not present

at the measured S_{21} and the stop band at 4.85GHz corresponding to $1.1\lambda_g$ is present and strong.

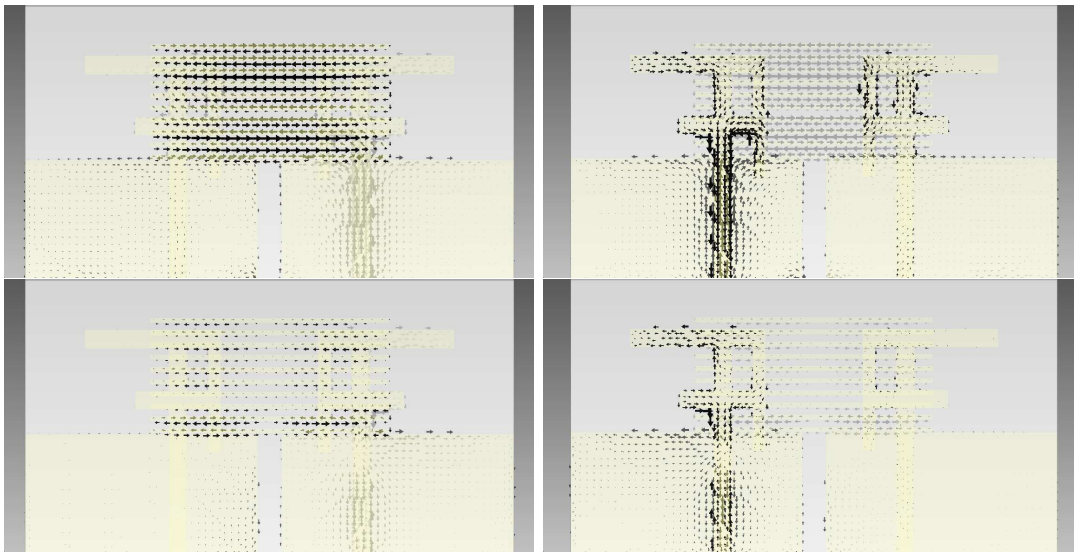

Figure 3.29: The top two firues present the surface current distribution at 2.27GHz in front and back view of the array structure. The figures just below them show the distribution at 5.42GHz. All are valid when antenna one is excited and antenna two is terminated in a matched load.

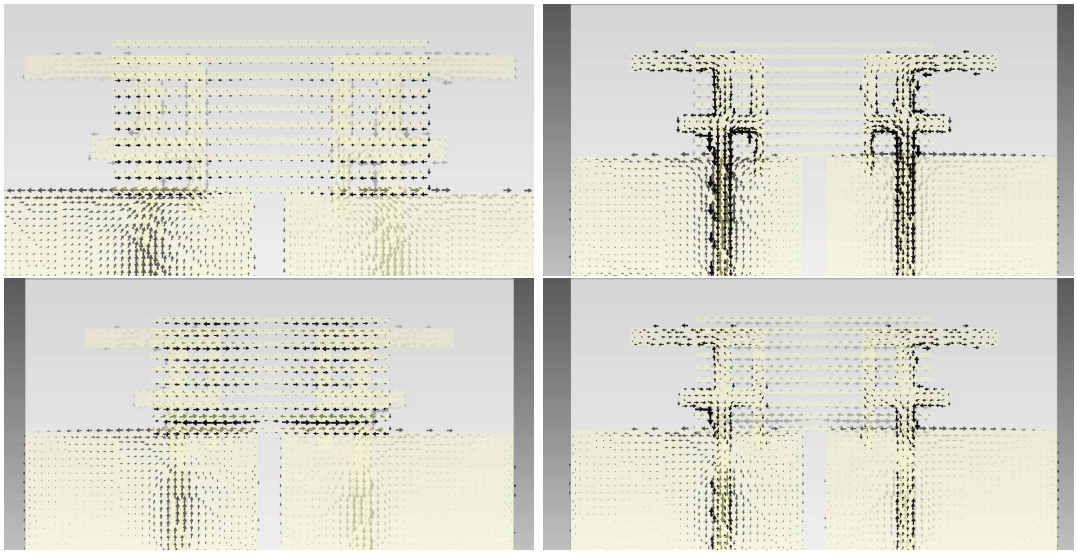

Figure 3.30: The top two firues present the surface current distribution at 2.27GHz in front and back view of the array structure. The figures just below them show the distribution at 5.42GHz. All are valid when both antennas are excited with equal amplitude and identical phase signals.

At the top left of figure 3.30, the surface current distribution for 2.27GHz is plotted for simultaneous excited PIFAs, comparing this to the plot shown earlier on figure 3.29 when one of the antennas was terminated, makes a clear difference, now at 2.27GHz the lines instead of having a distribution equal to a resonator of $0.5\lambda_g$ which represents their actual length, they appear to behave as a full one λ wave open resonator, having a standing wave pattern with two nodes and two antinodes for the electric voltage.

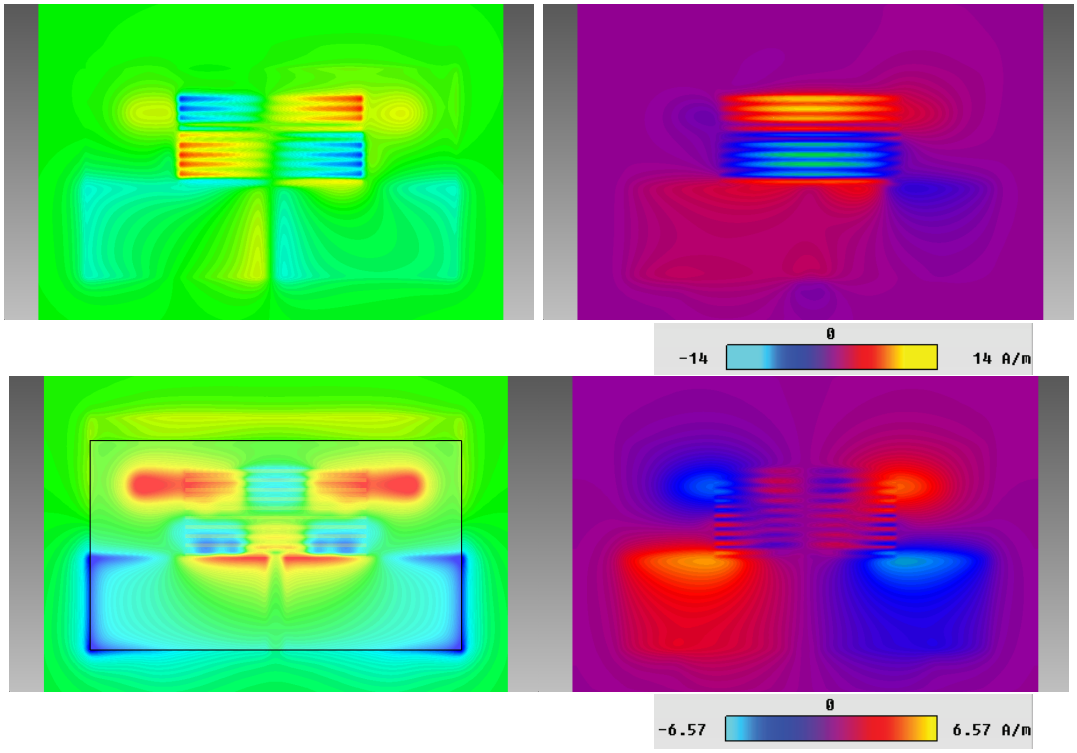

Figure 3.31: On the left of figure, the z component of the electric field is viewed in a z plane cut at 2.27GHz, the top plot is valid for one antenna fed while the other terminated, the bottom plot is valid for simultaneous excitation of both antennas with equal signals in phase and amplitude. On the right the above holds but for the magnetic field component y viewing in a z plane cut.

Perhaps the electric and magnetic field component distribution plots are clearer to interpret, the opposing colours indicate the polarity of the fields. For example considering figure 3.31, when both elements are simultaneously fed, the currents on the grounds flow naturally to opposing directions, also the currents on the arm of the top monopoles flow in opposing directions naturally, this is clearly indicated by the colour contrast in the magnetic field component having the left PIFA in blue colour while its ground is in red and the right PIFA in red colour while its ground is blue.

The direction and local minima and maxima of fields and current can be established from the figures. An interesting case to study would be to try a binomial distribution of resonator lengths and observed the bandwidth of the potential stopband then.

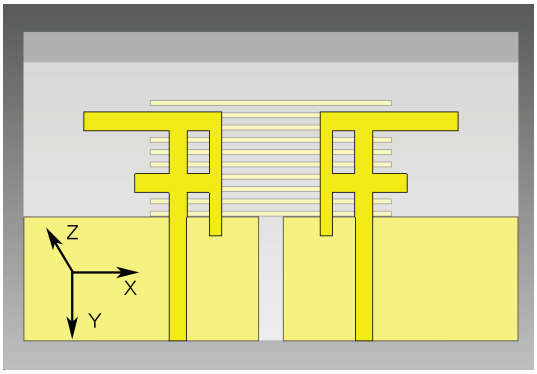

Figure 3.32: PIFA array with coordinate axis, the Z axis is perpendicular to the substrate surface, all the field cuts presented follow the coordinate axis shown in figure.

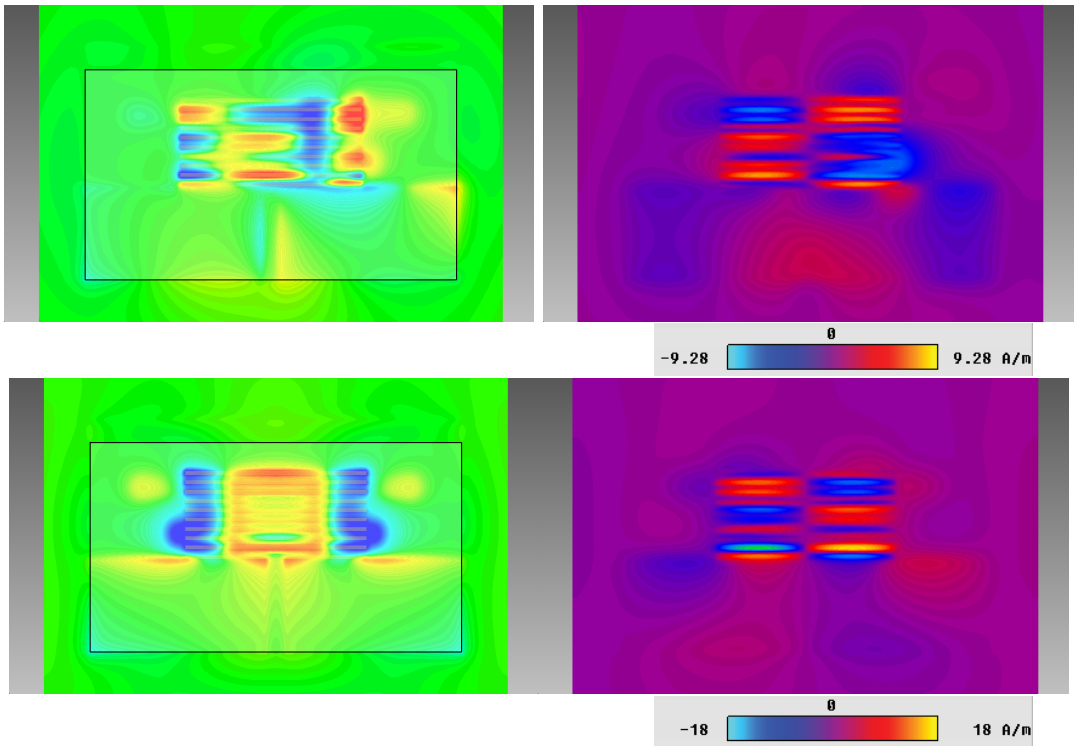

Figure 3.33: On the left of figure, the z component of the electric field is viewed in a z plane cut at 5.42GHz, the top plot is valid for one antenna fed while the other terminated, the bottom plot is valid for simultaneous excitation of both antennas with equal signals in phase and amplitude. On the right the above holds but for the magnetic field component y viewing in a z plane cut.

3.3.6 Array measured and simulated results

The design process and simulation results are verified by measurement of an experimental prototype. As the prototype required the alignment and joining of two substrate blocks, the possibility of reduced fabrication tolerances is present however the deviations can be kept and should be negligible.

Figures 3.34 and 3.35 compare simulated and measured S–parameters, measured data was obtained from an Agilent four port network analyser with the cables being calibrated. The impedance bandwidth is defined at point where S_{11} crosses the -10dB value. At the lower band it is more than 690MHz, while at the higher end of the operational spectrum a bandwidth of 600MHz is achieved.

Interestingly and as expected there exists an attenuation of the coupling between the elements at 2.4GHz, where $S_{12} = -18dB$, it is considerably less than the simulated value of -37dB nevertheless an improvement of 9dB compared to the case of no parasitic lines being present. Near 5GHz simulations predicted two close stopbands, measured data show a very strong attenuation at the exact position as the simulation suggested, however the second stop band is vaguely there, it becomes clear that the stop band at 5.42GHz corresponding to resonator line length of $1.22\lambda_g$ is not present at the measured S_{21} and the stop band at 4.85GHz corresponding to $1.1\lambda_g$ is present and strong.

The correlation of simulated and measured data is very satisfying, knowing that time domain solvers can be problematic when a multiple of high resonant structures are present in the computational space.

At the zoomed plot on the right of figure 3.35, the measured S–parameter S_{12} stays below $-16dB$ for a bandwidth of about 90MHz with an antenna spacing of $0.13\lambda_0$ at 2.45GHz.

Table 3.2 provides a summary of the properties of the array structures that were presented in this section. The data for the elements of section 3.3.2 and 3.3.3 are from simulations alone, while data of element 3.3.4 in the table are from measurement.

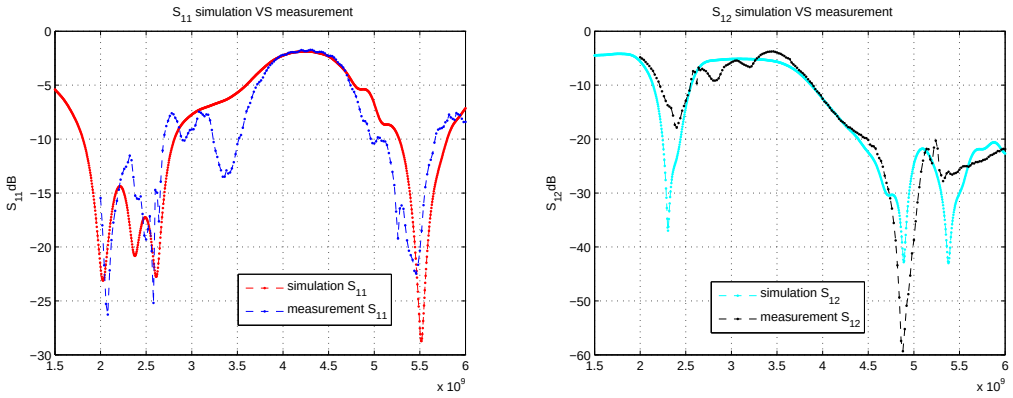

Figure 3.34: On the left of figure comparison of measured S_{11} with simulated is shown, on the right of figure a comparison of measured S_{12} data versus simulated values is provided.

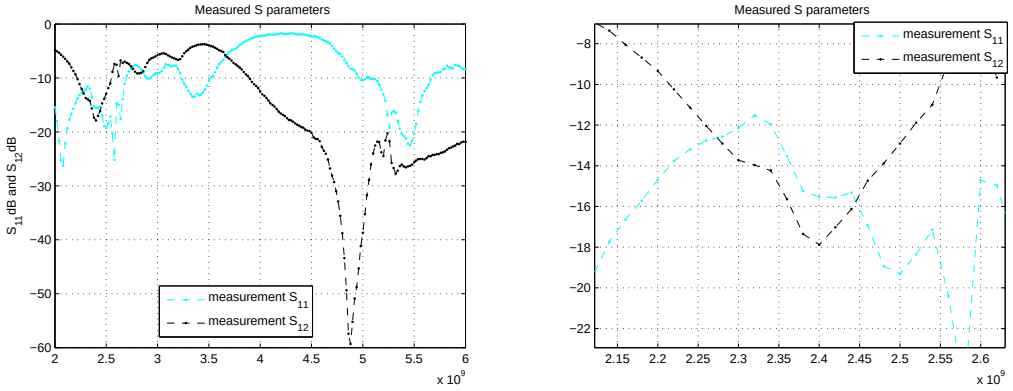

Figure 3.35: Measured S_{11} and S_{12} combined in one plot(left), and on the right a magnification of the region of the spectrum near 2.4GHz, showing that now the measured mutual coupling has reduced considerably.

Table 3.2: Simulated and measured resonant frequencies, isolation and bandwidth(defined at S_{11} -10dB)

Element	f_{lower}	f_{upper}	BW	$S_{12}@f_{center}$
of section 3.3.2	***(simulated)***			
IFA 1 (band 1)	$2.4GHz$	$2.94GHz$	$540MHz$	-7dB @ 2.66GHz
IFA 1 (band 2)	$5.5GHz$	$> 6GHz$	$> 500MHz$	-29dB @ 5.74GHz
of section 3.3.3	***(simulated)***			
IFA 1 (band 1)	$2.35GHz$	$2.85GHz$	$500MHz$	-9dB @ 2.6GHz
IFA 1 (band 2)	$5.5GHz$	$> 6GHz$	$> 500MHz$	-29dB @ 5.74GHz
of section 3.3.4	***(measured)***			
IFA 1 (band 1)	$< 2GHz$	$2.69GHz$	$> 690MHz$	-18dB @2.4GHz
IFA 1 (band 2)	$5GHz$	$5.6GHz$	$600MHz$	-21dB @5.25GHz, -26.4 @5.45GHz

Let us now examine the simulated and measured radiation characteristics of the array with the parasitically coupled lines. Figure 3.36 depicts the three dimensional pattern in two dimensional plot, on the left of figure the radiation properties of antenna one in the array are given while on the right the properties of antenna two in the array are given in order to visually asses any possible form of angular diversity. The maximum simulated directivity for the frequency 2.27GHz is 2.6dBi. In reference to figures 3.37-3.38 ,the XY plane cut at 2.27GHz is mainly sensitive to E_ϕ, in the ZX plane at the same frequency for a range of angles both E_ϕ and E_θ components can be received with almost similar efficiency, the same is true for the ZY plane.

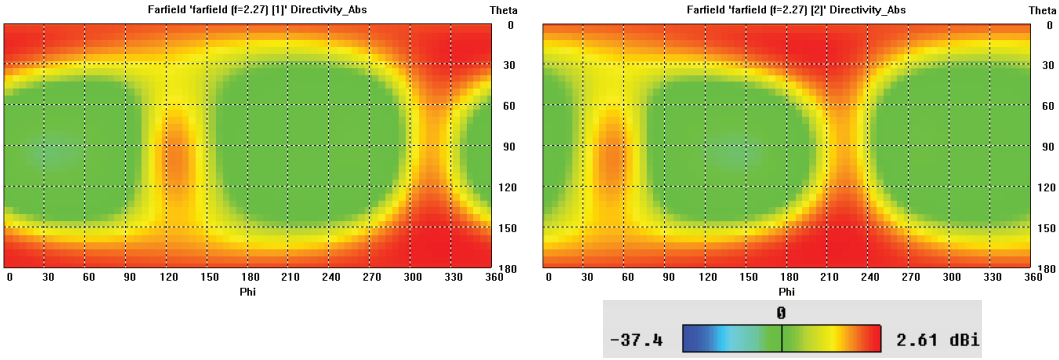

Figure 3.36: Simulated radiation pattern for both elements at 2.27GHz in 2dimensional plot, on left pattern element one, and on right pattern of element two.

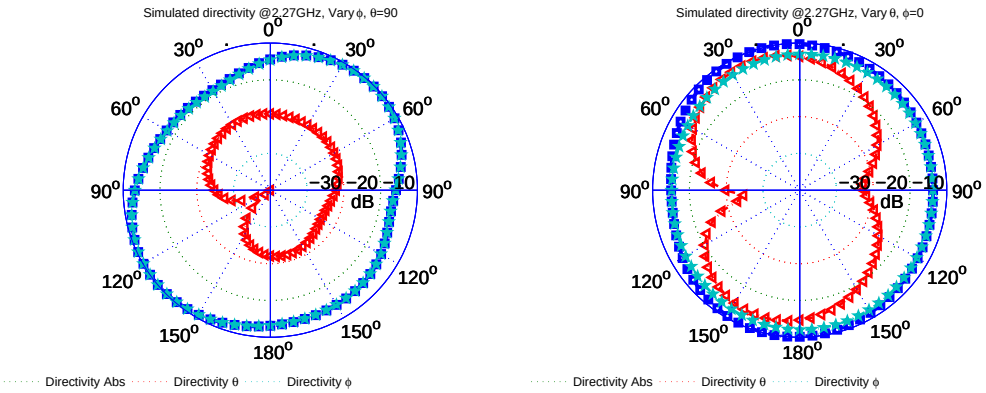

Figure 3.37: Simulated polar plot of element one in array with the other terminated in 50Ω load. Pattern is ploted at 2.27GHz, the absolute value directivity, the directivity in θ and ϕ components are shown in traces, in reference with figure 3.24, the principal axis cuts plotted are, the XY plane (left figure) and the ZX plane (right figure).

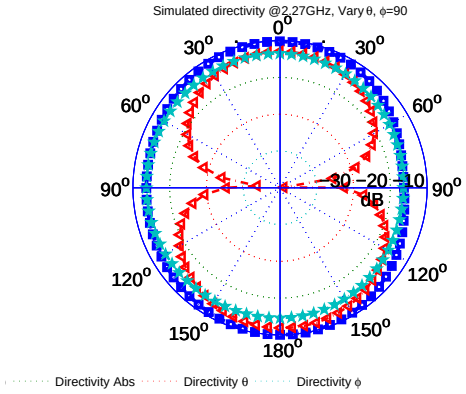

Figure 3.38: Simulated polar plot of element one in array with the other terminated in 50Ω load. Pattern is ploted at 2.27GHz, the absolute value directivity, the directivity in θ and ϕ components are shown in traces, in reference with figure 3.24, the principal axis cut plotted is the ZY plane.

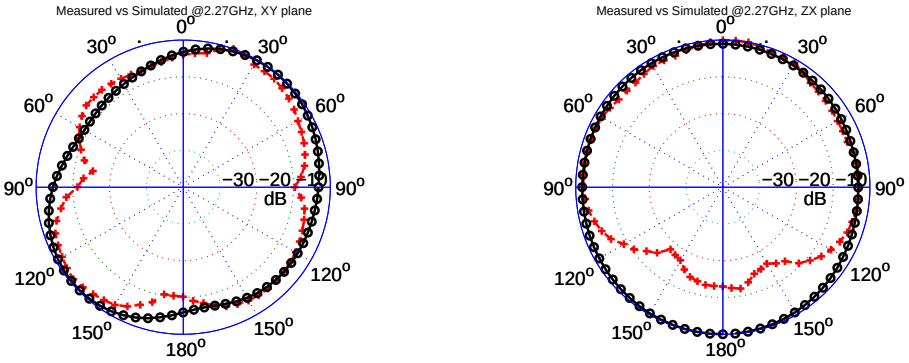

Figure 3.39: Measured(red) versus simulated(black) angular patterns at 2.27GHz for element one in array, the other was terminated in a 50Ω load. Polar plot on left is valid for the XY plane, while the polar plot on right of figure is taken in the ZX plane. Both compare the ϕ component .

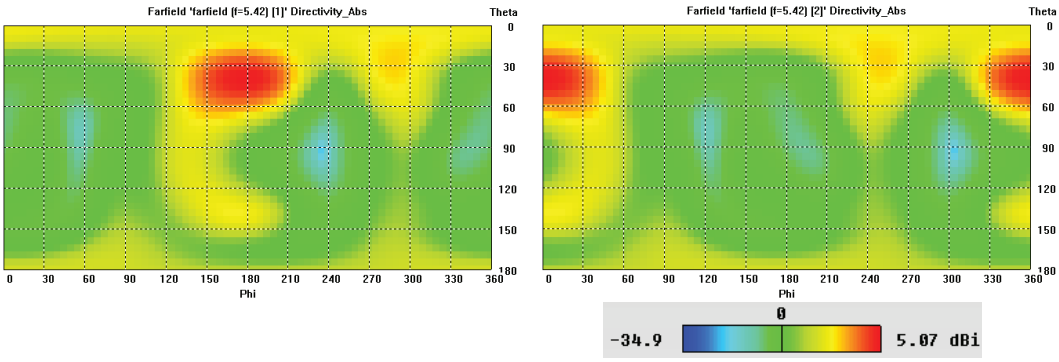

Figure 3.40: Simulated radiation pattern for both elements at 5.42GHz in 2dimensional plot, on left pattern element one, and on right pattern element two

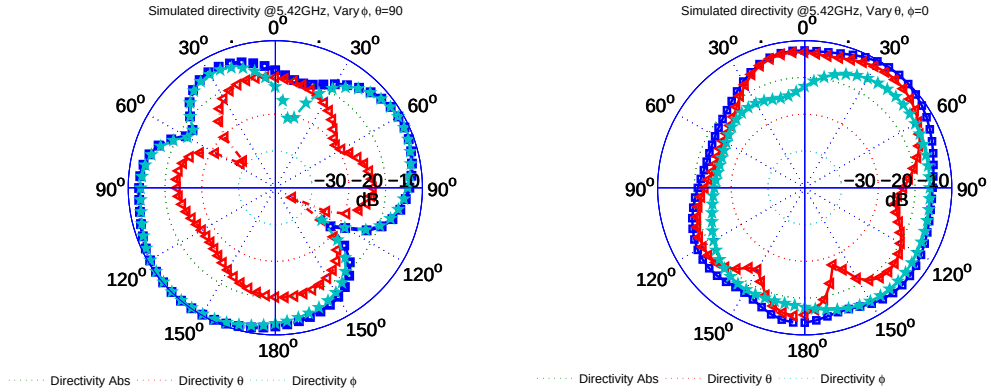

Figure 3.41: Simulated polar plot of element one in array with the other terminated in 50Ω load. Pattern is ploted at 5.42GHz, the absolute value directivity, the directivity in θ and ϕ components are shown in traces, in reference with figure 3.24, the principal axis cuts plotted are, the XY plane (left figure) and the ZX plane (right figure).

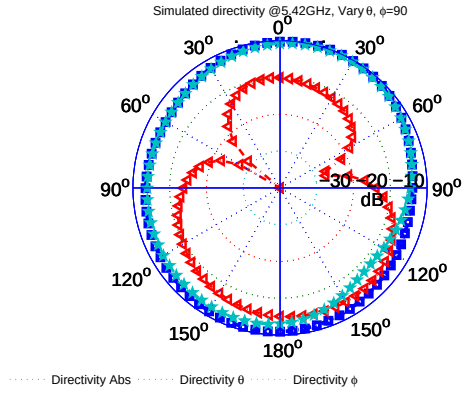

Figure 3.42: Simulated polar plot of element one in array with the other terminated in 50Ω load. Pattern is ploted at 2.27GHz, the absolute value directivity, the directivity in θ and ϕ components are shown in traces, in reference with figure 3.24, the principal axis cut plotted is the ZY plane.

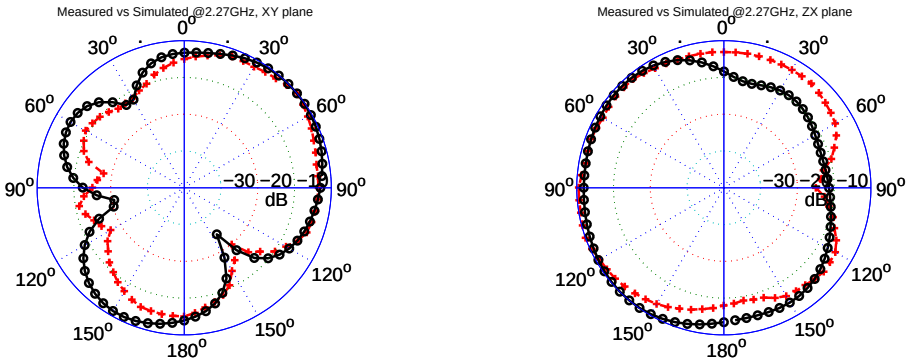

Figure 3.43: Measured(red) versus simulated(black) angular patterns at 5.42GHz for element one in array, the other was terminated in a 50Ω load. Polar plot on left is valid for the XY plane, while the polar plot on right of figure is taken in the ZX plane. Both compare the ϕ component

At the upper operating frequency the maximum simulated directivity is 5.07dBi. For all three principal plane cuts provided in figures 3.41-3.42 both electric field components can be recieved at various angle ranges, however the ϕ component of the incident electric field is for most angles the highest contributor to the total received power.

Table 3.3 provides the average gain of the PIFA element in the array for each of the three principal axis cuts, in addition the max gain values are stated next to the averages. Typically monopole designs of this scale, such as L shaped, F shaped, double L shaped, T shaped, double T shaped monopoles amongst other have peak gains in the region 1.5–3.5dB. Data for the average gain are not presented often, usually instead the mean effective gain is evaluated in this type of work. The mean effective gain for this array is given at the next section. While the peak and average gain lay inside the norms for a design of this type the average gains would be beneficial if they could improve. There are parameters that can be optimised and further developed to improve the average gain of the antennas.

The authors of [106] propose two dual band PIFA antennas, the mean gains they obtain are, at 2.45GHz, $y-z$ plane = -3dBi. At 5.25GHz they obtain, $y-z$ plane =-1.5dBi, $x-z$ plane =-5dBi. For the second antenna that they propose they get at 2.45GHz $y-z$ plane =-0.7dBi, and 1.16dBi at the same plane at 5.2GHz. The mean gain and directivity values presented in table 3.3 in general appear to compare with published literature of similar type of compact radiators.

Table 3.3: **Average** simulated Gain in dB for the three principal axis cuts and Max Gain

Frequency	**Average** ZY Gain db	**Average** ZX Gain db	**Average** XY Gain db	**Max** Gain dB
2.27GHz Abs Gain dB	-2.31	-2.13	-3.69	1.93
5.42GHz Abs Gain dB	-2.18	-5.92	-5.14	4.54

3.4 Diversity estimation

In chapter two the necessity and benefits of statistical independence and decorrelation of received signals was explained. In this section a brief diversity evaluation of the proposed array will be carried out. Three measures used in literature to quickly assess the diversity potential of an antenna system are applied to the array, of course these are approximate estimates nothing can replace actual field measuring campaigns. The correlation of the radiation patterns given two dimensional data from the principal planes is first measure of diversity examined, then the mean effective gain again based on two dimensional data from plane cuts is examined and finally correlation is evaluated from measured and simulated S–parameters and the impedance matrix.

The computation of antenna pattern correlation and MEG requires trhee dimensional radiation pattern measurements, it is not easy to obtain them and not many laboratories have the facilities to do so. Alternatively these parameters can be estimated in two dimensional models, for example assuming propagation and distribution of incoming waves in the horizontal plane only, then using the pattern data to asses the performance in the plane considered. Here we extracted from CST the complex E field radiation pattern vectors for both θ and ϕ components for the three principal plane cuts $(\pi/2, \phi), (\theta, \pi/2), (\theta, 0)$.

$$\rho_{c_{12}} = \frac{\int_0^{2\pi} A_{12}(\phi) d\phi}{\sqrt{\int_0^{2\pi} A_{11}(\phi) d\phi \int_0^{2\pi} A_{22}(\phi) d\phi}}. \tag{3.6}$$

Equation 3.6 gives the theoretical complex correlation of the received signals derived from the radiation pattern of the antennas in the horizontal plane only, where

$$A_{mn} = \Gamma E_{\theta m}\Big(\frac{\pi}{2}, \phi\Big) E^*_{\theta n}\Big(\frac{\pi}{2}, \phi\Big) + E_{\phi m}\Big(\frac{\pi}{2}, \phi\Big) E^*_{\phi n}\Big(\frac{\pi}{2}, \phi\Big). \tag{3.7}$$

The electric field radiation pattern vector is consisted of the θ and ϕ patterns, and is of the form

$$E_m(\theta,\phi) = E_{\theta m}(\theta,\phi)\hat{\theta} + E_{\phi m}(\theta,\phi)\hat{\phi}. \tag{3.8}$$

Equation 3.9-3.10 provide an exaple of the two dimensional data extracted from the results of the proposed array. The pattern for both θ and ϕ components for each plane are used to calculate the correlation.

$$E_m\Big(\frac{\pi}{2},\phi\Big) = E_{\theta m}\Big(\frac{\pi}{2},\phi\Big)\hat{\theta} + E_{\phi m}\Big(\frac{\pi}{2},\phi\Big)\hat{\phi} \qquad XY, \tag{3.9}$$

$$E_m\Big(\theta,\frac{\pi}{2}\Big) = E_{\theta m}\Big(\theta,\frac{\pi}{2}\Big)\hat{\theta} + E_{\phi m}\Big(\theta,\frac{\pi}{2}\Big)\hat{\phi} \qquad ZY. \tag{3.10}$$

Considering cross polar discimination $\Gamma = 1$, orthogonal polarizations uncorrelated, each polarization spatialy unorrelated and field arriving in one plane only, the envelop correlation for the PIFA array is given in table 3.4

Table 3.4: Envelop correlation, evaluated from radiation patterns

Frequency	**ZY**	**ZX**	**XY**
2.27GHz ρ_e	0.019	0.127	0.013
5.42GHz ρ_e	0.345	0.0346	0.046

For an efficient diversity system the mean received power from each branch should be similar. The mean power can be estimated from the radiation pattern and the characteristics of the propagation channel. In equation 3.11 G stands for the gain of the antenna, it was obtained from CST for each of the plane cuts for each component. XPR is the cross polar ratio and is assumed to be one, meaning that each polarization is equally probable [87]

$$MEG = \int_0^{2\pi} \frac{XPR}{1+XPR} G_\theta\Big(\frac{\pi}{2},\phi\Big) S_\theta\Big(\frac{\pi}{2},\phi\Big) + \frac{1}{1+XPR} G_\phi\Big(\frac{\pi}{2},\phi\Big) S_\phi\Big(\frac{\pi}{2},\phi\Big). \tag{3.11}$$

The angular density funtion of the incoming radiation is described by a θ and ϕ component and is of the form given in equation 3.12

$$S(\theta,\phi) = S_\theta(\theta,\phi)\hat{\theta} + S_\phi(\theta,\phi)\hat{\phi}. \tag{3.12}$$

In each of the plane cuts that were considered the angular density of the θ and ϕ component is assumed to be uniform, in essence the propagation environment is

uniform , having each field component equally probable and uniformly distributed in angle, equation 3.13 defines the angular density functions for both components in the aimuthal plane

$$S_\theta\left(\frac{\pi}{2},\phi\right) = S_\phi\left(\frac{\pi}{2},\phi\right) = \frac{1}{2\pi}. \tag{3.13}$$

Table 3.5 provides the mean effective gain of the proposed antenna in the array under the propagation conditions mentioned. It appears to compare with cited literature of the same type of antennas.

Table 3.5: Mean Effecive Gain, assuming propagation in principal planes only

Frequency	**ZY**	**ZX**	**XY**
2.27GHz MEG	-3.37dBi	-3.15dBi	-4.8dBi
5.42GHz MEG	-2.97dBi	-2.77dBi	-5.11dBi

Mutual coupling and the impedance matrix can also be used to establish the possible diversity behaviour of an antenna array system. Using a multiport network analyser the impedance matrix can be readily formed. From the measured S–parameters the Z matrix was constructed by using the transformation relations provided in the previous chapter. However in this study the network analyser was not located in an anechoic room so some error due to channel effects may be present.

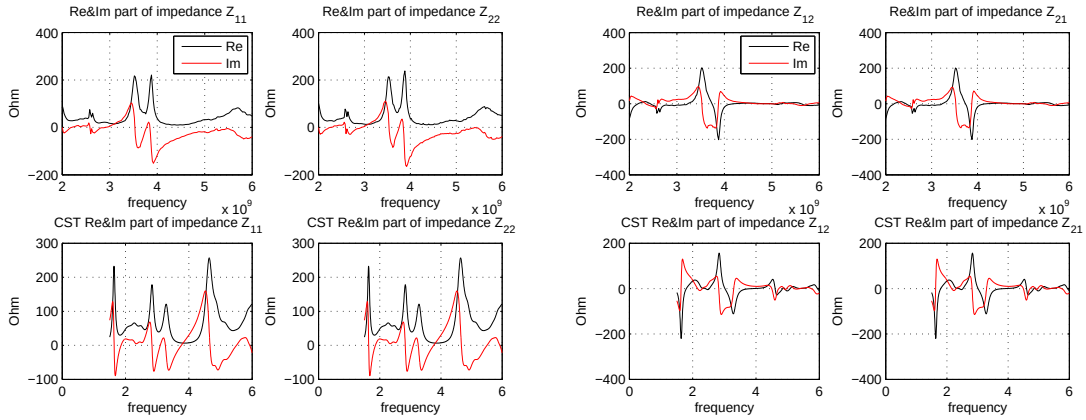

Figure 3.44: On the left group of figures the real and imaginary part of the self impedance from measurements and from CST are provided, on the right real and imaginary part of mutual impedance are given.

Figure 3.44 compares the real and imaginary parts of the impedance matrix from measured and simulated results.There is good agreement for most of the frequency range between the simulated and measured self impedance data, however there is a small deviation at few points. The mutual impedance is predicted more accurately

and the plots are fairly identical. The correlation coefficient can be evaluated from the normalised mutual impedance [46] [120] using the equation

$$\rho_{mn} \approx r_{mn}, \qquad r_{mn} = \frac{R_{mn}}{\sqrt{|R_{mm}|R_{nn}|}}. \tag{3.14}$$

Alternatively the envelop correlation coefficient can be estimated from the measured S–parameters of the antenna under test. The authors of [121] provide a step by step proof of the validity of this approach, starting from the correlation derived from the radiation patterns and equating it to the correlation derived from the S–parameters. For loss free networks the expression for correlation from the measured or simulated S–parameters is

$$\rho_e = \frac{|S_{11}^* S_{12} + S_{21}^* S_{22}|^2}{(1 - |S_{11}|^2 - |S_{21}|^2)(1 - |S_{22}|^2 - |S_{12}|^2)}. \tag{3.15}$$

There is a considerable difference in the value of the normalised mutual resistance when comparing results from simulation and measurement in the frequency range around 2.4GHz, that is due to the self impedance of the antennas as the imaginary part is not considered in this approximation. The envelop correlation established from the simulated and measured S–parameters versus frequency shows very low values of correlation for both operating bands as was also shown by the correlation evaluated from the radiation patterns of the antennas. In general the different values obtained for the correlation coefficient are expected as all of the approaches are approximations that hold under certain criteria, for example the authors of [117] [48] among others publish correlation values obtained from mutual coupling and ones obtained from radiation pattern and find them to be non matching.

The following matrices are populated with the normalised resistances and thus give an approximation of the correlation coefficient, values are at the subscripted frequencies

$$r_{mn,2.4GHz} = \begin{bmatrix} 1 & 0.147 \\ 0.1474 & 1 \end{bmatrix}, \quad r_{mn,2.4GHz-CST} = \begin{bmatrix} 1 & 0.039 \\ 0.039 & 1 \end{bmatrix}, \tag{3.16}$$

$$r_{mn,5.45GHz} = \begin{bmatrix} 1 & 0.097 \\ 0.097 & 1 \end{bmatrix}, \quad r_{mn,5.45GHz-CST} = \begin{bmatrix} 1 & 0.025 \\ 0.025 & 1 \end{bmatrix}. \tag{3.17}$$

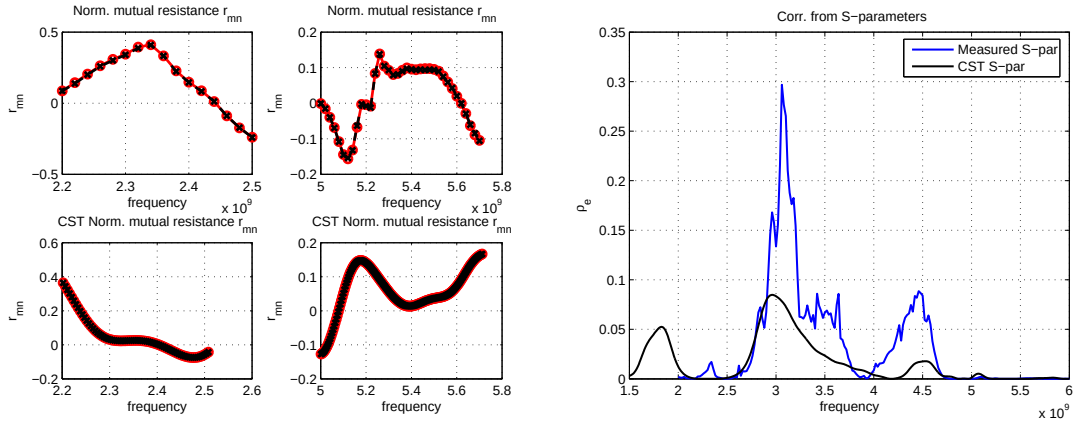

Figure 3.45: Left group of figures shows the normalised real part of the mutual impedance from measurements and from CST. On the right the envelop correltation is plotted agianst frequency computed from measured and simulated S–parameters.

3.5 Conclusion

A dual band printed inverted F stacked monopole antenna has been developed and parametrically studied. The element differs as there is no via shorting the impedance matching line to the ground, impedance matching is achieved by an open stub. It is shown that the resonances and thus the operating bands can be easily controlled and shifted to a desired location.

Having experimentally verified the design and performance of the single element, it was then used to form a compact array. As one of the main objectives was to produce an array of closely spaced and isolated elements the spacing was set at $0.13\lambda_0$. A novel approach to reduce the mutual coupling in such a compact system was presented and verified. The method proposed is to introduce a grid of parasitically coupled printed lines on a substrate tangent to the one hosting the PIFA array. By doing so the coupling was reduced by 9dB compared to the case of the array stand alone.

A theoretical approach to assess the diversity performance of the fabricated array was presented dictating that the structure can indeed exhibit the required criteria that are necessary for a MIMO candidate antenna array.

There are many degrees of freedom regarding the proposed array and there is confidence that it can be further improved.

Chapter 4

Printed Dipole Antenna

"Look and you will find it what is unsought,
will go undetected"
Sophocles

4.1 Introduction

The dipole antenna is perhaps the first radiator ever created, nevertheless it certainly is to this day one of the most popular antennas used, the majority of cellular base stations use them for the inherent bandwidth of fifteen percent and the omni–directional radiation pattern in the H–plane which with the use of reflectors can be made to form sectors allowing for diversity and increase of cell capacity. Compared to microstrip patch the cross polar discrimination is superior as the transverse currents are minimised as the width to length ratio is minimised. Dipole occupy less space than patch antennas and can achieve wide bandwidths when the shape changes from rectangular to triangular, a bow–tie printed dipole for example [122]. The printed dipole appeared after the printed patch antenna and can be categorised in two main types, microstrip dipole where there is no gap between the arms and the element is fed in a desired location along its length, and the printed dipole where a gap exists between the arms and represents the planar realisation of the wire dipole [123].

Microcellular and picocellular station are becoming more and more common and necessary in a manner of speaking as the user population and the number of wireless services increase continuously, there is a trend to provide service in hotels, airports, shopping centres and other public spaces, in such environment a traditional base

station can not be the optimum solution, thus relaying access points are placed, the dipole can be efficiently used in such systems given that it is optimised for the application and location of operation.

If MIMO can be thought as the renaissance in mobile communications, then Frequency selective surfaces can be thought as a renaissance in antenna and microwave engineering. These surfaces passively can control and manipulate EM waves. Some of their properties include the modification of the surface impedance in respect to one or both polarizations, alter the reflection phase, and control the propagation of surface waves. In essence they consist of new boundary conditions that small or large antennas and arrays can be deigned [124]

This chapter is organized as follows. First a dual band printed dipole will be presented, its performance and the effects of design parameters are to be studied. A dual band FSS will then be applied in proximity of the dipole so to improve its efficiency and gain, most importantly achieve a good radiation characteristics at both bands of operation, as the dipole although omni–directional at the lower band, the higher operating band suffers and its radiation performance was not adequate for efficient operation, this is mended with the application of the FSS.

Subsequently a two element array is designed, the elements exhibit low coupling and are spaced virtually at zero separation from arm to arm, with them being mirror images of each other. The dipoles are served by individual ground planes supporting the feed microstrip lines which incorporate a printed balun.

4.2 Single printed dipole antenna

Advantages of the proposed stand alone dipole design are low cost, ease of fabrication and high impedance bandwidth. The balun used provides a wide band input impedance match which is symmetrically disposed around a centre frequency. CST design studio was used to simulate and iterate the design cycle. The dipole performance is considerably different when stand alone as compared to when combined with a dual band frequency selective surface. Both configurations have unique attributes as will be demonstrated.

4.2.1 Antenna layout and design considerations

The dipole is printed on a Rogers Duroid 5870 substrate with dielectric constant of 2.33. Overall dimensions are $80 \times 45 \times 1.52$mm. The element and balun dimensions are shown in figure 4.1

The electric field of microstrip lines is mainly normal to the substrate, however the electric field across the gap between the arms of the dipole is along its length, thus, the dipole can not be fed directly from a microstrip line. This requires alternative feeding mechanisms, for example co planar strips or microstrip to slot line cross junction [123]. We chose to excite the dipole with a printed balun. A balun is a device used to balance an unbalanced transmission line. McLaughlin analysed the coaxial balun [125] and found that improvement in bandwidth can be made compared to the Roberts coaxial balun proposal [126]. Robert's approach assigns in both sections of the balun equal impedance and imposes the impedance of the balanced lines to be equal to the load impedance (dipole). As the balun provides no

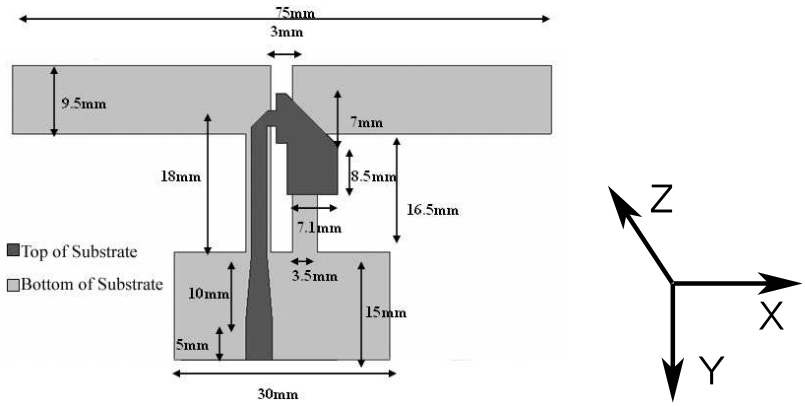

Figure 4.1: Topology and dimensions of printed dipole, the Z axis is normal to the substrate surface.

impedance transformation at the centre frequency and since impedance matching at two resonant frequencies is desired an impedance transformer is required. Tapering of the input transmission line can be applied.

A balanced line is defined as one in which the voltage to ground of the two conductors are equal and opposite. In an unbalanced line one of the conductors is at ground potential. Here two types of lines are involved, the first is the unbalanced lines Z_A and Z_B and the second is the balanced Z_{AB} line. Referring to Fig. 4.2, Z_A and Z_B represent the impedance of transmission lines A and B relating to the two sections of the balun. Z_{AB} is the characteristic impedance of the balanced transmission line

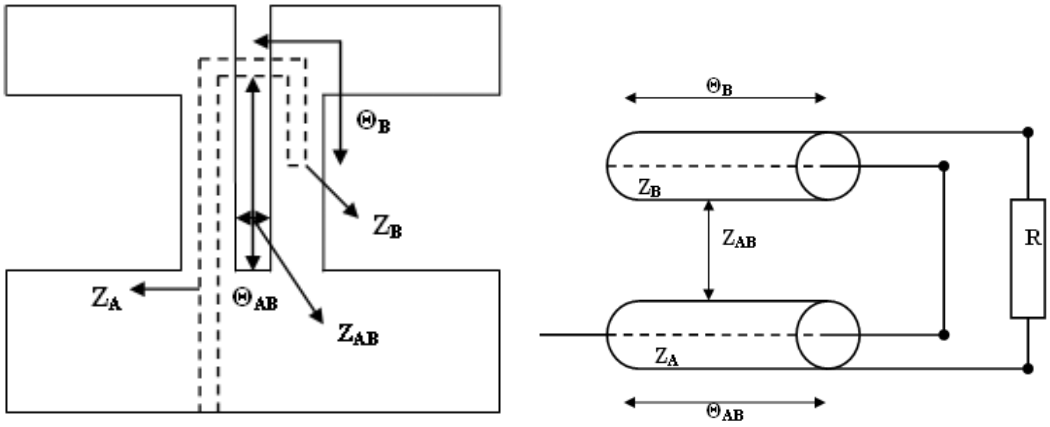

Figure 4.2: Printed Balun details

composed of the two stubs that connect the dipole to the ground plane. θ represents the electrical length of the lines.

We used McLaughlin's [125] approach that requires the impedance Z_{AB} of the balanced lines to be as large as possible, then Z_B is assigned according to $Z_B = R_B^2/Z_{AB}$. The input impedance is given as,

$$Z = -jZ_B cot\theta_B + \frac{jRZ_A tan\theta_{AB}}{R + jZ_{AB} tan\theta_{AB}} \tag{4.1}$$

The radiation resistance of a half wavelength dipole is in the region of 75Ω. The imaginary part associated with the input impedance of a dipole is a function of its length, for a half wave dipole it is $j42.5$. To reduce the imaginary part of the input impedance to zero the antenna is matched or changed in length until reactance vanishes, the width also affects the imaginary part.

The unbalanced lines transform a short circuit to open and maximize voltage at the gap, the open stub when 90 degrees is appearing as a short at the microstrip input line making current maximum, when the length of the open changes its impedance changes and tunes the dipole.

The microstrip line characteristic impedance matches that of the dipole feed point resistance, this is the reason that the tapering is required. The impedance of the balanced lines for this design was chosen to be approximately 140Ω. To prove the balun operation we examined the currents flowing on the two balanced lines. These were found to accommodate currents of equal magnitude with a phase difference of 180 degrees.

For the unbalanced strip transmission lines A and B of the balun structure it is well accepted that most of the field is contained in a region of three conductor widths, thus the ground plane (for A and B) should be at least three times the strip conductor widths. However, in this experimental configuration we did not follow this approach at the possible expense of radiation from the lines and in order to investigate the performance when an unbalanced line tends to look as balanced.

4.2.2 Surface current and E–Field distributions

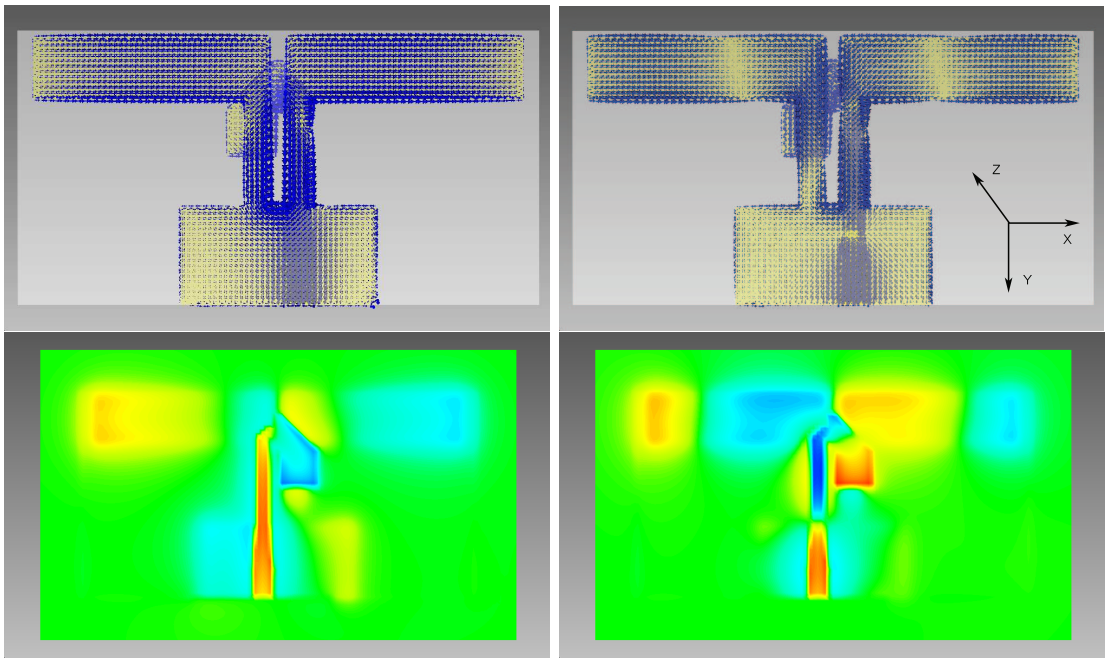

Figure 4.3: Surface current distribution for the dipole with the truncated ground, the plot shows the currents at 2.4GHz and at 5.2GHz. The figures below the current distribution portray the electric field along the structure at both frequencies of interest.

The surface current distribution was investigated in CST for the dipole under consideration. By inspecting the curves of S_{11} the plots were generated at the point of best impedance match and maximum resonance. Additionally the respective eclectic fields are presented as well. Figure 4.3 shows the distributions. It should be pointed that there is considerable radiation from the wide open stub at the upper band. Initially it was expected that this will introduce pattern diversity as it will distort the radiation pattern. Balanis [32] explains that the current standing wave pattern for dipoles longer than a wavelength exhibit 180° phase reversal between cycles due to the physical spatial length, thus the currents along the arms are not in phase at

all points, resulting in distortion and cancellation of radiation.

4.2.3 Single element measured and simualted results

Parametric simulations in CST indicated that the length of the section used as ground plane has minor influence on the resonances occurring in the antenna, however it can provide some control over the radiation pattern. For instance, if the length of the ground plane is equal to that of the dipole then radiation to the back is cancelled and towards the front reinforced, in [127] they show that by bending the arm of the dipole to an inclination the radiation pattern can also be modified to an extent.

It became evident that the electrical length (θ_B) of the open unbalanced line can shift the upper resonant frequency while there are small impedance matching condition variations at the lower band. The higher band can be shifted from 4.15 to 5.8 GHz. Upward shifting is achieved by reducing the electrical length (θ_B) and shifting downwards by increasing it, figure 4.4 illustrates the effect.

The width of the dipole arms has an important effect on the impedance matching conditions as well. For small widths ($0.025\lambda_0$) the antenna is well matched at the upper resonant frequency, for larger widths ($0.09\lambda_0$) the antenna is well matched at the lower resonant frequency, as this parameter affects inversely the real and imaginary parts of the input impedance at the two operating bands. Usually the width of a printed dipole is chosen to be about $0.05\lambda_0$, we found that for this particular element a width of $0.075\lambda_0$ produces good impedance matching for both frequency bands.

TThe dipole was fabricated and measured with a four port network analyser. Figure 4.5 compares the measured S_{11} with the simulated. The blue dash line represents the measured trace for the dipole with the short ground and should be compared with the red trace which is the simulated S_{11} for the same dipole structure. The figure contains a green trace which is the simulated response of the dipole with the long ground for completeness. Comparing the simulated and measured traces, it becomes apparent that the correlation of the shape and width of the resonances is good; however there is a shift on the position of the resonances of approximately 150MHz. There are a number of possible sources of error and inaccuracies. Con-

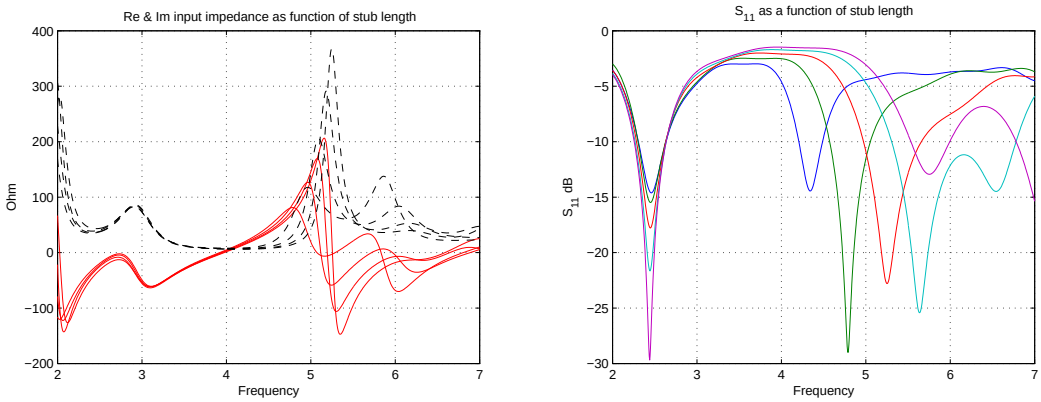

Figure 4.4: Effect of length of open stub on the input impedance of the antenna, real and imaginary parts shown, on the right S–parameters for various lengths, evidently the upper resonance can be shifted and controlled readily

sidering the software used, sources of error can be, the allocation and fine detail of the mesh grid relative to the simulated structure, inaccurate material model with not representative dispersion and dielectric constant, the boundary conditions of the computational space may affect the results, and the choice of port size in CST is fairly important. Nevertheless a shift in frequency can originate from fabrication issues, the application of the photo resist, mask and the etching processes can reduce tolerances, and finally the distance of the dipole conductors to the end of the substrate may influence the fields and the electrical length of the dipole (not the physical), which can also introduce differences in the prototype and the simulated model.

Table 4.1 summarises the location and width of the operating bands, where the impedance bandwidth is defined at $-10dB$ as is common practice. At the lower band an impedance bandwidth of 17.1 per cent is obtained and at the higher band the dipole achieves 27.6 per cent relative to the center frequencies.

Table 4.1: Measured resonant frequencies and bandwidth (defined at S_{11} -10dB)

Element	f_{lower}	f_{upper}	$BW_{measured}$
Dipole band (band 1)	$2.35GHz$	$2.79GHz$	$440MHz$
Dipole band (band 2)	$5.3GHz$	$7GHz$	$1.7GHz$

The bandwidth and easy tunability of the bands is very atractive and can comfortably cover services that fall in the ISM allocated spectrum. While it is reasonably easy to obtain dual, multiple or wide impedance bandwidths, the real challenge comes when the radiation characteristics are examined, usually such wide or multi-

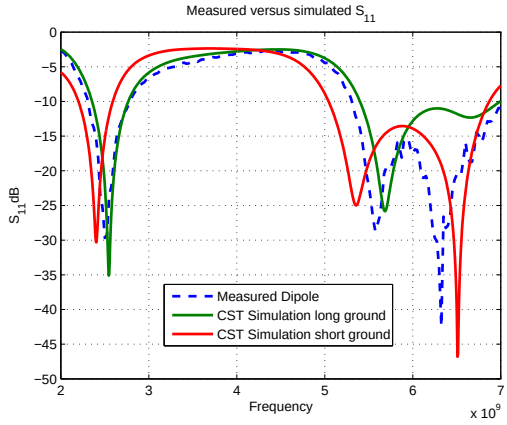

Figure 4.5: Measured versus simulated S–parameters of the single printed dipole antenna

band antennas may hide compromises as it is difficult to design efficient radiators over wide or multi band operation, that statement mainly applies to planar, compact, resonant antennas and not the likes of horn antennas, travelling wave antennas etc. Resonant or standing wave antennas are ones that exhibit current and voltage standing wave patterns created by reflections at open ends, popular examples are the dipole and microstrip patch antenna. Travelling wave or non–resonant antennas are designed to have a uniform pattern in current and voltage represented by one or more travelling waves. Aperture antennas can be treated as ravelling wave antennas. A horn antenna is an aperture antenna that has been tapered gradually to math the impedance of the feed waveguide to the one of free space. The orientation and magnitude of the taper has a strong influence on performance [32].

The radiation pattern of the dipole with the long ground at the region of 2.4GHz radiates mainly towards the endfire with maximum directivity of 5.91dBi and gain of 5.76dB, this is higher than the theoretical values of a free space dipole as the microstrip ground plane acts as a reflector enhances the directivity, however the distance of the reflector affects the possible directivity increase, in theory if the ground was placed at $\lambda/4$ and was infinite a higher value could be obtained, tables with achievable directivity as a function of the distance from a perfect electric conductor can be found in [3], but in this case the reflective ground was distanced at $\lambda/4$ at the centre frequency between the two operating bands, thus less than the possible maximum is observed due to the finite size of the ground and the distance set, which both influence the directivity.

For dipole configuration with long ground at 5.5GHz the maximum directivity was 3.7dBi and the gain 3.41dB, the total pattern though is modified from the theoretical expected due to the reflector and the radiation from the stub and feed.
The dipole with the truncated shorter ground has a directivity of 3.46dBi and a gain 3.32dB at 2.4GHz being omnidirectional in one plane. At 5.5GHz the reduction of the ground created on one side of the dipole a pattern similar to a 2*lambda* while on the opposite side part of the pattern is missing due to cancellation from radiation from the feed and stub. The maximum directivity is 4.21dBi and the gain is 4.13dB. To verify the results pattern measurements were performed in an anechoic chamber. The E and H plane of the dipole with the long ground are provided in figure 4.7, the plots compare measured versus simulated angular patterns.

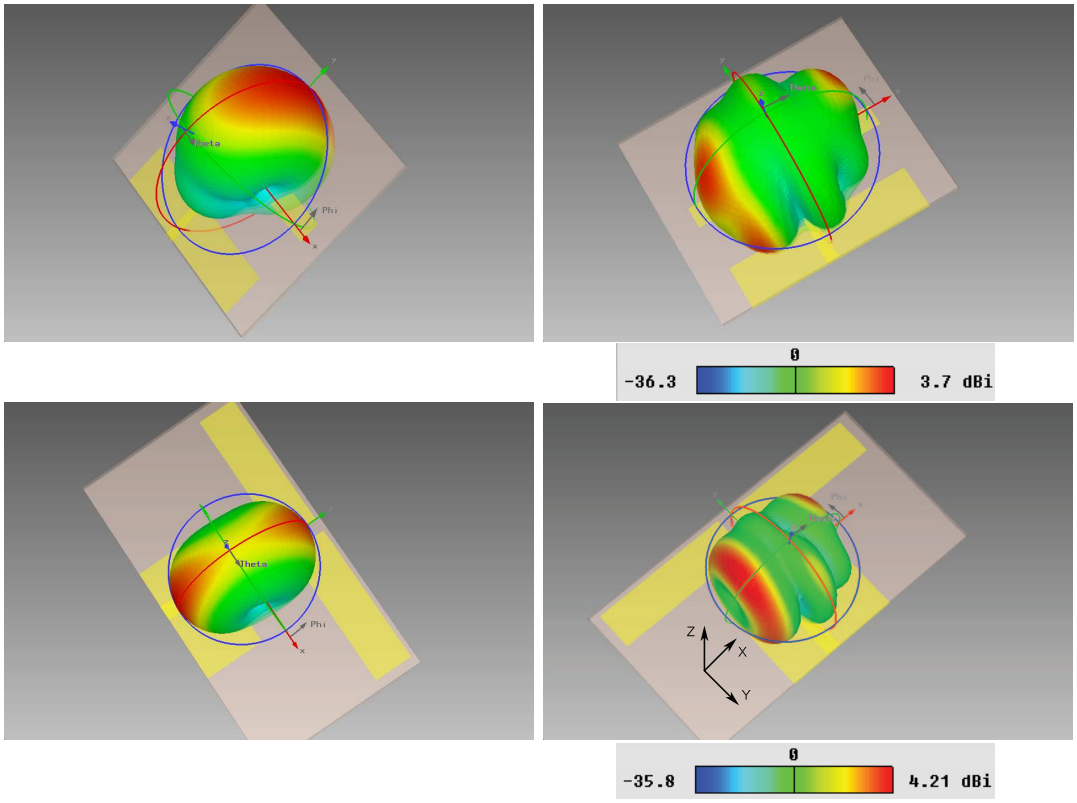

Figure 4.6: Three dimensional patterns at 2.4GHz(left) and 5.GHz(right) of dipole with long and short ground plane, at the top and bottom of figures respectively. Clearly the shorter ground provides increase omni–directionality with decreased directivity compared to the longer ground that acts as a reflector strengthening forward radiation. At 5GHz the patern of either configuration is not ideal.

To verify the results pattern measurements were performed in an anechoic chamber. The E and H plane of the dipole with the long ground are provided in figure 4.7, the plots compare measured versus simulated angular patterns.

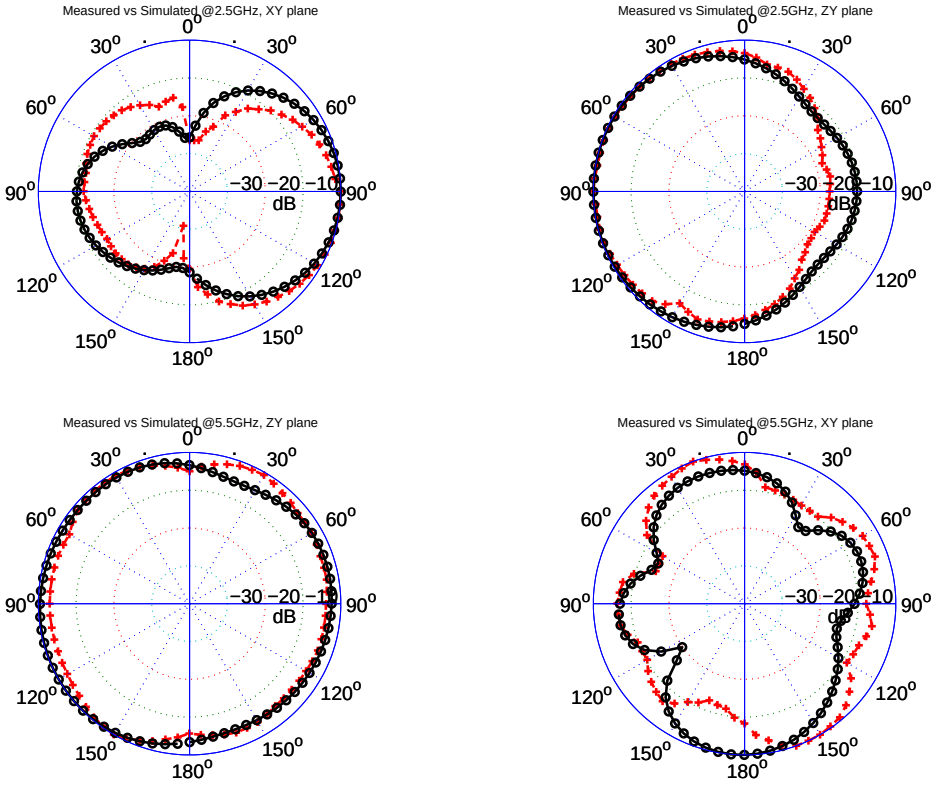

Figure 4.7: Measured and simulated radiation patterns for both frequencies, fot the long ground dipole realization. Principal axis cuts are XY and ZY.

4.3 Dual band dipole Frequency Selective Surface

Frequency selective surfaces have many applications, they were used initially in antenna radomes as filters [128], research then led to development of Electromagnetic Bang Gap lattices where one or both polarizations can exhibit a stop band and cease to propagate in the periodic structure for a certain band of frequencies. This allows for surface wave reduction and thus mutual coupling minimization and improvement of the radiation patterns of antennas on finite ground planes as the currents do not reach the outer edges with high density, thus limit the interfering radiation produced by the spurious waves radiated at the boundaries of the antennas.

One other interesting property is that the surface can be designed to operate as a Perfect Magnetic Conductor, these do not exist naturally. A Perfect Magnetic

Conductor is complementary to the Perfect Electric Conductor.

Traditionally antennas are placed in proximity of a PEC, however for such a scenario if the electric current is perpendicular to the surface then the image current has the same phase and radiation is reinforced resulting in good radiation efficiency, nevertheless the profile of the radiator is not planar consumes space and is for many systems not attractive. If the orientation of the electric current is horizontal in respect to the PEC surface then the image current has the opposite phase and thus there is cancellation of the currents, the spacing between them can be optimized to allow constructive interference, this though requires distances equal or grater than $\lambda/4$, thus once again increasing considerably the profile and volume of the radiating structure.

An Artificial Magnetic Conductor at certain frequencies can exhibit high surface impedance this can force the tangential to the surface magnetic field to vanish in contrast to PEC which is a low impedance surface that forces the tangential electric field to zero.

The impedance behaviour of the surface is controlled by the resonance properties of the periodic cells. At low frequencies below resonance the reflection phase $\Phi = \pi$ as is the case for a metallic sheet, at resonance the impedance approaches infinity and the reflection phase becomes $\Phi = 0$, above resonance the phase progresses to π. Φ is in the range $\pi/2$ to $-\pi/2$ while the surface impedance is larger than the impedance of free space[124].

The useful bandwidth of the AMC surface is when the reflection phase is in the range $-90°/90°$. Since the AMC does not reflect with an 180° degree phase reversal antennas can be placed very close to it with enhanced performance. The surface impedance can be evaluated from the sheet inductance and capacitance, where η in the equation is the impedance of free space [124].

$$Z_s = \frac{j\omega L}{1-\omega^2 LC}, \quad \omega_0 = \frac{1}{\sqrt{LC}}, \quad \Phi = \Im\left[\ln\left(\frac{Z_s-\eta}{Z_s+\eta}\right)\right]. \tag{4.2}$$

There is a plethora of geometries that can be used as the building blocks of the periodic lattice. In [128] [129] a comprehensive treatment of the main unit cell families is given. The choice of the unit cell element is important as it will influence the bandwidth of the AMC, the polarization sensitivity and the stop band characteris-

tics. The most widely used are the mushroom shape [130], the ring and split ring [131] [132] and the dipole [133]

Although many of the established geometries for the resonant elements that consist the periodic lattice own better bandwidth and are polarization insensitive, for the design of the artificial magnetic conductor that will be presented the dipole geometry was selected.

The main reasons are, it is easier to form dual band response with out the need for multiple layers, fabrication tolerances are excellent as no vias are necessary, also due to the low frequency other resonators would be prohibitively large and thus not allow adequate periodicity in a relatively small screen. The main disadvantages are, polarization sensitivity and inherent narrow band width. The bandwidth can be to an extent controlled and marginally improved by optimizing the distance of the elements in the structure. For an FSS made of printed dipoles AMC behaviour is observed when the incident field is perpendicular to the direction of the dipoles and is of TE polarisation and when the incident filed is impinging from a direction that is along the dipole length and is of TM polarization [134].

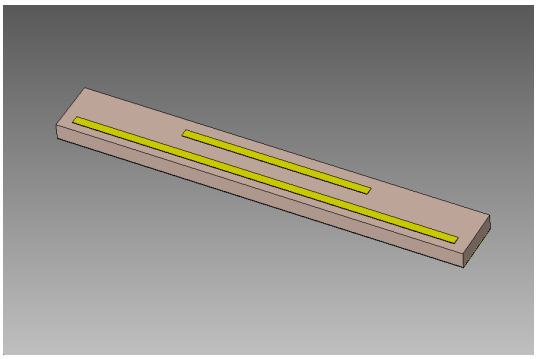

Figure 4.8: One unit cell of the periodic lattice

Figure 4.8 illustrates the topology of a unit cell, of the artificial magnetic conductor proposed. Two dipoles are used to obtain dual band behaviour. The longer dipole will provide the lower resonance at 2.4GHz and the short dipole will provide the resonance at 5.2GHz. The dipoles are placed on a grounded dielectric substrate. The substrate chosen is Taconic RF-30, which has an $\varepsilon_r = 3$ and thickness of 1.52mm. The dimensions of the long dipole are, length 37mm, width 0.8mm. The dimensions of the short dipole are, length 18mm, width 0.8mm. The size of the

substrate and thus the size of the unit cell in the simulations is, length 39.4mm, width 5.2mm and height 1.52mm. The distance between the long and short dipole in the unit cell is 1.6mm.

CST was used to analyse the properties of the FSS. The transient solver was applied with periodic boundary conditions in the x and y directions, a field probe was set in the computational domain to record amplitude and phase of incident and reflected fields and a plane wave was defined as an excitation source, the procedure resembles the physical measurement method for such surfaces, where the surface under test is compared to a surface of known reflection.

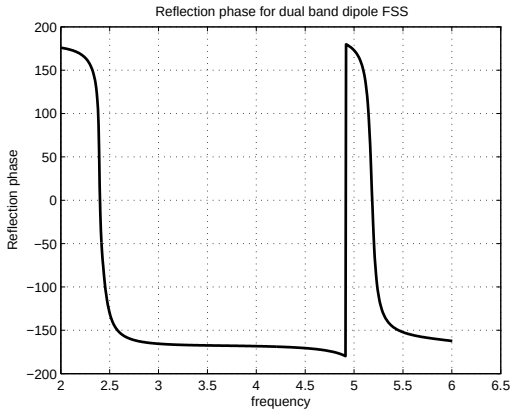

Figure 4.9: Reflection phase of frequency selective surface

The FSS behaves as an artificial magnetic conductor at two frequencies, figure 4.9 describes the reflection phase from the surface, there exist two bands where the phase crosses through zero, the first crossing is at 2.4GHz and the second at 5.185GHz, as is common with this type of FSS the bandwidth $(90°/-90°)$ is fairly narrow. At the lower AMC region the fractional bandwidth is 2.69%, while at the upper AMC region it is 1.43%.

4.4 Single printed dipole backed by FSS

As the artificial magnetic conductor can exhibit a dual band behaviour at the desired frequency ranges it is to be placed in close proximity to the dipole antenna presented. With adequate and proper matching good radiation and impedance characteristics can be obtained from the combination of the two structures.

The FSS is positioned at a distance of $0.032\lambda_0$ at 2.4GHz, tighter spacing is possible

by further tuning the dipole, a PEC surface at such a location will increase the directivity at the expense of the radiated efficiency which would approach zero as the dipole is virtually shorted to the ground, this is not the case with the AMC as will be demonstrated in this section. For a highly resonant structure of this type, precision meshing with enhancement in volume as well as at the conductor irregularities is recommended to reach a steady state in the solver and allow the energy in the computational domain to decay, ideal loss free material types should also be avoided for the same reasons.

4.4.1 Antenna & FSS Layout and design considerations

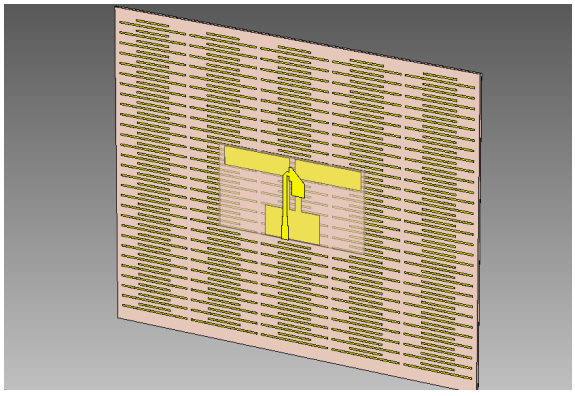

Figure 4.10: Single printed dipole antenna backed by a frequency selective surface

Figure 4.10 shows the combined antenna and FSS, the balun is on the top of the substrate holding the antenna, the dipole is at the back of the same substrate facing towards the periodic elements. The dipole is printed on a Rogers 5870 substrate with characteristics and dimensions as given in section 4.2.1, in reference to them the width of the dipole arm has been reduced by 2mm and the stub length is 1mm longer, this was to fine tune and match the antenna to the new conditions present. The FSS screen is placed 4mm away from the dipole surface and the two structures share a common centre in respect to the coordinate axis. It is printed on a grounded Taconic RF–30 substrate with $\varepsilon_r = 3$ and dimensions of $200 \times 180 \times 1.6$mm.
The screen consists of 5×34 unit cells across the width and length. The unit cell size is as given in section 4.3, for this design a relatively large screen and number of cells have been preferred to ensure good AMC properties, however the dimensions and number of cells can be reduced allowing for more compact design, this will

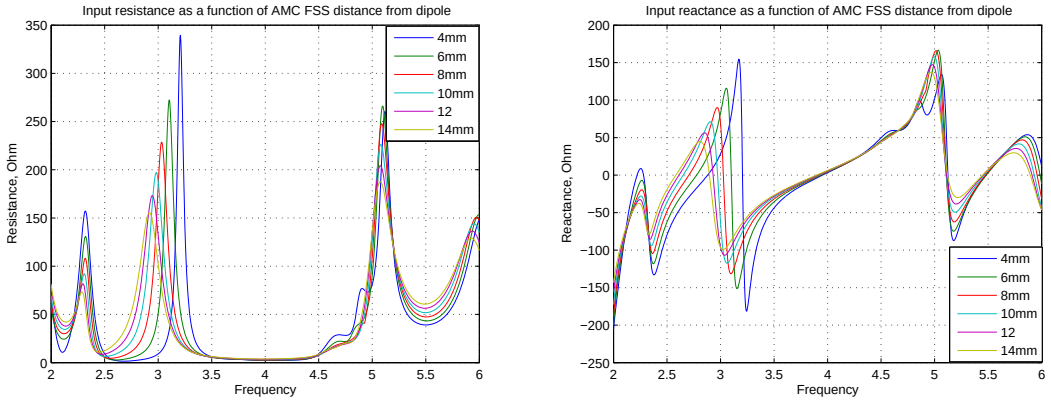

Figure 4.11: Real and imaginary part of input impedance of antenna as a function of the distance of the FSS screen from the dipole, while all other parameters are fixed.

influence the pattern and matching to an extent. A study on the effect of the screen dimensions and the number of cells to the performance of the FSS and antenna system is left for future work.

4.4.2 Parametric study on FSS distance

When a dipole is placed horizontally above a PEC, image theory suggest that this is equivalent to having another dipole at twice the distance from the PEC, the image will have opposing currents. The driving impedance of the real dipole will consist of the self impedance and the mutual impedance between the image and the physical dipole. For very close spacing the mutual impedance will be high and the opposing current will reduce the self impedance to a very low value, as $d \rightarrow 0, R \rightarrow 0\Omega$, thus a high VSWR can be present reducing efficiency and gain, in contrast the directivity increases [135]. On the other hand when the dipole is above an AMC, the image has in phase current thus the mutual impedance adds to the self impedance increasing the driving point resistance.

Figure 4.11 demonstrates the effect. The antenna was placed above the dual band FSS and the distance was varied from 4mm to 14mm in steps of 2mm. At the lower and upper AMC region where the reflection phase is zero we can see that the resistance increases with a reduction in the distance from the antenna, 4mm provides the highest resistance and 14mm the lowest, this is as expected, verifying that the surface is indeed operating as an AMC, for if it was a PEC the decrease in distance would reduce the resistance dramatically to a very low value for small

spacing.

4.4.3 Results of single dipole above FSS

Since the input resistance curves presented in the previous section indicated the surface is functioning as an AMC, the dipole was fine tuned to the dimensions discussed in section 4.4.1.

Given that the resonant element chosen to form the unit cell of the periodic structure has narrow bandwidth it was expected that there is going to be a penalty in the achievable bandwidth of the antenna, due to the limited frequency range that the reflection phase stays in a useful range. Many other resonators offer wider bands to the expense of fabrication complexity and or large size, loop elements could have been a good choice, however the low frequency and the desire to achieve precise dual band behaviour at selected frequencies discouraged the use of them. It should be pointed out that at the lower band the length of the open stub of the feed balun did provide some matching, while at the higher band it can provide good control of impedance thus allowing wider bandwidth to be achieved.

The dipole backed with the FSS achieved a bandwidth of 90MHz centred at 2.3GHz and a bandwidth of 560MHz cantered at 5.39GHz. The fact that the upper band is matched for a wider range of frequencies suggests that this can be applied to the lower band and thus increase its bandwidth, this though will require further fine tuning and perhaps a feed impedance matching network of different nature, this is left as future work and not attempted here. The initial aim and quest set for this design was to produce an antenna of low profile that can exhibit good radiation characteristics at two desired bands

Figure 4.13 shows the three dimensional radiation patterns of the antenna at 2.31GHz and at 5.39GHz. It is apparent that radiation now is focused to the broadside, normal to the surface of the antenna at both bands. There is a tilt and distortion at the upper operating frequency yet the reason for this is not clear, it could be due to the original pattern of the dipole in the region of 5GHz being distorted.

The maximum simulated directivity at 2.31GHz is 7.57dBi and the gain 5.82dB, while at 5.39GHz the directivity is 8.66dBi and the gain 7.98dB.

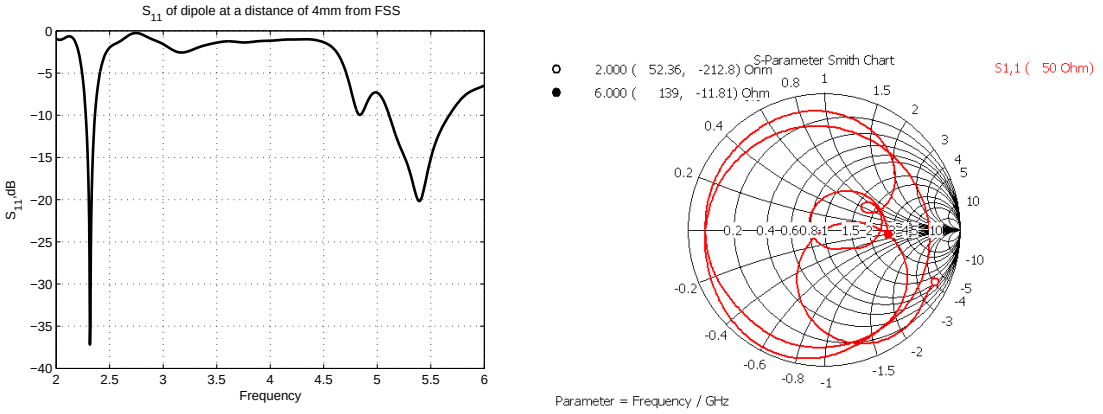

Figure 4.12: S_{11} of the combined structure, dipole is placed at a distance of 4mm from the surface of the AMC. The smith chart shown the locus of the impedance for this configuration.

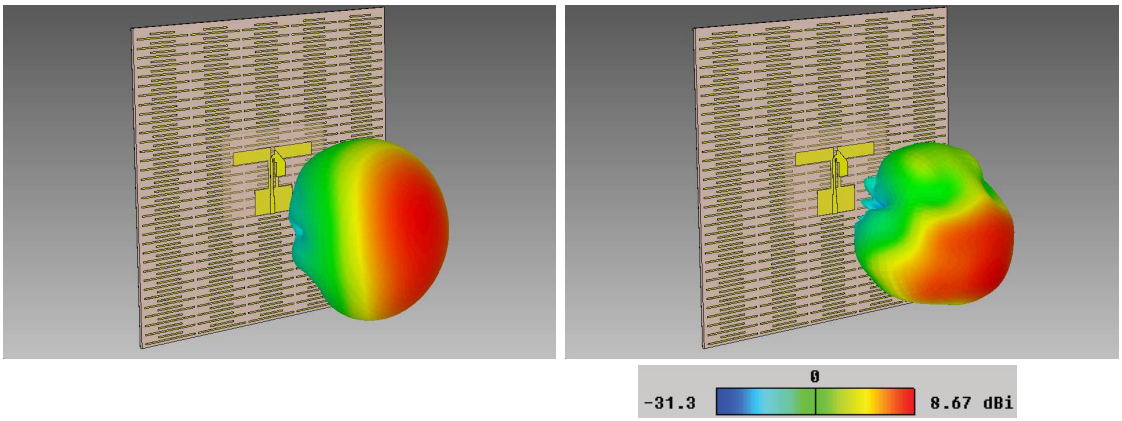

Figure 4.13: Three dimensional radiation pattern of the dipole supported by the FSS, on the left pattern is plotted at 2.31GHz and on the right at 5.39GHz

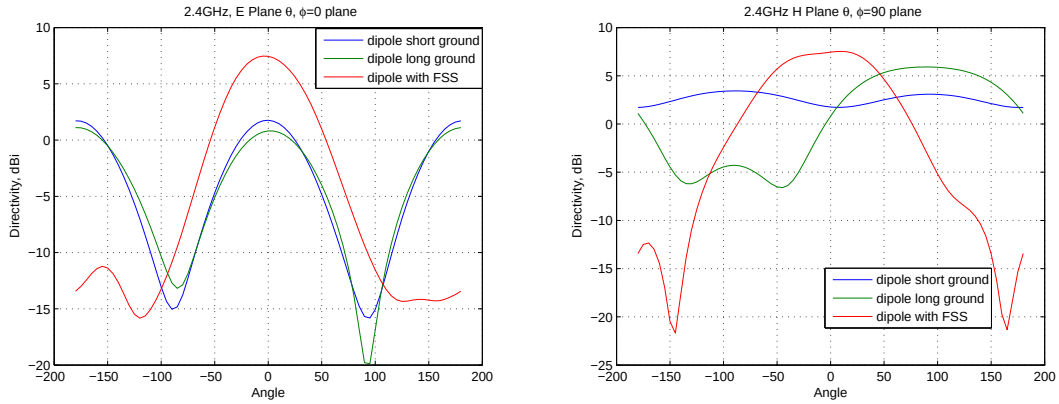

Figure 4.14: Directivity in dB at 2.4GHz at the two principal planes that are orthogonal to the substrate surface.

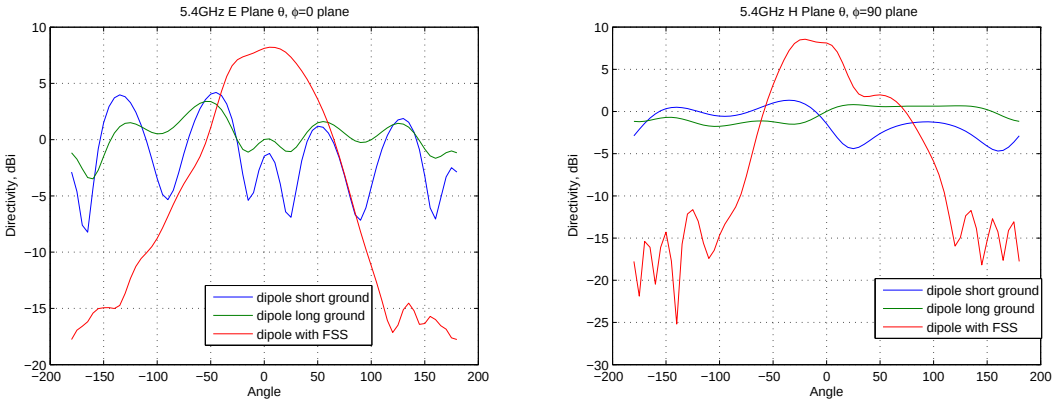

Figure 4.15: Directivity in dB at 5.4GHz at the two principal planes that are orthogonal to the substrate surface.

For comparison purposes the radiation pattern directivity at both bands of all three dipoles discussed so far is plotted in a cartesian axis system, this is shown in figure 4.14 and 4.15, the plane cuts in the graphs are the two that are orthogonal to the substrate surface. The half power beam width for the dipole backed by the FSS is 70° for the E plane and 110° for the H plane at 2.4GHz, while at 5.4GHz is 75° for the E plane and 55° for the H plane. As a reference, free space $\lambda/2$ wire dipole has an elevation 3dB beamwidth of 78° and directivity of 2.16dB, in general the beamwidth becomes narrower as the length of the dipole increases [32].

4.5 Two element printed dipole array

As the main focus here is to develop antenna arrays for MIMO applications, the dipole and FSS presented earlier will be used to form a two element array. First the array will be studied stand alone and its characteristics examined, then once more the FSS screen will be applied to the proximity of the dipole array and performance investigated. Note that as was the case with the PIFA antenna presented in the previous chapter, here the dipoles are spaced very close together, their geometry centers are separated by 75mm, however the arm ends are virtually on zero horizontal separation. Due to the geometry of the ground the feed type and the orientation of the radiation patterns the mutual coupling remains below -20dB for nearly all measurement frequencies.

4.6 Array layout and design considerations

The topology of the printed dipole array is shown in figure 4.16. Both antennas are printed on the same face of the substrate, while the feeds are both on the opposite face. The physical dimensions of each of the dipoles are as defined in section 4.2.1. The overall dimension are $40 \times 150 \times 1.575$mm. The structure is printed on Rogers Duroid 5870 substrate with $\varepsilon = 2.33$.

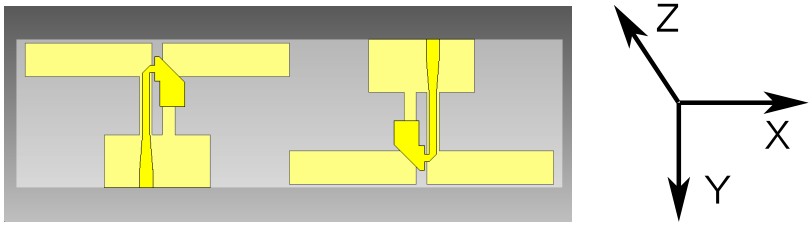

Figure 4.16: Topology of the proposed printed dipole array, Z axis normal to substrate surface.

4.6.1 Array measured and simulated results

The fabricated array reflection and transmission response versus frequency was measured with an Agilent network analyser. Fig. 4.17 illustrates measured against simulated S paramters. The impedance bandwidth is defined at -10 dB. For IEEE 802.11b the required 10 dB bandwidth is about 83.5 MHz centred at 2.44 GHz and for IEEE 802.11a it is about 800 MHz, that is to cover all three possible bands. It is common practice to design the radiators with larger bandwidth than that required to account for various performance variations that may arise due to the antenna's operational environment. The lower band measured bandwidth is 699 MHz (2.036–2.735 GHz) and the upper band measured bandwidth is 1.483 GHz (4.872–6.355 GHz).

In Fig. 4.17 the measured transmission coefficient from one element to the other is measured and presented. It is clear that its value is below -20 dB from 2 to 6.6 GHz. This is highly desirable as higher values can compromise MIMO capacity if no decoupling network is employed due to increased correlation of the received signals. On the right of Fig. 4.17 the locus of complex impedance is illustrated on a Smith chart. Three tight loops exist around the centre of the chart.

Table 4.2: Measured resonant frequencies, bandwidth and isolation

Element	f_{lower}	f_{upper}	$BW_{measured}$	S_{12}
Array band (band 1)	$2.036GHz$	$2.735GHz$	$699MHz$	$-24dB@2.45GHz$
Array band (band 2)	$4.872GHz$	$6.355GHz$	$1.483GHz$	$-33.5@5.2GHz$

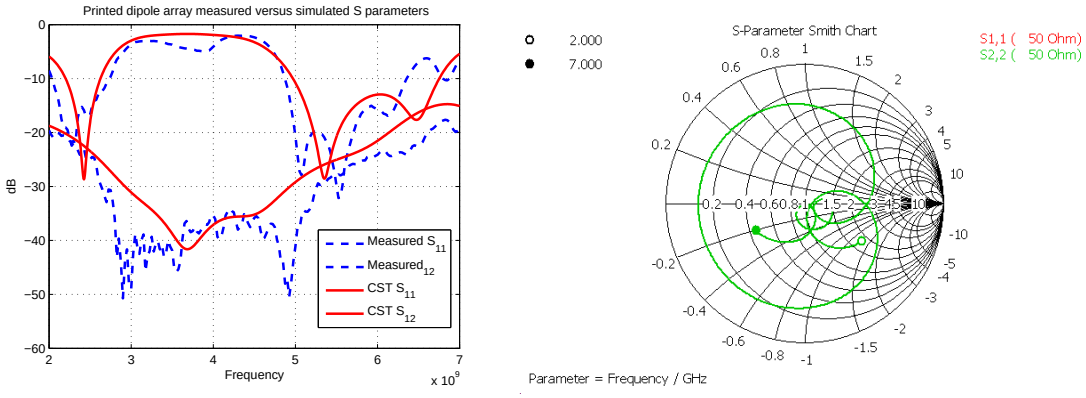

Figure 4.17: On the left of figure measured S–parameters are compared to the simulated ones, there is a good correlation between them. The smith chart shows the impedance locus computed with CST.

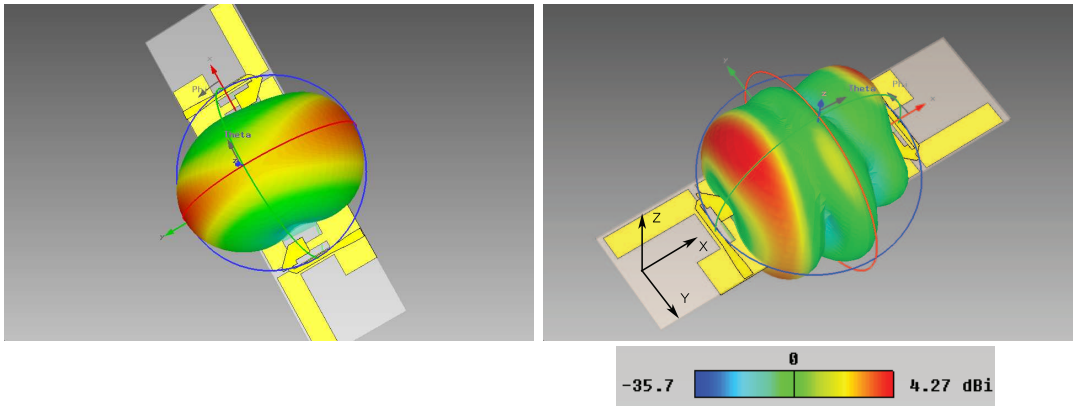

Figure 4.18: Three dimensional radiation pattern of one of the elements at 2.4GHz(left) and at 5.5GHz(right), the second element at the higher band has a complementary pattern.

The three dimensional radiation patterns of the array, show that there is little change from the single isolated case, the patterns shown are for one of the elements. At the 5.5GHz band one of the dipoles captures mainly waves coming towards the left in respect with the array topology while the other capture waves coming mainly from the right, their directivity is maximum at different angular ranges, this was thought that will be a nice measure for MIMO directed systems, however this might not allow the dipoles to harvest enough incoming energy or even illuminate the space in

case of transmission adequately.

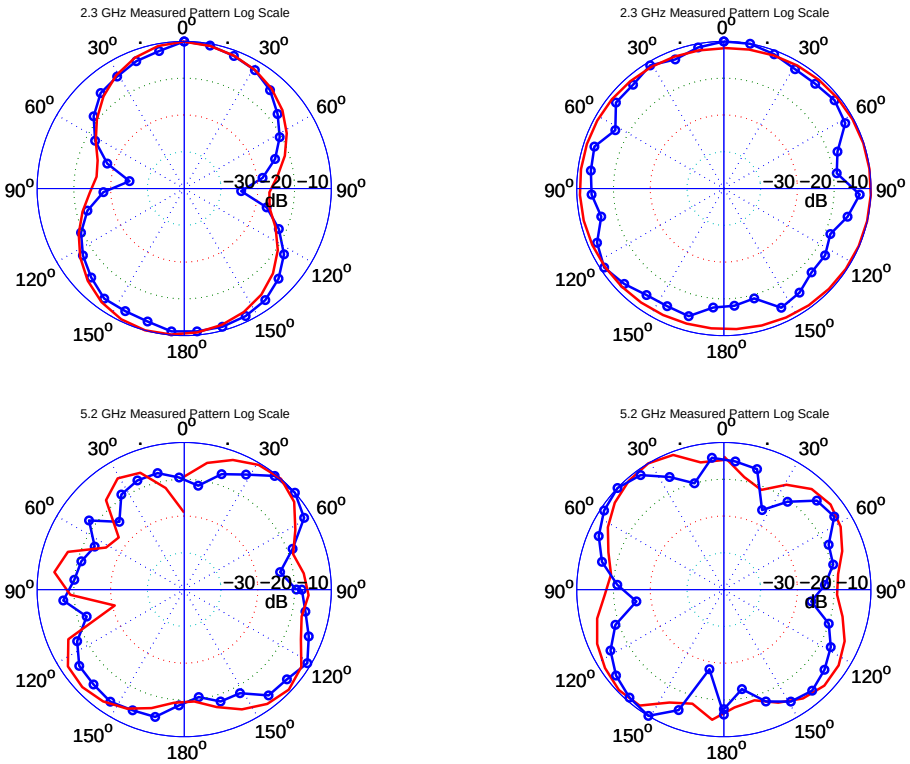

Figure 4.19: Measured and simulated radiation patterns for the dipole array, at 2.3 and 5.2GHz, one of the elements was terminated in a matched load during the measurement

The simulated maximum directivity at 2.4GHz is 3.47dBi while the gain is 3.41dB, at 5.5GHz the directivity is 4.27dBi and the gain is 4.13dB. Measured and simulated radiation patterns are plotted in Fig. 4.19. Measurements were done in an anechoic chamber using an Agilent signal generator and spectrum analyser. During measurement one of the elements was terminated in a 50Ω load while the other's pattern was measured. Polar plots at 2.3 GHz present XY and ZY planes while polar plots for 5.2 GHz present ZX and XY planes (see Fig. 4.18 for dipole orientation),with Z being the axis normal to the surface of the antenna. The measured 3 dB elevation beamwidth for the lower band is about 60 degrees while the simulated value was 53 degrees. The pattern at the higher band resembles that of a 2λ dipole with a part missing. The measured 3 dB elevation beamwidth for the lobe of maximum gain is about 30 degrees while the simulated value was 35 degrees. For the ZX plane at 5.2 GHz the 3 dB measured beamwidth is about 45 degrees while the simulated value

is 39 degrees.

There is significant pattern distortion especially in the upper operating frequency due to radiation from the balun and the ground plane, this also introduces cross polarization.

The shape of the radiation pattern, the directivity, the gain and the 3dB beamwidth values presented for the dipoles without the AMC, either in the array form or stand alone, are consistent with an electrical equivalent length of approximately one wavelength at the lower frequency and two wavelengths at the upper frequency. Recalling the physical dimensions given at the beginning of this chapter, the physical length at the 2.4GHz is $0.92\lambda_g$ and at 5.2GHz it is $2\lambda_g$, where λ_g is the guided wavelength. In terms of the free space wavelength the physical length is $0.6\lambda_0$ and $1.3\lambda_0$ respectively.

4.7 Two element printed dipole array backed by FSS

The dual band dipole array presented in the previous section is now to be placed above the FSS screen. As before the distance between the array and the screen is kept at 4mm. To keep symmetry along all directions the size of the sheet with the periodic element was increased to $280 \times 185 \times 1.6$mm. The number of unit cells is 7×35. Light tuning of the dipole dimensions was necessary to obtain reasonable impedance matching, the dimensions are as mentioned earlier with the exception of the dipole arm being 1.5mm shorter and the length of the open stub being 1mm longer. The topology of the proposed structure is shown in figure 4.20 .

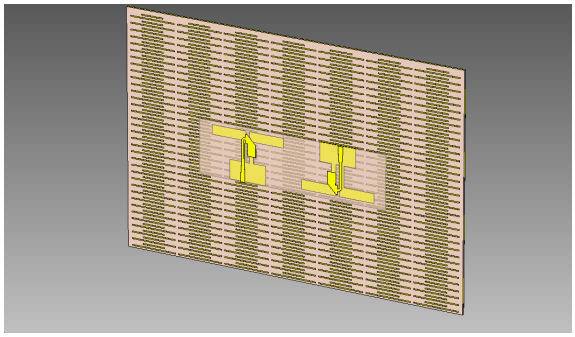

Figure 4.20: Simulated S parameters of dipole array with FSS screen at distance of 4mm

As was observed for the case of the single dipole and the array, the open stub can provide control of real and imaginary part of the impedance at the higher band allowing for adequate band width, this is not the case for the lower frequency where once more the achieved bandwidth is relatively narrow. At the lower band the bandwith is 75MHz while at the higher 473MHz. The simulated S parameters are provided in figure 4.20. It is clear that as was the case for the dipole array stand alone, the coupling between the dipoles is below 20dB for the whole simulated frequency range, keeping in mind that the separation from arm to arm is virtually zero.

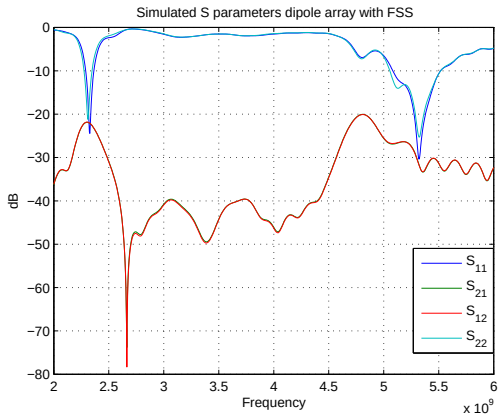

Figure 4.21: Simulated S parameters of dipole array with FSS screen at distance of 4mm

The radiation patterns are not modified relatively to the single dipole case backed by the AMC surface, except the fact that now the directivity and efficiency have improved slightly. Apparently the achieved patterns can compare to the microstip patch antennas and even surpass their performance, as with the proposed arrangement good radiation characteristics can be obtained at two predetermined selected frequencies, with low antenna profile and ease of fabrication that requires no vias, foam materials or other complex feed networks.

The maximum simulated directivity at 2.32GHz is 7.71dBi while the gain is 6.77db, at 5.32GHz the directivity is 9.23dBi and the gain is 7.98dB. The three dimensional patterns for each of the elements in the array is shown in figure 4.22, while figure 4.23 provides the angular patterns in a polar plot, where the E and H planes are given for both operating bands. The 3dB beamwidth at 2.32GHz for the E plane is 70° with a side lobe level of -17dB, for the H plane the beamwidth is 117° and the side lobe level is -18dB. At 5.32GHz the half power beam width for the E plane is

73° with a side lobe level of -23dB, the *H* plane has a 3dB beamwidth of 58° and a side lobe level of -20dB.

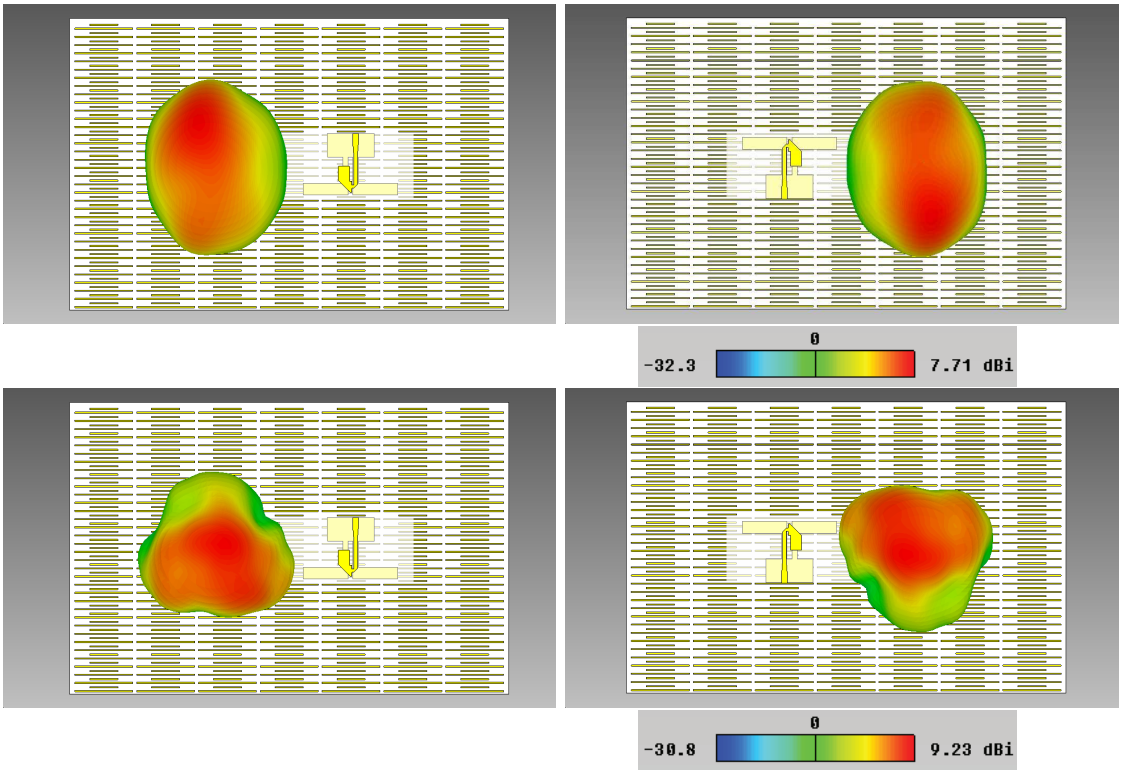

Figure 4.22: 3D radiation patterns at 2.32GHz(top) and at 5.32GHz(bottom), for each of the antenna in the array.

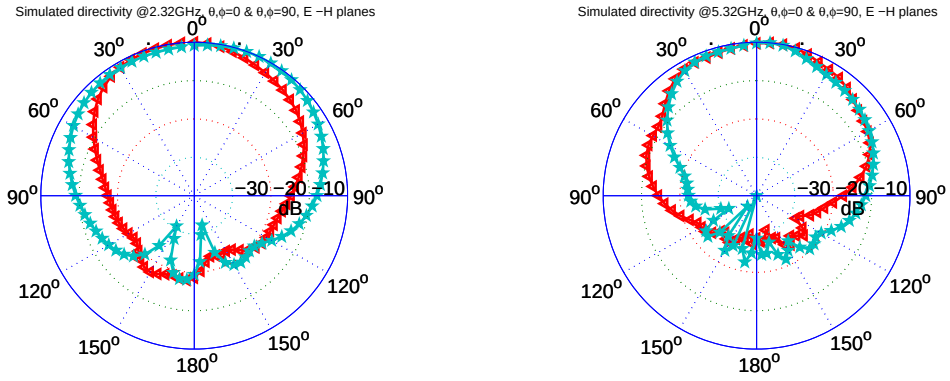

Figure 4.23: Simulated *E* and *H* planes for the array backed with FSS, at 2.23GHz and 5.32GHz

Not many articles in available literature examine the effect of the combined radiation pattern to the performance of a MIMO system as the distance between the antennas and the statistics of the applied signal will influence the resulting patterns. Papers usually examine the single isolated radiation pattern of each of the elements in the arrays. However in a MIMO system if it employs spatial multiplexing as is

BLAST systems the excitation signals at the antenna terminals will be random in nature in amplitude and phase, for Alamouti where diversity is used across space and time the orthogonal matrices will pose signals that will affect the total pattern. For illustration purposes and to get a fair understanding of the performance of the proposed dipole array above the FSS, CST was used to excite the antenna ports with signals of equal amplitude yet with different phase. Figure 4.24 demonstrates the resulting patterns for both bands at three different phase values, the combined patterns are valid for equal amplitude equal phase (0,0), equal amplitude phase (0 ,90), equal amplitude phase(0,180). Evidently from the combined results the directivity remains high for all combinations and there are lobes of wide beamwidths.

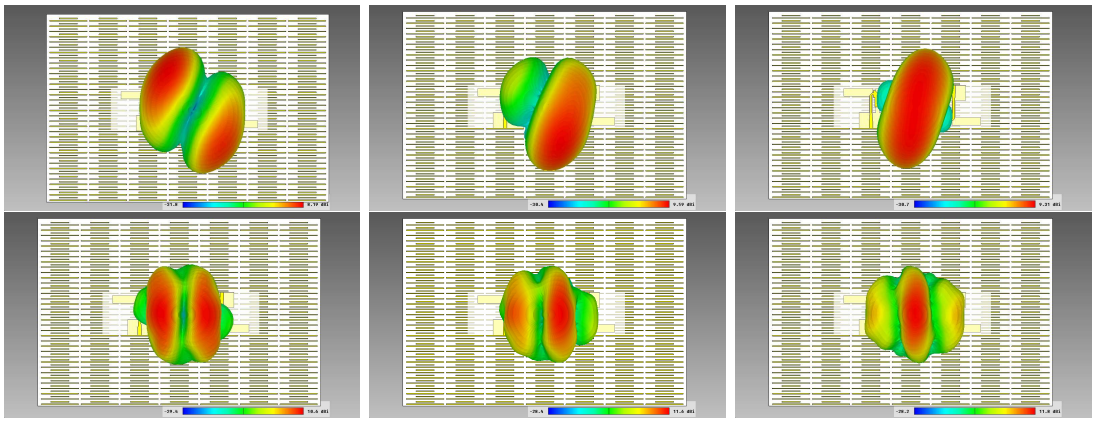

Figure 4.24: Combined 3D radiation patterns at 2.32GHz(top) and 5.32GHz(bottom), from left to right the phases of the signals at the ports are (0,0),(0,90),(0,180), amplitudes being equal.

4.8 Conclusion

A dual and wide band printed dipole has been designed, parametrically studied and experimentally verified, the dipole has a balun the allows wide impedance match. The radiation of the wide open stub of the balun was expected to provide some form of pattern diversity. The dipoles radiation pattern at the lower band is omnidirectional and can be controled by the length of the ground plane supporting the feed microstrip line. At the higher band the radiation is similar to a dipole with physical length just above a two wavelength, a part of the expected pattern is missing from canceling effects from the open stub. The fact that there was a strong desire to obtain good radiation and efficiency at both operating bands led to the application

and investigation of the performance when an artificial magnetic conductor is placed in close proximity of $0.032\lambda_0$.

A dual band FSS behaving as an AMC was designed for the purpose of improving the radiation and efficiency of the dipole at two bands. With the application of the FSS the patterns indeed improved. There was a penalty at the impedance band width at the lower band, this is mainly due to the narrow bandwidth of the reflection phase of the selected resonator consisting the unit cell of the FSS, and the fact that the open stub did not provide adequate control of the impedance at the lower band as it did at the higher.

Following the dipole was used to form an array of two elements that are very close spaced and are positioned as images of one another. The dipole array achieved wide impedance bandwidth at two bands and a coupling level below 20 dB for nearly the whole measurement frequency range, given the close spacing, this was mainly achieved due to the type of feed the individual grounds and the orientation of the elements. However although at the lower band the dipoles are omnidirectional with patterns that can be controlled by the ground plane and be made into endfire directional, at the higher band the patterns suffer and are similar to dipoles of length little above two wavelength with one half missing. Thus to maintain low profile an AMC was placed in close proximity to the array to improve its characteristics.

The dipole array above the AMC behave analogously to the single dipole above the AMC. Directive and relatively wide angle beams were obtained for both bands, the patterns are along the broadside, normal to the surface hosting the dipoles. At the upper operating frequency there is enough band width to accommodate systems operating at the 5GHz ISM bands, however the lower operaing frequency needs a feed method to improve and gain control of the impedance, of course it may be simpler to use a different type of FSS that has inherent wide bandwidth of reflection phase if the manufacturing complexity and multilayered FSS structure is not an issue. There are many degree of freedom to explore.

Chapter 5

Dual Band Surface Wave Suppression For Printed Antennas

"Nothing exists except atoms and empty space,
everything else is opinion"
Democritus

5.1 Introduction

In this brief chapter a combination of two mutual coupling suppression techniques will be proposed for use in printed antennas, the design and experiments performed are as a proof of concept. As further work will be left to apply the techniques to a dual band printed antenna array.

Given their attractive properties printed antennas may soon replace most other types, this is due to the extensive research that has taken place since they were first introduced by Deschamps in 1953 [136]. It took twenty years since their introduction to really become popular and start to be used in applications. Improvement in laminate fabrication and processing and the increasing need for low profile antennas to be used in air borne systems, aircraft, missiles, and the need to have antennas integrated in monolithic microwave circuits drove their explosive growth and development.

Among other disadvantages, patch antennas suffer from strong surface wave excitation. Surface waves are TM and TE propagation modes in the substrate, they have a real propagation constant above cut off and their phase velocity is influenced by the substrate height and ε_r [123]. In theory ε_r should be low to reduce losses originating from trapping the fields in the substrate and in contrast enhance the

fringing field that actually produces the radiation from the antenna. Regarding coupling in patch arrays the authors of [137] point the following facts. The coupling can be due to near field, far field and surface waves. They also explain that for low ε_r the size of the patches is large as is the wavelength of the guided wave in the substrate thus the element separation may appear small, placing each other in their near field zones. Far field coupling is mainly to the property of horizontal radiation of the patch. Surface waves give rise to losses, mutual coupling and radiation from the edges of the antenna structure. The surface waves start to contain considerable power when,

$$\frac{h}{\lambda_0} \geq \frac{0.3}{2\pi\sqrt{\varepsilon_r}}, \tag{5.1}$$

Articles in literature on methods to reduce surface wave coupling are focused on micro–machining [138][139], this frequently implies a micro cavity below the patch yet it is not hard to realise that is not very attractive, and reduction by the use of Electromagnetic Band Gap lattices, these provide a stop band for the TM and TE waves in the substrate [130][140][141]. The power of these waves instead is radiated to add with the antenna radiated fields.

At the previous chapter a dual band FSS was investigated for its artificial and attractive reflection properties, the dipole FSS was used as an AMC reflector, in this chapter a mushroom type periodic structure first introduced by [130] will be applied as a an electromagnetic band gap lattice. The mushroom type periodic element is polarization insensitive and exhibits large bandwidth in respect to the stop band characteristics.

The authors in [142] introduce an analytical method to eliminate surface waves present and improve performance of printed antennas by means of dielectric superstrates. They demonstrate how the cover affects the gain, radiation resistance and efficiency. It is possible they argue to achieve 100% efficiency with proper selection of the superstrate qualities. They give analytical equations that allow the thickness and dielectric constant to be evaluated so that surface waves are eliminated, therefore reducing mutual coupling in arrays, increasing efficiency and reducing end fire radiation that was originally from surface waves reaching the boundary. Additionally they provide the analysis to produce nearly omnidirectional radiation in the E

or H plane if that is desired to be.

The combination of a dielectric superstrate with an EBG can be a fairly interesting approach to dual band systems that operate at relatively low GHz frequencies. Here an elementary patch antenna array of two elements operating at 2.4GHz is designed on a thick substrate, this can be attractive in applications to increase easily the bandwidth and it provides a challenge as the surface waves and coupling increase as the height increases, thus making more desirable the suppression of them. Each patch is covered by a dielectric superstrate of different size to investigate pattern distortion and coupling reduction at 2.4GHz. Between the two patches three periods of a mushroom type EBG are placed these are designed to operate near 5GHz, the stop band and the effect of the resonant frequency of the two patches is observed. In effect means to gain control of mutual coupling and possibly radiation and gain characteristics at two frequencies is proposed.

5.2 Surface waves and surface impedance

In virtually all applications surface waves are not desirable, they are the source of reduced efficiency, radiation pattern distortion and increased mutual coupling. In this section a simple example of the relation of the surface waves to the surface impedance of an arbitrary media will be discussed.

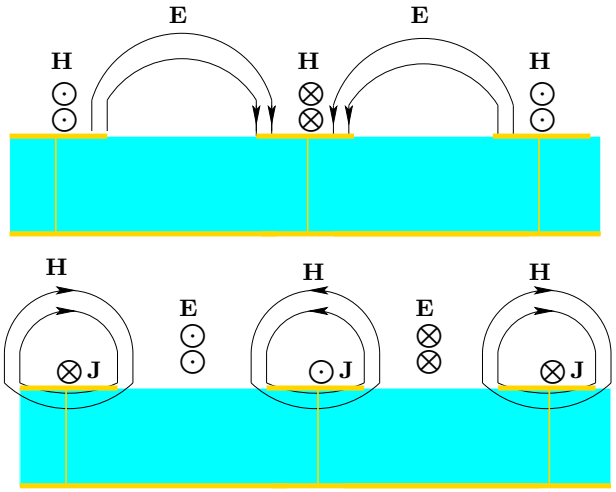

Figure 5.1: Top diagram a simplified TM surface wave configuration. Bottom diagram depicts a TE surface wave configuration.

A surface wave by definition is a wave that is bound to the interface between two different materials. The surface waves are taken to decay exponentially away from the interface. Surface waves can be classified as transverse magnetic or transverse electric. Figure 5.1 illustrates in a simplified manner TM and TE surface wave configurations along a textured surface. For TM waves the magnetic field is tangent to the surface and entirely transverse to the direction of propagation while the electric field jumps out of the surface. For the TE surface wave configuration the electric field is tangent to the surface and entirely transverse to the direction of propagation while the magnetic field jumps out of the surface. The behaviour of the surface wave is determined by the surface impedance. An inductive surface impedance will support TM surface waves, while a capacitive surface impedance will support TE surface waves.

The surface impedance can be defined as the ratio of the tangential electric field over the tangential magnetic field at the surface.

Consider an arbitrary surface with an impedance Z_s. The surface is occupying space in the yz plane. The geometry of the problem space is shown in figure 5.2 .

The surface wave is taken to propagate in the z direction and decays exponentially in the x direction, with a decay constant α and a propagation constant β. For brevity we assume the fields below the surface to be zero and the space above the surface to be air, with ε_0 μ_0.

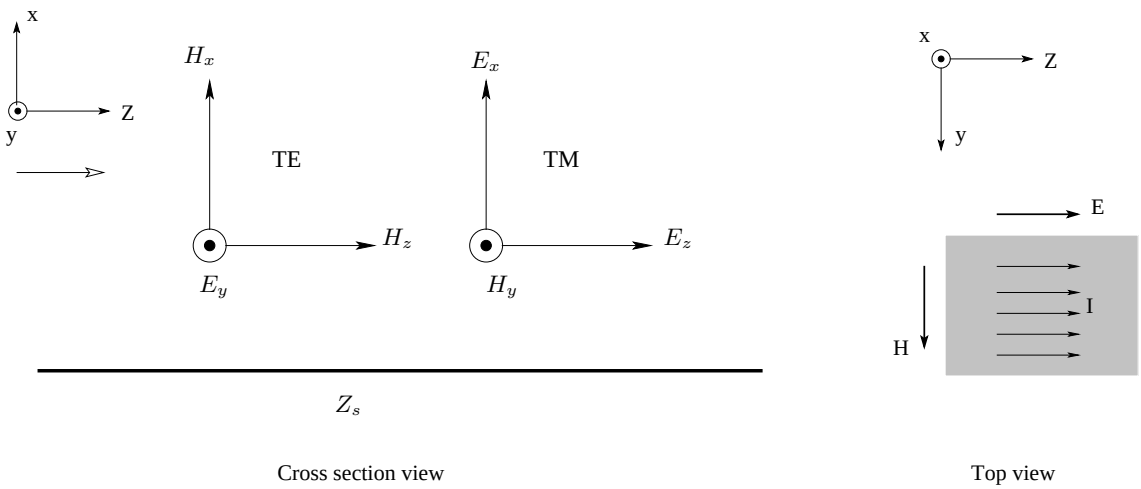

Figure 5.2: Left, TE or TM surface waves along an arbitrary surface with an impedance Z_s. The direction of propagation is along the z axis. On the right top view shows the tangential field components, which define the surface impedance.

On the arbitrary surface which exhibits a surface impedance Z_s, the tangential electric field, the tangential magnetic field along the surface and the electric current density are related. The relation of the electric current density to the tangential magnetic field is given by [3] [118]

$$J_s = \hat{n} \times H, \tag{5.2}$$

therefore the following boundary condition is valid,

$$E_t = Z_s J_s = Z_s \hat{n} \times H. \tag{5.3}$$

It should be noted that surface waves are bound to the interface and that the surface impedance is defined from the tangential field components along the interface, for example for the TM surface wave configuration shown in figure 5.2, the magnetic field has only a y component, which is tangential to the surface and transverse to the direction of propagation (z), the electric field may have a longitudinal and transverse component however in the configuration shown the tangential component of the electric field is along the z coordinate.
The surface impedance can be defined as the ratio of the electric and magnetic fields in the plane of the surface. For the geometry shown [130][118]

$$Z_s(TM) = \frac{E_z}{H_y}, \qquad Z_s(TE) = \frac{-E_y}{H_z}. \tag{5.4}$$

For TE waves, and for this example $E_x = E_z = H_y = 0$. The electric field component can be written as

$$E_y = Ae^{-j\beta z - \alpha x}. \tag{5.5}$$

However we know that all field components obey the Helmholtz equation, thus

$$\nabla^2 E_y + k_0^2 E_y = 0, \tag{5.6}$$

where $k_0 = \omega\sqrt{\varepsilon_0 \mu_0}$, leading to

$$\alpha^2 - \beta^2 = k_0^2. \tag{5.7}$$

The magnetic field component for the case of the TE wave defined earlier can be obtained from Faraday's law

$$\begin{aligned} H &= -\frac{1}{j\omega\mu_0}\nabla \times E \qquad (5.8)\\ &= -\frac{1}{j\omega\mu_0}\nabla \times (\hat{a}_x E_x + \hat{a}_y E_y) \\ &= -\frac{1}{j\omega\mu_0}\begin{bmatrix} \hat{a}_x & \hat{a}_y & \hat{a}_z \\ \frac{\partial}{\partial_x} & \frac{\partial}{\partial_y} & 0 \\ E_x & E_y & 0 \end{bmatrix} \\ &= -\frac{1}{j\omega\mu_0}\left\{\hat{a}_x(0) + \hat{a}_y(0) + \hat{a}_z\left(\frac{E_y}{\partial_x} - \frac{E_x}{\partial_y}\right)\right\} \\ &= -\frac{1}{j\omega\mu_0}\hat{a}_z\frac{E_y}{\partial_x} \\ &= H_z = \frac{\alpha}{j\omega\mu_0}E_y. \qquad (5.9) \end{aligned}$$

The surface impedance for TE waves is thus

$$Z_s = -\frac{E_y}{H_z} = -\frac{j\omega\mu_0}{\alpha}. \qquad (5.10)$$

The decay constant is related to the surface impedance as follows

$$\alpha = -\frac{j\omega\mu_0}{Z_s}. \qquad (5.11)$$

It becomes evident that TE waves are supported only if the surface impedance has a negative reactance, else α will be negative. The propagation constant can be defined as

$$\beta^2 = k_0^2 - \frac{\omega^2\mu_0^2}{Z_s^2}. \qquad (5.12)$$

For TM waves considering the topology shown in figure 5.2, and with $H_x = H_z = E_y = 0$, the magnetic field can be written as

$$H_y = Be^{-j\beta z - \alpha x}. \qquad (5.13)$$

Using Ampere's law

$$E = \varepsilon j\omega \nabla \times H \tag{5.14}$$

$$= \hat{a}_z \frac{\partial H_y}{\partial_x}$$

$$= E_z = -\frac{\alpha}{\varepsilon j\omega} H_y. \tag{5.15}$$

The surface impedance for TM waves is thus

$$Z_s = \frac{E_z}{H_y} = -\frac{\alpha}{\varepsilon j\omega}. \tag{5.16}$$

The decay and propagation constants therefore are

$$\alpha = -j\omega\varepsilon Z_s, \tag{5.17}$$

$$\beta^2 = k_0^2 - \omega^2\varepsilon^2 Z_s^2. \tag{5.18}$$

Clearly for TM modes to be supported by the arbitrary surface the impedance must have a positive inductive nature so to keep α positive.

5.3 Mushroom EBG

The electromagnetic band gap structure discussed in this section consists of a periodic positioning of metallic patches supported by a grounded substrate, where vias at the centre of each patch connect them to the ground plane. The parameters that describe EBG structure are the patch width W, substrate thickness h, gap width of adjacent patches g, dielectric constant ε_r and via radius r.

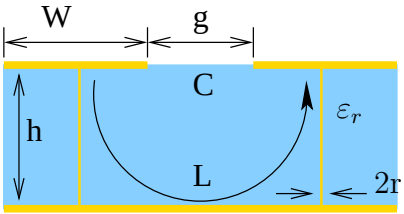

Figure 5.3: Mushroom EBG topology

If the unit cell of the periodic lattice is small compared to the wavelength then it can be represented by an effective medium model of LC elements [143]. The capacitance is due to the fields between adjacent patches and the capacitance to the ground while the inductance is from the current loops flowing through the vias and the ground sheet to each adjacent patch. Therefore the lattice can be represented as a parallel resonant LC circuit.

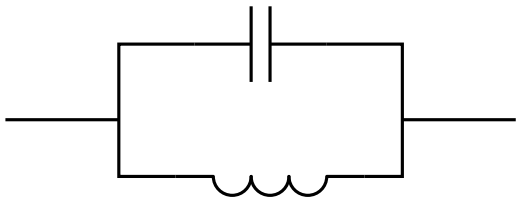

Figure 5.4: LC resonant circuit

The impedance of a parallel resonant LC circuit is given as

$$Z = \frac{j\omega L}{1-\omega^2 LC}, \qquad \omega_0 = \frac{1}{\sqrt{LC}}. \tag{5.19}$$

Using quasi static techniques approximate values of L and C can be obtained. These are fit for an initial estimation of the properties of the EBG. For low frequencies where small values of L and C may be required corrections may be necessary, [118] addresses this issue and the effects of oblique incidence of plane waves on the surface impedance and reflection phase. Sievenpiper [130] derived the following expressions for the capacitance and inductance. The capacitance in the expression is due to the gap between the patches and the inductance due to the current in the vias and the metal sheet,

$$C = \frac{W\varepsilon_0(\varepsilon_r+1)}{\pi}\log\left(\frac{2W}{\pi g}\right), \tag{5.20}$$

$$L = \mu h. \tag{5.21}$$

The mushroom type unit cell, can form a high impedance surface. Considering surface wave propagation, below resonance the surface behaves inductively and allows TM waves, above resonance its behaviour changes to capacitive and TE waves are supported, near resonance no surface waves are supported[124]. In the case where a plane wave strikes the surface then, at and near resonance it behaves as an AMC.

The muchroom type is perhaps the most widely applied type of periodic element to improve antenna rerformance [144][145][143].

A unit cell of the designed lattice has the following dimensions; the patch is $8 \times 8 \times 3.2$mm, via is placed at the centre of each patch and has a diameter of 0.4 mm. The distance between elements is 0.5 mm making the lattice period equal to 8.5 mm corresponding to about seven per cent of free space wavelength ($0.069\lambda_0$) at 2.4GHz, however the EBG is designed to operate at 5GHz, it is the effects of the presence of three periods of the EGB cell will have on the resonant frequency of the antenna patches that is to be observed and the effect that the antenna patches will have on the resonant band of the EBG .

Figure 5.5 shows an alternative equivalent circuit representations for the mushroom EBG cell which takes into consideration the capacitance to the ground and the possible capacitance from opposing edges of each patch, the lumped equivalents can be calculated while the voltage and current on either side of the nth unit cell can be related using the ABCD matrix [146]. Since the periodic structure is passive and reciprocal an appropriate propagation constant can be defined.

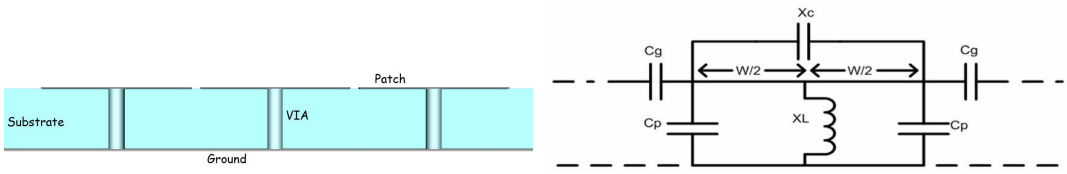

Figure 5.5: Cross section of the mushroom EBG(left), equivalent representation(right)

The substrate thickness will influence the resonant conditions of the high impedance surface. Using CST a parametric study on the effect of the substrate thickness was performed. Three common thickness values were simulated, namely, 1.6mm, 3.2mm and 4.8mm, the substrate is a lossy model of Rogers RO3003.

When the thickness is increased the length of the thin vias increases as does the associated inductance, the capacitance of the unit cell patch to the ground decreases this though is less significant than the effect of the inductance, the distance from edge to edge of each unit cell element has remained the same and thus the capacitance from edge to edge. Figure 5.6 illustrates the results.

Clearly by increasing the thickness of a substrate one can achieve better impedance bandwidth in microstrip patch antennas with the risk of increasing surface waves,

however since this appears to lower the resonant frequency of the EBG then at low operating frequencies the combination of these two can become attractive. For example with identical unit cell dimension varying only the height, for 1.6mm the reflection phase shows that the surface achieves resonance at about 6.7GHz, while for a height of 4.8mm the surface with identical unit cell dimension resonates at 3.8GHz, this is a considerable reduction in frequency and thus can be though as means to reduce the size of unit cell in expense of cell thickness, at low frequencies where resonators are prohibitively large this may be beneficial.

Based on the simulation results it can be suggested that for a substrate thickness of 1.6mm and a unit cell periodicity defined from a constant separation of 0.5mm between cells, the length and width dimension of the patch in a unit cell must be approximately 28mm $\times$ 28mm in order to resonate and achieve a stopband at 2.4GHz. In general for a periodic structure it is usually required to have at least three periods. This immediately creates a problem as the space required to accommodate three periods of a unit cell of these dimensions is unacceptable. Interestingly enough the traces shown in figure 5.6 indicate that keeping all the unit cell dimensions constant, only by increasing the substrate thickness the resonant frequency and thus the stopband can be controlled. It becomes apparent that a substrate with more height can lower the resonant frequency for a given fixed size of a cell, therefore, allowing for a more compact design of unit cell.

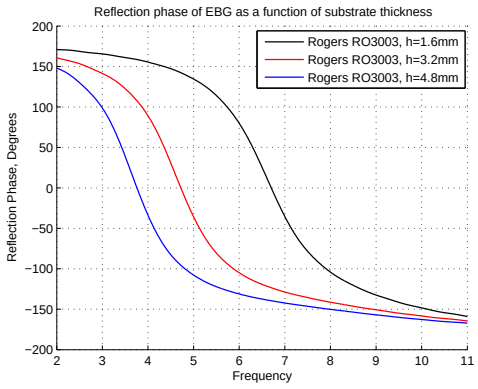

Figure 5.6: Reflection phase of mushroom EBG as a function of substrate thickness

Other degrees of freedom exist in the design process of the EBG, tuning of size, frequency and bandwidth can be achieved by altering effective parameters of the structure.

Figure 5.7 on the left shows plots of the reflection phase for various different substrate dielectric constants. The height of the substrate is 1.6mm and the dimensions of the metallic parts are as given earlier. For this parametric run three commonly used substrates for antenna development are compared, first is a Rogers 5870 with $\varepsilon_r = 2.33$, then Rogers RO3003 with $\varepsilon_r = 3$ and FR4 with $\varepsilon_r = 4.6$. As is expected the higher dielectric constant reduces the resonant frequency for a structure with all other dimensions fixed. Of course this outcome can be attractive for its potential to allow for smaller unit cells, however it is evident that there is a price to pay in reduced bandwidth of the inphase region, clearly the slope of the low ε_r is more relaxed and provides a higher in phase bandwidth.

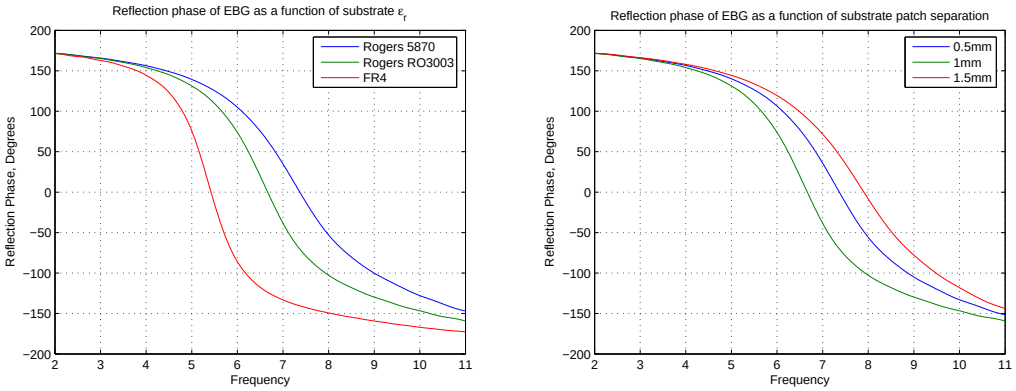

Figure 5.7: Reflection phase of mushroom EBG as a function of substrate ε_r (left) and as a function of gap width (right)

As the main source of capacitance in the *LC* representation of [130] is due to the gap between adjacent patches, then the effect of this parameter should be studied. Figure 5.7 on right shows plots of the reflection phase for three different gap widths. The height of the substrate is 1.6mm, Rogers RO3003. The size of the patch and via are fixed and as given earlier. Apparently increasing the gap width increases the resonant frequency, nevertheless for this scenario the slope of the reflection phase is similar for all three gap width cases, thus the inphase bandwidth is not significantly affected by the gap width of the EBG.

To obtain the reflection phase diagram, the reflected phase from the EBG screen is normalised with respect to the reflected phase of a PEC screen as follows

$$\phi = \phi^{EBG} - \phi^{PEC} + \pi. \tag{5.22}$$

To put the reflection phase properties in to context, consider figure 5.2 where the arbitrary surface is placed to occupy a space in the yz plane, if a wave is incident perpendicular to surface from the x direction, the surface impedance is defined as the ratio of the tangential electric field to the tangential magnetic field. A good electric conductor with high yet finite conductivity is considered as a low impedance inductive surface, where the ratio of the tangential electric field to the tangential magnetic field is small because the tangential electric field is negligible. In contrast in a high impedance surface the tangential electric field is high while the tangential magnetic field is negligible, thus becoming the equivalent of a magnetic conductor. Consequently for a wave with a normal incident from the x direction on the surface (yz), an incident forward running and a reflected wave are present. The reflection phase is the phase difference of the incident and reflected waves [130][124],

$$\Phi = Im\left\{ ln\left(\frac{E_{in}}{E_{ref}} \right) \right\}, \tag{5.23}$$

where the expression can be written in terms of the free space impedance η and the impedance of the surface,

$$\Phi = Im\left\{ ln\left(\frac{Z_s - \eta}{Z_s + \eta} \right) \right\}. \tag{5.24}$$

According to the effective medium model the surface impedance can be approximated by the impedance of a parallel LC resonant circuit, where C originates from the sheet capacitance and L from the sheet inductance [147],

$$Z_s = \frac{j\omega L}{1 - \omega^2 LC} \tag{5.25}$$

The surface impedance has a resonance at $\omega_0 = 1/\sqrt{LC}$. At resonance the impedance becomes very high. At lower frequencies the impedance gets smaller and inductive while at higher frequencies becomes smaller and capacitive.

At resonance the reflection phase is zero and the reflected waves are in phase with the incident. When the reflection phase lays inside $\pi/2$ to $-\pi/2$ the reflected waves are more in phase than out of phase, in this region the impedance of the surface is larger than the impedance of free space, also for mushroom periodic lattices it is

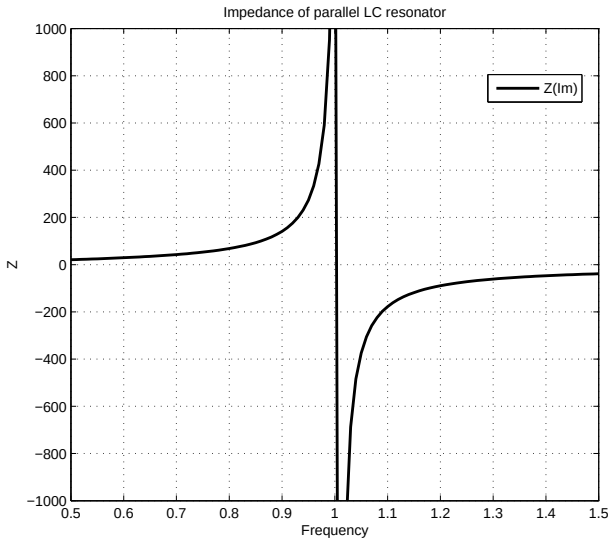

Figure 5.8: Typical impedance response of a parallel LC resonator

in this region that the surface wave stop band occurs. At frequencies considerably away either side from resonance the reflected waves are out of phase with the incident wave.

For the effective medium model the bandwidth where the reflection phase is between $\pi/2$ and $-\pi/2$ where image currents are rather inphase than out of phase is [148],

$$BW = \frac{1}{Q} = \frac{\sqrt{\frac{L}{C}}}{\sqrt{\frac{\mu_0}{\epsilon_0}}} \tag{5.26}$$

Bandwidth varies inversely with the quality factor Q, substrate parameters such as ϵ_r and h can be varied to obtain different Q and thus affect the bandwidth [123].

5.4 Patch antenna layout

The array is fabricated on 3.2 mm thick Rogers RO3003 substrate with dielectric constant of 3.04, element separation is $0.32\lambda_0$ from edge to edge and $0.67\lambda_0$ from antennas centre. The overall dimension of the structure is 160 mm x 80 mm x 3.2 mm. Simulation was performed on CST Microwave Studio, where a transient solver with hexahedral meshing employing the finite integration technique was used.

On the left of fig. 5.7 we can see clearly the three periods of the mushroom elements,

at the centre of each a via exists that shorts them to ground. On the right of fig. 5.1, relative size and placement of superstrates is provided, the smaller has dimensions of 27.5 x 65 x 6.4 mm while the larger has dimensions of 57.5 x 65 x 6.4 mm both are consisted of 3.2 mm Tufnol merged with 3.2 mm ordinary plastic. The patch antennas have dimensions of 40 x 32 mm with an inset of 12 x 10.2 mm and a feed line of width 6 mm. The position of dielectric materials above the radiating elements can provide means to modify radiated fields [149][150]. Also impedance matching conditions are modified, in a sense allowing for bandwidth improvement, coupling reduction and shifting of the operating band, some due to the changes in the effective dielectric constant, the losses and Q factor [151]

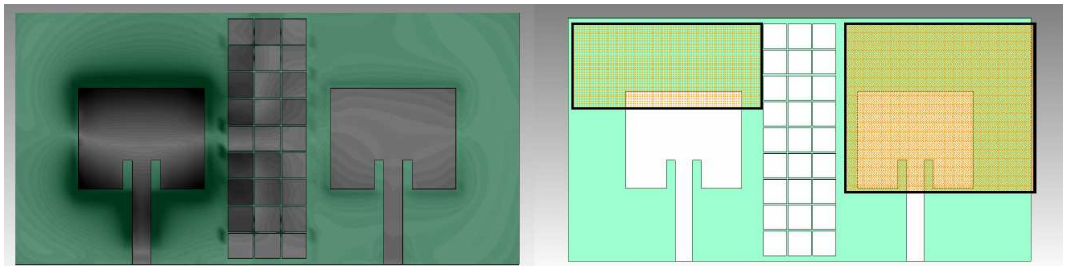

Figure 5.9: Array layout(left) and layout with superstrates(right)

For the case of uneven, asymmetrical and partially covered printed antennas it appears that there exist no model or considerable study present to date. Alexopoulos and Jackson [142] derived the optimum parameters for a given set of substrate and superstate. They show that for elimination of surface waves the critical superstrate thickness t_c can be estimated from

$$\cot\left[2\pi\left(\frac{n_2 t_c}{\lambda_0}\right)\sqrt{1-\left(\frac{n_1}{n_2}\right)^2}\right]=\frac{\sqrt{n_2^2-n_1^2}}{\varepsilon_2\sqrt{n_1^2-1}}, \tag{5.27}$$

where $n_1=\sqrt{\varepsilon_1\mu_1}$, $n_2=\sqrt{\varepsilon_2\mu_2}$, defined from the constitutive parameters of the two media, while at the same time the maximum allowable substrate thickness B_{max} can be obtained from

$$\frac{1}{\sqrt{n_2^2-1}}\tan^{-1}\frac{\mu_1\sqrt{n_1^2-1}}{\mu_2\sqrt{n_2^2-1}}\cot\left[2\pi\frac{n_1 B_{max}}{\lambda_0}\sqrt{1-\frac{1}{n_1^2}}\right]=\frac{1}{\sqrt{n_2^2-n_1^2}}\tan^{-1}\left[\frac{\varepsilon_2\sqrt{n_1^2-1}}{\sqrt{n_2^2-n_1^2}}\right]. \tag{5.28}$$

Interestingly enough the authors also derive equations and show that with appropri-

ate selection of superstrate and substrate parameters the radiation pattern in the H or E plane can be made nearly omnidirectional, this is possible by switching on the TE or TM modes. Considering the H plane the values of superstrate and substrate thickness can be estimated from

$$\frac{n_2 t}{\lambda_0} = \frac{n_2}{2\pi\sqrt{n_2^2-1}} \tan^{-1}\left[\frac{\frac{\mu_2}{\mu_1}\sqrt{n_1^2-1}}{\sqrt{n_2^2-1}\tan\left[2\pi\frac{n_1 B}{\lambda_0}\sqrt{\frac{n_1^2-1}{n_1}}\right]}\right], \tag{5.29}$$

Similarly the parameters that produce near omnidirectionality in the E plane can be obtained from

$$\frac{\sqrt{\varepsilon_2}t}{\lambda_0} = \frac{\sqrt{\varepsilon_2}}{2\pi\sqrt{\varepsilon_2-1}} \tan^{-1}\left[-\frac{\varepsilon_2}{\varepsilon_1}\sqrt{\frac{\varepsilon_1-1}{\varepsilon_2-1}}\tan\left[\pi\frac{\sqrt{\varepsilon_1}B}{\lambda_0}\sqrt{\frac{\varepsilon_1}{\varepsilon_1-1}}\right]\right]. \tag{5.30}$$

5.5 Measured results

The array was fabricated on two joined Rogers RO3003 substrates to achieve the 3.2mm thickness. The size position and material types that were used as superstrates was due to experimentation and not by using the analytical approach cited, this is mainly due to the asymmetrical offset shape of the superstrate used to cover the antennas and the EBG. The main focus was to establish the fact of surface wave suppression due to superstrate, thus coupling reduction, pattern distortion due to superstrate, and behaviour of resonant frequency of the EBG due to superstrate. The array was measured using a four port Agilent network analyser. Figure 5.10 shows measured S parameters. On the left of figure the measured parameters are without the superstrates applied. A stop band appears at the region from 4.8GHz–5.4GH, this is as expected and shown by simulations in figure 5.6 where the reflection phase suggests that the surface is resonating at 4.9GHz. On the right of figure 5.10 the measured S parameters are shown for the case of the superstrates applied in position as discussed in section 5.1. Each patch now operates with different effective dielectric constants due to the dissimilar dielectric covers, this is manifested in the shift of the return loss resonance positions, however what is important is that having kept all other parameters fixed, comparing the S parameter curves with and without the superstrates, it is clear the there is an increase in bandwidth defined at -10dB

and there is a distinct fade attenuating the transmission coefficient heavily.

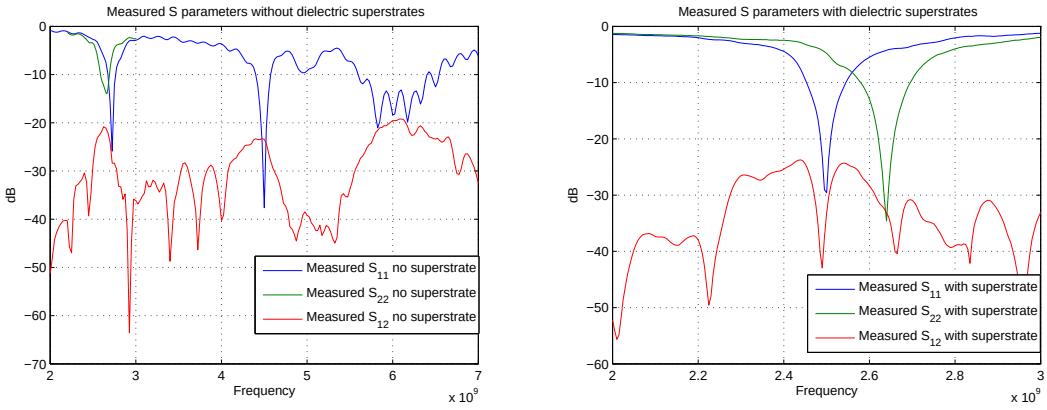

Figure 5.10: Measured S parameters with and without the dielectric superstrtes

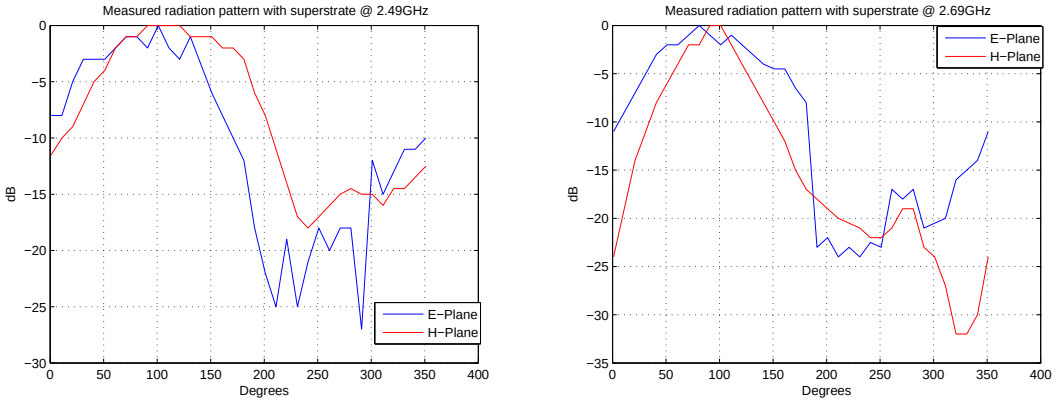

Figure 5.11: Measured radiation patterns of each patch wifht superstrates, E and H Planes.

The radiation patterns were measured in an anechoic chamber in ten degree increments. While measuring the radiation pattern of one element the other was terminated in a 50Ω load. The measured 3 dB elevation beamwidth for element with large superstrate is 118 degrees while azimuth is 131. For the patch with the small dielectric above it; elevation 3 dB beamwidth is 100 degrees and in azimuth is 56. The results are interesting, as keeping one plane wide while reducing the beam width in the other can reduce the mutual coupling by reducing the amount of power radiated from one antenna towards the other and in case of diversity systems provide means to improve the orthogonallity of the angular radiation functions, this combined with the analysis of [142] which may ensure high efficiency and gain are appearing as promising approaches for improving diversity.

5.5.1 Simple example of potential application

Finally a dual band microstrip patch antenna array is presented as an example of a potential candidate for application of the dual band coupling suppression and radiation pattern modification methods discussed in this chapter. The superstrates and EBG lattice is not applied for the simulation results that follow, this is left as a future work. As we are interested in developing a radiator operating at two frequency bands we felt that we should experiment with the possibility of using aperture coupling to achieve this. This design uses a near resonant aperture at 5.2 GHz and a patch with dimensions that correspond to resonance of 2.4 GHz. Stacking of patches, as for example an addition of a patch that resonates at 5.3GHz or at 2.3GHz can introduce new resonances in the vicinity of the existing ones and thus allow for larger bandwidths to be achieved, also etching of slots can provide means for bandwidth improvent, however here no stacking or slots are applied. Duroid is used as substrate material. When a resonant aperture is used its size can not be varied in order to control the coupling. This approach provides strong coupling thus high input impedance which must be reduced to impedance match the antenna to the feed line. One way to do this is to use dual offset feed lines each of characteristic impedance of 100Ω. The lines are joined with a reactive power combiner. Other methods exist but this one is attractive because due to its symmetric structure it does not contribute to cross polarization.

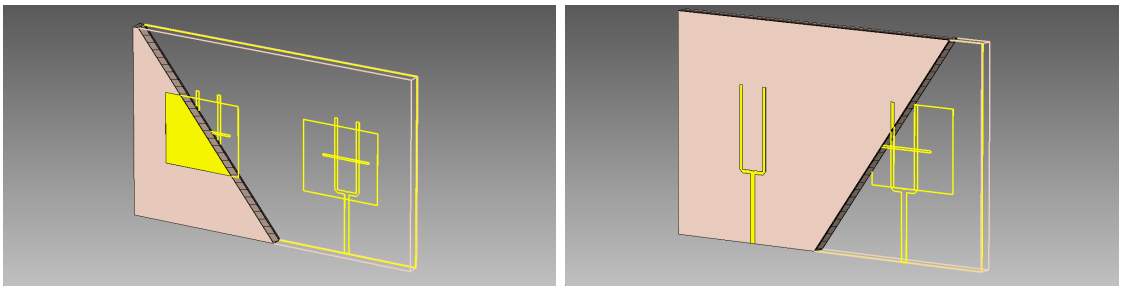

Figure 5.12: Dual band aperture coupled microstrip patch array with reactive combiner as a feed line. Front and back view.

The element separation of the array is $0.37\lambda_0$ at 2.4GHz, from edge to edge. The arrangement of the patches implies H plane coupling, which for probe fed antennas produces lower coupling levels however for an antenna that is fed with an aperture the currents on the common ground plane originating from the resonant slots can introduce higher levels of mutual coupling, therefore suppression may be highly

desirable. In addition usually aperture fed patch antennas have relatively thick substrates in order to increase the bandwidth, for the presented array the antenna substrate thickness is 4.8mm, while a second substrate that holds the feed line is of 0.8mm thickness. The feed line consists of a reactive combiner and two offset open stubs that couple to the aperture and is located at the bottom side of the structure. The dimensions of the structure are $140 \times 88 \times 5.65$, the patch length is 16.5mm and the width is 18.5mm, finally the aperture is 11.5mm in length and 0.8mm wide.
Many models are available for the study of patch antennas with different levels of accuracy. These include the transmission line model, the cavity model and full wave spectral domain method. A detailed analysis based on the transmission line and cavity model for aperture and slot antennas can be found in [123]. Figure 5.13 illustrates the transmission line representation of the aperture coupled antenna, design equations can be found in [123], the topology discussed in this section requires a modification of the simple transmission line model shown and presented in [123] because the feed line does not couple at the centre of the aperture but rather at two offset locations toward the edges of the aperture, this will have an effect on the impedance of the slot, thus offset feeding of slot must be included in the standard transmission line model in order to be accurate.

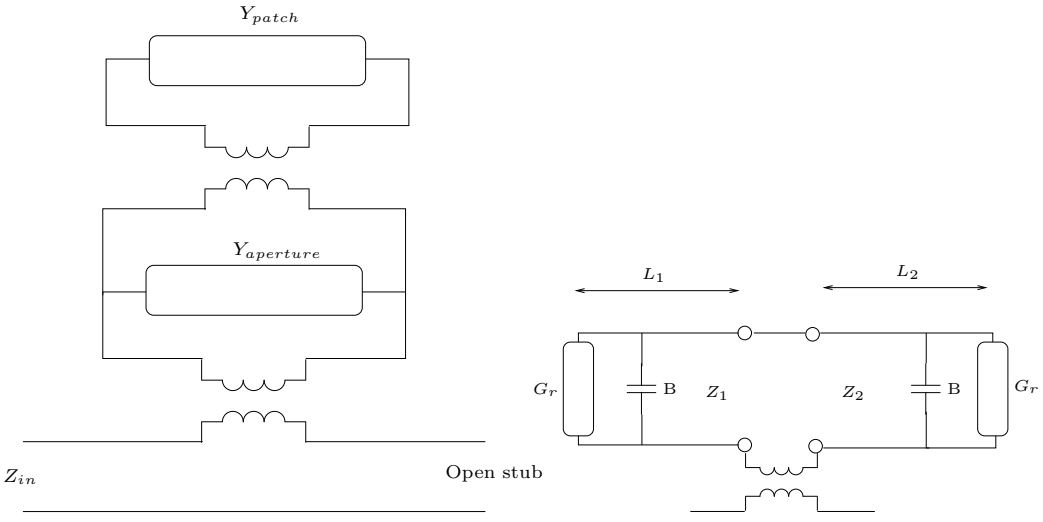

Figure 5.13: On left a simple representation of the feed line, aperture and patch structure, on the right transmission line representation of the patch fed by an aperture

The simulated S parameters provided in figure 5.14 show that indeed two resonances occur, the impedance bandwidth at the lower band is 132MHz while at the higher

band is 170MHz, both are enough to cover WLAN networks and higher bandwidth are possible with further optimization of the effective parameters of the array. At the lower band S_{12} is -18.5dB while at the higher S_{12} is -17dB.

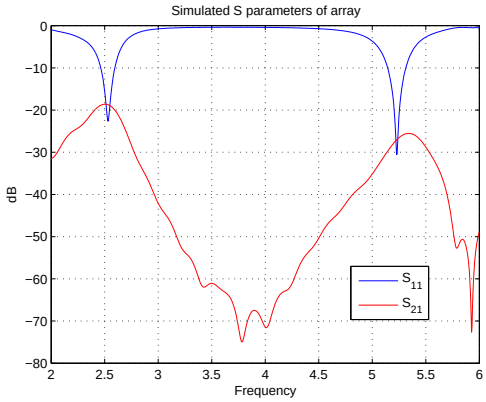

Figure 5.14: Dual band aperture coupled microstrip patch array simulated S parameters

The radiation pattern at 2.5GHz resemble and compares fairly to a line or probe fed patch antenna. In the H plane the maximum directivity is 7.4dBi with a side lobe level of -16.7dBi and a 3dB beamwidth of 88.7 degrees. At the same frequency the E plane has a maximum simulated directivity of 7dBi with a side lobe level of -16.4dB and a 3dB beamwidth of 78.8 degrees. The back radiation levels are comparable to finite ground plane size patch arrays as there is always back radiation from the boundaries of the structure. At 5.2GHz the E plane has a maximum simulated directivity of 5.7dBi with a side lobe level of -5dB and 3dB beamwidth of 37.2 degrees. In the H plane directivity is at 5.7dBi while the side lobe level is 6dB and the 3dB beamwidth is 60.6 degrees. Evidently at the higher operating band there is considerable radiation at the back side of the antenna coming from the aperture and the feed lines. The radiation patterns for both frequencies and planes are plotted in Cartesian form in figure 5.15

As future work a combination of methods presented in the thesis may be applied to the aperture coupled array. For example an FSS screen can be applied at the back side of the array designed to operate at 5.2GHz which is the resonant frequency of the aperture that causes the high back radiation and thus eliminate this issue without increasing the profile considerably. Additionally a mushroom EBG lattice can be applied between the elements to reduce surface waves at one of the bands and thus increase efficiency, while a superstrate can be applied to eliminate surface

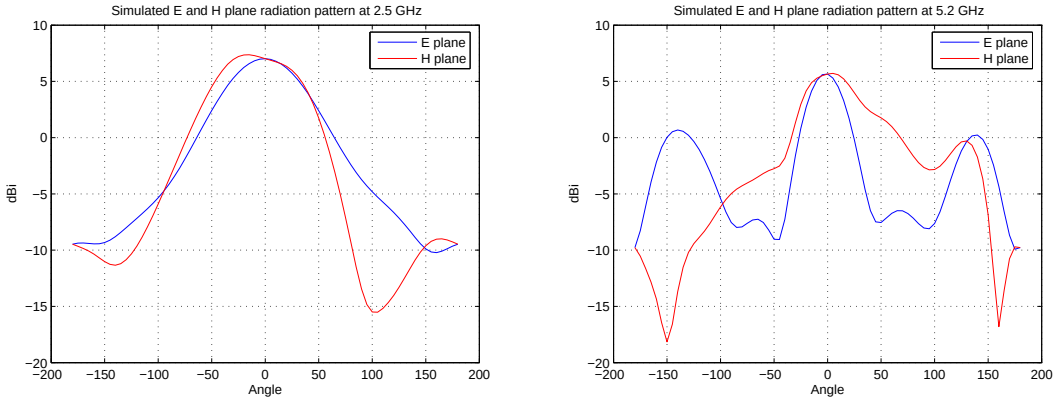

Figure 5.15: Simulated radiation pattern for the E and H planes at both operating frequencies

waves at the other operating band and thus increase efficiency and perhaps modify the radiation patterns of the elements. Of course stacking of patches can also be applied to improve the radiation at 5.2GHz with the superstrate being above of the top patch.

5.6 Conclusion

This chapter presented the combinations of two very efficient techniques to improve antenna array performance. The first method is to employ superstrates, if these are chosen with care then total elimination of surface waves is possible, in addition gain and efficiency can be enhanced, and the radiation in the E and H planes modified, of course not all these characteristics can be optimum at the same time. The second method is the use of EBG to suppress the surface waves within a predetermined stop band region.

The aim was to introduce one more way to reduce coupling and surface waves at two bands. The microstrip array fabricated and measured can achieve this with the dielectric cover at 2.4GHz and with a mushroom type EBG at 5GHz. The application of the dielectric cover showed in measurement that deep attenuation of the transmission coefficient is possible with simultaneous increase of impedance bandwidth. The H plane beamwidth of one of the patch antennas is made now to have roughly half the beamwidth of the other indicating that shaping of the patterns is feasible with ease.

The mushroom EBG creates a stop band cantered at 5.1GHz and is relatively wide

band as is expected for this type of periodic element. The application of the EBG near the edges of the two patch antennas has increased their resonating frequency, this may be due to the extra capacitance created between the EBG and the antennas, however this may not pose a significant issue and can be factored in the design process. The placement of the superstrates did at some level account for the increase in resonant frequency by lowering it, thus the EBG and the selected superstrate seem to have a complementary effect on the resonance of the patch antennas. Finally an example of a potential application of the methods presented in this chapter was discussed, this is left as a future work.

Chapter 6

Conclusions & Future Work

"No man ever steps in the same river twice,
for it is not the same river,
and he is not the same man"
Heraclitus

6.1 Conclusion

The multiple input multiple output signalling approach is already employed in WLAN, being at the final draft at the present day, and is planed to be used in platforms such as WiMax and 4G, among others. Such systems are important as these platforms perhaps own the biggest share of consumer population. It widely accepted now that conventional systems be it SISO or simple diversity systems can not support or accommodate the volume and flow of information that is demanded presently. MIMO systems can dramatically increase the capacity–throughput of a link with no considerable increase on transmit power or spectrum use. On the signal processing level spatial multiplexing and space time block codes are used to exploit the multipath propagation environment. Space time block codes employ diversity measures across space and time implying a reduction on the data rate, while spatial multiplexing offers higher data rates compared to space time codes as no code diversity measures are used, data are simply randomized and transmitted. At this stage there is plenty of room to argue as which is the best strategy to use, for example would a MIMO system with smart antennas and the possibility of beamforming be more efficient than a uniform power fixed beam spatially multiplexing system, the answer probably lies with the choice of the environment and application to be used.

A plethora of successful and popular commercial communication protocols exist in present days, therefore when one sets to design and develop antenna systems immediately a decision of the operational protocol must be made or assigned. The work undertaken here is based for communications within the ISM bands and more specifically the IEEE 802.11n protocol was the driving force that dictated design requirements. The dual band criterion is desired for interoperability capabilities within all bands of the WLAN protocol.

In this thesis first an overview of the potential platforms that MIMO is planned to be used in the near future and the actual need for doing so was presented. Given the astonishing properties of this new technology initially research was mainly focused on signal processing, however recently and increasingly the RF front end, and wave propagation get the attention they deserve. At chapter two MIMO systems and diversity are discussed, from a theoretical point of view. The basic principles of a MIMO systems are outlined indicating that diversity is the most important metric for a successful system. Therefore diversity measures are then examined. Out of all the diversity measures, antenna diversity is of interest for the work presented here. Antenna diversity consists of spatial, pattern and polarization diversity. Although guidelines exist for optimum diversity, it is paramount in an implementation that the propagation characteristics be integrated in evaluating and optimizing diversity. Having established and identified the requirements for a diversity system, in chapter three we propose a novel compact antenna array. Initially a single dual band printed inverted F stacked monopole antenna is parametrically studied and consequently used to form the compact array. The single elements differ from similar types published by not having a via that shorts the impedance line to the ground, usually the via is applied to cancel the capacitance created by the parallel section of the arms with the ground plane, the element presented here achieves impedance matching by controlling the length of an open line. The motivation of this approach was that most mobile terminals have limited real estate to accommodate for the antennas, thus the two PIFA antennas were placed in very close proximity, this however creates the problem of mutual coupling with the further consequences that this implies, therefore a novel technique to suppress the coupling at two bands is proposed. A set of parasitically coupled printed grid lines appears to cancel the RF currents at both operating bands providing a considerable decrease of mutual cou-

pling. The coupling reduction of the measured prototype was 9dB when compared to the simulated array stand alone. Reducing mutual coupling especially when it has high values is essential as otherwise can be detrimental to the radiation efficiency of the antenna furthermore high correlation of signals may hinder the benefits of using multiple antennas.

The PIFA array concept was aimed at the mobile terminal, chapter four investigates an arrangement perhaps better suited for an access point in a pico–micro cell scenario. Achieving relatively wide dual band impedance bandwidth with reasonable radiation at both bands can be a considerable challenge. For this study a printed dipole was selected as the radiating element, to obtain good matching at two bands a printed balun with tapered impedance at the input is applied as the feed to the dipole. The impedance characteristics of the dipole are exciting dual and wide band return loss response is measured. The radiation pattern at the lower band is identical to the theoretical one of a dipole element while its directivity can be controlled by modifying the length of the ground plane that supports the microstrip feed line, making it from omnidirectional to endfire directional, however at the higher operating band radiation resemble that of a marginally larger than a full wave dipole with a part missing due to the radiation of the wide stub of the printed balun. Interestingly enough the upper resonant frequency and bandwidth can be controlled with ease by the open stub of the balun. Having measured a prototype then a dual and wide band printed dipole array is proposed. The dipoles are virtually on zero horizontal separation yet the mutual coupling is below 20dB, this can mainly be attributed to the geometry, the type of feed and the separate grounds. The measured prototype array provides a band width of 699MHz and 1.483GHz for the low and high operating bands respectively, radiation metrics are as discussed for the single element. A dipole with no modifications has a low gain and in the case of multiband operation the higher bands can suffer from unattractive radiation patterns. For this reason base stations and other conventional systems apply PEC reflectors to create sectors or increase the gain, nevertheless a PEC reflector requires large separation from the antenna to maintain radiation efficiency. To solve the problem of large separation and produce a high performance dipole array it is suggested through simulated results that an AMC could be placed at 0.03λ away from the antenna. The AMC screen is composed of dipole resonating elements and is polarization sensitive, dual

band AMC characteristics are established by building a unit cell that consists of two dipoles one for each desired frequency. A main issue with the selected type of unit cell is the relatively low inphase bandwidth, nevertheless ease of fabrication with very good tolerances, low profile and easy dual band response make this unit cell attractive.

Finally an approach to combat coupling and surface waves at two operating bands is briefly presented. Dielectric covers are documented to achieve total elimination of surface waves in addition to improving the gain and efficiency. In chapter six initial experiments with variable offset dielectric covers are presented. The covers are applied on printed patch antennas and appear to introduce a deep fade in the transmission coefficient, increase the bandwidth and shift the resonant frequency to a lower value. Due to the asymmetrical size of the covers the shift in frequency of the two antennas is not identical and the H plane radiation of one is considerably modified with respect to the other. On the same array substrate, three periods of mushroom type EBG are implemented to operate at a higher frequency. The EBG appear to introduce a stop band were surface waves are suppressed, resulting in reduction of the transmission coefficient. Therefore it becomes apparent that in a dual band system one can position the elements such that, in one band eliminate surface waves with a dielectric cover which can also reduce the radiation of one element into another, and in the second band the surface waves can be suppresses by a EBG lattice. An example of a potential application of the superstrate EBG antenna enhancement method is proposed, however this left as future work.

6.2 Future work

Every solution, every idea and every new piece of information most certainly creates multiples of new questions and challenges to the inquisitive mind. The limitations of the work presented suggest that there are areas and topics that have not been explored and the ones that were explored could possibly be further optimised, these options may be important and interesting, leading to possibilities of further work to be carried out on

In relation to chapter 3

- For the case of the stacked monopole inverted F antenna the ground plane operates as the other half of the antenna thus a detailed study of the optimum distance and position of each of the arms to the ground plane is essential as this may further improve the radiation pattern of the element. Also perhaps shaping of key elements of the ground plane can aid the radiation performance, for example observing the current distributions on the ground one can determine areas that are responsible to reinforcement or cancellation of fields and thus try to modify the distributions.

- Apply the concept to other types of antennas, it would interesting to apply the parasitically coupled lines to a dipole array that in a sense resembles the operational concept of the inverted F antennas presented here, also there is of course the possibility to investigate the application to a microstrip patch array.

- Perform a field measurement campaign for the compact PIFA array, thus assess the diversity in a real world environment, for example assess the performance in indoor and outdoor propagation environments.

- The physical length of the lines that are used to suppress the coupling will influence the bandwidth of the stop band, it could be a fair assumption that perhaps a binomial distribution of line length can improve the width of the stop band, a highly desirable issue because ideally coupling should be below 20dB for the operational impedance bandwidth.

In relation to chapter 4

- When the FSS surface is applied as an AMC to enhance the radiation performance of the antenna while maintaining it's low profile, the size and periodicity of the frequency selective surface will be of high importance to all antenna metrics. Therefore an investigation on the effect of FSS screen size and the optimum number of cells in each direction that provides good antenna characteristics while at the same time maintains small dimensions is essential.

- Increase the bandwidth of the useful reflection phase at both bands by either modifying the dipoles or by inventing new types of resonators for the unit cell. For example, in dipole antennas bow–tie shape of arms is well known to have superior and much wider impedance bandwidth than the conventional rectangular strip type, by analogy, it may be possible to construct a unit cell with two bow–tie shaped resonators and examine if any gain in reflection phase bandwidth is possible.

- Keeping the same feeding structure and topology of the printed dipole array, a different shape of the arms may be beneficial, as already mentioned bow–tie shape is widely used and has many advantages, also tilting of the angle of the dipole arms has been reported to modify the radiation pattern.

- In a MIMO system each antenna is excited by either a totally random signal in phase and amplitude in case of spatial multiplexing or by a pre determined signal in amplitude and phase when space time block codes are used were the coding diversity measures here allow to know the amplitude and phase of the elements in respect to each other. Apparently there exists no considerable study on the effects of the combined radiation pattern of antennas under the excitation conditions that are employed in MIMO communications systems.

In relation to chapter 6

- Suppressing surface waves at two bands within a fairly low complexity structure requires innovative solutions, especially if at the same time the measures taken can increase the bandwidth and improve efficiency and radiation patterns of the antennas involved, in chapter six the proof of concept that the combination of two already available techniques can be very attractive was demonstrated. However the concept needs to be applied, prototyped and measured in an actual dual band array. A design of a dual band patch array is completed and briefly presented, the next step is to integrate the supestrate and the EBG.

- Cited work addressed the issue of covering the antennas in an even and symmetric way, yet interesting properties and results may arise if one finds the

optimum thickness and dielectric constant of superstrates for cases of loading the antennas in an irregular antisymmetric fashion.

- Investigate the effects of dielectric covers on the bandwidth and resonant frequency of mushroom type EBG lattices.

Bibliography

[1] S. Generics, "Understanding the scope for a power increase for wireless broadband access at 2.4ghz & 5.xghz final report: V1.0," Scientific Generics Limited, Tech. Rep. Ofcom Reference C31400/013/1510, May 2006.

[2] E. Perahia and R. Stacey, *Next GenerationWireless LANs*. Cambrdge University Press, 2008.

[3] C. Balanis, *Advanced Engineering Electromagnetics*. Wiley & Sons, 1989.

[4] F. Perez-Fontan and P. M. Espineira, *Modeling the wireless propagation channel, a simulation approach with MATLAB*. Wiley, 2008.

[5] C. C. Chiau, "Study of the diversity antenna array for the mimo wireless communication systems," Ph.D. dissertation, Queen Mary, University of London, United Kingdom, 2006.

[6] J. Erceg *et al.*, "Tgn channel models," IEEE, Piscataway, NJ, Tech. Rep. IEEE 802.11-03/940r4.

[7] J. Ramsay, "Highlights of antenna history," *IEEE Antennas and Propagation society Newsletter*, vol. 23 Issue 6, Dec. 1981.

[8] J. L. Volakis, *Antenna Engineering Handbook*. New York, NY: McGraw Hill, 2007.

[9] P. K. Bondyopadhyay, "The first application of array antenna," in *Proc. IEEE International Conference on Phased Array Systems and Technology 2000*.

[10] J. G. Proakis and M. Salehi, *Communication Systems Engineering*. New Jersey, NJ: Prentice Hall, second edition, 2007.

[11] D. M. Pozar, *Microwave Engineering*. New Jersey, NJ: John Wiley & Sons, Inc, third edition, 2005.

[12] I. P. W. G. for Wireless Personal Area Networks (WPANs), "Multi-band ofdm physical layer proposal for ieee 802.15 task group 3a," IEEE, Piscataway, NJ, Tech. Rep. IEEE P802.15-03/268r2, Nov. 2003.

[13] J. H. Winters, "On the capacity of radio communication systems with diversity in a rayleigh fading environment," *IEEE J. Sel. Areas Commun.*, vol. SAC-5, no 5, Jun. 1987.

[14] G. J. Foschini and M. J. Gans, "On limits of wireless communications in a fading environment when using multiple antennas," *Wireless Personal Communications*, vol. 6, no 3.

[15] I. E. Telatar, "Capacity of multi antenna gaussian channels," *European Transactions on Telecommunications*, vol. 10, no 6, 1999.

[16] G. J. Foschini, "Layered space time architecture for wireless communication in a fading environment when using multiple antennas," *Bell Labs, Syst. Tech. J.*, vol. 1, 1996.

[17] P. W. Wolnainsky *et al.*, "V–blast: An architecture for achieving very high data rates over the rich scattering wireless channel," in *Proc. ISSSE–98*.

[18] G. J. Foschini *et al.*, "Simplified processing for high spectral efficiency wireless communications," *IEEE J. Sel. Areas Commun.*, vol. 16 no 8, Oct. 1998.

[19] S. M. Alamouti, "A simple transmit diversity technique for wireless communications," *IEEE J. Sel. Areas Commun.*, vol. 17 no 11, Nov. 1999.

[20] A. R. C. V. Tarokh, N. Seshadri, "Space time codes for high data rate communication: Performance criteria and code construction," *IEEE Trans. Inf. Theory*, vol. 44 no 2, Mar. 1998.

[21] H. Nyquist, "Certain topics in telegraph transmission theory," *Transactions of the A.I.E.E*, Feb. 1928.

[22] C. E. Shannon, "Communication in the presence of noise," *Proceedings of the IRE*, vol. 37 no 1, Jan. 1949.

[23] M. Schwartz, *Information, Transmission, Modulation and Noise.* McGraw Hill, Third Edition, 1980.

[24] R. V. Hartley, "Transmission of information," *Bell Labs, Syst. Tech. J.*, Jul. 1928.

[25] A. G. C. Berrou and P. Thitimajshima, "Near shannon limit error correcting coding and decoding: Turbo codes," in *Proc. IEEE ICC 93*, Geneva, Switzerland, May 1993.

[26] B. K. Khoo, "Coded modulation with itarative decoding and multicarrier modulation for wireless communications," Ph.D. dissertation, Univ. of Newcastle, Newcastle upon Tyne, UK, Sep. 2007. [Online]. Available: http://www.ncl.ac.uk/

[27] E. Perahia and S. Li, "p802.11n coexistence assurance document," IEEE, Tech. Rep. doc. IEEE 802.11-06/0338r4, 2006.

[28] M. Wennstrom, "On mimo systems and adaptive arrays for wireless communications," Ph.D. dissertation, Univ. of Uppsala, Sweden.

[29] F. de Flaviis *et al.*, *Multiantenna Systems for MIMO Communications.* Morgan & Claypool Publishers, 2008.

[30] R. Allan, "Application of fss structures to selectively control the propagation of signals into and out of buildings annex 2: Radio system issues," ERA Technology, Surrey,UK, Tech. Rep. ERA Report 2004-0072 A2, 2004.

[31] S. R. Saunders and A. A. Zavala, *Antennas and Propagation for Wireless Communication Systems.* Wiley and Sons, 2nd Ed, 2007.

[32] C. A. Balanis, *Antenna Theory analysis and design.* Wiley, 1997.

[33] K. Fujimoto and J. James, *Mobile antenna systems handbook.* Artech House, 2nd Ed, 2001.

[34] Antenova, "Antenna designs for mimo," Antenova, Queen Mary university London, Tech. Rep.

[35] M. Jensen and J. W. Wallace, "A review of antennas and propagation for mimo wireless communications," *IEEE Trans. Antennas Propag.*, vol. 52 no11, Nov. 2004.

[36] M. Jankiraman, *Space-time codes and MIMO systems.* Norwood, MA: Artech House, 2004.

[37] R. U. Nabar *et al.*, "Performance of multiantenna signaling techniques in the presence of polarization diversity," *IEEE Trans. Signal Process.*, vol. 50 no10, Oct. 2002.

[38] P. Soma *et al.*, "Analysis and modeling of multiple-input multiple output (mimo) radio channel based on outdoor measurements conducted at 2.5ghz for fixed bwa applications," in *Proc. IEEE ICC conf.*, New York, 2002.

[39] B. Vucetic and J. Yuan, *Space-Time Coding.* Wiley, 2003.

[40] D. S. Shium *et al.*, "Fading correlation and its effect on the capacity of multiantenna systems," *IEEE Trans. Commun.*, vol. 48 No 3, Mar. 2000.

[41] S. Wang *et al.*, "Time-varying mimo channels: Parametric statistical modeling and experimental results," *IEEE Trans. Veh. Technol.*, vol. 56 no4, 2007.

[42] C. Oestges, V. Erceg, and A. Paulraj, "A physical scattering model for mimo macrocellular broadband wireless channels," *IEEE J. Sel. Areas Commun.*, vol. 21 no5, 2003.

[43] G. Turin *et al.*, "A statistical model of urban mutlipath propagation," *IEEE Trans. Veh. Technol.*, vol. VT-21, Feb. 1972.

[44] S. Salous and N. Ravazi-Ghods, "Semi-sequencial mimo channel measurements in indoor environments," EURO-COST, Gothenburg Sweeden, Tech. Rep. COST 273 TD(04)079, 2004.

[45] C. Oestges and B. Clerckx, *MIMO wireless communications, from real world propagation to space time code design.* AP.

[46] R. Vaughan and J. B. Andersen, "Antenna diversity in mobile communications," *IEEE Trans. Veh. Technol.*, vol. VT-36 no4, Nov. 1987.

[47] M. K. Ozdemir, E. Avras, and H. Arslan, "Dynamics of spatial correlation and implications on mimo systems," *IEEE Commun. Mag.*, vol. 42 issue 6, 2004.

[48] M. Karaboikis *et al.*, "Three-brach antenna diversity systems on wireless devices using various printed monopoles," in *Proc. Electromagnetic Compatibility, 2003. EMC '03. 2003 IEEE International Symposium on*, Istanbul, May 2003.

[49] R. G. Vaughan, "Pattern translation and rotation in uncorrelated source distributions for multiple beam antenna design," *IEEE Trans. Antennas Propag.*, vol. 46 no7, 1998.

[50] K. Yu *et al.*, "Modeling of wide-band mimo radio channels based on nlos indoor measurements," *IEEE Trans. Veh. Technol.*, vol. 53 no3, May 2004.

[51] J. P. Kermoal *et al.*, "A stochastic mimo radio channel model with experimental validation," *IEEE Electron Device Lett.*, vol. 20 no 6.

[52] J. W. Wallace and M. J. Jensen, "Power and complex envelope correlation for modeling measured indoor mimo channels a beamforming evaluation," in *Proc. Vehicular Technology Conference, 2003. VTC 2003-Fall. 2003 IEEE 58th*, Oct. 2003.

[53] C. Oestges, "Validity of the kronecker model for mimo correlated channels," in *Proc. Vehicular Technology Conference, 2006. VTC 2006-Spring. IEEE 63rd*, Melbourne, Vic, May 2006.

[54] A. A. Saleh and R. A. Valenzuela, "A statistical model for idoor multipatch propagation," *IEEE J. Sel. Areas Commun.*, vol. SAC -5 no2, Feb. 1897.

[55] Q. H. Spencer *et al.*, "Modeling the statistical time and angle of arrival characteristics of an indoor multipath channel," *IEEE J. Sel. Areas Commun.*, vol. 18 no3, 2000.

[56] J. W. Wallace and M. J. Jensen, "Statistical characteristics of measured mimo wireless channel data and comparison to conventional models," in *Proc. VVehicular Technology Conference, 2001. VTC 2001 Fall. IEEE VTS 54th*, Atlantic City, NJ, Aug. 2002.

[57] ——, "Modeling the indoor mimo wireless channel," *IEEE Trans. Antennas Propag.*, vol. 50 no5, May 2002.

[58] Weichselberger *et al.*, "A stochastic mimo channel model with joint correlation at both ends," *IEEE Trans. Wireless Commun.*, vol. 20 no 6.

[59] H. Ozcelik, N. Czink, and E. Bonek, "What makes a good mimo channel model?" in *Vehicular Technology Conference, 2005. VTC 2005-Spring. 2005 IEEE 61st*, Dec. 2005.

[60] R. Janaswamy, *Radiowave Propagation and smart antennas for wireless communications.* Kluwer Academic Publishers, 2000.

[61] L. C. Godara, *Handbook of antennas in wireless communications.* CRC, 2002.

[62] A. B. Gershman and N. D. Sidiropoulos, *Space-Time processing for MIMO communications.* Wiley, 2005.

[63] T. Taga, "Analysis for mean effective gain of mobile antennas in land mobile radio environments," *IEEE Trans. Veh. Technol.*, vol. 39 no2, May 1990.

[64] R. Vaughan, J. B. Andersen, and M. H. Langhorn, "Circular array of outward sloping monopoles for vehicular diversity antennas," *IEEE Trans. Antennas Propag.*, vol. 36 no10, Oct. 1988.

[65] B. T. Quist and M. J. Jensen, "Optimal antenna pattern design for mimo systems."

[66] M. J. Jensen and J. W. Wallace, "Antenna-independent capacity bound of electromagnetic channels," in *Proc. Antennas and Propagation Society International Symposium, 2005 IEEE*, 2005.

[67] ——, "Electromagnetic considerations for communicating on correlated mimo channels with covariance information," *IEEE Trans. Wireless Commun.*, vol. 7 no2, Feb. 2008.

[68] ——, "Capacity of the continuous-space electromagnetic channel," *IEEE Trans. Antennas Propag.*, vol. 56 no2, Feb. 2008.

[69] A. Forenza and R. W. Heath, "Benefit of pattern diversity via two-element array of circular patch antennas in indoor clustered mimo channels," *IEEE Trans. Commun.*, vol. 54 no5, May 2006.

[70] B. Wang and A. G. Burr, "Effect of element radiation patterns on the capacity of mimo system," in *Proc. IEEE International Symposium on Microwave, Antenna, Propagation and EMC Technologies for Wireless Communications.*

[71] L. Dong, H. Ling, and R. W. Heath, "Multiple-input multiple-output wireless communication systems using antenna pattern diversity," in *Proc. Global Telecommunications Conference, 2002. GLOBECOM '02. IEEE*, Nov. 2002.

[72] P. L. Perini and C. L. Holloway, "Angle and space diversity comparisons in different mobile radio environments," *IEEE Trans. Antennas Propag.*, vol. 46 no6, 1998.

[73] C. Waldschmidt and W. Wiesbeck, "Compact wide-band multimode antennas for mimo and diversity," *IEEE Trans. Antennas Propag.*, vol. 52 no8, Aug. 2004.

[74] R. Vaughan, "Switched parasitic elements for antenna diversity," *IEEE Trans. Antennas Propag.*, vol. 47 no2, Feb. 1999.

[75] W. C. Lee and Y. S. Yeh, "Polarization diversity system for mobile radio," *IEEE Trans. Commun.*, vol. com-20 no5, Oct. 1972.

[76] T. T. Shigeru Kozon and and M. Sakamoto, "Base station polarization diversity reception for mobile radio," *IEEE Trans. Veh. Technol.*, vol. VT-33 no4, Nov. 1984.

[77] R. Vaughan, "Polarization diversity in mobile communications," *IEEE Trans. Veh. Technol.*, vol. 39 no3, Aug. 1990.

[78] P. C. Eggers, J. Toftgard, and A. M. Oprea, "Antenna systems for base station diversity in urban small and micro cells," *IEEE J. Sel. Areas Commun.*, vol. 11 no7, Sep. 1993.

[79] T. Svantesson, M. A. Jensen, and J. W. Wallace, "Analysis of electromagnetic field polarizations in multiantenna systems," *IEEE Trans. Wireless Commun.*, vol. 3 no2, 2004.

[80] T. C. Brown, "Antenna diversity for mobile terminals," Ph.D. dissertation, University of Surrey, Guildford, Surrey, 2002.

[81] C. Waldschmidt, C. Kuhnert, and W. Wiesbeck, "Compact mimo-arrays based on polarization-diversity."

[82] T. Taga and M. Aikawa, "A method of estimating antenna effective gain in land mobile communication environments."

[83] W. C.-Y. Lee, "Effects on correlation between two mobile radio base-station antennas," *IEEE Trans. Commun.*, vol. 21 no11, Nov. 1973.

[84] K. Pedersen, P. Mogensen, and B. Fleury, "Spatial channel characteristics in outdoor environments and their impact on bs antenna system performance," in *Proc. Vehicular Technology Conference 1998 VTC 98 48th IEEE*, Ottawa, Canada, May 1998.

[85] F. Adachi *et al.*, "Crosscorrelation between the envelopes of 900 mhz signals received at a mobile radio base station site," in *IEE Proc. -F Communications, Radar, and Signal Processing*, Oct. 1986, p. vol 133 issue 6.

[86] K. Kalliola *et al.*, "Angular power distribution and mean effective gain of mobile antenna in different propagation environments," *IEEE Trans. Veh. Technol.*, vol. 51 no5, Sep. 2002.

[87] A. Ando *et al.*, "Mean effective gain of mobile antennas in line-of-sight street microcells with low base station antennas," *IEEE Trans. Antennas Propag.*, vol. 56 no11, Nov. 2008.

[88] K. Ogawa *et al.*, "Channel capacity of a handset mimo antenna infuenced by the effects of 3d angular spectrum, polarization and operator," in *Proc. Antennas and Propagation Society International Symposium 2006, IEEE*, Albuquerque, NM, 2006.

[89] L. Shumacher, K. Pedersen, and P. Mogensen, "From antenna spacings to theoretical capacities-guidelines for simulating mimo systems," in *Proc. Personal indoor and mobile radio communications 2002. The 13th IEEE international symposium on*, 2002.

[90] J. Andersen and R. Vaughan, "Transmitting, receiving and scattering properties of antennas," *IEEE Antennas Propag. Mag.*, vol. 45 no4, 2003.

[91] O. Norklit, P. Teal, and R. Vaughan, "Measurement and evaluation of multi–antenna handsets in indoor mobile communication," *IEEE Trans. Antennas Propag.*, vol. 49 no3, 2001.

[92] W. Stutzman and G. Thiele, *Antenna theory and design.* Wiley, Second edition, 1998.

[93] B. Lindmark, "Capacity of a 2 x 2 mimo antenna system with mutual coupling losses," in *Proc. IEEE Antennas and Propagation Society International Symposium*, Monterey, CA, Jun. 2004.

[94] B. Lau, S. Ow, G. Kristensson, and A. Molisch, "Capacity analysis for compact mimo systems," in *Proc. Vehicular Technology Conference, 2005. VTC 2005-Spring. 2005 IEEE 61st Symposium on*, Jun. 2005.

[95] J. Wallace and M. Jensen, "Mutual coupling in mimo wireless systems: a rigorous network theory analysis," *IEEE Trans. Wireless Commun.*, vol. 3 no4, Jul. 2004.

[96] C. Waldschmidt, S. Schulteis, and W. Wiesbeck, "Complete rf system midel for analysis of compact mimo arrays," *IEEE Trans. Veh. Technol.*, vol. 53 no3, May 2004.

[97] J. Wallace and M. Jensen, "Termination–dependent diversity performance of coupled antennas: network theory analysis," *IEEE Trans. Antennas Propag.*, vol. 52 no1, Jan. 2004.

[98] M. Martnez-Vazquez, "ACE deliverable 2.2D1 report on the state of the art in small terminal antennas: Technologies, requirements and standards," ACE Antenna Centre of Excellence, Tech. Rep. FP6-IST 508009, Dec. 2004.

[99] T. Taga and K. Tsunekawa, "Performance analysis of a built-in planar inverted-f antenna for 800MHz band portable radio units," *IEEE J. Sel. Areas Commun.*, vol. 5 no5, 1987.

[100] L. Chu, "Physical limitations of omni-directional antennas," *Journal of Applied Physics*, vol. 19, 1948.

[101] J. McLean, "A re–examination of the fundamental limits on the radiation Q of electrically small antennas," *IEEE Trans. Antennas Propag.*, vol. 44, 1996.

[102] G. Thiele, P. Detweiler, and R. Penno, "On the lower bound of the radiation Q for electrically small antennas," *IEEE Trans. Antennas Propag.*, vol. 51, 2003.

[103] R. Rowell and R. Murch, "A compact PIFA suitable for dual–frequency 900/1800 MHz operation," *IEEE Trans. Antennas Propag.*, vol. 46, 1998.

[104] P. Ciais, R. Staraj, G. Kossiavas, and C. Luxey, "Design of an internal quad-band antenna for mobile phones," *IEEE Microw. Wireless Compon. Lett.*, vol. 14 issue 4, 2004.

[105] P. LeThuc, R. Staraj, and G. Kossiavas, "Dual wideband radiating element for mobile handsets," *Microwave and optical technology letters*, vol. 39 issue 4, 2003.

[106] H. Wang, "Input impedance–tuning slots of PIFA antennas," *Microwave and optical technology letters*, vol. 49 issue 6, Jun. 2007.

[107] Y. Wang, M. Lee, and S. Chung, "Two PIFA related miniaturized dual–band antennas," *IEEE Trans. Antennas Propag.*, vol. 55, 2007.

[108] C. Soras, M. Karaboikis, G. Tsachtsiris, and V. Makios, "Analysis and design of an inverted–F antenna printed on a PCMCIA card for the 2.4GHz ISM band," *IEEE Antennas Propag. Mag.*, vol. 44 no1, Feb. 2002.

[109] J. Flint, "Numerical analysis of detuning in printed inverted F antennas for bluetooth applications," in *Proc. Personal Mobile Communications Conference, 2003. 5th European (Conf. Publ. No. 492)*, 2003.

[110] L. Ukkonen, D. Engels, L. Sydanheimo, and M. Kivikoski, "Planar wire–type inverted–F RFID tag antenna mountable on metallic objects," in *Proc. Antennas and Propagation Society International Symposium, 2004 IEEE*, 2004.

[111] K.-L. Wong, *Planar antennas for wireless communications.* Wiley, 2003.

[112] G. Mavridis, E. Karapistoli, C. Christodoulou, and M. Chryssomallis, "Spatial diversity performance of printed dual band antennas for WLAN operations," in *Proc. Antennas and Propagation Society International Symposium, 2005 IEEE*, 2005.

[113] M. Manteghi and Y. Rahmat-Samii, "A novel miniaturized triband PIFA for MIMO applications," *Microwave and optical technology letters*, vol. 49 issue 3, 2007.

[114] T. Kokkinos, E. Liakou, and A. Feresidis, "Decoupling antenna elements of PIFA arrays on handheld devices," *Electron. Lett. IET*, vol. 44 no25, Dec. 2008.

[115] M. Huynh and W. Stutzman, "Ground plane effects on planar inverted–F antenna (PIFA)performance," *IET Proc.-Microw. Antennas Propag.*, vol. 150 no4, Aug. 2003.

[116] CST, "Advance topics, CST Microwave Studio," Computer Simulation Technology, Tech. Rep. User manual.

[117] M. Karaboikis, C. Soras, G. Tsachtsiris, and V. Makios, "Compact dual–printed inverted–F antenna diversity systems for portable wireless devices," *IEEE Antennas Wireless Propag. Lett.*, vol. 3, 2004.

[118] S. Tretyakov, *Analytical Aodeling in Applied Electromagnetics.* Norwood MA: Artech House, 2003.

[119] S. Best and J. Morrow, "On the significance of current vector alignment in establishing the resonant frequency of small space-filling wire antennas," *IEEE Antennas Wireless Propag. Lett.*, vol. 2, 2003.

[120] J. Yun and R. Vaughan, "Multiport impedance testing of antennas for mimo systems," in *Proc. Antennas and Propagation Society International Symposium, 2007 IEEE*, Honolulu, 2007.

[121] S. Blanch, J. Romeu, and I. Corbella, "Exact representation of antenna system diversity performance from input parameter description," *IET Electron Lett.*, vol. 39 issue 9, May 2003.

[122] K. Kiminami, A. Hirata, and T. Shiozawa, "Double-sided printed bow-tie antenna for uwb communications," *IEEE Antennas Wireless Propag. Lett.*, vol. 3, 2004.

[123] R. Garg, P. Bhartia, I. Bahl, and A. Ittipiboon, *Microstrip antenna design Handbook*. Norwood, MA: Artech House, 2001.

[124] N. Engetha and R. Ziolkowski, *Metamaterials, Physics and Engineering Explorations*. Wiley–Interscience, 2006.

[125] J. McLaughlin, "A wide band balun," *IRE Trans. On Microwave Theory and Techniques*, vol. MTT6, 1958.

[126] W. Roberts, "A new wide band balun," *Proc. IRE*, vol. 45, Dec. 1957.

[127] U. Revankar and Harishchandra, "Printed dipole radiating elements for broadband and wide scan angleactive phased array," in *Proc. Antennas and Propagation Society International Symposium, 2001 IEEE*, Boston, Aug. 2004.

[128] B. Munk, *Frequency Selective Surfaces, theory and design*. Wiley and Sons, 2000.

[129] ——, *Finite Antenna Arrays and FSS*. Wiley Interscience, 2003.

[130] D. Sievenpiper, "High–impedance electromagnetic surfaces," Ph.D. dissertation, Univ. of California, Los Angeles.

[131] Y. Qi, B. Hou, and W. Wen, "Band gaps from ring resonators and structural periodicity," *J. Phys. D: Appl. Phys.*, vol. 38, Feb. 2005.

[132] H. Chen *et al.*, "Magnetic properties of S–shaped split ring resonators," *Progrees in Electromagnets Research, PIER*, vol. 51, 231–247.

[133] M. C. S. Maci and A. Cucini, "A pole–zero matching method for EBG surfaces composed of a dipole FSS printed on a grounded slab," *IEEE Trans. Antennas Propag.*, vol. 53.

[134] M. Hiranandani, A. Yakovlev, and A. Kishk, "Artificial magnetic conductors realised by frequency–selective surfaces on a grounded dielectric slab for antenna applications," *IET Proc.-Microw. Antennas Propag.*, vol. 153 no5, 2006.

[135] S. Best and D. Hanna, "Design of a broadband dipole in close proximity to an EBG ground plane," *IEEE Antennas Propag. Mag.*, vol. 50 no6, Dec. 2008.

[136] G. Deschamps, "Microstrip microwave antennas," *3rd USAF Symposium on Antennas*.

[137] M. Nikolic, A. Djordjevic, and A. Nehorai, "Microstrip antennas with suppressed radiation in horizontal directions and reduced coupling," *IEEE Trans. Antennas Propag.*, vol. 53 no11, Nov. 2005.

[138] P. Gauthier, A. Courtay, and G. Rebeiz, "Microstrip antennas on synthesized low dielectric–constant substrates," *IEEE Trans. Antennas Propag.*, vol. 45, 1997.

[139] J. Yook and L. Katehi, "Micromachined microstrip patch antenna with controlled mutual coupling and surface waves," *IEEE Trans. Antennas Propag.*, vol. 49, 2001.

[140] E. Rajo-Iglesias *et al.*, "Design of a planar EBG structure to reduce mutual coupling in multilayer patch antennas," in *Proc. Loughborough Antennas and Propagaton Conference, LAPC2007*, Loughborough, UK, 2007.

[141] F. Y. Y. Rahmat-Samii, "Microstrip antennas integrated with electromagnetic band gap EBG structures: A low mutual coupling design for array applications," *IEEE Trans. Antennas Propag.*, vol. 51 no 10, Oct. 2003.

[142] N. Alexopoulos and D. Jackson, "Fundamental superstrate (cover) effects on printed circuit antennas," *IEEE Trans. Antennas Propag.*, vol. AP-32 no8, Aug. 1984.

[143] F. Yang and Y. Rahmat-Samii, *Electromagnetic band gap strucures in antenna engineering.* Cambridge University Press, 2008.

[144] ——, "Reflection phase characteristics of the EBG ground plane for low profile wire antennas," *IEEE Trans. Antennas Propag.*, vol. AP 51, Oct. 2003.

[145] F. Elek, R. Abhari, and G. Eleftheriades, "A uni–directional ring–slot antenna achieved by using electromagnetic band–gap surface," *IEEE Trans. Antennas Propag.*, vol. 53no1, 2005.

[146] G. Eleftheriades, *Negative–Refraction Metamaterials: Fundamental Principles and Applications.* IEEE, 2005.

[147] F. Cappolino, *Theory and Phenomena of Metamaterials.* CRC Press, 2009.

[148] C. Balanis, *Modern Antenna Handbook.* Wiley, 2008.

[149] D. Jackson and N. Alexopoulos, "Gain enhancement methods for printed circuit antennas." *IEEE Trans. Antennas Propag.*, vol. AP–33, 1985.

[150] Y. Yang and N. Alexopoulos, "Gain enhancement methods for printed circuit antennas through multiple superstrates." *IEEE Trans. Antennas Propag.*, vol. 35, 1987.

[151] S. Zhong, G. Liu, and G. Quasim, "Closed–form expressions for resonant frequency of rectangular patch antennas with multidielectric layers," *IEEE Trans. Antennas Propag.*, vol. AP–42, 1994.

[152] H. Arai, *Measurement of Mobile Antenna Systems.* Norwood, MA: Artech House, 2001.

[153] M. Clements and T. Weiland, "Discrete electromagnetism with the finite integration technique," *Progress In Electromagnetics Research.*

Appendix A

Antenna Theory Fundamentals

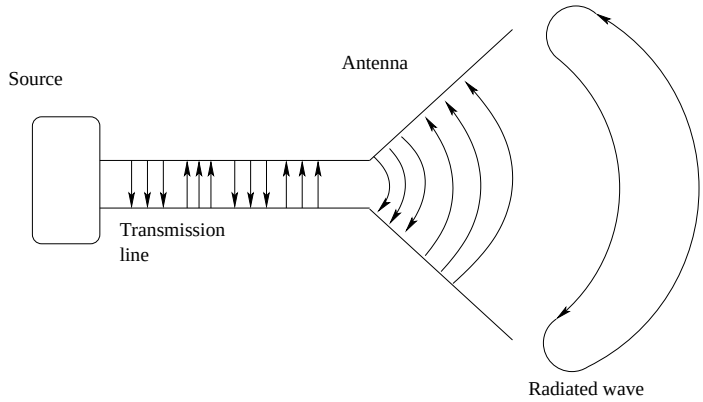

Figure A.1: A transmitting antenna

Electromagnetic energy can be travelling in free space or be guided by transmission lines and electronic systems. An antenna serves as a means to capture free space travelling EM energy and supply it to guided transmission lines and systems, or as a means to radiate the guided EM energy fed at its input. For this reason alone they are essential and play a critical role in all wireless communications systems. Realising that depending on the application different expectations are required by the candidate antenna perhaps in respect to directional illumination of space, or to the operational frequency and bandwidth, leads to the creation and necessity of many and various types of antennas. These can be, wire antennas, printed patch, reflector, lens, aperture in addition to many other.

Figure A.2 shows the equivalent circuit of a transmitting antenna, where, a source with open circuit amplitude V_S and internal impedance $Z_S = R_S + jX_S$, excites an antenna with input impedance $Z_A = R_A + jX_A$, where $R_A = R_L + R_R$, representing the radiation resistance and the dielectric and conductor losses present in the antenna. Therefore the voltage and current at the terminals of the antenna are

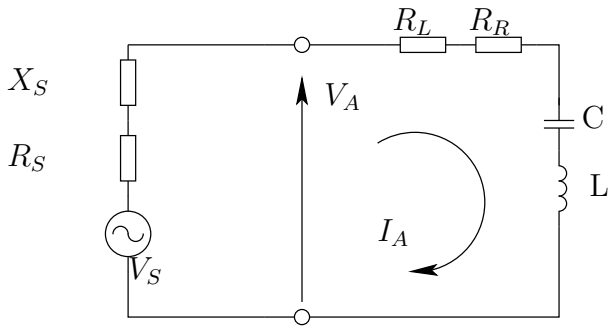

$$Z_S = R_S + jX_S$$
$$Z_A = R_L + R_R + jX_A$$

Figure A.2: Circuit of a transmitting antenna

$$I_A = \frac{V_S}{Z_S + Z_A}, \tag{A.1}$$

$$V_A = \frac{V_S Z_A}{Z_S + Z_A}. \tag{A.2}$$

From the voltage and current relations the time average absorbed power by the antenna is

$$P_A = \frac{1}{2}\Re\big[V_A I_A^*\big]. \tag{A.3}$$

As it is possible that an impedance mismatch may be present between the feed element and the antenna acting as the load, a reflection coefficient Γ is defined according to

$$\Gamma = \frac{Z_A - Z_S}{Z_A + Z_S}. \tag{A.4}$$

High frequency measurement equipment usually measure the reflected power and relate it to the impedance mismatch factor. The reflected power is called return loss and it relates the the reflection coefficient and scattering parameter as follows [152]

$$RL = 20\log_{10}|\Gamma| = 20\log_{10}|S_{11}|. \tag{A.5}$$

Due to the ohmic conductor and dielectric (if present) losses that are inevitable the radiated power will be less than the power absorbed by the antenna terminals. If we define e as the antenna efficiency, then the actual radiated power can be related

to the input power as follows

$$P_R = eP_A. \tag{A.6}$$

The power dissipated is equal to the difference between the input power and the radiated power

$$P_L = P_A - P_R. \tag{A.7}$$

Consequently the total power delivered to the antenna, the radiated power and the dissipated power are expressed as

$$P_A = \frac{1}{2}R_A|I_A|^2, \quad P_L = \frac{1}{2}R_L|I_A|^2, \quad P_R = \frac{1}{2}R_R|I_A|^2, \tag{A.8}$$

leading to an expression for the radiation efficiency

$$e = \frac{R_R}{R_L + R_R}. \tag{A.9}$$

The antenna input impedance as measured by most equipment consists of the combined radiation and loss resistance, however to evaluate the radiation efficiency both resistances must be known. The loss resistance can be measured with the Wheeler cap method [152].

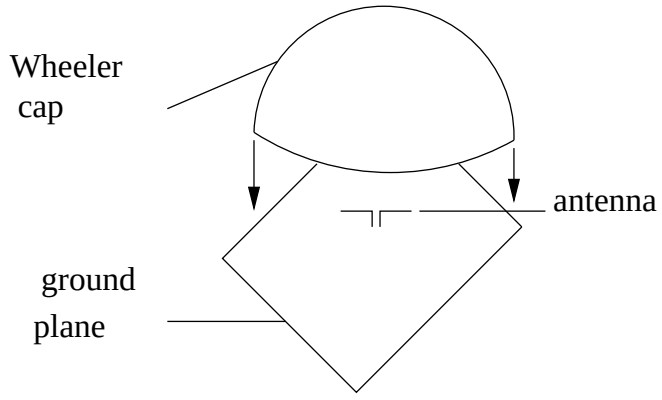

Figure A.3: Wheeler cap measurement method for radiation efficiency

Wheeler suggested that the loss resistance can be measured by placing the antenna under test above a ground plane and then covering it by a conductive cap. The cap length should be less that half wavelength so not to excite resonances in the cap, which will introduce measurement errors. The flow of currents on the antenna is

not modified by this procedure and the measured resistance with the cap cover is equal to the loss resistance, therefore knowing that the measured resistance without the cap consists of both radiation and loss resistance the radiation efficiency can be readily calculated.

A.1 Antenna Far Field

In the far field region the electric field generated by a transmitting antenna at an observation point r can be expressed as [61]

$$\begin{aligned} E(\mathbf{r}) &= \frac{e^{-jkr}}{r} F(\theta, \phi), \\ &= \frac{e^{-jkr}}{r} \left[F_\theta(\hat{\mathbf{k}})\hat{\theta} + F_\phi(\hat{\mathbf{k}})\hat{\phi} \right]. \end{aligned} \tag{A.10}$$

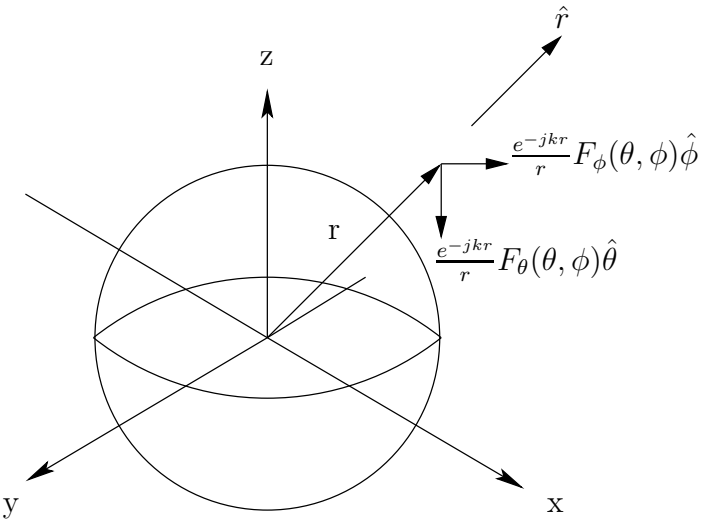

Figure A.4: Far field

The expressions only hold for far field region and do not apply to near field, simple conditions that must be met to qualify as far filed are, with d as the largest dimension of the antenna and r as the distance from the antenna,

$$r >> d, \quad r >> \lambda, \quad r >> \frac{2d^2}{\lambda}. \tag{A.11}$$

To compute the far field functions F_θ and F_ϕ knowledge of the electric currents on the antenna under consideration must be available, then the source field relationships

are

$$F(\hat{\mathbf{k}}) = \frac{1}{4\pi}\int\int\int \mathbf{J}(\mathbf{r})e^{jk\mathbf{r}\cdot\hat{\mathbf{k}}}d\mathbf{r}, \tag{A.12}$$

$$F_\theta(\hat{\mathbf{k}}) = -j\omega\mu_0\mathbf{F}(\hat{\mathbf{k}})\cdot\hat{\theta}, \tag{A.13}$$

$$F_\phi(\hat{\mathbf{k}}) = -j\omega\mu_0\mathbf{F}(\hat{\mathbf{k}})\cdot\hat{\phi}. \tag{A.14}$$

In all the expressions, $\hat{\mathbf{k}} = \hat{\mathbf{x}}\sin\theta\cos\phi + \hat{\mathbf{y}}\sin\theta\sin\phi + \hat{\mathbf{z}}\cos\theta$ and is representing a unit vector along the direction of the observation point $\mathbf{r}$, $k = 2\pi/\lambda$ and is the wavenumber, and $r = |\mathbf{r}|$. Due to conservation of energy and due to spherical spreading of the radiated wave the electric field attenuates as $1/r$. There is no component of the electric field on the direction of propagation, $\hat{\mathbf{r}}$, which is $\hat{\mathbf{r}} = \mathbf{r}/r$. Consequently the magnetic field in the far field in given as

$$H(\mathbf{r}) = \frac{1}{\eta}\big[\hat{\mathbf{r}}\times E(\mathbf{r})\big], \tag{A.15}$$

where η is the free space impedance. The radiation intensity is the power radiated per unit solid angle, with r being the distance from the antenna, it is expressed as

$$U(\hat{\mathbf{k}}) = r^2|W(\mathbf{r})|, \tag{A.16}$$

where $|W(\mathbf{r})|$ is the time average Poynting vector or average power density per m^2, as E is in (V/m) and H is in (A/m), and is defined as

$$W(\mathbf{r}) = \frac{1}{2}[E(\mathbf{r})\times H(\mathbf{r})^*]. \tag{A.17}$$

The unit of a solid angle is the steradian, in a sphere of radius r the surface area is $A = 4\pi r^2$, where there are 4π steradian $(4\pi r^2/r^2)$. The infinitesimal area of a sphere and the elemental solid angle are related as follows [32]

$$dA = r^2\sin\theta d\theta d\phi \quad (m^2), \tag{A.18}$$

$$d\Omega = \frac{dA}{r^2} = \sin\theta d\theta d\phi \quad (sr). \tag{A.19}$$

Since the Poynting vector is the power density per meter square, the total radiated power can be calculated by integrating the normal component of the Poynting vector

over a surface of a sphere that contains the antenna,

$$P = \oiint_S W(\mathbf{r}) \cdot d\mathbf{s} = \oiint_S W(\mathbf{r}) \cdot \hat{\mathbf{r}} dA = \frac{1}{2} \oiint_S \Re\big[E(\mathbf{r}) \times H(\mathbf{r})^*\big] \cdot d\mathbf{s}, \tag{A.20}$$

alternatively the total radiated power can be computed from the radiation intensity of the total solid angle of the sphere that contains the antenna,

$$P = \oiint_\Omega U(\hat{\mathbf{k}}) d\Omega = \int_0^{2\pi} \int_0^{\pi} U(\hat{\mathbf{k}}) \sin\theta \ \theta d\phi \tag{A.21}$$

A.2 Directivity and Gain

The directional properties of the radiation pattern of an antenna are described by its directivity D, which is defined as the ratio of the radiation intensity in a given direction over that of an isotropic source. An isotropic source has a radiation intensity equal in all directions, being the total radiated power divided by 4π, the total solid angle of a sphere. Therefore the directivity is defined as,

$$D = \frac{U}{U_0} = \frac{4\pi U}{P_{rad}}, \tag{A.22}$$

where D_0 denotes the directivity of an isotropic source. The gain of an antenna is essentially equivalent to the directivity with the antenna efficiency being taken into account, where now instead of the radiated power the input power at the antenna terminals is used, the gain is given as

$$G = eD \tag{A.23}$$

A.3 Quality factor and Bandwidth

The operational bandwidth of an antenna is closely related to the quality factor Q and the radiation efficiency, as well as the physical dimensions of the structure. Resonant antennas under simplifying assumptions, near resonance can be modelled as a series RLC microwave resonator, the equivalent circuit for such a case is shown

in figure A.2. In general a series RLC resonant circuit has an input impedance of the form,

$$Z_{in} = R + j\omega L - j\frac{1}{\omega C}. \tag{A.24}$$

The power dissipated in the antenna is

$$P_A = \frac{1}{2}|I|^2(R_L + R_R), \tag{A.25}$$

while the average magnetic and electric energy stored in the inductor and capacitor is , respectively [11]

$$W_m = \frac{1}{4}|I|^2 L, \qquad W_e = \frac{1}{4}|I|^2\frac{1}{\omega^2 C}. \tag{A.26}$$

The quality factor Q is defined as the average energy stored in the antenna over the power dissipated in the antenna, that is the radiated power plus the power lost due to ohmic and other losses. The resonant frequency is $\omega_0 = 1/\sqrt{CL}$ and at the resonance $W_m = W_e$. Therefore Q can be obtained from,

$$\begin{aligned} Q &= \omega\frac{W_m + W_e}{P_A} \\ &= 2\pi f_0 \frac{\frac{1}{4}|I|^2 L + \frac{1}{4}|I|^2\frac{1}{(2\pi f_0)^2 C}}{\frac{1}{2}|I|^2(R_L + R_R)} \\ &= \frac{1}{2\pi f_0(R_L + R_R)C} = \frac{1}{2\pi f_0 R_R C}\,\frac{R_R}{R_L + R_R} \\ &= Q_{lossless}\, e_{rad} \end{aligned} \tag{A.27}$$

Examining the input impedance behaviour of the antenna near resonance, for the series type the quality factor is related to it as follows,

$$Z_{in} = (R_A)(1 + jQv), \quad \text{with,} \quad v = \frac{f}{f_0} - \frac{f_0}{f}. \tag{A.28}$$

Therefore the half power fractional bandwidth, where $Z_{in} = 2R^2$ is inversely proportional to the quality factor and is given as

$$B = \frac{1}{Q} \tag{A.29}$$

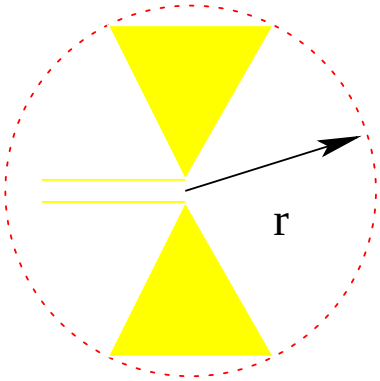

Figure A.5: Spehere of radius a containing the antenna

The bandwidth of an antenna is controlled by the resonant frequency and the quality factor, however the quality factor is related to the size of the antenna, for electrically small antennas there exists a limit on the achievable Q. This limit was first investigated by Chu [100] and later corrected by McLean [101]. To obtain the Q, Chu used spherical wave functions and the expression he derived is accurate when only the single lowest mode is excited be it TE or TM. The electrically small antenna ($ka < 1$) is enclosed by the smallest possible sphere with a radius a, that can contain it, the radiation Q_r in such a scenario is given as

$$Q_r = \frac{1}{(ka)^3} + \frac{1}{(ka)}, \quad \text{with} \quad k = \frac{2\pi}{\lambda}. \tag{A.30}$$

The above expression accounts for radiation alone and does not take into account other losses. Conductor and dielectric losses can be incorporated as follows,

$$Q_0 = \frac{1}{Q_r} + \frac{1}{Q_c} + \frac{1}{Q_d} = \left(\frac{1}{(ka)^3)} + \frac{1}{(ka)}\right) e_{rad}. \tag{A.31}$$

A.4 Linear wire antenna

Linear wire antennas are perhaps some of the oldest available and are widely used to this day due to ease of construction and analysis and due to some useful properties they may have. An infinitesimal dipole is a dipole with a length much smaller that the wavelength of the excited wave, it is then fair to assume that the current

distribution along the extremely small length is constant, additionally the radius of the dipole is extremely thin. Figure A.6 shows an infinitesimal dipole positioned symmetrically at the origin and aligned with the z axis.

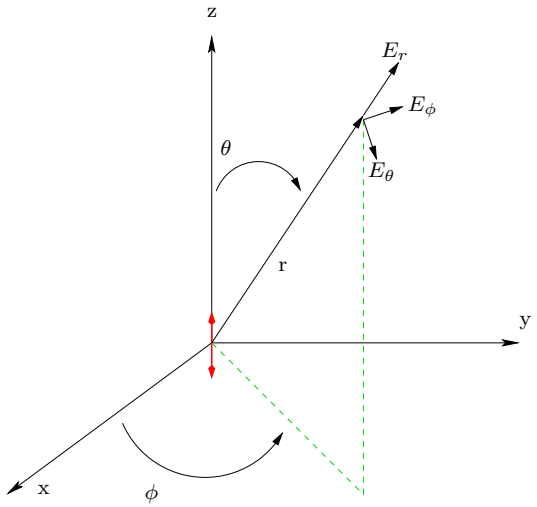

Figure A.6: Infinitesimal dipole aligned with the z axis

To find the radiated fields of the infinitesimal dipole and in fact most electromagnetic problems may require to determine auxiliary potential functions, that may appear as extra steps toward the solution where they actually simplify the problem. The auxiliary potential functions **A** and **F** are computed from an electric current source **J** and a magnetic current source **M** respectively. Where if **J** current density is known then **A** can be computed from [32]

$$\mathbf{A}(x,y,z) = \frac{\mu}{4\pi}\iiint_V \mathbf{J}(x',y',z')\frac{e^{-jkR}}{R}dv', \tag{A.32}$$

while **F** due to a magnetic current density **M** is obtained from,

$$\mathbf{F}(x,y,z) = \frac{\varepsilon}{4\pi}\iiint_V \mathbf{M}(x',y',z')\frac{e^{-jkR}}{R}dv', \tag{A.33}$$

where R is the distance from the source to the observation point, $k^2 = \omega^2\mu\varepsilon$, the primed coordinates represent the location of the source and the un–primed coordinates represent the observation point. The auxiliary vector potential functions are solutions of the inhomogeneous vector wave equation. The total electric and magnetic fields then can be obtained from the following relations [32]

$$\mathbf{E} = \mathbf{E}_A + \mathbf{E}_F = -j\omega\mathbf{A} - j\frac{1}{\omega\mu\varepsilon}\nabla(\nabla\cdot\mathbf{A}) - \frac{1}{\varepsilon}\nabla\times\mathbf{F}, \tag{A.34}$$

$$\mathbf{H} = \mathbf{H}_A + \mathbf{H}_F = \frac{1}{\mu}\nabla\times\mathbf{A} - j\omega\mathbf{F} - j\frac{1}{\omega\mu\varepsilon}\nabla(\nabla\cdot\mathbf{F}). \tag{A.35}$$

The infinitesimal dipole mentioned has only an electric current thus only $\mathbf{A}$ can be defined with $\mathbf{F}$ being zero. The current densities can be defined over a volume, or a surface or reduce to an electric current $\mathbf{I_e}$ along a line path . For the dipole of figure A.6 the potential function reduces to the line integral

$$\mathbf{A}(x,y,z) = \frac{\mu}{4\pi}\int_C \mathbf{I_e}(x',y',z')\frac{e^{-jkR}}{R}dl', \tag{A.36}$$

recalling that the dipole is at the origin, $x' = y' = z' = 0$, and due to the small length and orientation, $\mathbf{I_e}(x',y',z') = \hat{z}I_0$, therefore the vector potential $\mathbf{A}$ is expressed as

$$\mathbf{A}(x,y,z) = \hat{z}\frac{\mu I_0}{4\pi r}e^{-jkr}\int_{-l/2}^{l/2} dz' \tag{A.37}$$

In spherical coordinates the components of the auxiliary potential are written as

$$A_\phi = 0, \tag{A.38}$$

$$A_\theta = -A_z\sin\theta = -\frac{\mu I_0 l}{4\pi r}e^{-jkr}\sin\theta, \tag{A.39}$$

$$A_r = A_z\cos\theta = \frac{\mu I_0 l}{4\pi r}e^{-jkr}\cos\theta. \tag{A.40}$$

The relationship between the magnetic field $\mathbf{H}$ and the auxiliary vector potential $\mathbf{A}$ is

$$\mathbf{H} = \frac{1}{\mu}\nabla\times\mathbf{A}, \tag{A.41}$$

which leads to

$$H_\phi = j\frac{kI_0 l\sin\theta}{4\pi r}\left[1 + \frac{1}{jkr}\right]e^{-jkr}, \tag{A.42}$$

$$H_\theta = H_r = 0. \tag{A.43}$$

The electric field is related to the magnetic,

$$\mathbf{E} = \frac{1}{j\omega\varepsilon}\nabla \times \mathbf{H}, \tag{A.44}$$

which finally leads to the electric field components

$$E_\phi = 0, \tag{A.45}$$

$$E_\theta = j\eta\frac{kI_0 l\sin\theta}{4\pi r}\left[1 + \frac{1}{jkr} - \frac{1}{(kr)^2}\right]e^{-jkr}, \tag{A.46}$$

$$E_r = \eta\frac{I_0 l\cos\theta}{2\pi r^2}\left[1 + \frac{1}{jkr}\right]e^{-jkr}. \tag{A.47}$$

The electric field and its magnitude are equal to

$$\mathbf{E} = \hat{a}_r E_r + \hat{a}_\theta E_\theta \tag{A.48}$$

$$|\mathbf{E}| = \sqrt{|E_r|^2 + |E_\theta|^2} \tag{A.49}$$

Depending on the distance from the dipole antenna three regions can be defined, near field region where ($kr << 1$), intermediate region where ($kr > 1$), and far field region where ($kr >> 1$). In the far field region waves are TEM with a wave impedance equal to the intrinsic impedance of the medium, the components of E and H are perpendicular to each other and transverse to the radial direction of propagation, while the r variations are separable from those of θ and ϕ.

Recalling that the radiation resistance is related to the total radiated power, then for a lossless antenna by integrating the Poynting vector over a closed surface the total radiated power can be obtained, and consequently the real part of the total radiated power can be related to the radiation resistance. The Poynting vector of the dipole is

$$W = \frac{1}{2}(\hat{a}_r E_r + \hat{a}_\theta E_\theta) \times (\hat{a}_\phi H_\phi^*), \tag{A.50}$$

thus the complex total power in the radial direction is

$$P = \oiint_S W \cdot ds = \int_0^{2\pi}\int_0^{\pi}(\hat{a}_r W_r + \hat{a}_\theta W_\theta)\cdot \hat{a}_r r^2\sin\theta d\theta d\phi, \tag{A.51}$$

which finally gives the radiation resistance from the expression

$$P = \eta\Big(\frac{\pi}{3}\Big)\Big|\frac{I_0 l}{\lambda}\Big|^2 = \frac{1}{2}|I_0|^2 R_r \tag{A.52}$$

Appendix B

Time Domain Techniques

Advances in digital computing over the past few decades allowed numerous electromagnetic numerical modelling approaches to be employed. Simple electromagnetic guiding or radiating structures, as for example transmission lines or a half wave dipole may be possible to be analysed in closed form design equations or analytically thus providing acceptable designs and behaviour prediction. Nevertheless complex electromagnetic problems that may not have design rules or theory or methods that can be approximated by closed form equations that can be incorporated in a computer code to provide a quick yet relatively accurate design tool can only be solved with numerical electromagnetic techniques, for example how can one predict the radar cross section of a battle ship of an arbitrary shape, or how can one evaluate the performance of various antennas mounted on the body of satellite with no prototyping or measurement campaigns?

Due to the variety of the types of problems that can be solved in electromagnetism there exist different numerical techniques that each can be best suited for a given problem type.

The numerical methods used by most commercial software packages are the full wave Moment Method, the Finite Element Method and the Finite Difference Time Domain, however other methods exist as for example the Geometric Theory of Diffraction and Uniform Theory of Diffraction. The techniques can be combined to obtain tools that are more accurate and robust, able to handle most types problems. An advance tool could employ a hybrid MoM/UTD/FDTD code that then allows the simulation of planar antennas, 3 dimensional antennas and microwave components, radar cross section, propagation and even illumination of a detailed biological tissue. In general all numerical techniques will attempt to provide solutions either by us-

ing differential equation methods or by using integral equation methods applied to Maxwell's equations and the appropriate boundary conditions. Maxwell's equations in differential and integral form are given as

$$\nabla \times H = \frac{\partial D}{\partial t} + J \quad \text{Ampere Law} \tag{B.1}$$

$$\nabla \times E = -\frac{\partial B}{\partial t} - M \quad \text{Faraday Law} \tag{B.2}$$

$$\nabla \cdot D = \rho_e \quad \text{Gauss Law} \tag{B.3}$$

$$\nabla \cdot B = \rho_m \quad \text{Gauss Law} \tag{B.4}$$

The Maxwell's equations given are in the Partial Differential Equation formulation, the integral form of the equations can be derived using the Stokes and the divergence theorems.

$$\oint_C A \cdot dl = \iint_S (\nabla \times A) \cdot ds \quad \text{Stokes theorem} \tag{B.5}$$

$$\oiint_S A \cdot ds = \iiint_V \nabla \cdot A dv \quad \text{Divergence theorem} \tag{B.6}$$

$$\oint H \cdot dl = \iint_S J \cdot ds + \frac{\partial}{\partial t} \iint_S D \cdot ds \tag{B.7}$$

$$\oint E \cdot dl = -\iint_S M \cdot ds - \frac{\partial}{\partial t} \iint_S B \cdot ds \tag{B.8}$$

$$\oiint_S D \cdot ds = \iiint_V \rho_e dv = Q_e \tag{B.9}$$

$$\oiint_S B \cdot ds = \iiint_V \rho_m dv = Q_m \tag{B.10}$$

B.1 CST Microwave Studio and Finite Integration Technique

The finite integration technique is a time domain method that instead of the differential form of Maxwell's equations discretizes and solves the integral form of the equations. This technique was first introduced by Weiland,[116] [153]. The computational domain is a bounded space that is terminated in a perfectly absorbing medium, the domain encloses the simulated structure which can usually be treated as an open boundary problem. The computational space is then divided into grid cells by appropriate meshing methods. CST is actually constructing two computational grid meshes that are orthogonal to each other, the first is visible to the user from the graphical user interface while the second is not. The first grid is G while the second $\tilde{G}$. The grid of $\tilde{G}$ is defined by taking the foci of a cell of G as the grid position of an equivalent cell of mesh of $\tilde{G}$. This is shown in figure B.1. The first and primary grid defined as G is used to calculate the electric voltages e and magnetic fluxes b, the second grid orthogonal to the first defined as $\tilde{G}$ is used to compute the dielectric fluxes d and the magnetic voltages h. Fluxes are defined on facet of cells while voltages on the edges of cells.

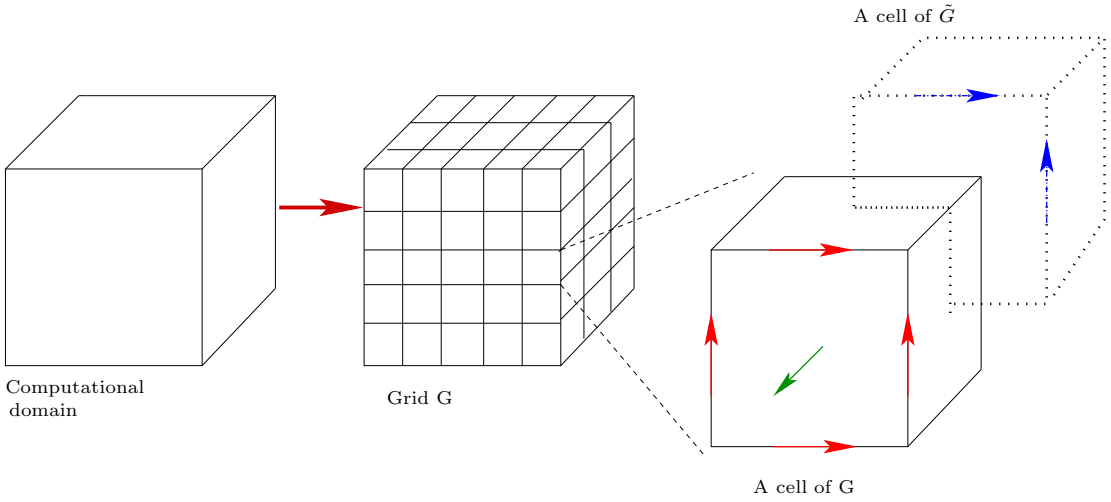

Figure B.1: Meshing and discetization method of finite integral technique

The concept is better understood when one considers a single cell in one of the grids and the Maxwell's equations. Figure B.2 shows a single cell of grid G, as was already mentioned mesh grid G holds the electric voltages along the edges of a cell

defined as the closed integral of the voltage values along the cell mesh edges and the magnetic flux on the cell facet defined as the integral of the magnetic flux value across the cell facet.

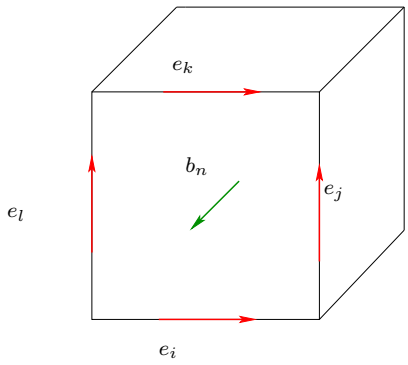

Figure B.2: One cell of the primary grid mesh G, where the electric voltages are allocated on the edges of the cell and the magnetic flux is allocated on the facet of the cell.

If the integral form of Faraday's law is applied to the cell shown in figure B.2 at the facet towards the reader, then the four electric voltages and the magnetic flux can be written as

$$e_i + e_j - e_k - e_l = -\frac{\partial}{\partial t} b_n \tag{B.11}$$

The procedure can be repeated for all cell facets. Therefore the discrete form of Faraday's law can be represented as

$$Ce = -\frac{\partial}{\partial t} b \tag{B.12}$$

where C is a matrix that stores topological and incidence relations in a cell within the grid G and represents the discrete equivalent of the curl operator. Figure B.3 shows the same cell as figure B.2 however now the magnetic fluxes on all six facets are shown on the cube, this allows to apply Gauss magnetic law which implies that the integration of the flux over a closed surface equals the total charge contained in the volume that is defined by the closed surface, recalling that there may be no magnetic charges inside the cell volume, leads to the expression

$$-b_1 + b_2 - b_3 + b_4 - b_5 + b_6 = 0 \tag{B.13}$$

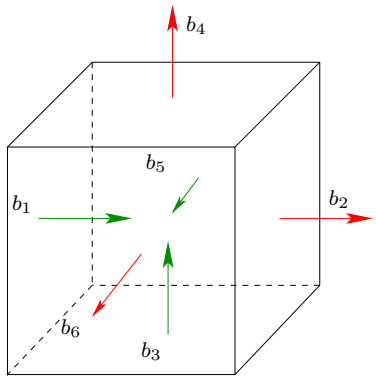

Figure B.3: One cell of the primary grid mesh G, showing all the magnetic fluxes on the six cell facets.

The discrete form of the divergence operator can be represented by a matrix that as before contains incidence and topology information in relation to the cells and facets of the mesh grid G,

$$Sb = 0 \tag{B.14}$$

So far two of Maxwell's equations have been applied to the cells of mesh grid G, the remaining two of Maxwell's equations are to be applied on the secondary orthogonal mesh grid $\tilde{G}$. This operation requires the definition of two more discrete matrices for the curl and divergence of the dual grid, in all of these matrices the elements that populate them are either $0, 1, -1$.

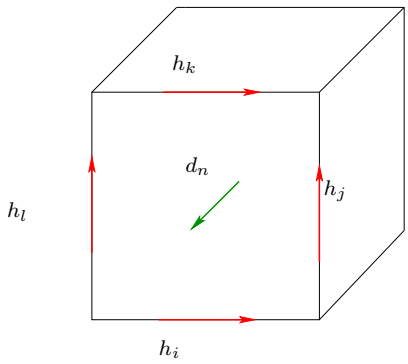

Figure B.4: One cell of the dual grid mesh $\tilde{G}$, showing the magnetic voltages along the cells facet edges and the electric flux crossing the surface of the facet.

Figure B.4 is an implementation of Ampere's law on a cell of the dual mesh grid $\tilde{G}$, the magnetic voltages the displacement current and the electric current can be expressed as follows

$$h_i + h_j - h_k - h_l = \frac{\partial}{\partial t} d_n + j \tag{B.15}$$

Therefore the discrete form of Ampere's law defined on the dual mesh grid $\tilde{G}$ is written as

$$\tilde{C}h = \frac{\partial}{\partial t} d + j \tag{B.16}$$

By analogy the discrete form of Gauss electric law is as follows

$$\tilde{S}d = q \tag{B.17}$$

where as previously the matrix operators $\tilde{C}$ and $\tilde{S}$ represent discrete versions of the curl and divergence respectively. Equations B.12, B.14, B.16, B.17 are Maxwell's Grid Equations in an finite integral technique formulation. The discrete versions of curl and divergence maintain their properties

$$SC = \tilde{S}\tilde{C} = 0, \quad C\tilde{S}^T = \tilde{C}S^T = 0 \tag{B.18}$$

The constitutive parameters describe material properties and can relate the voltages to the fluxes, they introduce errors due to spatial discretization were the grid resolution will produce approximations and averaging of their values. The parameters can be expressed in terms of matrices [116]

$$d = M_\varepsilon e \tag{B.19}$$

$$b = M_\mu h \tag{B.20}$$

$$j = M_\sigma e + j_s \tag{B.21}$$